SAPIENZA
UNIVERSITÀ DI ROMA

A search for third-generation leptoquarks in the non-resonant production with the ATLAS experiment and development of the Level-0 muon trigger for the High Luminosity LHC

Scuola di dottorato Vito Volterra

Dottorato di Ricerca in Fisica – XXXVI Ciclo

Candidate

Federico Morodei
ID number 1696103

Thesis Advisor

Dr. Massimo Corradi

A thesis submitted in partial fulfillment of the requirements
for the degree of Doctor of Philosophy in Physics

February 2024

Thesis defended on 20 May 2024
in front of a Board of Examiners composed by:

Prof. Francesca Di Lodovico
Prof. Caterina Doglioni
Dr. Marco Rescigno (chairman)

A search for third-generation leptoquarks in the non-resonant production with the ATLAS experiment and development of the Level-0 muon trigger for the High Luminosity LHC

Ph.D. thesis. Sapienza – University of Rome

This thesis has been typeset by LaTeX and the Sapthesis class.

Version: May 20, 2024

Author's email: federico.morodei@uniroma1.it

Abstract

Recent observations performed by several high-energy physics experiments have shown anomalies in b-hadron decays, which could be explained by assuming the existence of a particle, the leptoquark, coupled both to leptons and quarks. Such measurements also suggest a preferential coupling to third-generation fermions. In this thesis, a search for third-generation leptoquarks is presented, considering the non-resonant leptoquark production. The non-resonant production is expected to yield high sensitivity from the large interference term between the Standard Model Drell-Yan process and the leptoquark t-channel exchange. The leptoquark search uses the $140\,\text{fb}^{-1}$ of pp collision data collected by the ATLAS detector during the LHC Run 2 and considers di-lepton final state events, with at least one hadronically decaying tau-lepton. Deviations from the Standard Model predictions are looked for in the visible invariant mass spectrum of the di-lepton system, binned in b-jet multiplicity. In the absence of a significant deviation, exclusion limits are determined on the leptoquark coupling for different leptoquark mass values.

This thesis also presents a contribution to the upgrade of the ATLAS Muon Spectrometer in preparation for the High-Luminosity LHC. In order to cope with the much harsher conditions of the high-luminosity phase of the LHC, the entire trigger and readout electronics of the Resistive Plate Chamber detectors in the barrel region of the Muon Spectrometer will be replaced and novel FPGA-based boards will be installed. On-detector Data Collector and Transmitter boards will collect the front-end data and transmit them to off-detector Sector Logic boards, which will execute the Level-0 Muon trigger algorithm and the readout logic. In this thesis, the development of the firmwares that will be implemented in the FPGAs of the Data Collector and Transmitter boards and of the barrel Sector Logic boards is presented.

Acknowledgments

Here we are, at the end of a long and difficult journey, undertaken many years ago. When it started, achieving this goal looked almost impossible to me, but the help of a lot of people along the way made it feasible. And, to those people, I would like to express all my gratitude. To Massimo, who accepted to be my thesis director and has always given me good advice in any situation. To Riccardo and Matteo, who have always been willing to help and guided me through the countless issues encountered in these years. To Stefano, who introduced me to the ATLAS group at the time of my Master Degree thesis and has always supported my choices. To Giovanni, Elena, Graziella, Davide, Lorenzo and all the other people of the ATLAS saletta, with whom I shared anxieties, frustrations, doubts, but also laughter and moments of lightness throughout these years. To Simone, Antonio and Tiziano, for the poker nights and all the other moments spent together, even if from a long distance, which gave me some distraction from work. To my mother, my father, Ilaria and all my family, who always supported me in everything and gave me all the help I needed. And finally, to Valentina, who has always been by my side, with extreme patience and affection. I don't know how I would have done it without her.
So, to all of you, sincerely, thank you!

Contents

Introduction

The Standard Model is currently the most accurate and elegant theory to describe and predict the fundamental interactions between all known particles. Despite its huge success, however, observations from high-energy physics experiments, which cannot be explained inside the Standard Model frame, are piling up. Countless theoretical models have been proposed in the attempt to extend the Standard Model with additional interactions and particles and give an explanation for the observed anomalies. Task of the experiments studying the physics processes produced at a collider like the LHC is testing these models to confirm or reject their hypotheses. In order to perform this task, the experiments have to employ particle detectors which have to be continuously upgraded to achieve increasingly higher precision and efficiency and adapt to the changing conditions of the collider. The work presented in this thesis can be broadly divided into two parts, each corresponding to one of the two main aspects of a high-energy physics experiment: the analysis of the data collected by the particle detector and the development, maintenance and upgrade of the detector components.

The part of the thesis dealing with data analysis presents a search conducted in the ATLAS experiment at the LHC looking for a theoretical particle, the leptoquark, coupling both with leptons and quarks. Great interest in the leptoquark models has been aroused recently in the high-energy physics community since such models are able to give an explanation of anomalies observed in the decay of b-hadrons by the BaBar and LHCb experiments. The analysis presented in this thesis assumes a simplified leptoquark model, the U_1 model, in which the leptoquark couples only to tau-leptons and b-quarks. The analysis focuses on the non-resonant leptoquark production, which, through a large interference term with the Drell-Yan Standard Model process, allows it to achieve a high signal sensitivity. The search is performed by selecting events with a couple of leptons in the final state, of which at least one is a tau-lepton, and analysing the distribution of the visible invariant mass of the di-lepton system, looking for deviations from the Standard Model expectation. The analysis of a process involving tau-leptons is not trivial, due to the large background contamination from events with fake tau-leptons deriving from hadronic jets misreconstructed as tau-leptons. Such background cannot be modelled accurately by Monte Carlo simulations and therefore an innovative data-driven technique is used in this analysis to predict the fake-tau background contribution. A profile-likelihood fit is then performed and the distributions obtained with the full Run 2 dataset collected by the ATLAS detector are used to test the two hypotheses, the one assuming only the Standard Model and the one including also the leptoquark signal. In the

case no significant deviation from the Standard Model prediction is observed, exclusion limits are set on the leptoquark coupling parameter for several leptoquark mass scenarios.

The second part of the thesis deals instead with the development and upgrade of some components of the ATLAS detector. The ATLAS detector will undergo a major upgrade, referred to as Phase-II Upgrade, in which many parts of the detector will be improved or replaced to adapt to the much harsher radiation levels and luminosity conditions expected for the High-Luminosity LHC program, foreseen to start in 2029. In particular, the entire trigger and readout electronics of the Resistive Plate Chambers (RPCs), which are the detectors used to generate muon trigger candidates in the barrel region of the ATLAS Muon Spectrometer, will be replaced. New boards will be installed to collect the detector hits, perform the trigger algorithm, store the muon hit data and transmit them to the rest of the ATLAS systems. These boards are based on advanced FPGA devices, which allow them to run complex algorithms in a very short time. The Data Collector and Transmitter (DCT) boards will be installed on-detector to collect and digitise the RPC front-end signals. The barrel Sector Logic (SL) boards will instead be placed off-detector to receive the muon hit data from the DCT boards, execute the trigger algorithm and perform the readout logic. In this thesis, the development of the firmwares to be implemented on the DCT and the SL FPGAs is presented. The design of such firmwares has been a particularly challenging task, due to the limited resources available in the FPGA devices and the very strict timing constraints to satisfy.

The thesis is organised as follows. Chapter 1 presents the Standard Model of particle physics, describing briefly the fundamental particles currently known and their interactions, and introduces a leptoquark model which could explain some of its open issues. Chapter 2 describes the LHC and the ATLAS detector with all its components. Chapter 3 illustrates the techniques employed by the ATLAS experiment to reconstruct and identify all the types of Standard Model particles from the signals collected by its sub-detectors. Chapter 4 presents the analysis searching for third-generation leptoquarks in the non-resonant production and the preliminary results obtained so far. Chapter 5 introduces the main changes that the ATLAS detector will undergo during the Phase-II Upgrade, describes the Level-0 Muon Barrel trigger system designed for the High-Luminosity LHC and presents a test performed to validate the DCT-SL communication protocol. Chapter 6 presents the development and implementation of the DCT FPGA firmware, while Chapter 7 describes the development and implementation of the SL FPGA firmware.

Chapter 1

The Standard Model and beyond

The Standard Model of particle physics is currently the theory that best describes three out of the four known fundamental interactions between elementary particles. This theory has been developed starting from the 1960s and in the following decades it grew, becoming more and more complete and receiving countless confirmations from all kinds of high-energy physics experiments. With the discovery of the Higgs boson by the ATLAS and CMS experiments at the LHC, all the particles foreseen by the Standard Model have been discovered and their properties measured with high precision, showing an impressive agreement with the theoretical predictions. However, the Standard Model has its limits, since there are several open issues, both theoretical and experimental, which it is still not able to explain. Among the several Standard Model extensions that have been developed to try to explain the deviations from the Standard Model predictions coming from different experimental observations, the leptoquark models are particularly appealing for their capability to explain the anomalies in B-meson decays.

In this chapter, the fundamentals of the Standard Model theory of particle physics are presented, with a brief description of electroweak and strong interactions and of the Higgs-Brout-Englert mechanism. Then the limits and the open issues of the Standard Model are discussed, followed by the presentation of a theoretical model which introduces a leptoquark field to explain B-meson anomalies.

1.1 The elementary particles of the Standard Model

All the forces known in Nature can be traced back to four fundamental interactions: strong, electromagnetic, weak and gravitational. They have different strengths and ranges and are conveyed by distinct carriers, called *gauge bosons*, which mediate the interactions between the particles (see Table 1.1). The Standard Model (SM) is the quantum field theory (QFT) that describes the first three interactions. The gravitational interaction is not included in this model, but its strength, with respect to the other interactions, is so weak that its effects are completely

negligible at the particle level for energies below the Planck scale ($\mathcal{O}(10^{19})$ GeV). Attempts are being made to unify also the fourth interaction with the others, trying to construct a quantum theory of gravity. However, there is still no experimental evidence of the existence of a hypothetical carrier of the gravitational interaction (referred to as graviton).

Table 1.1. The four fundamental interactions with the corresponding strength, the typical interaction range and their carriers.

Interaction	**Relative strength**	**Range [m]**	**Carriers**
Strong	1	10^{-15}	gluons
Electromagnetic	10^{-2}	∞	photon
Weak	10^{-6}	10^{-18}	$W^{\pm}/Z$
Gravitational	10^{-38}	∞	graviton

The Standard Model is a non-abelian gauge theory where the dynamic variables are *quantised fields* $\psi(x)$, linear operators on the Hilbert space of the state operators, which depend on the space-time location and have definite transformation properties for changes from one reference system to another. The field dynamics can be generated from the Lagrangian density $\mathcal{L}(\psi, \partial_\mu \psi)$, a function of the local fields and their space-time derivatives. The equation of motion of the fields is derived by applying the principle of least action to $\mathcal{L}(\psi, \partial_\mu \psi)$:

$$\delta \left(\int d^4x \mathcal{L}(\psi, \partial_\mu \psi) \right) = 0, \tag{1.1}$$

from which

$$\partial^\mu \left(\frac{\partial \mathcal{L}}{\partial \partial_\mu \psi} \right) = \frac{\partial \mathcal{L}}{\partial \psi}. \tag{1.2}$$

The SM Lagrangian density is constructed requiring all its terms to be translational, rotational and boost invariant. It has to take into account also the conserved currents and charges observed in nature, which, according to Noether's theorem, correspond to continuous symmetries of the Lagrangian density. Hence, the SM Lagrangian density must be gauge invariant under the local symmetry group

$$SU(3)_C \otimes SU(2)_L \otimes U(1)_Y. \tag{1.3}$$

$SU(3)_C$ is the symmetry group of strong interactions and its conserved charge is called *colour* charge, while $SU(2)_L \otimes U(1)_Y$ is the symmetry observed by the electroweak interactions, which unify the electromagnetic and the weak forces and conserve the *weak isospin* and the *weak hypercharge*.

All the elementary particles of the Standard Model, which are the excitations of the respective fields, can be divided into two categories: *fermions* and *bosons*. Fermions are the constituents of ordinary matter, have half-integer spin and are divided into 3 generations. Each generation consists of a neutrino, electrically neutral, a lepton of unitary electric charge and two quarks, with electric charges respectively $2/3$ and $-1/3$. Neutrinos are subject only to the weak interaction, while charged leptons also to the electromagnetic one. Quarks, instead, interact through all of the three SM interactions and are the constituents of mesons and baryons, heavier composite particles. Gauge bosons are the quanta of the gauge fields[1], have integer spin and mediate the interactions between the other particles. Lastly, there is the Higgs boson, quantum excitation of the Higgs scalar field, which is responsible for the mass of SM particles. The Higgs boson represented the last missing piece of the Standard Model and its discovery in 2012 by the ATLAS and CMS experiments [1,2] constituted a very strong confirmation of the validity of this theory. For each particle, there exists a corresponding *antiparticle*, connected to the particle by the CPT transformation, a combination of charge conjugation, parity inversion and time reversal. The *CPT theorem* guarantees that the mass, spin and lifetime of a particle and its antiparticle are exactly equal, while their other quantum numbers are opposite[2]. A scheme of all the Standard Model elementary particles is shown in Figure 1.1.

1.2 Electroweak interactions

Electroweak interactions [3] unify the electromagnetic and the weak interactions and are based on the $SU(2)_L \otimes U(1)_Y$ symmetry group, whose conserved charges are the *weak isospin* (I_W) and the *weak hypercharge* (Y_W). These two charges are related to the electric charge Q by the following expression:

$$Q = I_{3_W} + \frac{Y_W}{2}, \tag{1.4}$$

where I_{3_W} is the third component of the weak isospin. The $SU(2)_L$ symmetry group has 3 generators, while $U(1)_Y$ only one, so there are in total four gauge fields for electroweak interactions: a triplet $\vec{W}_\mu = (W^1_\mu, W^2_\mu, W^3_\mu)$ with $I_W = 1$ and $Y_W = 0$, which interacts with the weak isospin of particles, and a singlet B_μ with $I_W = 0$ and $Y_W = 0$, which interacts with the weak hypercharge. However, these four fields are not the physical fields that mediate the interactions. The fields $W^\pm_\mu$, which mediate the charged current weak interactions, A_μ and Z_μ, which mediate the electromagnetic and the neutral current weak interactions respectively, are obtained

[1] The number of the gauge fields is equal to the number of generators of each symmetry group.

[2] To each particle, several quantum numbers are associated, such as lepton number, baryon number, electric charge, parity.

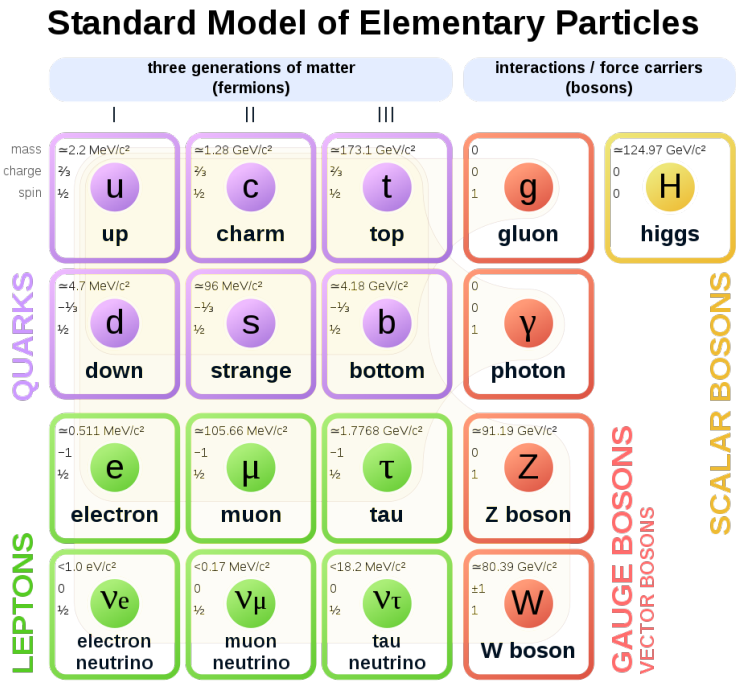

Figure 1.1. Elementary particles of the Standard Model with the respective mass, electric charge and spin values.

through a linear combination of the $\vec{W}_\mu$ components and B_μ in the following way:

$$\begin{aligned} W_\mu^\pm &= \frac{1}{\sqrt{2}}\left(W_\mu^1 \mp i W_\mu^2\right), \\ A_\mu &= \sin\theta_W\, W_\mu^3 + \cos\theta_W\, B_\mu, \\ Z_\mu &= \cos\theta_W\, W_\mu^3 - \sin\theta_W\, B_\mu, \end{aligned} \tag{1.5}$$

where θ_W is the Weinberg angle, defined by the following relations between the coupling constants of the weak isospin (g_w) and of the weak hypercharge (g_y):

$$\cos\theta_W = \frac{g_w}{\sqrt{g_w^2 + g_y^2}}, \qquad \sin\theta_W = \frac{g_y}{\sqrt{g_w^2 + g_y^2}}. \tag{1.6}$$

The coupling between the vector bosons and the other particles depends on their chirality. The $W^\pm$ is coupled only to states with left-handed chirality, while the Z boson and the photon also to right-handed states. For this reason, the left-handed components of SM fermions are organised in weak isospin doublets with $I_W = 1/2$:

$$\begin{pmatrix} \nu_e \\ e^- \end{pmatrix}_L, \quad \begin{pmatrix} \nu_\mu \\ \mu^- \end{pmatrix}_L, \quad \begin{pmatrix} \nu_\tau \\ \tau^- \end{pmatrix}_L \tag{1.7}$$

for the lepton sector and

$$\begin{pmatrix} u \\ b \end{pmatrix}_L, \quad \begin{pmatrix} c \\ s \end{pmatrix}_L, \quad \begin{pmatrix} t \\ b \end{pmatrix}_L \tag{1.8}$$

for the quark sector[3]. The right-handed fermions, instead, are weak isospin singlets ($I_W = 0$):

$$(e^-)_R, \quad (\mu^-)_R, \quad (\tau^-)_R \tag{1.9}$$

for the lepton sector and

$$(u)_R, \quad (d)_R, \quad (c)_R, \quad (s)_R, \quad (t)_R, \quad (b)_R \tag{1.10}$$

for the quark sector. Right-handed neutrinos do not appear in the previous list because they are not included in the Standard Model[4]. For the antiparticles, instead, there are right-handed doublets and left-handed singlets.

A Lagrangian density invariant under the $SU(2)_L \otimes U(1)_Y$ symmetry can be expressed as follows:

$$\mathcal{L}_{EW} = \mathcal{L}_g + \mathcal{L}_f. \tag{1.11}$$

The first term in 1.11 describes the evolution of the free gauge fields:

$$\mathcal{L}_g = -\frac{1}{4} W^A_{\mu\nu} W_A^{\mu\nu} - \frac{1}{4} B_{\mu\nu} B^{\mu\nu} \tag{1.12}$$

with $B_{\mu\nu}$ and $W^A_{\mu\nu}$ ($A = 1, 2, 3$) the gauge field tensors, given respectively by

$$B_{\mu\nu} = \partial_\mu B_\nu - \partial_\nu B_\mu \tag{1.13}$$

and

$$W^A_{\mu\nu} = \partial_\mu W^A_\nu - \partial_\nu W^A_\mu - g_w f^{ABC} W^B_\mu W^C_\nu, \tag{1.14}$$

where g_w is the coupling constant and f^{ABC} the weak isospin structure constants, which are defined by the following commutation rule between the weak isospin generators τ^A ($A = 1, 2, 3$):

$$\left[\tau^A, \tau^B\right] = i f^{ABC} \tau^C. \tag{1.15}$$

The second term in 1.11 is the fermion kinetic term, which describes also the interaction of fermions with the gauge bosons through the use of the covariant derivative D_μ:

$$\mathcal{L}_f = \sum_l \bar{\psi}_l i \not{D} \psi_l + \sum_r \bar{\psi}_r i \not{D} \psi_r, \tag{1.16}$$

where the index l runs over all the left-handed doublets and the index r over the right-handed singlets of the fermion states. In 1.16, $\not{D} = \gamma^\mu D_\mu$ is the contraction between the Dirac matrices γ^μ and the covariant derivative, which has a different expression depending on the chirality of the state it is applied to (for the fact that $W^\pm$ is not coupled to right-handed fermions):

$$\begin{aligned} (D_\mu)_L &= \partial_\mu - i\frac{g_w}{2}\tau^A W^A_\mu - i\frac{g_y}{2} Y_W B_\mu, \\ (D_\mu)_R &= \partial_\mu - i\frac{g_y}{2} Y_W B_\mu. \end{aligned} \tag{1.17}$$

[3] Actually the $W^\pm$ are coupled not directly to the d, s and b quarks but to rotated states d', s' and b' obtained through the application of a rotation matrix (the Cabibbo-Kobayashi-Maskawa matrix) to the original states.

[4] Right-handed neutrinos do not exist or, at least, they cannot interact with any SM particle, making it impossible to prove their existence.

1.3 The Higgs-Brout-Englert mechanism

1.3.1 Electroweak symmetry breaking

In the Lagrangian density of electroweak interactions it is not possible to introduce explicitly mass terms, because they do not respect invariance under $SU(2)_L \otimes U(1)_Y$ symmetry transformations. As a consequence, all SM particles should be massless, in contradiction with experimental evidence. However, particles can acquire a mass through a mechanism postulated by Higgs, Brout and Englert in 1964 [4, 5] and then experimentally confirmed in 2012 with the discovery of a particle compatible with the Higgs boson. The idea behind the Higgs-Brout-Englert mechanism is to introduce in the electroweak Lagrangian density a complex scalar field ϕ, referred to as Higgs field, which is a weak isospin doublet ($I_W = 1/2$) and has weak hypercharge $Y_W = 1$:

$$\phi(x) = \begin{pmatrix} \phi^+(x) \\ \phi^0(x) \end{pmatrix}. \tag{1.18}$$

This means adding in 1.11 the terms describing the dynamics and the potential of the Higgs field:

$$\mathcal{L}_h = (D_\mu \phi)^\dagger (D^\mu \phi) - V(\phi), \tag{1.19}$$

where the covariant derivative D_μ has the same expression as the first in 1.17. The potential of the Higgs field in 1.19 can be expressed as

$$V(\phi) = \mu^2 \phi^\dagger \phi + \lambda (\phi^\dagger \phi)^2, \tag{1.20}$$

where the parameter λ must be positive to obtain a stable theory. Since $\lambda > 0$, the potential has a finite lower bound, which defines a ground state (*vacuum* state). The sign of μ^2 determines if the vacuum state is degenerate or not. If $\mu^2 > 0$ the potential has a minimum in $\phi = 0$ and the vacuum state is unique. If instead $\mu^2 < 0$, the potential assumes the form illustrated in Figure 1.2. In this case the configuration with $\phi = 0$ is no longer a minimum of the potential, but a local maximum. The minimum of the potential is reached at all the points of a circle centred at the origin, resulting in a degenerate vacuum state. The degeneracy of the minimum of the potential can be resolved by introducing a *driving term* in 1.19, a small additional term with a complex parameter ϵ, which eventually is made tend to zero. The Higgs Lagrangian term thus becomes

$$\mathcal{L}_\epsilon = (D_\mu \phi)^\dagger (D^\mu \phi) - \left[V(\phi) - \epsilon^* \phi - \epsilon \phi^\dagger \right]. \tag{1.21}$$

The driving term forces the potential to have only one minimum, steering it in a preferential direction, and the vacuum state assumes the following form:

$$\phi_{ground} = \frac{1}{\sqrt{2}} \begin{pmatrix} 0 \\ v \end{pmatrix}, \tag{1.22}$$

where $v = \sqrt{-\mu^2/\lambda}$ is called the vacuum expectation value of the Higgs field and its measured value is 246 GeV.

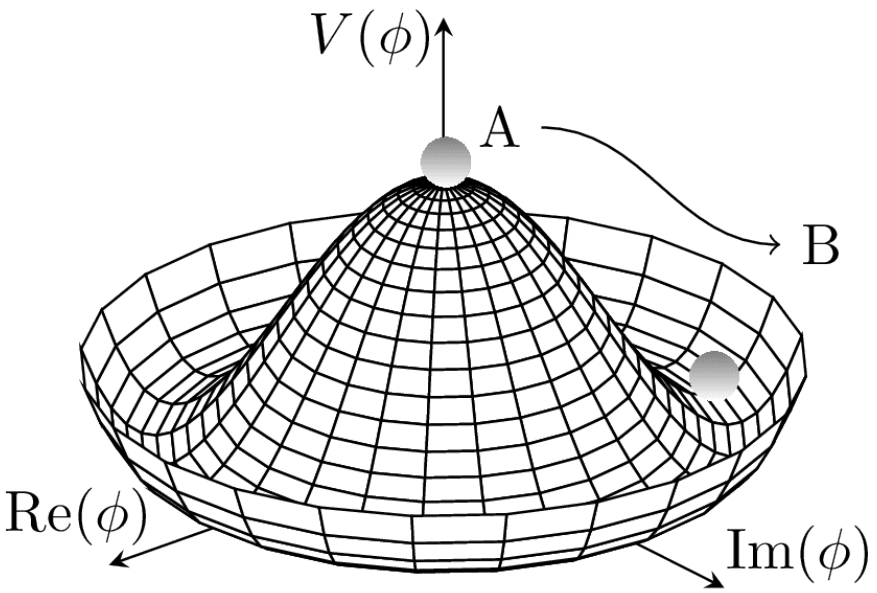

Figure 1.2. The Higgs potential with $\lambda > 0$ and $\mu^2 < 0$.

By the application of perturbation theory around the minimum, two particles are obtained, one with a mass of $2\lambda v^2$ and the other one massless (*Goldstone boson*). Since no particle observed in nature corresponds to the Goldstone boson, it can be removed through the application of an opportune gauge (*unitary gauge*), which yields two massive fields, a scalar field h and a vector field A, with masses

$$\begin{aligned} m_h^2 &= -2\mu^2 = 2\lambda v^2, \\ m_A^2 &= e^2 v^2. \end{aligned} \tag{1.23}$$

As a consequence of the unitary gauge, the expression of the field ϕ around the minimum now includes a massive scalar field $h(x)$, which represents the Higgs boson:

$$\phi(x) = \frac{1}{\sqrt{2}} \begin{pmatrix} 0 \\ v + h(x) \end{pmatrix}. \tag{1.24}$$

Therefore, through the Higgs-Brout-Englert mechanism, the minimum energy configuration is no longer symmetric, the electroweak symmetry is spontaneously broken and in its place the electric charge symmetry is left:

$$SU(2)_L \otimes U(1)_Y \longrightarrow U(1)_{EM}. \tag{1.25}$$

1.3.2 Gauge boson masses

After the spontaneous symmetry breaking, the interaction of the Higgs boson with the other particles gives rise to their masses. The mass of the gauge bosons can be derived from the kinetic term in 1.19 evaluated on the vacuum state of the

Higgs field. Indeed, considering that the covariant derivative has the form expressed in the first equation of 1.17, the kinetic term becomes

$$(D_\mu\phi)^\dagger(D^\mu\phi) = \\ = \frac{1}{2}\left(\frac{v^2 g_w^2}{4}\right)\left[\left(W_\mu^1\right)^2 + \left(W_\mu^2\right)^2\right] + \frac{1}{2}\frac{v^2}{4}\left(g_w W_\mu^3 - g_y B_\mu\right)^2, \quad (1.26)$$

which, considering the relations in 1.5, can be expressed in terms of the physical fields $W_\mu^\pm$, A_μ and Z_μ:

$$\begin{aligned}(D_\mu\phi)^\dagger(D^\mu\phi) &= \frac{g_w^2 v^2}{4} W_\mu^+ W^{-\mu} + \frac{1}{2}\frac{(g_w^2+g_y^2)v^2}{4} Z_\mu Z^\mu \\ &= M_W^2 W_\mu^+ W^{-\mu} + \frac{1}{2} M_Z^2 Z_\mu Z^\mu.\end{aligned} \quad (1.27)$$

In 1.27 it is possible to recognise the mass terms of the $W_\mu^\pm$ and Z_μ bosons and identify their masses as

$$\begin{aligned}M_W &= \frac{g_w v}{2}, \\ M_Z &= \frac{\sqrt{g_w^2+g_y^2}\,v}{2} = \frac{M_W}{\cos\theta_W}.\end{aligned} \quad (1.28)$$

Therefor, the mass terms of the $W_\mu^\pm$ and Z_μ bosons are generated dynamically through the symmetry breaking of the electroweak symmetry. However, after the symmetry breaking, the Lagrangian density is still invariant under $U(1)$ and no mass term is generated for the electromagnetic field A_{mu}: the photon indeed is massless.

1.3.3 Fermion masses

As in the case of gauge bosons, it is not possible to introduce explicitly a mass term for the fermion fields ψ in the electroweak Lagrangian density. Indeed a mass term like

$$\mathcal{L}_{mass} = -m\bar{\psi}\psi = -m(\bar{\psi_L}\psi_R + \bar{\psi_R}\psi_L) \quad (1.29)$$

would be not invariant under the $SU(2)_L \otimes U(1)_Y$ symmetry. However, after the symmetry breaking introduced through the Higgs-Brout-Englert mechanism, the fermion masses are generated from the interaction term between the fermion fields and the Higgs field (*Yukawa term*). The Yukawa term is invariant under the electroweak symmetry and for the lepton sector is given by the following expression:

$$\mathcal{L}_y = \sum_i Y_i(\bar{\psi}_L^i \phi \psi_R^i + \bar{\psi}_R^i \phi^\dagger \psi_L^i), \quad (1.30)$$

where the index i runs over the three lepton generations, Y_i are the Yukawa coupling constants and ψ_L and ψ_R denote respectively the left-handed and the right-handed

lepton states. For the quark sector instead, the Yukawa term can be expressed in the form

$$\mathcal{L}_y = \sum_{ij} \left[Y^D_{ij} \bar{Q}^i_L \phi d^j_R + Y^U_{ij} \epsilon_{ab} \bar{u}^i_R Q^{a,j}_L \phi^b + h.c. \right], \tag{1.31}$$

where the indices i and j run over the three quark generations, the indices $a, b = 1, 2$ represent the weak isospin components, Q^i_L are the quark left-handed doublets, u^i_R and d^i_R denote the right-handed fields of *up* type (u, c, t) and *down* type (d, s, b) respectively, Y^D_{ij} and Y^U_{ij} are the elements of the coupling constant matrices, ϵ_{ab} is the Levi-Civita symbol and $h.c.$ denotes the hermitian conjugate of the preceding terms.

To obtain the mass of the electron, for instance, let's consider the Yukawa term of Equation 1.30 only for the first lepton generation:

$$\mathcal{L}_y = Y_e \left[\begin{pmatrix} \bar{\nu}_e & \bar{e} \end{pmatrix}_L \begin{pmatrix} \phi^+ \\ \phi^0 \end{pmatrix} e_R + \bar{e}_R \begin{pmatrix} \phi^{+*} & \phi^{0*} \end{pmatrix} \begin{pmatrix} \nu_e \\ e \end{pmatrix}_L \right]. \tag{1.32}$$

After the spontaneous symmetry breaking, by replacing the field ϕ with the form in 1.24, Equation 1.32 becomes

$$\mathcal{L}_y = \frac{Y_e v}{\sqrt{2}} \left(\bar{e}_L e_R + \bar{e}_R e_L \right) + \frac{Y_e h}{\sqrt{2}} \left(\bar{e}_L e_R + \bar{e}_R e_L \right), \tag{1.33}$$

where the first term can be identified as the electron mass term, with the electron mass given by

$$m_e = \frac{Y_e v}{\sqrt{2}}, \tag{1.34}$$

and the second term represents the interaction between the Higgs boson and the electron. It is worth noticing that no mass term is generated for neutrinos, which in the Standard Model are indeed massless. The masses of all the other massive fermions are generated similarly.

After all these considerations, a complete form of the electroweak Lagrangian density can be expressed as

$$\mathcal{L}_{EW} = \mathcal{L}_g + \mathcal{L}_f + \mathcal{L}_h + \mathcal{L}_y, \tag{1.35}$$

in which the kinetic terms of the gauge bosons and of the fermions (Equations 1.12 and 1.16), the Higgs term (Equation 1.19) and the Yukawa term (sum of Equations 1.30 and 1.31) have been added.

1.4 Strong interactions

Strong interactions are described by the Quantum Chromodynamics (QCD) [6], a theory based on the $SU(3)$ local gauge symmetry, which explains the interactions between quarks. $SU(3)$ has eight generators $t^A = \lambda^A/2$ $(A = 1, ..., 8)$, with λ^A the Gell-Mann matrices, so there must be eight gauge bosons as carriers of strong interactions, which are called *gluons*. The conserved charge associated with this

symmetry is called *colour charge*[5], which is carried only by quarks and gluons with the consequence that only quarks and gluons are subject to strong interactions. Since gluons carry a colour charge, it is possible to have self-interactions between them (contrary to what happens in electrodynamics, where the photon, which has no electric charge, cannot couple with itself).

The Lagrangian density of QCD is given by

$$\mathcal{L}_{QCD} = \sum_q \bar{\psi}_{q,a}(i\gamma^\mu \partial_\mu \delta_{ab} - g_s \gamma^\mu t^C_{ab} G^C_\mu)\psi_{q,b} - \frac{1}{4} G^A_{\mu\nu} G^{\mu\nu}_A, \tag{1.36}$$

where γ^μ are the Dirac matrices, $\psi_{q,a}$ is the field spinor for a quark of flavour q and colour charge index a ($a = 1, 2, 3$), g_s is the QCD coupling constant, t^C are the generators of SU(3) and G^C_μ are the gluon fields, with the index C running from 1 to 8. The gluon field tensor $G^A_{\mu\nu}$ ($A = 1, ..., 8$) in 1.36 is given by

$$G^A_{\mu\nu} = \partial_\mu G^A_\nu - \partial_\nu G^A_\mu - g_s f^{ABC} G^B_\mu G^C_\nu, \tag{1.37}$$

with the structure constants f^{ABC} given by the usual commutation rule between the generators of the symmetry group:

$$\left[t^A, t^B\right] = i f^{ABC} t^C. \tag{1.38}$$

Unlike other elementary particles, quarks and gluons cannot be observed as free states. They can only be found tied together by strong interactions forming composite particles called *hadrons*, which are colour singlets[6] (this property is called *confinement*). So as soon as quarks are created by some process, they must undergo a mechanism that in the end produces only colour singlets, usually in the form of bunches of particles called *jets*. This process is called *hadronisation*. The confinement of quarks and gluons is a consequence of the fact that the coupling constant of strong interactions α_s[7] is actually not constant at all, but a function of the energy scale (or equivalently of the distance). At small interaction distances and large momentum transfer (i.e. inside the hadrons), α_s is small, and so quarks behave as quasi-free objects (*asymptotic freedom*), while as the distance increases and the momentum transfer decreases, α_s increases, giving rise to the confinement. If in a process the distance between quarks is highly increased, the potential that binds them together grows fast and at some distance the available energy becomes sufficient to create a new quark-antiquark pair, eventually leading to the production of new hadrons, but preventing the emission of quarks as free particles. The hadronisation process still lacks well-founded theoretical calculations, due to the fact that it cannot be studied with perturbation theory, because of the great distances at which it occurs. However, it plays a very important role from an experimental point of view, because the original quark properties can only be studied through the measurement of the jets arising from the hadronisation.

[5] The name comes from the fact that there are three colour charges. So in analogy to the RGB colours they have been given the names *red*, *green* and *blue*.

[6] i.e. with no colour charge

[7] $\alpha_s = g_s^2/4\pi$

As mentioned before, hadrons are composite particles formed by quarks and gluons. Quarks are combined such that the sum of their colour charges turns out to be null. There are mainly two ways to obtain such result and hadrons can be classified according to them: if they are composed of three quarks (with different colour charges), they are called *baryons*, while if they are made by a quark-antiquark pair (with opposite colour charges), they are called *mesons*. These quarks are the main components of hadrons and are known as *valence* quarks. It is also possible, according to the uncertainty principle, that, inside the hadron, quark-antiquark pairs are created for short time intervals. They are given the name of *sea* quarks and can take part in the interactions between hadrons as well. The total momentum of a hadron is given by the sum of the momenta of its constituents (also called *partons*). In a hadronic interaction, each parton is described by the fraction x of the hadron momentum it carries. These fractions are described by their distribution functions $f_i(x, Q^2)$, which are called *Parton Distribution Functions* (PDFs) and depend both on x and on the momentum transfer Q^2. The evolution of the PDFs is regulated in non-perturbative QCD by the Dokshitzer-Gribov-Lipatov-Altarelli-Parisi (DGLAP) equation [7–9]. Naturally, the PDFs must respect the following relation:

$$\sum_i \int x f_i(x)\, dx = 1, \tag{1.39}$$

where x is the fraction of the total hadron momentum carried by the parton and the sum is over all the possible quarks, both valence and sea. In the interaction between two hadrons, most of the partons do not participate. They are called *spectator* partons and continue in a direction quasi-parallel to the hadron original one. The cross-section of the interaction is then given by

$$\sigma(P_1, P_2) = \sum_{i,j} \int f_i^1(x_i, Q^2)\, f_j^2(x_j, Q^2)\, \hat{\sigma}_{ij}(\sqrt{\hat{s}})\; dx_i\, dx_j, \tag{1.40}$$

where $P_{1,2}$ are the momenta of the hadrons colliding at a center of mass energy $\sqrt{s}$ and $\hat{\sigma}_{ij}(\sqrt{\hat{s}})$ is the cross-section of the interaction between partons i and j, which occurs at a centre of mass energy $\sqrt{\hat{s}} = \sqrt{x_i x_j s}$. The sum in 1.40 is extended to all the partons from both hadrons that participate in the interaction.

1.5 Success and limits of the Standard Model

The Standard Model is currently the most accurate and elegant theory to describe the fundamental interactions between all known particles. With only 18 free parameters, which are being measured with always higher precision, the Standard Model is able to make extremely accurate predictions on a great number of processes in a very wide energy scale range. Several sets of independent constants can be chosen to represent the SM free parameters: the set with the smallest experimental errors is reported in Table 1.2 along with the most recent measured values. The Standard Model predictions are being continuously tested by the experiments at the Large Hadron Collider (LHC), receiving throughout the years countless confirmations. Figure 1.3 for instance reports the cross-sections measured by the ATLAS

experiment at the LHC for a large set of SM processes, from the most common to the rarest ones spanning over 14 orders of magnitude. For all these cross-sections, there is no significant disagreement between the measured values and the SM predictions.

Table 1.2. The free parameters of the Standard Model with the corresponding measured values [6].

Parameter	Description	Value
m_e	Electron mass	$0.51099895000(15)\,\text{MeV}$
m_μ	Muon mass	$105.6583755(23)\,\text{MeV}$
m_τ	Tau mass	$1776.86(12)\,\text{MeV}$
m_u	Up quark mass	$2.16^{+0.49}_{-0.26}\,\text{MeV}$
m_d	Down quark mass	$4.67^{+0.48}_{-0.17}\,\text{MeV}$
m_c	Charm quark mass	$1.27(2)\,\text{GeV}$
m_s	Strange quark mass	$93.4^{+8.6}_{-3.4}\,\text{MeV}$
m_t	Top quark mass	$172.69(30)\,\text{GeV}$
m_b	Bottom quark mass	$4.18^{+0.03}_{-0.02}\,\text{GeV}$
$\sin\theta_{12}$	CKM 12-mixing angle	0.22500(67)
$\sin\theta_{23}$	CKM 23-mixing angle	$0.04182^{+0.00085}_{-0.00074}$
$\sin\theta_{13}$	CKM 13-mixing angle	0.00369(11)
δ	CKM CP-violating phase	1.144(27)
m_Z	Z boson mass	$91.1876(21)\,\text{GeV}$
m_H	Higgs boson mass	$125.25(17)\,\text{GeV}$
G_F	Fermi constant	$1.1663788(6) \times 10^{-5}\,\text{GeV}^{-2}$
α_s	Strong coupling constant	0.1180(9)[8]
α	Fine structure constant	$7.2973525693(11) \times 10^{-3}$

Despite its great success, the Standard Model is not a complete theory of all particle physics phenomena. There are indeed still many open issues, both theoretical and experimental, that the Standard Model cannot explain. Some of them are listed below.

- As already mentioned, the Standard Model describes only three of the four fundamental interactions. Even if the gravitational effects are completely negligible at the energy scale of current particle physics experiments, they would become relevant at the Planck energy scale ($\mathcal{O}(10^{19})\,\text{GeV}$). Therefore

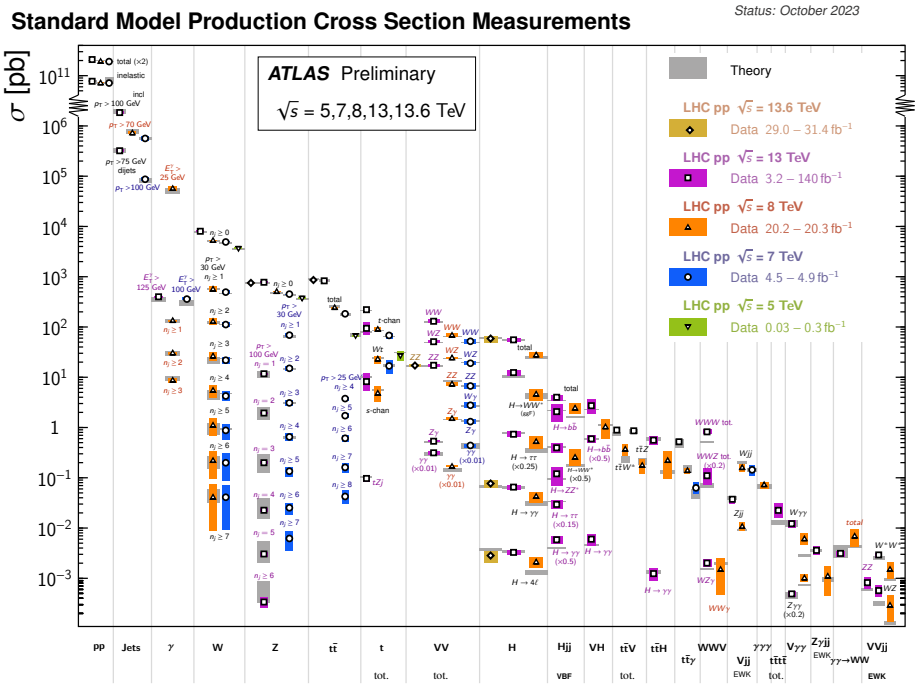

Figure 1.3. Summary of several Standard Model cross-section measurements made by the ATLAS experiment at the Large Hadron Collider [10]. The measurements are compared to the corresponding theoretical expectations.

a complete model should include also a quantum theory of gravity.

- A theory is considered *natural* if the dimensionless ratios between its parameters are of $\mathcal{O}(1)$. This condition is not respected by the Standard Model (see for instance the great differences between fermion masses), giving rise to the so-called *naturalness problem*.

- Another theoretical question comes from the great difference between the energy scale typical of the electroweak processes (fixed by the vacuum expectation value of the Higgs field $v = 246\,\text{GeV}$) and the Planck scale ($10^{19}\,\text{GeV}$), at which the quantum effects of gravity are no more negligible. This issue is called *hierarchy problem*. In theory, the radiative corrections would make the Higgs mass much greater than its measured value. So in order to obtain an effective Higgs mass of $m_H = 125\,\text{GeV}$, an incredible fine-tuning cancellation process between the corrections is necessary, and this seems to be unnatural, as if there was some missing piece in the model.

- A very important experimental question arises from the neutrino sector. In the Standard Model neutrinos are massless particles. However, several experimental observations demonstrated that there exists an oscillation mechanism between the three neutrino flavours (ν_e, ν_μ, ν_τ), which can be explained only if their mass is non-null. The experimental results show that the neutrino

[8] The strong coupling constant value reported here is measured at $Q^2 = m_Z^2$.

masses are much smaller than the masses of the other SM particles, so a hypothesis is that the neutrino mass term may come from a mechanism different from the Higgs-Brout-Englert one.

- The Standard Model is not able to explain the matter-antimatter asymmetry in the universe. Indeed SM processes are symmetric for particles and antiparticles, with the only exception being the CP symmetry violation, which, alone, cannot justify the huge asymmetry we observe in the universe: all known galaxies are supposed to be made of matter, while only small amounts of antimatter can be found, mainly in cosmic rays.

- Many cosmological and astrophysical observations show that SM particles constitute only 16% of the matter of the universe (*ordinary* matter). The other 84% should be composed of a kind of matter invisible to any type of radiation and interacting only through gravity. The Standard Model does not include any particle that could explain this kind of matter, which has been given the name of *Dark Matter*.

Many theoretical models have been proposed to explain one or more of the previous open issues. Such theories are referred to as beyond Standard Model (BSM) theories and have been experimentally investigated by the experiments at the LHC since the beginning of its operations, but up to now none of them has received a strong confirmation from the experimental results.

1.6 The leptoquark hypothesis

In the last decade, several observations performed by collider experiments have shown deviations from the SM predictions in the semileptonic decays of B mesons[9] suggesting the existence of a new short-distance interaction violating Lepton Flavour Universality (LFU). According to the SM theory, the coupling of leptons to gauge bosons does not depend on the lepton flavour and therefore electrons, muons and taus are treated identically, except for differences related to their masses. Nevertheless, deviations from τ/μ and τ/e universality in $b \to c\ell\bar{\nu}$ (with $\ell = e, \mu$) charged-current transitions have been reported by several measurements performed by the BaBar [11, 12], Belle [13, 14] and LHCb [15, 16] experiments. In particular, these experiments measured branching fraction ratios like $\mathscr{R}(D^0)$ and $\mathscr{R}(D^*)$, which are defined as

$$\mathscr{R}(D^0) = \frac{\mathscr{B}(B^- \to D^0 \tau^- \bar{\nu}_\tau)}{\mathscr{B}(B^- \to D^0 \mu^- \bar{\nu}_\mu)}, \qquad \mathscr{R}(D^*) = \frac{\mathscr{B}(\bar{B}^0 \to D^{*+} \tau^- \bar{\nu}_\tau)}{\mathscr{B}(\bar{B}^0 \to D^{*+} \mu^- \bar{\nu}_\mu)}, \tag{1.41}$$

obtaining values which, on average, are about 3 standard deviations larger than the SM predictions. The results of the $\mathscr{R}(D^0)$ and $\mathscr{R}(D^*)$ measurements performed

[9] B mesons are composite particles made of a b antiquark and a quark of up type (B^+), down type (B^0), strange type (B_s^0) or charm type (B_c^+). Analogously, D mesons, which appear in Equation 1.41, are particles made of a charm quark and a down (D^+), up (D^0) or strange (D_s^+) antiquark.

by the BaBar, Belle and LHCb experiments are summarised in Figure 1.4. Such deviations are commonly referred to as *B anomalies*.

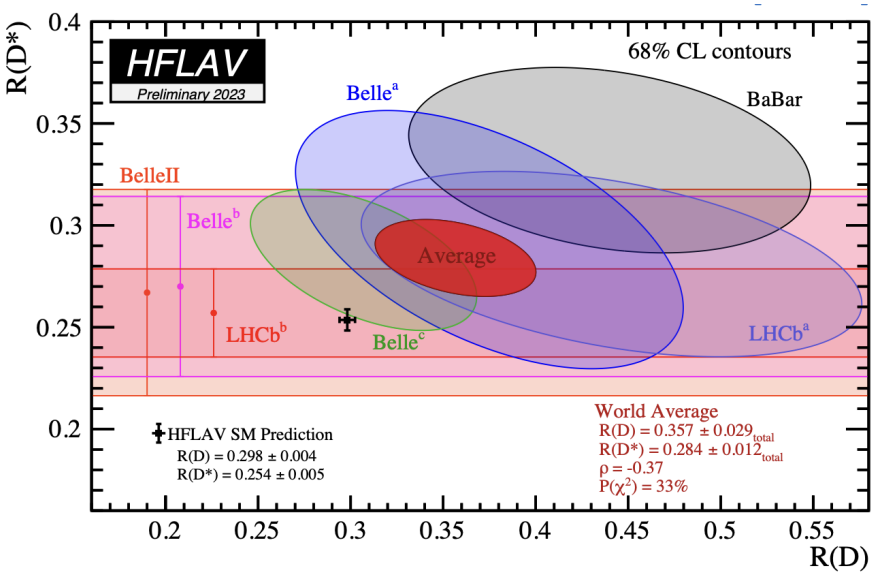

Figure 1.4. Measurements of $\mathscr{R}(D^0)$ and $\mathscr{R}(D^*)$ and their SM prediction (updated to 2023) [17].

Among the different theoretical extensions of the Standard Model, leptoquark models are particularly suitable to explain the anomalies observed in B-meson decays. They introduce a field, called *leptoquark* field, which carries both baryon and lepton quantum numbers and therefore is able to produce interaction vertices involving both quarks and leptons. The leptoquark field can be either scalar (spin 0) or vector (spin 1) and is charged under the weak isospin and the weak hypercharge.

In addition to explaining B anomalies, the leptoquark hypothesis arouses theoretical interest since it naturally points to an underlying $SU(4)$ symmetry unifying leptons and quarks, like the one proposed by Pati and Salam in 1974 [18]. In a similar theoretical scenario, Lepton Flavour Universality is no longer respected. Besides the $SU(4)$ symmetry, the leptoquark field is involved in many other theoretical BSM frameworks, such as grand-unification theories based on $SU(5)$ and $SO(10)$ symmetries, supersymmetric theories and composite quarks and leptons models.

1.6.1 EFT interpretation

Flavour anomalies can be analysed in terms of an Effective Field Theory (EFT) approach considering the possible semileptonic four-fermion operators allowed by the constraints set by the experimental observations [19, 20]. These operators coincide with the ones generated at the tree-level by the exchange of a vector $SU(2)_L$-singlet leptoquark and are given by the following expressions:

$$\begin{aligned}\mathcal{O}_{LL}^{ij\alpha\beta} &= (\bar{q}_L^i \gamma_\mu \ell_L^\alpha)(\bar{\ell}_L^\beta \gamma^\mu q_L^j),\\ \mathcal{O}_{LR}^{ij\alpha\beta} &= (\bar{q}_L^i \gamma_\mu \ell_L^\alpha)(\bar{e}_R^\beta \gamma^\mu d_R^j),\\ \mathcal{O}_{RR}^{ij\alpha\beta} &= (\bar{d}_R^i \gamma_\mu e_R^\alpha)(\bar{e}_R^\beta \gamma^\mu d_R^j).\end{aligned} \tag{1.42}$$

The effective Lagrangian density describing the BSM contribution is given by

$$\mathcal{L}_{EFT}^{BSM} = -\frac{2}{v^2}\left[\mathcal{C}_{LL}^{ij\alpha\beta}\mathcal{O}_{LL}^{ij\alpha\beta} + \mathcal{C}_{RR}^{ij\alpha\beta}\mathcal{O}_{RR}^{ij\alpha\beta} + \left(\mathcal{C}_{LR}^{ij\alpha\beta}\mathcal{O}_{LR}^{ij\alpha\beta} + \text{h.c.}\right)\right], \tag{1.43}$$

where $v = (\sqrt{2}G_F)^{-1/2} \approx 246\,\text{GeV}$ and the Wilson coefficients $\mathcal{C}_{LL}^{ij\alpha\beta}$, $\mathcal{C}_{RR}^{ij\alpha\beta}$ and $\mathcal{C}_{LR}^{ij\alpha\beta}$ are inversely proportional to the square of the new-physics scale Λ. The coefficients in Equation 1.43 respect the following assumptions:

- coefficients of operators containing first- or second-generation right-handed fields are negligibly small (i.e. $\mathcal{C}_{RR}^{ij\alpha\beta} \approx 0$ unless $i = j = 3$ and $\alpha = \beta = \tau$ and $\mathcal{C}_{LR}^{ij\alpha\beta} \approx 0$ unless $j = 3$ and $\beta = \tau$);
- coefficients associated with second-generation left-handed particles are suppressed by factors of order 10^{-1} and a further suppression arises in the case of operators involving first-generation fields.

1.6.2 The simplified U_1 vector leptoquark model

Among the various theoretical models involving leptoquarks, the simplified U_1 vector leptoquark model [20] is particularly appealing since it is able to explain the B anomalies and, at the same time, it connects them to an underlying theory of flavour. This model introduces a massive TeV-scale leptoquark field U_1^μ, having spin 1, weak isospin $I_W = 1$, weak hypercharge $Y_W = 2/3$ and colour charge = 3. The U_1 vector leptoquark couples both to quarks and leptons and is responsible for new flavour-changing interactions. The simplified U_1 model is not UV-complete (namely not renormalisable), but it is able to predict all the UV-insensitive flavour anomalies. The most general Lagrangian density for a U_1 vector leptoquark coupling to SM particles is given by

$$\begin{aligned}\mathcal{L}_U = &-\frac{1}{2}U_{\mu\nu}^\dagger U^{\mu\nu} + M_U^2 U_\mu^\dagger U^\mu - ig_s(1-k_c)U_\mu^\dagger T^a U_\nu G^{\mu\nu,a}\\ &-\frac{2}{3}ig_Y(1-k_Y)U_\mu^\dagger U_\nu B^{\mu\nu} + \frac{g_U}{\sqrt{2}}(U^\mu J_\mu^U + \text{h.c.}),\end{aligned} \tag{1.44}$$

where $U_{\mu\nu} = D_\mu U_\nu - D_\nu U_\mu$, with $D_\mu = \partial_\mu - ig_s G_\mu^a T^a - i\frac{2}{3}g_Y B_\mu$. $G_\mu^a\,(a = 1, \ldots, 8)$ and B_μ denote the $SU(3)_c$ and $U(1)_Y$ gauge bosons, g_s and g_Y are the correspondent gauge couplings, g_U the leptoquark coupling and T^a are the generators of $SU(3)_c$. In models in which the leptoquark has a gauge origin, $k_c = k_Y = 0$. The interaction of the leptoquark with the SM fermions involves the following currents:

$$J_\mu^U = \beta_L^{i\alpha}(\bar{Q}_L^i \gamma_\mu L_L^\alpha) + \beta_R^{i\alpha}(\bar{d}_R^i \gamma_\mu \ell_R^\alpha), \tag{1.45}$$

where Q_L^i are the quark left-handed doublets, L_L^α the left-handed lepton doublets, d_R^i the right-handed quark fields of *down* type, ℓ_R^α the right-handed lepton fields and β_L and β_R complex 3×3 matrices in flavour space (the U_1 model allows a non-universal gauge structure). In the flavour structure with a preferential coupling to third-generation fermions, as suggested by the experimental observations, the β_L and β_R matrices can be expressed as

$$\beta_L = \begin{pmatrix} 0 & 0 & \beta_L^{d\tau} \\ 0 & \beta_L^{s\mu} & \beta_L^{s\tau} \\ 0 & \beta_L^{b\mu} & 1 \end{pmatrix}, \qquad \beta_R = \begin{pmatrix} 0 & 0 & 0 \\ 0 & 0 & 0 \\ 0 & 0 & \beta_R^{b\tau} \end{pmatrix}, \tag{1.46}$$

with $|\beta_L^{d\tau,s\mu}| \ll |\beta_L^{s\tau,b\mu}| \ll 1$ and $\beta_R^{b\tau} = \mathcal{O}(1)$.

The β_L and β_R couplings of the simplified U_1 model can be related to the Wilson coefficients used in the EFT approach by the following expressions:

$$\mathfrak{C}_{LL}^{ij\alpha\beta} = C_U \beta_L^{i\alpha} (\beta_L^{j\beta})^*, \qquad \mathfrak{C}_{LR}^{ij\alpha\beta} = C_U \beta_L^{i\alpha} (\beta_R^{j\beta})^*, \qquad \mathfrak{C}_{RR}^{ij\alpha\beta} = C_U \beta_R^{i\alpha} (\beta_R^{j\beta})^*, \tag{1.47}$$

where $C_U \equiv g_U^2 v^2/(4M_U^2)$.

UV-completion of the simplified U_1 model can be achieved starting from a global $U(2)^5$ symmetry under the assumption that the electron and muon masses are negligible with respect to the tau mass. After spontaneous symmetry breaking, the global symmetry reduces to the local gauge symmetry

$$\mathcal{G}_{4321} = SU(4) \otimes SU(3) \otimes SU(2) \otimes U(1). \tag{1.48}$$

The UV-complete U_1 model introduces several particles in addition to leptoquarks: a massive vector colour octet, a heavy resonance Z' with preferential coupling to third-generation fermions and vector-like leptons. The model based on the $\mathcal{G}_{4321}$ symmetry revisits the original $SU(4)$ model proposed by Pati and Salam by including the lepton universality violation.

1.6.3 Leptoquark processes

The leptoquark interaction vertices involve both SM lepton and quark fields. In general, leptoquark couplings are possible with all combinations of leptons and quarks. However, according to the considerations reported in the previous sections, couplings involving first- and second-generation fermions are suppressed with respect to couplings involving third-generation fermions only.

Several processes involving leptoquarks can be searched for by exploiting the particle collisions generated by an accelerator like the LHC. The Feynman diagrams of the main leptoquark processes are illustrated in Figure 1.5. Leptoquark production mechanisms can be broadly classified into single- or pair-production and non-resonant production [21]. In the former case, the leptoquark decays into a pair made of one lepton and one quark, while the latter case is analogous to a t-channel Drell-Yan process with the exchange of a leptoquark. Under the assumption that

the leptoquark interacts only with one type of leptons and quarks at a time with coupling constant λ (Minimal Leptoquark Model), the following dependences of the process amplitudes on the couplings can be obtained:

- pair-production processes with two interaction vertices in which the leptoquark couples with a gluon (diagrams from PP-1 to PP-4 in Figure 1.5) have an amplitude proportional to g_s^2;
- the pair-production not involving gluons (diagram PP-5) and the Drell-Yan leptoquark exchange (diagram DY) yield amplitudes proportional to λ^2;
- single-production processes (diagram SP-1 and SP-2) have an amplitude scaling with $g_s \cdot \lambda$.

The coupling dependence in the amplitudes determines which process dominates in the total cross-section: for small couplings ($\lambda \lesssim 1$) the main contribution to the total cross-section is given by the pair-production processes whose amplitude only depends on g_s. For large leptoquark couplings instead ($\lambda > 1$), the single-production and the non-resonant t-channel exchange, having λ-dependent amplitudes, become dominant.

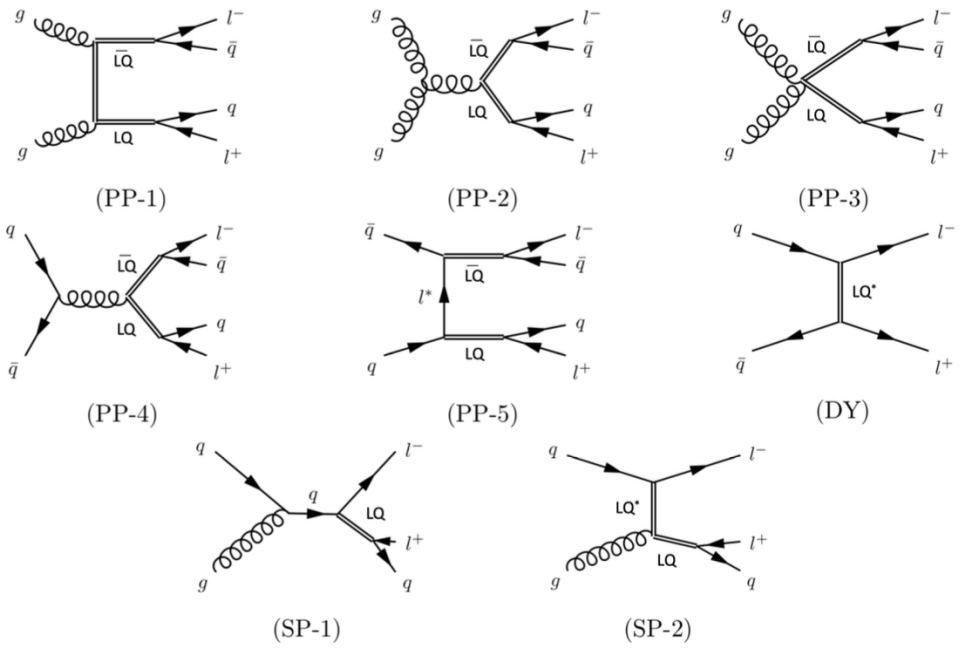

Figure 1.5. Leading order diagrams for leptoquark pair-production (from PP-1 to PP- 5), Drell-Yan t-channel exchange (DY) and single-production (SP-1 and SP-2) [21].

1.6.4 Leptoquark searches

The wide variety of leptoquark production processes accessible at a collider like the LHC allows the experiments placed along its ring to conduct an extensive search

of possible leptoquark signatures. The main decay channels in models where the leptoquark predominantly couples to third-generation fermions are $U_1 \to b\tau^+$ and $U_1 \to t\bar{\nu}_\tau$. Searches for leptoquark single- and pair-production have been performed both by the ATLAS [22–25] and CMS [26–28] experiments at the LHC considering these decay channels. These searches set a lower bound on the leptoquark mass of $M_U \geq 1.7\,\text{TeV}$, which, however, only covers a small region of the parameter space relevant for the explanation of the charged-current B anomalies. In the case where $g_U \geq g_s$, the most stringent constraints on the leptoquark parameter space come from the Drell-Yan production. Exclusion limits can be set from the $pp \to \tau\tau$ measurements performed by ATLAS [29] and CMS [28]. These studies were aimed mainly at searching for heavy resonances, but their results can be used also to constrain the parameter space of the U_1 leptoquark model and the coefficients of the EFT approach. Figure 1.6 shows exclusion limits set by the ATLAS and CMS experiments in the leptoquark coupling g_U versus leptoquark mass M_U plane, together with the region preferred by the B anomalies. Only a small portion of the preferred region is ruled out by these measurements and a large region of the parameter space still remains viable.

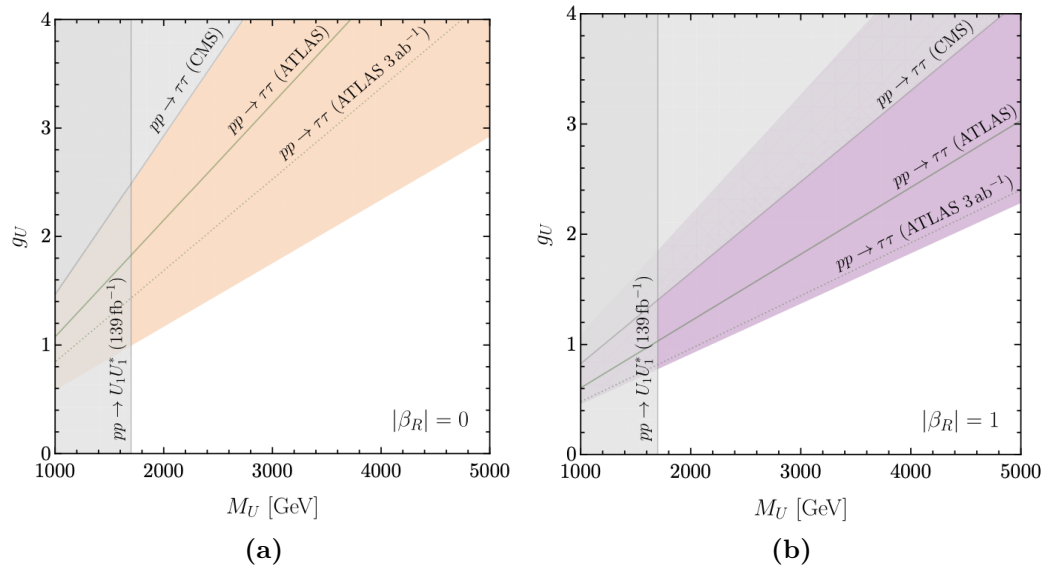

Figure 1.6. Preferred region at 90 % CL from the R_D and R_{D^*} measurements in the leptoquark mass (M_U) and leading fermion coupling (g_U) plane in the pure left-handed case ($\beta_R = 0$) (a) and in the case with $|\beta_R| = 1$ (b). The grey region and solid lines indicate constraints of ATLAS and CMS searches at 95% CL, while the dotted line gives the projected sensitivity at the HL-LHC with a luminosity of $3\,\text{ab}^{-1}$ [30].

The constraints on the EFT coefficients related to the $b \to c\ell\bar{\nu}$ transitions set by the ATLAS and CMS searches are reported in Figure 1.7. The regions preferred by the B anomalies are also represented, together with the result of the fit of the combination of the R_D and R_{D^*} measurements performed by the BaBar, Belle and LHCb experiments. The comparison between ATLAS and CMS results with the

R_D and R_{D^*} measurements shows that a U_1 explanation of the B anomalies is compatible with the current $pp \to \tau\tau$ data.

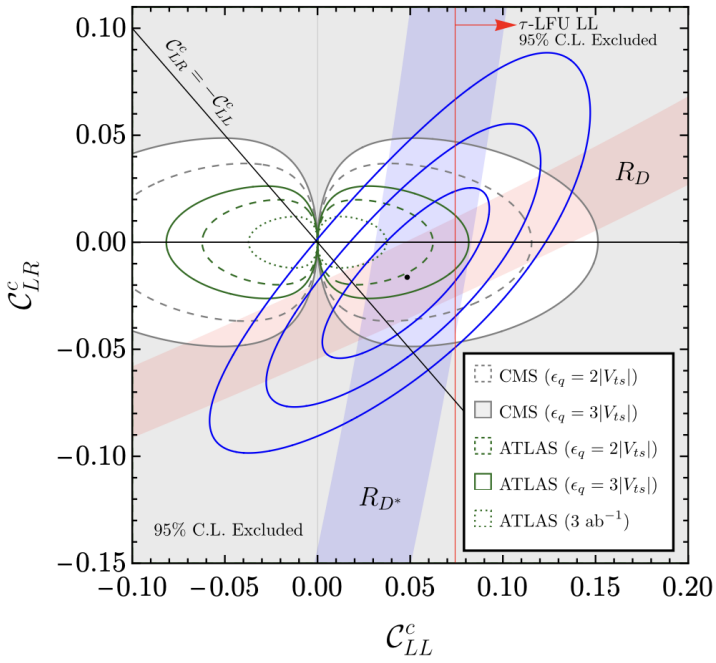

Figure 1.7. Constraints on the EFT coefficients $\mathcal{C}^c_{LL}$ and $\mathcal{C}^c_{LR}$ imposed by the ATLAS [29] (green lines) and CMS [28] (grey lines) searches [30]. The region outside the lines is excluded at 95% CL. The red and blue bands represent the regions preferred by R_D and R_{D^*}. The blue ellipses denote the 1, 2, and 3σ contours of the combined fit including all the R_D and R_{D^*} measurements. The SM prediction corresponds to $\mathcal{C}^c_{LL} = \mathcal{C}^c_{LR} = 0$.

A very promising channel for leptoquark searches is the non-resonant t-channel exchange. So far, this production channel has been investigated only by the CMS experiment [31] and the measurement results have been used to widen the exclusion region in the leptoquark parameter space. The CMS results, reported in Section 4, show a 2.8 σ discrepancy between the expected and observed limits.

Chapter 2

The ATLAS experiment at the Large Hadron Collider

In order to study the fundamental laws that govern elementary particle interactions, we need a machine able to produce high-energy processes. For this purpose, the Large Hadron Collider at CERN is currently the most advanced particle accelerator, able to collide protons and heavy ions at extremely high energies and thus ideal for particle physics studies and searches. Such a powerful machine needs as well adequate instruments to measure with high precision the high-energy collision products and the ATLAS detector is optimal for this task. Indeed, it has been designed to cover the entire solid angle around the interaction point of the collider and optimised to reconstruct and identify all kinds of particles, from the most common to the most elusive ones.

This chapter presents the Large Hadron Collider and the ATLAS detector, whose collected data have been used to perform the analysis reported in this thesis. In particular Section 2.1 describes the Large Hadron Collider machine and some physical quantities useful for collider physics, while Section 2.2 presents a detailed description of the ATLAS experiment and its sub-detectors.

2.1 The Large Hadron Collider

The Large Hadron Collider (LHC) [32] is the largest and most powerful particle accelerator in the world. It is the latest of a series of accelerators built at the CERN[1] laboratories, placed on the France-Switzerland border near Geneva, to investigate the fundamental laws that govern particle physics. The LHC was built between 1998 and 2008 in the 26.7 km long circular tunnel placed at a depth between 45 and 175 m below the earth's surface that had been excavated to house the Large Electron Positron Collider (LEP), which operated from 1989 to 2000. The LHC is a hadronic machine aimed mainly at proton (p-p) collisions, but it can accelerate and collide also heavy ions, and the p-p physics programme is alternated with periods

[1] *Conseil européen pour la recherche nucléaire* (European Organization for Nuclear Research).

of Pb-Pb, Xe-Xe and p-Pb collisions.

The LHC operation plan, schematised in Figure 2.1, is divided into three data-taking periods, called *Runs*, interleaved with periods dedicated to maintenance and upgrade of both the machine and the detectors, referred to as *Long Shutdowns*. Although the first p-p collisions were realised in 2008, the first data-taking period (Run 1) was held between 2010 and 2013. Initially operating at a centre-of-mass energy $\sqrt{s} = 7\,\text{TeV}$ (each proton beam having an energy of 3.5 TeV), for the second half of Run 1 the LHC increased the centre-of-mass energy of the colliding beams to 8 TeV. In 2015, after the Long Shutdown 1, collisions in the LHC started again with $\sqrt{s} = 13\,\text{TeV}$ and lasted until the end of 2018 (Run 2). In the following three years (Long Shutdown 2) the main LHC experiments had their detectors underwent an important upgrade (referred to as *Phase-I* upgrade) in order to improve their physics performance. The last LHC data-taking period (Run 3) began in 2022 with a centre-of-mass energy of $\sqrt{s} = 13.6\,\text{TeV}$ and it is foreseen to last until the end of 2025, when the Long Shutdown 3 will be used for the installation of an upgraded version of the LHC, called *High-Luminosity* LHC (HL-LHC), whose operation is foreseen to start in 2029. In preparation for the HL-LHC, during Long Shutdown 3 the LHC experiments will undergo a major upgrade, which is referred to as *Phase-II* upgrade. The innovative aspect of the High-Luminosity phase of the LHC does not reside in the centre-of-mass energy, which is expected to reach the nominal LHC design value of 14 TeV, but rather in the luminosity, a quantity proportional to the number of collisions (see Section 2.1.3), which could reach up to 7.5 times the nominal LHC value, with a consequent increase of the discovery potential of the collider.

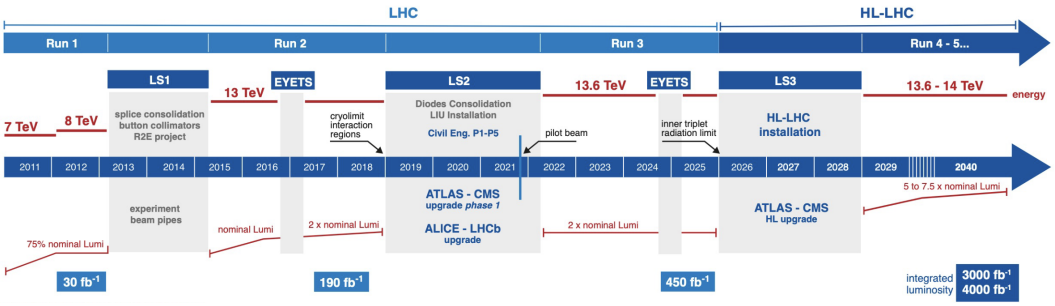

Figure 2.1. The LHC operation plan (as in February 2022) [33]. The division between Runs and Long Shutdown periods is shown together with the corresponding centre-of-mass energy and integrated luminosity delivered. The first part of the HL-LHC plan is also reported.

2.1.1 The CERN accelerator complex

In order to reach the desired collision energy inside the LHC ring, protons have to pass through a succession of machines that accelerate them to increasingly higher energies. This series of machines represents the CERN accelerator complex (shown in Figure 2.2) and it is composed of several accelerators that have been operating at CERN throughout the years and have been modified to provide the proton beams

needed by the LHC and the other CERN facilities.

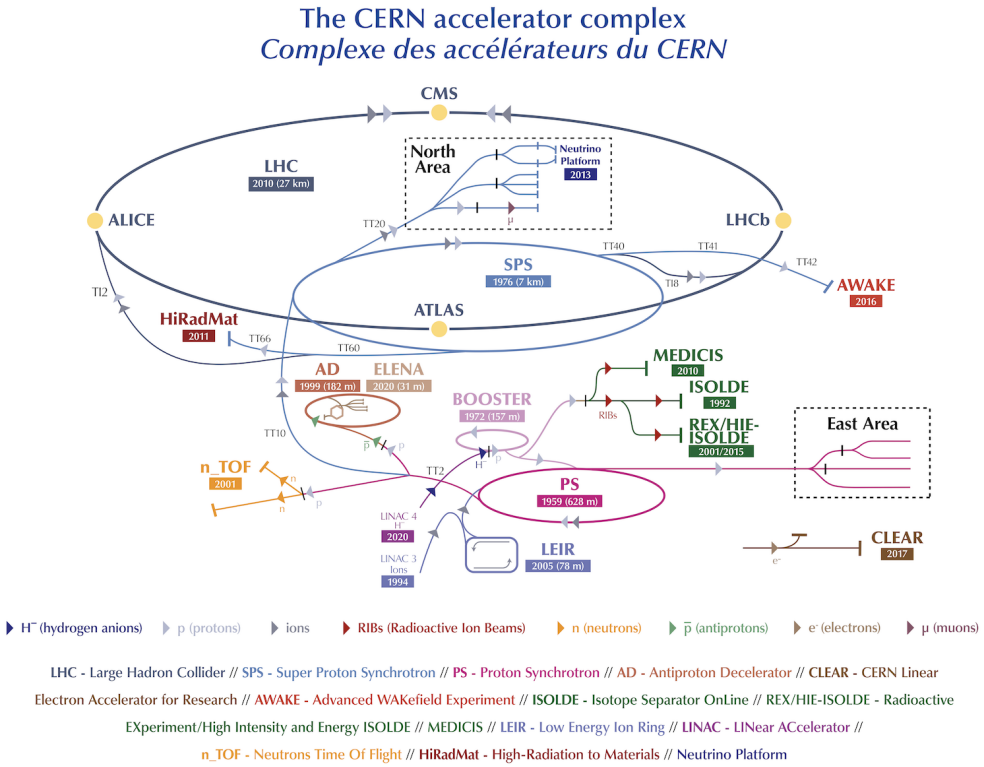

Figure 2.2. The CERN accelerator complex [34].

During LHC Run 2 the proton beams were created starting from negative hydrogen ions, which were boosted to the energy of 50 MeV by the linear accelerator Linac2 and then injected into the Proton Synchrotron Booster (PSB). The ions were stripped of their electrons during the injection from Linac2 leaving only protons, which were then accelerated by the four superimposed synchrotron rings of PSB to the energy of 1.4 GeV. Hence the protons were transferred to the Proton Synchrotron (PS), which accelerated the beam up to 26 GeV, and then to the Super Proton Synchrotron (SPS), where they reached the energy of 450 GeV. For Run 3 some changes have been applied to the acceleration stages: Linac2 has been replaced by Linac4, which is able to boost hydrogen ions up to 160 MeV, and the PSB now accelerates protons to 2 GeV. From the SPS protons are injected into the two beam pipes of the LHC and accelerated up to the target energy (6.5 TeV for Run 2, 6.8 TeV for Run 3).

2.1.2 The LHC machine

When being injected into the LHC, protons are grouped in bunches separated by a bunch spacing of 25 ns, providing a bunch collision rate of 40 MHz. During Run 2 a maximum of 2556 proton bunches, made of 1.15×10^{11} protons each, circulated inside the accelerator. The hadrons are accelerated by 16 radio-frequency

(RF) cavities, which use a 400 MHz frequency to keep the bunch structure.

Since the colliding proton beams have the same electric charge, two separate vacuum pipes are used to make them circulate in opposite directions in the 26.7 km LHC ring. The collisions between the two beams take place at four interaction points, where the two pipes intersect. Hadrons are kept on the circular trajectory by the 8.3 T magnetic field generated by 1232 superconductive magnetic dipoles. Quadrupole and higher-order magnets are instead used to focus the beams and regulate their optics. The LHC superconductive magnets, 9300 in total, are made of NbTi cables and are kept at a temperature of 1.9 K by 96 tonnes of superfluid helium.

There are nine particle detectors installed in the LHC cavern. At each interaction point there is one of the four major LHC detectors: ATLAS (*A Toroidal LHC ApparatuS*) [35] and CMS (*Compact Muon Solenoid*) [36] are multi-purpose experiments designed for Higgs boson search, precision measurements of Standard Model processes and searches of beyond Standard Model physics; ALICE (*A Large Ion Collider Experiment*) [37] is designed to study heavy-ion collisions, investigating in particular the properties of the quark-gluon plasma; LHCb (*LHC beauty*) [38] is dedicated to bottom quark physics. The other five detectors are smaller and designed for very specialized researches: TOTEM (*TOTal cross-section, Elastic scattering and diffraction dissociation Measurement at the LHC*) [39], located near the CMS interaction point, is aimed at the precise measurement of p-p interaction cross-section and the study of physics processes in the region very close to the beams; FASER (*ForwArd Search ExpeRiment*) [40], located near the ATLAS interaction point, is designed to search for light and extremely weak interacting particles, like neutrinos or possible dark matter candidates; MoEDAL (*the Monopole and Exotics Detector at the LHC*) [41], deployed close to LHCb, searches for the magnetic monople and other exotic particles; LHCf (*LHC forward*) [42], installed near the ATLAS collision point, uses particles from LHC collisions as a source to simulate cosmic rays in laboratory conditions; SND@LHC (*Scattering and Neutrino Detector at the LHC*) [43] is installed in an unused tunnel that links the LHC to the SPS, near the ATLAS experiment, and is designed to study neutrinos.

2.1.3 Luminosity and pileup

The LHC is the most powerful accelerator in the world, not only for its unprecedented centre-of-mass energy of 13.6 TeV, but also for its luminosity, a parameter that in collider physics relates the number of interactions N_p per unit time and the cross-section σ_p of a given process p:

$$\frac{dN_p}{dt} = \mathscr{L}\sigma_p. \tag{2.1}$$

The parameter $\mathscr{L}$ defined in Equation 2.1 is called *instantaneous luminosity*, is measured in $\mathrm{cm}^{-2}\,\mathrm{s}^{-1}$ and depends only on accelerator properties. For a collider like the LHC that accelerates two beams structured in bunches of particles, given the number of bunches per beam (k), the revolution frequency (f), the number of particles per bunch for the two beams (n_1, n_2) and the dimensions of the bunches

in the plane transverse to the beam axis (σ_x, σ_y), the instantaneous luminosity can be computed as

$$\mathscr{L} = \frac{k\,\mathrm{f}\,n_1 n_2}{4\pi\sigma_x\sigma_y}. \tag{2.2}$$

Equation 2.2 holds in the case the angle α between the directions of the colliding beams is equal to 0. If instead the directions of the beams are not parallel, as in the LHC case where $\alpha \simeq 300\,\mu\mathrm{rad}$, Equation 2.2 becomes

$$\mathscr{L} = \frac{k\,\mathrm{f}\,n_1 n_2}{4\pi\sigma_x\sigma_y} f(\alpha), \tag{2.3}$$

where $f(\alpha)$ is a geometric factor < 1 given by

$$f(\alpha) = \frac{1}{\sqrt{1+\phi^2}}. \tag{2.4}$$

The parameter ϕ in Equation 2.4 is known as Piwinski angle and can be computed as

$$\phi = \alpha\frac{\sigma_L}{2\sigma_T}, \tag{2.5}$$

with σ_L the longitudinal and σ_T the transverse effective dimension of the bunches. Considering the LHC parameters, the nominal instantaneous luminosity of LHC is $10^{34}\,\mathrm{cm}^{-2}\,\mathrm{s}^{-1}$. Luminosity can be increased in different ways: the most direct way is to focus the beam more tightly at the collision point using more powerful quadrupole magnets, in order to reduce the transverse dimensions of the bunches σ_x and σ_y. Other options could be increasing the number of bunches or the number of protons per bunch, but these parameters cannot be raised beyond a certain limit because of beam-beam interactions, machine protection and pileup. Anyway, exploiting these mechanisms, the LHC instantaneous luminosity increased from $4.7 \times 10^{32}\,\mathrm{cm}^{-2}\,\mathrm{s}^{-1}$ at the beginning of Run 1 to the current value of $2 \times 10^{34}\,\mathrm{cm}^{-2}\,\mathrm{s}^{-1}$ for Run 3.

During the *stable beam* condition, in which the LHC experiments can collect data for physics analyses, the instantaneous luminosity does not remain constant, but decreases exponentially over time due to several effects: the main reason is the collisions at the interaction points, but also collisions with gas residues inside the vacuum pipe and intra-beam scattering are responsible for beam quality degradation. The instantaneous luminosity as a function of time can be expressed by the exponential law

$$\mathscr{L}(t) = \mathscr{L}_0\, e^{-\frac{t}{\tau}}, \tag{2.6}$$

where $\mathscr{L}_0$ is the peak luminosity and the time constant τ is given by the sum of the different contributions:

$$\frac{1}{\tau} = \frac{1}{\tau_{\mathrm{IP}}} + \frac{1}{\tau_{\mathrm{gas}}} + \frac{1}{\tau_{\mathrm{IBS}}}, \tag{2.7}$$

where $\tau_{\mathrm{IP}} \simeq 30\,\mathrm{h}$ is the contribution from collisions in the interaction points, $\tau_{\mathrm{gas}} \simeq 100\,\mathrm{h}$ is the contribution from scattering with gas molecules and $\tau_{\mathrm{IBS}} \simeq 80\,\mathrm{h}$ is the contribution from intra-beam scattering. After several hours from the beginning of data taking (about $10 \div 15$ hours), the beam quality becomes so poor that it is better to dump the beams and inject new ones into the ring. During Run 2 it took

between 90 and 120 minutes to fill the LHC rings with new proton bunches and accelerate them to the energy of 6.5 TeV. An example of the LHC filling cycle is given in Figure 2.3.

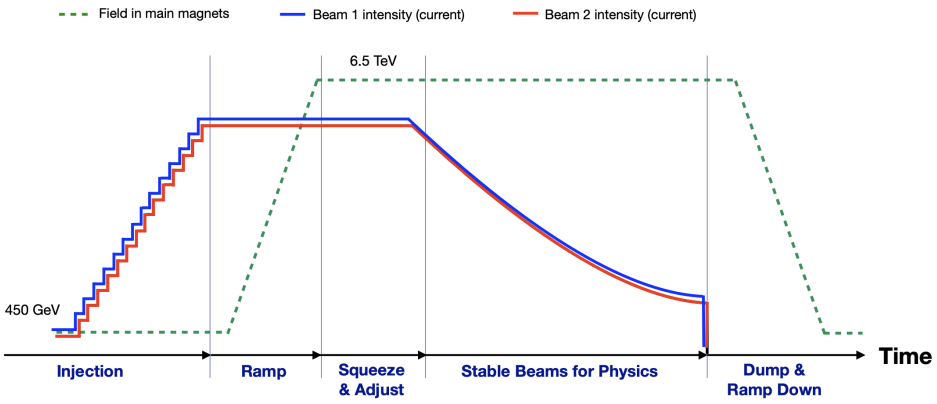

Figure 2.3. Example of LHC filling cycle [44].

The integral of the instantaneous luminosity over a time interval T is called *integrated luminosity* $\mathscr{L}_{int}$ and relates the total number of events of a given process p occurring in that time interval to the process cross-section σ_p:

$$\mathscr{L}_{int}(T) = \int_0^T \mathscr{L}(t)\, dt, \qquad N_p^{tot} = \mathscr{L}_{int}\, \sigma_p. \tag{2.8}$$

Since the cross-section is usually expressed in *barn* ($1\,\mathrm{b} = 10^{-24}\,\mathrm{cm}^2$), the integrated luminosity is measured in inverse barn (b^{-1}). Figure 2.4 shows the integrated luminosity delivered to the ATLAS detector as a function of time for each year of Run 1 and Run 2. During Run 1, the LHC delivered to ATLAS a total integrated luminosity of $28.3\,\mathrm{fb}^{-1}$, 24.9 of which are good for physics [45], while, during Run 2, on a total delivered integrated luminosity of $156\,\mathrm{fb}^{-1}$, $139\,\mathrm{fb}^{-1}$ are good for physics [46]. Figure 2.5 reports the integrated luminosity delivered by the LHC, recorded by ATLAS and usable for physics purposes during Run 2. By the end of Run 3, a total integrated luminosity of $450\,\mathrm{fb}^{-1}$ (including Run 1 and Run 2 luminosities) is expected to be delivered by the LHC to its experiment.

Through the years of its operation, the LHC machine has been continuously upgraded in order to increase its luminosity. The higher the luminosity, the larger the amount of data collected by the LHC experiments and therefore the probability of observing rare physics processes. However, with the increase of luminosity, also the number of proton-proton collisions per bunch crossing increases, making it harder to reconstruct and separate particles coming from different superimposed events. This effect is commonly called event *pileup* and can be estimated by the average number of interactions per bunch crossing μ:

$$\mu = \frac{\mathscr{L}\,\sigma_{tot}}{k\,\mathrm{f}}, \tag{2.9}$$

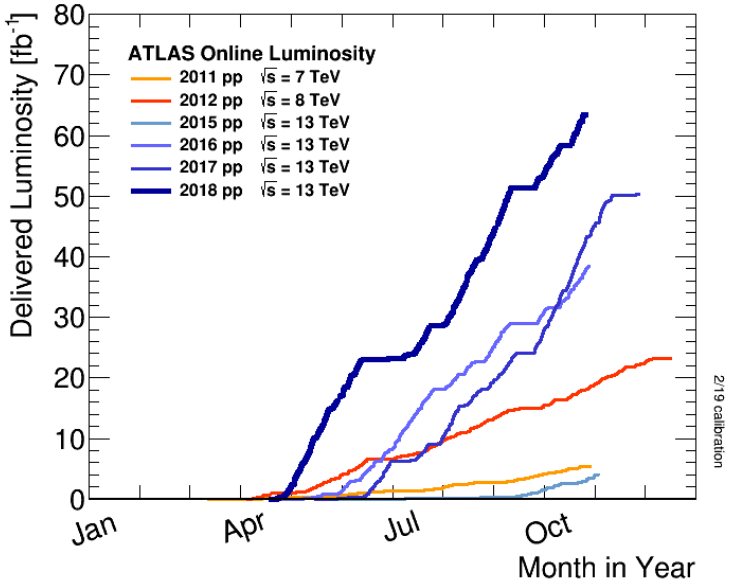

Figure 2.4. Integrated luminosity delivered to the ATLAS detector for each year of Run 1 and Run 2 [46].

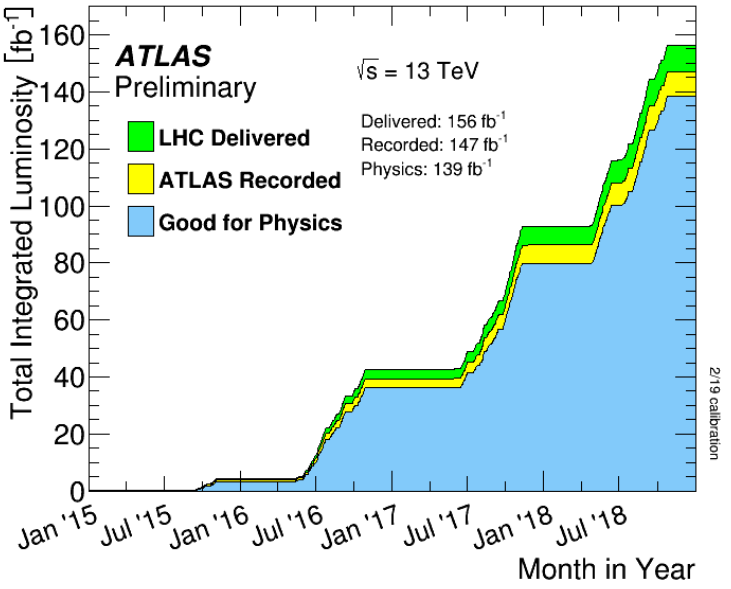

Figure 2.5. Total integrated luminosity delivered by the LHC, recorded by ATLAS and good for physics during Run 2 [46].

where σ_{tot} is the total p-p inelastic cross-section, which was measured to be $\sigma_{tot} = 78.1 \pm 2.9$ mb at 13 TeV by ATLAS [47]. Figure 2.6 shows the pileup measured by ATLAS from Run 1 to Run 3 (using data collected up to July 2023). The average pileup for Run 1 is 18.5, for Run 2 33.7 and for Run 3 46.5 [48]. With the HL-LHC the pileup is expected to go over 200.

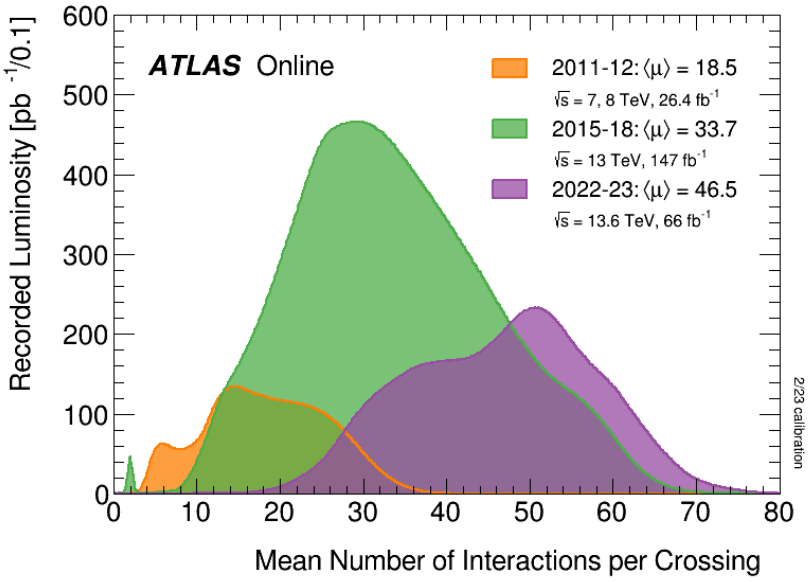

Figure 2.6. Average number of interactions per bunch crossing measured by ATLAS from Run 1 to Run 3 (updated to July 2023) [48].

2.2 The ATLAS detector

The ATLAS experiment is one of the two general-purpose detectors along the LHC ring. With its 25 m height, 44 m length and a weight of approximately 7000 tonnes, ATLAS is the biggest particle detector ever built. It was designed to search for the Higgs boson (which was indeed discovered in 2012 by ATLAS and CMS), to perform precision measurements of the Standard Model parameters and to look for new physics. Each particle interacts in a peculiar way and therefore different kinds of detectors, both for the materials they are built with and the physical processes they exploit, have been conceived to identify and measure each type of particle and ATLAS takes advantage of several of them to detect all types of Standard Model particles. Indeed, ATLAS is made of a set of concentric sub-detectors arranged around the LHC Interaction Point 1 (IP1) with cylindrical symmetry, to guarantee almost a full coverage of the entire solid angle (a characteristic that is commonly referred to as *hermeticity*). The ATLAS sub-detectors, pointed out in Figure 2.7, work in perfect symbiosis to provide a full reconstruction of the LHC collision products and are briefly described below, from the innermost to the outermost one.

- The Inner Detector (ID) is the closest one to the beam pipe and it is made of several concentric layers of tracking systems, which, exploiting different tech-

niques, allow the tracks of electrically charged particles to be reconstructed and their momentum to be measured. The Inner Detector is also responsible for the identification of primary and secondary interaction vertices.

- The electromagnetic calorimeter (ECAL) identifies electrons and photons and measures their energy deposited through the electromagnetic showers originated by them.
- The hadronic calorimeter (HCAL) reconstructs the hadronic showers from charged and neutral hadrons and measures their energy.
- The Muon Spectrometer (MS) is the outermost ATLAS sub-detector. It uses gaseous detectors to reconstruct the tracks of muons and any other charged particle escaping the calorimeter system.

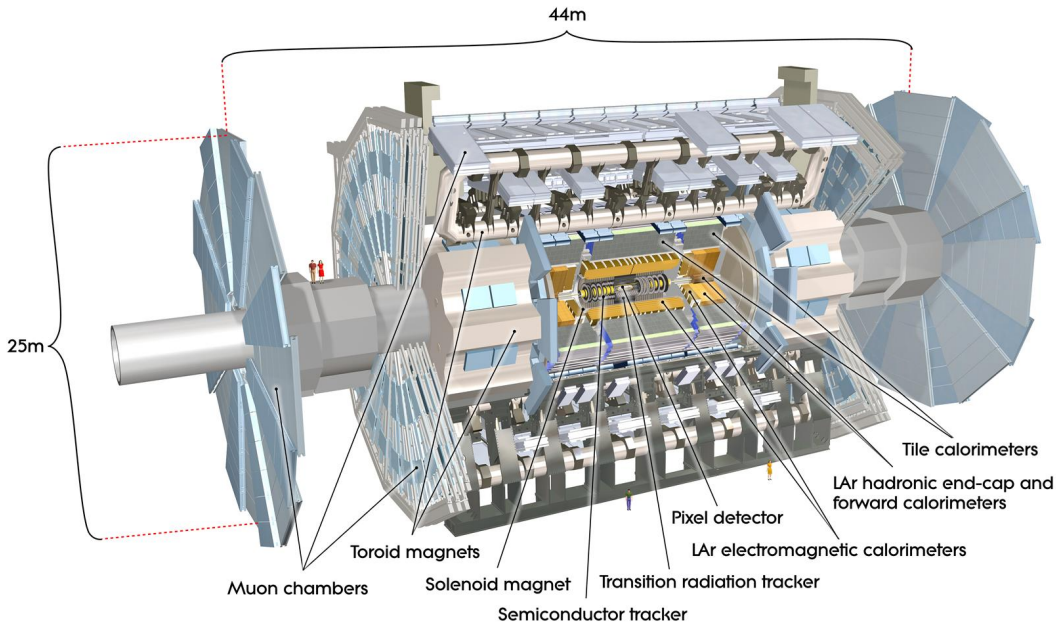

Figure 2.7. Cut-away view of the ATLAS detector displaying the positions of all its sub-detectors [35].

A more detailed description of all ATLAS sub-detectors is given in the following sections.

2.2.1 The coordinate system

The ATLAS experiment uses a right-handed coordinate system defined as follows:

- the origin of the coordinate system is identified in the nominal interaction point;

- the x axis is horizontal and points to the centre of the LHC ring;
- the y axis is vertical and points upwards;
- the z axis coincides with the beam axis, oriented so as to have a right-handed system.

The ATLAS detector is divided into two symmetric parts by the transverse plane passing at the interaction point ($z = 0$): the region with positive z is called side A, while the region with negative z side C[2]. Another way to divide the ATLAS detector components is based on their position inside the cylindrical structure: the main body of the cylinder is defined as *barrel*, while the regions closing the volume on the two sides are called *end-caps*.

Usually, for physics analyses and detector description, the coordinates (r, ϕ, θ), based on the cylindrical symmetry of the system, are preferred to the Cartesian coordinates, with r being the distance from the z axis, ϕ the azimuthal angle and θ the polar angle. The azimuthal angle ϕ is defined as the angle in the (x, y) plane ranging in the interval $(-\pi, \pi]$ with $\phi = 0$ along the x axis positive direction, while the polar angle θ is the angle with respect to the beam axis, ranging in the interval $[0, \pi]$ with $\theta = 0$ along the z axis positive direction. Figures 2.8(a) and 2.8(b) give a visual representation of both the Cartesian and the cylindrical coordinates used by the ATLAS experiment.

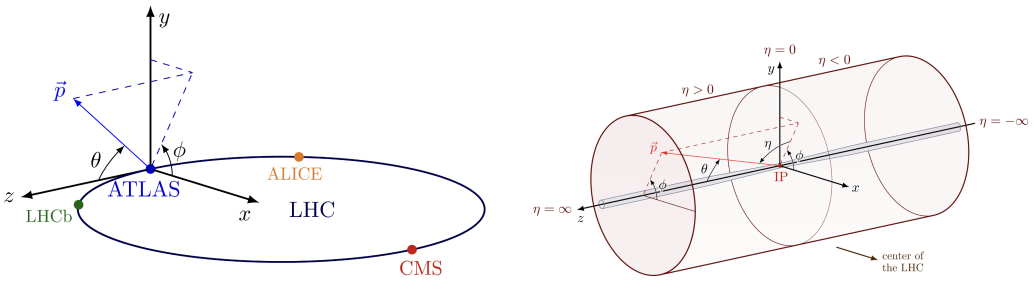

(a) **(b)**

Figure 2.8. Visual representations of the ATLAS coordinate system.

A useful quantity for collider physics is the *rapidity* y defined as

$$y = \frac{1}{2} \ln \left(\frac{E + p_z}{E - p_z} \right), \tag{2.10}$$

where E is the energy of the particle and p_z the projection of the particle momentum along the z axis. The advantage of this quantity is that its differential dy is invariant under Lorentz transformations along the beam axis. Moreover, for ultra-relativistic particles, the rapidity converges to the *pseudorapidity* η, which is related to the

[2]There is also a region defined as side B, which is made by detector components located on the plane with $z = 0$.

polar angle θ by the following expression:

$$\eta = -\ln\left(\tan\frac{\theta}{2}\right). \tag{2.11}$$

Pseudorapidity has the advantage of expanding the scale at small angles with respect to the beam axis, as represented in Figure 2.9, so, usually, a system based on the (η, ϕ) coordinates is preferred in physics analyses. With this coordinate system, it is possible to define the distance ΔR between two objects inside the detector as

$$\Delta R = \sqrt{\Delta\eta^2 + \Delta\phi^2}. \tag{2.12}$$

Since the parton momentum in the transverse plane is considered negligible, the ϕ coordinate is Lorentz-invariant and therefore also the distance ΔR is Lorentz-invariant.

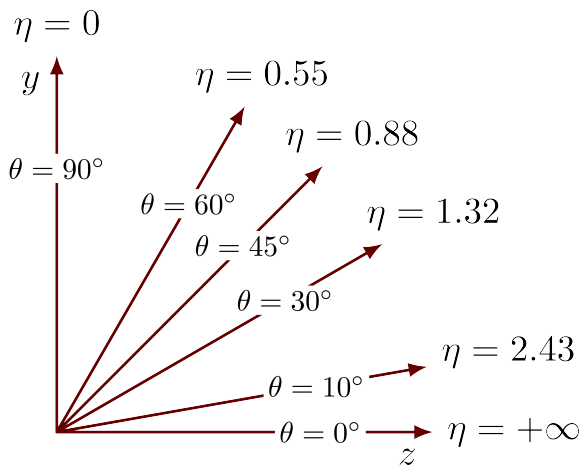

Figure 2.9. Relation between the polar angle θ and the pseudorapidity η.

Proton-proton collisions at the LHC involve composite particles, so, when the partons (i.e. quarks and gluons) that constitute protons interact, they carry only a fraction of the original proton momentum, which is unknown. Therefore, it is not possible to verify the total four-momentum conservation. However, since the initial parton momentum in the (x, y) plane is negligible with respect to the longitudinal component, the sum of the transverse momentum p_{T}, defined as

$$p_{\mathrm{T}} = \sqrt{p_x^2 + p_y^2}, \tag{2.13}$$

of all the final particles must be zero. Using the conservation of total transverse momentum ($p_{\mathrm{T}}^{tot} = 0$), it is possible to reconstruct the total transverse momentum ($E_{\mathrm{T}}^{\mathrm{miss}}$) of all the particles invisible to the ATLAS detector systems (neutrinos or BSM particles). $E_{\mathrm{T}}^{\mathrm{miss}}$ is defined as the magnitude of the negative sum of the transverse momenta associated with the visible particles (see Section 3.6).

2.2.2 The magnet system

Magnetic fields represent an essential element for particle detectors because they allow them to reconstruct the momentum of charged objects. ATLAS magnetic field is generated by four superconductive magnetic systems: a central solenoid that embeds the Inner Detector, an external toroidal system that generates the magnetic field in the barrel region, and two toroids that generate the field in the end-caps. The ATLAS magnet system [49] is shown in Figure 2.10.

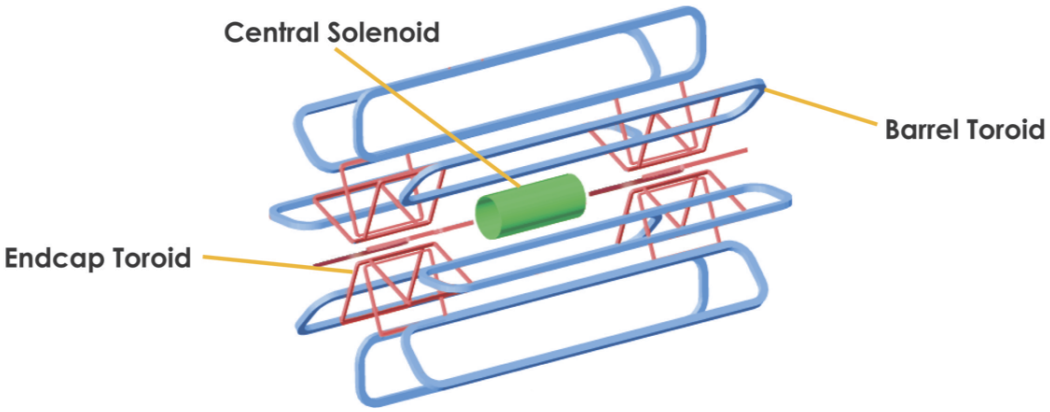

Figure 2.10. Geometry of the magnets that generate ATLAS magnetic fields [50].

The central solenoid, coaxial to the beam axis, generates a 2 T axial magnetic field. It is 5.8 m long and its internal and external diameters are respectively 2.46 m and 2.56 m long. This solenoidal magnetic field makes charged particles bend in the (x, y) plane. The solenoid has been designed so as to minimise the material in front of the calorimeters and therefore to make as small as possible the energy loss of particles when passing through it. For this reason, the cryostat, necessary for its functioning, is the same used for the electromagnetic calorimeter.

The barrel toroid, clearly visible in Figure 2.11, is made of 8 superconductive coils of 25.3 m length and forms a cylindrical region of internal and external diameters respectively of 9.4 m and 20.1 m. The generated toroidal magnetic field has an intensity that varies between 0.15 T and 2.5 T, depending on the values of r and ϕ. Field lines are circumferences with the axis that coincides with the beam axis and so this field makes charged particles bend in the plane (r, z). The end-cap toroids are 5 m long and have internal and external diameters respectively 1.65 m and 10.7 m long. Their magnetic field varies between 0.2 T and 3.5 T.

Thanks to these magnetic fields, the Inner Detector and the Muon Spectrometer can measure the momentum of charged particles. Indeed, a particle of charge q crossing a magnetic field $\vec{B}$ with velocity v is subject to the Lorentz force,

$$\vec{F} = q\vec{v} \times \vec{B}, \tag{2.14}$$

and makes a helical trajectory in the plane orthogonal to $\vec{B}$. The helix radius R

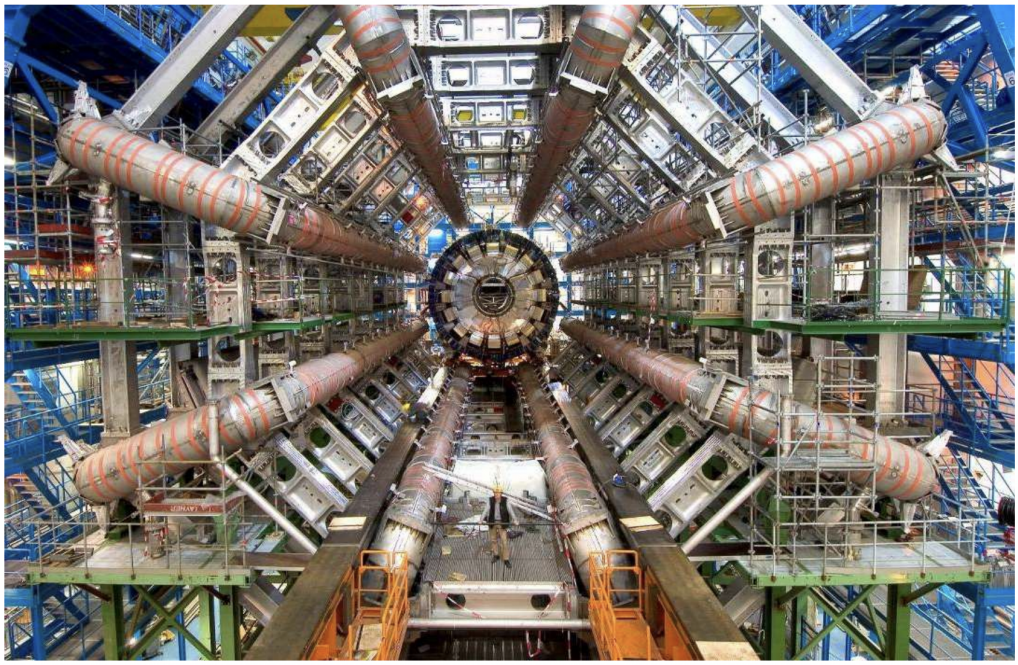

Figure 2.11. The barrel toroid just after its installation in the ATLAS cavern [35].

is related to the momentum component $p_\perp$ perpendicular to $\vec{B}$ by the following relation:

$$p_\perp[\text{GeV}] = 0.3 \cdot B[\text{T}] \cdot R[\text{m}]. \tag{2.15}$$

Thus, by measuring the curvature radius and knowing the magnitude of the magnetic field, it is possible to obtain the particle momentum. In ATLAS, the solenoidal field allows us to obtain the momentum transverse to the beam axis, while the toroidal field the total momentum.

2.2.3 The Inner Detector

The Inner Detector [51] is designed to provide a robust pattern recognition, excellent momentum resolution and both primary and secondary vertex measurement for charged tracks above a given p_T threshold (nominally 0.5 GeV). It is composed of three sub-detectors made with fine detector granularity, which work together to achieve an excellent momentum and vertex resolution: the Pixel Detector, the Semiconductor Tracker and the Transition Radiation Detector. All these sub-detectors are divided into a barrel and an end-cap part. The ID, whose layout is illustrated in Figure 2.12, is entirely contained in a cylinder of radius 1150 mm and length 7024 mm centred in the interaction point and immersed in the 2 T magnetic field generated by the central solenoid. The ID is able to identify charged tracks up to $|\eta| < 2.5$. Overall the combined momentum resolution of the Inner Detector is

$$\frac{\sigma_{p_\text{T}}}{p_\text{T}} = 0.05\% \cdot p_\text{T} \oplus 1\%, \tag{2.16}$$

where $\oplus$ means that the two contributions are summed in quadrature.

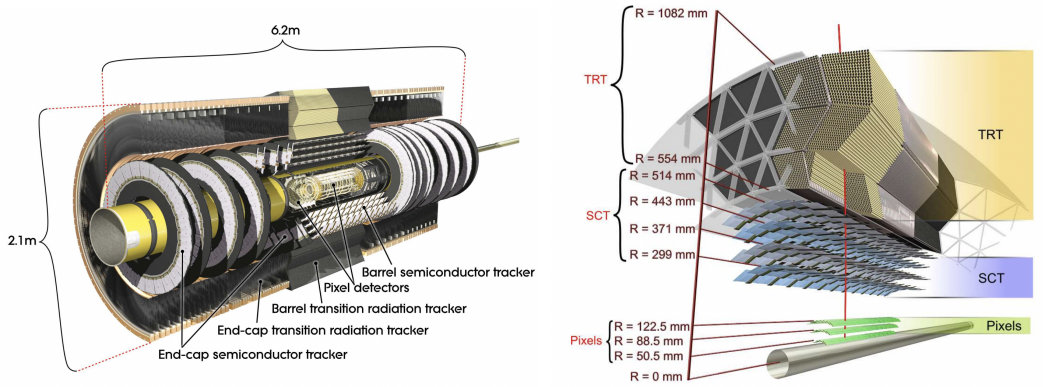

(a) (b)

Figure 2.12. Cut-away view of the ATLAS Inner Detector (a) and representation of all the layers of the Pixel Detector (apart from the Insertable B-Layer), the SCT and the TRT traversed by a charged track (red line) in the barrel region (b) [35].

Pixel Detector

The Pixel Detector is the ATLAS sub-detector closest to the beam pipe. It is made of four layers of silicon pixel detectors in the barrel and three disks in each end-cap region. The innermost layer is called Insertable B-Layer (IBL) and was installed during the Long Shutdown 1 [52] for a more precise reconstruction of secondary vertices and a more efficient B meson identification. The IBL extends from a radial distance of 33.5 mm to 40 mm from the interaction point and consists of 50×250 µm^2 sensors with a resolution of 8 µm in the transverse plane and 40 µm along the z axis.

The other three layers of the Pixel Detector in the barrel, present since Run 1, are placed at a distance of 50.5 mm, 88.5 mm and 122.5 mm from the beam pipe respectively and are made of 50×400 µm^2 sensors having a resolution of 10 µm in the transverse plane and 115 µm along z. The same sensors compose also the three end-cap disks, which are positioned at a longitudinal distance of 49.5 mm, 58 mm and 65 mm from the interaction point.

Semiconductor Tracker

The Semiconductor Tracker (SCT) surrounds the Pixel Detector and is made of silicon microstrips with a resolution of 17 µm in the (r, ϕ) plane and 580 µm along the z axis. The SCT is divided into four cylindrical layers in the barrel region, covering the region $299\,\text{mm} < r < 514\,\text{mm}$, while in each end-cap region it is composed of 9 disks that extend from $|z| = 839\,\text{mm}$ to $|z| = 2735\,\text{mm}$.

Transition Radiation Tracker

The outer part of the Inner Detector is constituted by the Transition Radiation Tracker (TRT). The TRT is a detector made of straw tubes of 4 mm diameter filled

with a mixture of 70% Xe, 27% CO_2 and 3% O_2 and interleaved with polypropylene fibres. When a charged particle passes through the plastic fibres, it emits transition radiation photons. The gaseous tubes therefore are used both to reconstruct the track of the charged particle and to detect the transition radiation photons. Since the emitted transition radiation depends on the mass of the particle, the TRT provides an additional discrimination between particles with the same momentum but different mass (e.g. electrons from charged pions). The TRT can reconstruct charged tracks up to $|\eta| = 2$ with a resolution of 130 µm in the (r, ϕ) plane.

2.2.4 The calorimeter system

The ATLAS calorimeter system, represented in Figure 2.13, surrounds the central solenoid and is composed of an electromagnetic calorimeter, which measures the energy deposited by electrons and photons through electromagnetic showers, and a hadronic calorimeter, which reconstructs hadronic jets. Both detectors are sampling calorimeters, divided into a barrel and an end-cap region and overall cover the pseudorapidity range $|\eta| < 4.9$.

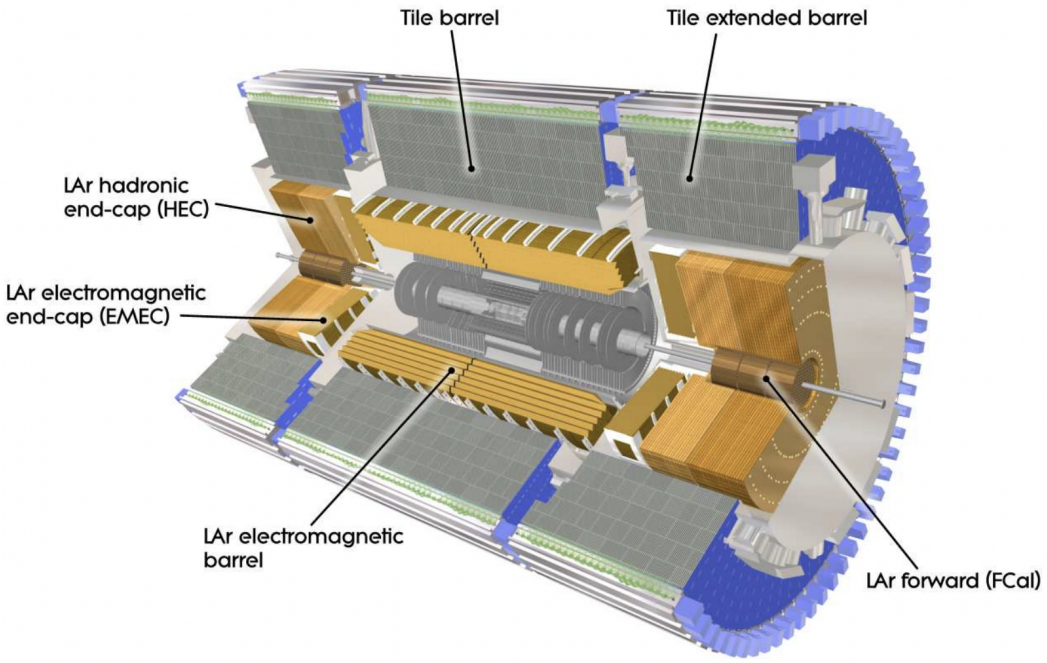

Figure 2.13. The ATLAS calorimeter system [35].

Electromagnetic calorimeter

The electromagnetic calorimeter (ECAL) [53] is a sampling calorimeter that uses liquid argon (LAr) as the active material and lead plates as the absorber. The choice of the material was driven by the need to make electromagnetic showers fully develop in a limited space: an electromagnetic shower, indeed, usually develops

completely within 25 radiation lengths[3] (denoted with X_0) and the ECAL thickness is between 22 and 33 X_0, depending on the pseudorapidity. The electrodes and the lead plates follow an accordion geometry, which provides complete coverage in ϕ and a fast signal extraction. The ECAL is divided into a barrel part, covering the region $|\eta| < 1.475$, and two end-cap parts (EMEC), which cover the region $1.375 < |\eta| < 3.2$. The liquid argon is kept at a temperature of 89 K by three different cryostats: the barrel part of the ECAL uses the same cryostat as the central solenoid, while the two cryostats of the EMEC are shared with the LAr hadronic calorimeter. The gaps between the cryostats, called *transition regions*, are filled with cables and services and therefore, in these regions, the precision of the measurements is lower.

The ionisation signal in the liquid argon is read out by electrodes made of three conductive copper layers separated by Kapton foils, placed in the gap between the lead plates. In the barrel, the distance between lead plates and electrodes is constant and equal to 2.1 mm, while in the end-caps the gap varies as a function of the radius. The electrode edges are kept at a difference of potential of 2 kV, while in the end-caps the difference of potential varies from 1 to 2.5 kV to obtain a uniform detector response independently from η.

The barrel part of the ECAL covers the region $|\eta| < 1.475$, while the end-cap parts cover the range $1.375 < |\eta| < 2.5$. The ECAL barrel is divided into two parts symmetric with respect to the interaction point, each one long 3.2 m. The internal and external diameters measure respectively 2.8 m and 4 m and the total width in terms of radiation lengths varies from 22 to 30 X_0 between $|\eta| = 0$ and $|\eta| = 0.8$, and from 24 to 33 X_0 between $|\eta| = 0.8$ and $|\eta| = 1.3$. Each half of the ECAL barrel is divided into 16 modules, each one covering an interval $\Delta\phi = 22.5°$. Each module is segmented in depth into three layers with different granularity. The first one, called Strip Layer, has a thickness that corresponds to 4 X_0 and is highly segmented ($\Delta\eta \times \Delta\phi = 0.003 \times 0.1$), so that it can measure with great precision the beginning of electromagnetic showers. Then, there is the Middle Layer, 16 X_0 thick, with a granularity $\Delta\eta \times \Delta\phi = 0.025 \times 0.025$, in which most of the electromagnetic shower energy is deposited. Lastly, there is the Back Layer, 2 X_0 deep, less segmented than the previous ones ($\Delta\eta \times \Delta\phi = 0.05 \times 0.025$), whose task is the collection of shower tails. Before the Strip Layer, a Presampler Layer is placed, made up of a small thickness (11 mm) of liquid argon, which is necessary to correct the shower energy leakage before the ECAL. Figure 2.14 shows the granularity of an ECAL module at $\eta = 0$ and the dimensions of the three layers that compose it. The EMEC consists of two wheels of 63 cm thickness and internal and external radius respectively of 33 cm and 2.1 m. It covers the region $1.375 < |\eta| < 3.2$ and has a presampler calorimeter covering the region $1.5 < |\eta| < 1.8$.

[3]The *radiation length* X_0 is defined as the thickness of material that reduces the energy of an electron by $1/e$.

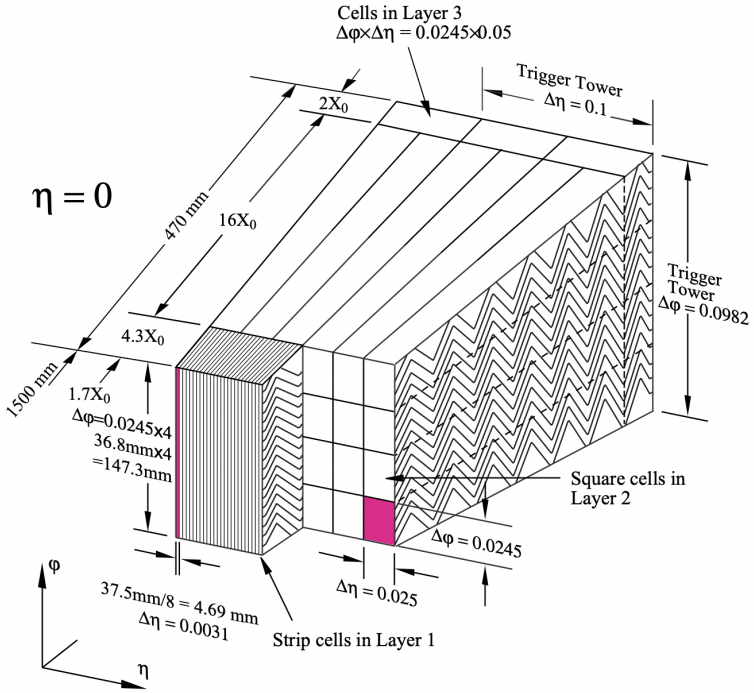

Figure 2.14. A barrel module of the ATLAS electromagnetic calorimeter [35].

The energy resolution of the electromagnetic calorimeter is given by

$$\frac{\sigma_E}{E} = \frac{10\%}{\sqrt{E}} \oplus 0.7\%. \tag{2.17}$$

Hadronic calorimeter

The hadronic calorimeter (HCAL) [54] is composed of a set of sub-detectors, which employ different technologies depending on the pseudorapidity interval they cover.

The Tile Calorimeter surrounds the electromagnetic calorimeter envelope and is divided into a barrel part, which covers the region $|\eta| < 1$, and two extended barrels, which cover the range $0.8 < |\eta| < 1.7$. It is a sampling calorimeter, which uses steel as the absorber and scintillating tiles as the active material. The Tile Calorimeter extends from a radius of 2.28 m to 4.25 m and is segmented into three layers. The layers of the barrel have a thickness of 1.5, 4.1 and 1.8 interaction lengths[4] (λ) respectively, while the extended barrel layers are 1.5, 2.6 and 3.3 λ thick. The total thickness of the Tile Calorimeter is 9.7 λ at $\eta = 0$. The ultraviolet scintillation light emitted by particles crossing the Tile Calorimeter is converted into visible light by wavelength shifting fibres (WLS) and then collected by photomultiplier tubes (two separate tubes per scintillating tile, to read out the two sides).

[4]The *interaction length* λ is defined as the average distance travelled inside a medium by a hadron before interacting with it. Usually a hadronic shower fully develops within 10 interaction lengths.

The Hadronic End-cap Calorimeter (HEC) consists of two independent wheels per end-cap and covers the region $1.5 < |\eta| < 3.2$. It is a sampling calorimeter made of copper plates interleaved with liquid argon gaps and shares the cryostat with the EMEC. The resolution from the combination of Tile Calorimeter and HEC is given by

$$\frac{\sigma_E}{E} = \frac{50\%}{\sqrt{E}} \oplus 3\%. \tag{2.18}$$

The region $3.1 < |\eta| < 4.9$ is covered by the Forward Calorimeter (FCal), which is designed to operate at extremely high radiation levels. In order to reduce the amount of neutron albedo in the inner detector cavity, the FCal position is displaced by 1.2 m with respect to the EMEC front face. The FCal is 10 λ deep and is divided into three modules: the first one uses copper as the absorber and is optimised for electromagnetic measurements, while the other two use tungsten and measure the energy of hadronic showers. All the modules of the FCal, which is integrated into the end-cap cryostat, employ liquid argon as the sensitive medium. The resolution of the FCal is

$$\frac{\sigma_E}{E} = \frac{100\%}{\sqrt{E}} \oplus 10\%. \tag{2.19}$$

2.2.5 The Muon Spectrometer

The Muon Spectrometer (MS) [55], depicted in Figure 2.15, is the most external sub-system of ATLAS and it is composed of four sub-detectors exploiting different technologies. Two of them are dedicated to reconstructing the tracks and measuring the momentum of particles that cross the calorimeters and reach the MS, the other two are used to trigger muons. The MS, as all the other ATLAS sub-systems, is made of a barrel, covering the region $|\eta| < 1.05$, and two end-caps, for $1.05 < |\eta| < 2.7$. The MS is immersed in the magnetic field generated by the ATLAS toroids. For $|\eta| < 1.4$ the magnetic field is provided by the barrel toroid, while for the range $1.6 < |\eta| < 2.7$ by the end-cap magnets. In the transition region ($1.4 < |\eta| < 1.6$) the field is a combination of the fields generated by the barrel and the end-cap magnets. This magnet configuration provides a field which deflects the particles in the (z, r) plane and which is mostly orthogonal to their trajectories, providing a momentum resolution of $2 \div 3\%$ for most of their kinematic range.

The barrel part of the MS consists of three coaxial cylinders called *Barrel Inner* (BI), *Barrel Medium* (BM) and *Barrel Outer* (BO), installed at a radial distance from the beam axis of 5 m, 7.5 m and 10 m respectively. The MS barrel is divided into two sides by a gap at $\eta = 0$, which is needed for cables and services for the inner ATLAS sub-systems. Additional gaps in acceptance are in correspondence with the detector support structure (feet). In the barrel, the precision momentum measurement is performed by the *Monitored Drift Tubes* (MDT), while the trigger task is demanded to the *Resistive Plate Chambers* (RPC). The three cylinders of the MS barrel are divided in the azimuthal direction into 16 sectors, eight large (L)

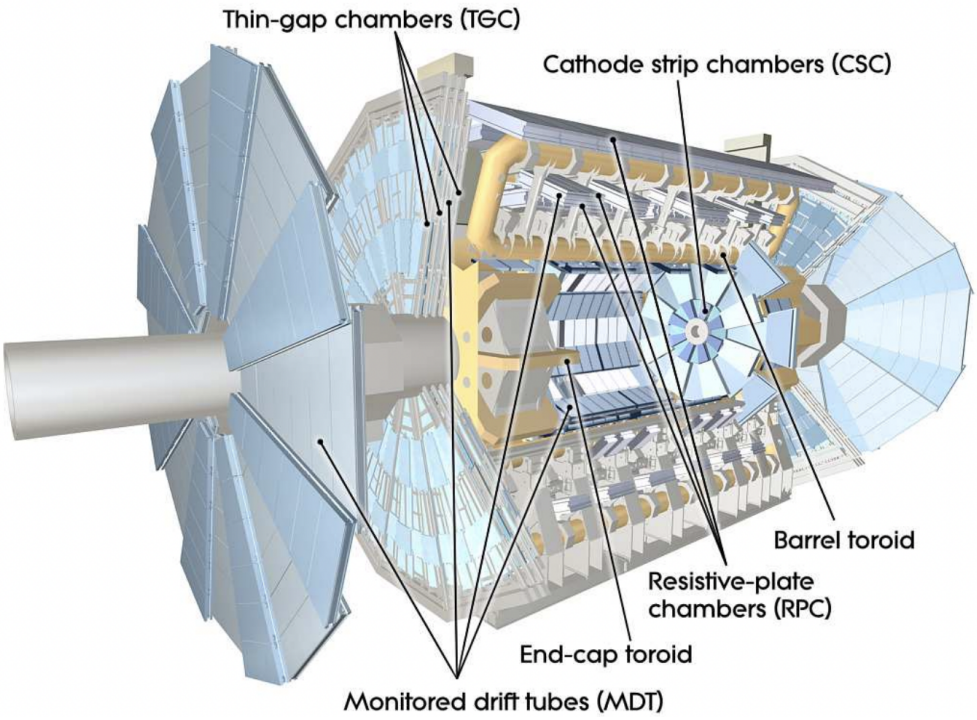

Figure 2.15. Cut-away view of the ATLAS muon system [35].

and eight small (S), covering 14° and 8.5° respectively, as shown in Figure 2.16.

Each MS end-cap is made of three wheels named *End-cap Inner* (EI), *End-cap Medium* (EM) and *End-cap Outer* (EO), placed respectively at a distance $|z|$ from the interaction point of 7.4 m, 14 m and 21.5 m. These three wheels are also known as *Small Wheel*[5], *Big Wheel* and *Outer Wheel* respectively. A further set of muon chambers, called *End-cap Extra* (EE), is placed at $|z| = 10.8$ m to identify muons crossing the transition region between barrel and end-caps. The MS end-caps employ MDTs and *Cathode Strip Chambers* for precision measurement and *Thin Gap Chambers* (TGC) for trigger. Figure 2.17 shows a schematic view of the cross-section of the MS in the transverse and the longitudinal planes, indicating the positions of the different muon chambers that make up the three barrel cylinders and the three end-caps wheels.

MDTs are aluminium drift tubes with a 30 mm diameter and a variable length (between 1 m and 6 m) and are filled with a 93% : 7% mixture of Ar:CO_2 at a pressure of 3 bar. They use a coaxial anode wire kept at 3 kV to collect the ionisation products generated by muons crossing the tubes. MDT chambers are used for the precision measurement of muon tracks in the region $|\eta| < 2.7$ (except in the innermost end-cap wheel where their coverage is limited to $|\eta| < 2.0$). The chambers

[5]The Small Wheels have been operational for Run 1 and Run 2. During the Phase-I upgrade, they have been replaced by the *New Small Wheels*, designed to work even in the high particle rate environment of HL-LHC (see Chapter 5).

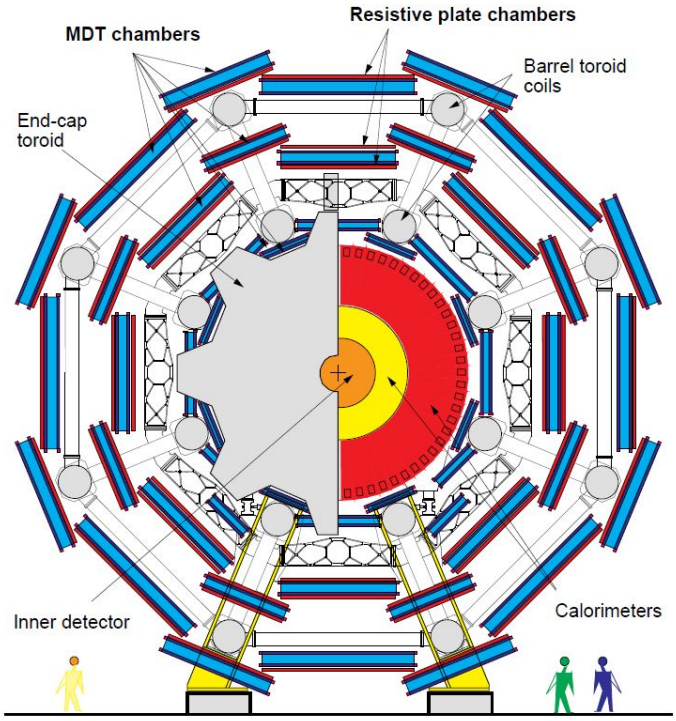

Figure 2.16. Schematic view of the transverse section of the ATLAS barrel, showing the Inner Detector, the calorimeters and the Muon Spectrometer [55].

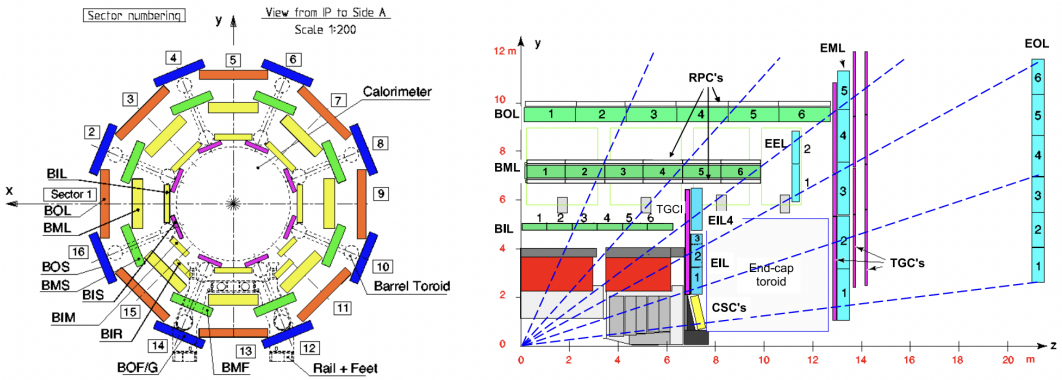

Figure 2.17. On the left, the cross-section of the barrel Muon Spectrometer in the (x, y) plane (non-bending plane). On the right, the cross-section of the Muon Spectrometer in the (y, z) plane (bending plane). Blue dashed lines represent infinite momentum muons propagating along straight trajectories [35].

consist of three to eight layers of drift tubes and achieve a resolution of 80 µm per tube and 35 µm per chamber.

In the region $2 < |\eta| < 2.7$ of the Small Wheels, the particle rate is above the safe limit of the MDTs, so CSCs are used instead of MDTs to measure the muon momentum. CSCs are multi-wire proportional chambers filled with a 80% : 20% mixture of Ar:CO_2. The CSCs have cathode planes segmented into strips in orthogonal directions and therefore they are able to measure both the η and the ϕ coordinate. The resolution of a chamber is 40 µm in the bending plane and about 5 mm in the transverse plane.

Besides the precision tracking chambers, the MS is provided also with a system of very fast chambers, which can deliver track information within a few tens of nanoseconds ($15 \div 25$ ns) after the passage of the particle and so can be used to trigger on muon tracks. In the barrel region ($|\eta| < 1.05$) this task is performed by the RPCs while in the end-caps ($1.05 < |\eta| < 2.4$) by the TGCs. The RPCs consist of two bakelite resistive plates kept a potential difference of 9.8 kV and separated by a 2 mm gap filled with a gas mixture made of $C_2H_2F_4$: C_4H_10 : SF_6 with ratios of 94.7% : 5.0% : 0.3%. The high voltage provides a trigger time resolution of 1.5 ns. The plates are segmented into strips with a width between 25 mm and 35 mm, which gives the RPCs the possibility also to measure the track position with a 10 mm spatial resolution. There are in total three layers of RPC doublet chambers in the barrel: two in the BM region and one in the BO. The TGCs are multi-wire proportional chambers where the distance between the anode and the cathode is smaller than the anode wire pitch. In this way, they can collect ionisation signals very quickly, with a time resolution typically of 5 ns. The TGCs are installed in the EI and EE layers of the end-cap MS and are filled with a gas mixture of 55% : 45% of CO_2 and n-pentane. Having the anodes parallel to the MDT wires and the cathode strips along the radial direction, the TGCs can provide a two-dimensional measurement of the muon tracks.

2.2.6 The trigger and data acquisition system

At the LHC every 25 ns a bunch crossing takes place, providing an event rate of 40 MHz. Since each event corresponds to approximately 1.5 MB of data to be recorded on disk, recording all the events produced by LHC collisions would translate into saving 60 TB of data per second, which is inconceivable even with the most recent data storage technologies. Anyway, most of the events consist of soft parton scatterings, which are not interesting for physics analyses and therefore do not need to be recorded. The task of deciding which events are worth saving and which are not is assigned to the ATLAS trigger and data acquisition (TDAQ) system, which is also responsible for storing them. In Run 2 the trigger decision was made using a two-stage system: the first stage, the *Level-1* (L1) trigger, consists of a hardware-based system that uses coarse information from the calorimeters and the Muon Spectrometer, while the second stage, the *High Level Trigger* (HLT), is software-based and runs more complex algorithms to make the trigger decision [44].

Figure 2.18 schematises the ATLAS TDAQ system in Run 2.

The Level-1 trigger

The L1 trigger [56] uses custom electronics to make the trigger decision based on information from the calorimeter system (L1Calo), the muon system (L1Muon) and the L1 topological (L1Topo) trigger. The L1Calo trigger receives the analog signals from the calorimeter detectors, digitises and calibrates them through the Preprocessor and elaborates them with the Cluster Processor (CP) and the Jet/Energy-sum Processor (JEP) in parallel. The CP identifies electron, photon and τ-lepton candidates above a programmable threshold, while the JEP identifies jet candidates and computes the total energy and the missing transverse momentum. The L1Muon trigger uses information from the three RPC stations in the barrel and the three TGC stations in the end-caps to generate muon candidates. This information is used to form hit patterns, which are matched with pre-defined coincidence matrices centred on the middle trigger station and depending on the trigger threshold. To reduce the fake trigger rate, the L1Muon trigger applies coincidence requirements between the outer and the inner TGC stations, as well as between the TGC and the Tile Calorimeter. The trigger objects from the L1Calo and the L1Muon are then combined by the L1Topo trigger, which makes a trigger decision considering topological requirements (such as invariant masses or angular distances). The final L1 trigger decision is made by the Central Trigger Processor (CTP), which receives inputs from the L1Calo trigger, the L1Muon trigger through the L1Muon Central Trigger Processor Interface (MUCTPI), the L1Topo trigger and several other detector sub-systems. In order to stay within the constraints of detector read-out latency and prevent front-end buffers from overflowing, the CTP can apply *dead time*, a mechanism that sets a minimum time between two consecutive L1 accepts and restricts the number of L1 accepts allowed in a given number of bunch crossings. The L1 trigger accepts events with a rate up to 100 kHz (maximum rate of the detector read-out) and within a latency of 2.5 µs.

The High Level Trigger

The HLT is entirely software-based and runs on a farm of Processing Units. It receives the *Regions of Interest* (RoIs) in η and ϕ identified by the L1 trigger and processes them first with fast trigger algorithms for a preliminary rejection, and then with more precise and more CPU-intensive algorithms, similar to those used for offline object reconstruction, to make the final decision. For some physics objects, the HLT requests information from the full detector (for example for $E_{\mathrm{T}}^{\mathrm{miss}}$ reconstruction). The HLT software is largely based on the offline software Athena [57], which is used also for physics analyses. The output rate of the HLT was of 1.2 kHz during Run 2, translating into 1.2 GB/s of data sent to permanent storage.

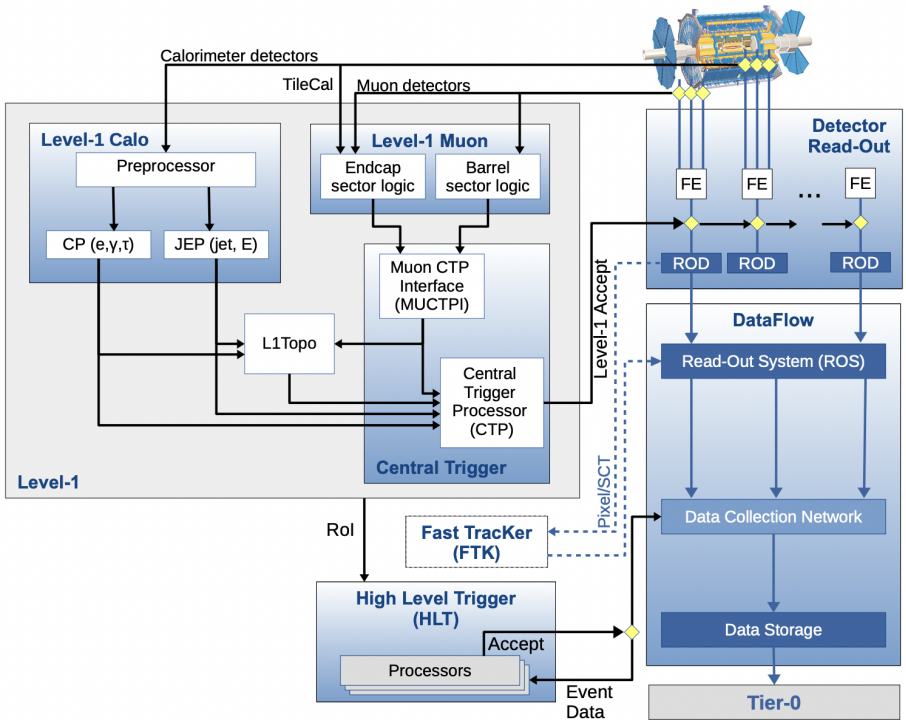

Figure 2.18. The ATLAS TDAQ system in Run 2 [44].

Read-out

Every time an event is accepted by the L1 trigger, the Front-End (FE) electronics read out the data relative to that event for all the ATLAS sub-detectors. The data are first sent to ReadOut Drivers (RODs), which perform the initial processing and formatting, and then to the ReadOut System (ROS) to buffer the data. The ROS sends the data to the HLT when requested and once an event is accepted also by the HLT, the corresponding data are sent to permanent storage for offline reconstruction.

2.2.7 Event simulation

Most physics analyses, including the one presented in this thesis, are based on the comparison of the data measured by the ATLAS detector with the number of events expected from the theoretical predictions and the knowledge of the detector response. The simulation of particle collisions, performed by the ATLAS Simulation Infrastructure [58], consists of three steps: event generation, detector simulation and digitisation.

The first step relies on Monte Carlo (MC) generators to produce the particles originating from the hard scattering process. The parton level processes are generated using perturbation theory, while the hadronisation cannot be derived perturbatively. Particles with a proper lifetime $c\tau > 10\,\text{mm}$ are considered stable by the

event generator. Their interaction with the detector material and their decay are handled by the simulation step. Any particles with $c\tau < 10\,\text{mm}$ are instead decayed by the event generator and their interactions with the detector material or curving in the magnetic field are ignored. Among the most used event generators there are PYTHIA [59], SHERPA [60] and POWHEG [61]. PYTHIA and SHERPA provide a full event generation, while POWHEG generates only parton-level events and therefore it has to be interfaced with parton showering simulators like PYTHIA.

The generated events are then propagated through the simulation of the ATLAS detector, which is modelled with GEANT4 [62]. In this step the interactions of all the generated particles with the detector elements are simulated, taking into account the detector sensitivity, geometric acceptance and resolution. The traces deposited in the sensitive portions of the detector, containing the deposited energy, position and time information, are referred to as *hits*. They are recorded and passed to the digitisation step.

In the digitisation stage, the simulated detector hits from the hard scattering process are overlaid with the *underlying event*[6] and other cavern background events, producing in this way the pileup. Detector noise is also added to the event. The output of this stage is a byte-stream format file, which emulates the data-taking procedure and conditions.

In both event generation and detector simulation, the *truth* information is also recorded for each event, including information on the incoming and outgoing particles and their interaction history. Truth information is employed to measure the performance of the object reconstruction algorithms but may be also useful for physics analyses.

[6]The non-interacting partons of the two protons that generate the hard scattering process (i.e. the interaction with the highest transverse momentum transfer) may produce minor energy deposits in the detector, which are referred to as *underlying event*.

Chapter 3

Object reconstruction in ATLAS

After being selected by the ATLAS two-level trigger system, the events are stored permanently to memory by the ReadOut System. All the recorded data need then to be processed and organised to reconstruct the physical objects to be used by the analyses. Even though already at the trigger level a partial object reconstruction is performed, the physics analyses need much more detailed information than the rough one associated with the *trigger objects* by the fast L1 and HLT algorithms to perform the trigger decision.

The object reconstruction step assembles the signals collected by all the ATLAS sub-detectors to produce the most accurate representation of the particles that left those signals. A calibration step is also needed to correct the construction imperfections. The software used for the reconstruction and the calibration, and also for the HLT algorithm implementation, is Athena [57], which is based on the Gaudi framework [63] for building data processing applications in high-energy physics experiments.

This Chapter presents how the different physics objects have been reconstructed and calibrated in ATLAS during Run 2.

3.1 Inner Detector tracks

The identification of the tracks left by charged particles in the Inner Detector is a challenging task due to the high number of pileup events that may originate from a single bunch crossing, as can be evinced from Figure 3.1, which shows the charged tracks identified in a $Z \to \mu\mu$ candidate event with 65 additional reconstructed primary vertices recorded by ATLAS during Run 2.

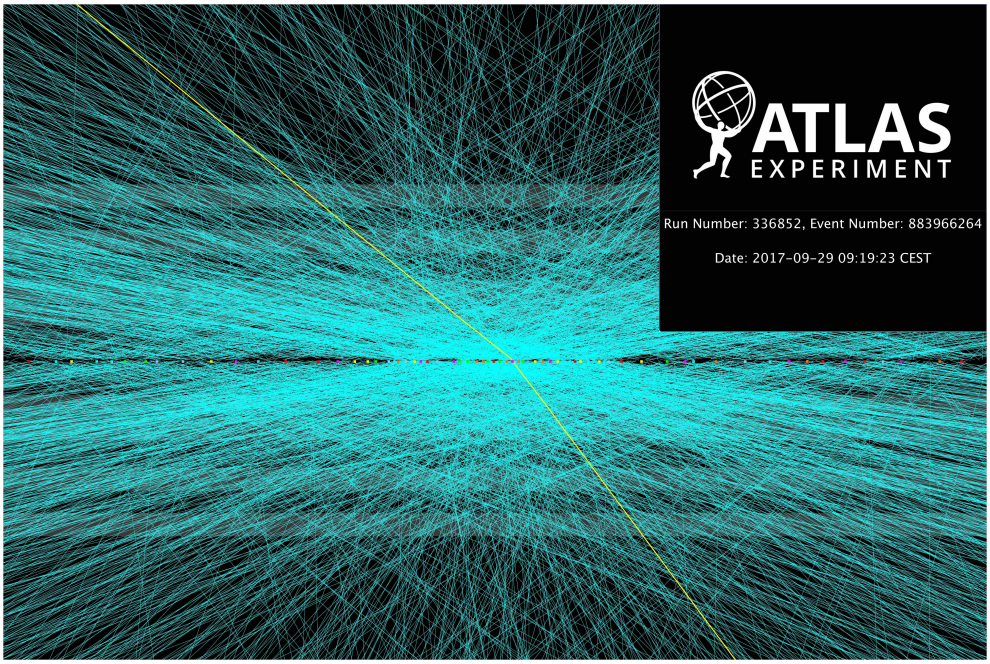

Figure 3.1. Event display for a $Z \to \mu\mu$ candidate event with 65 additional reconstructed primary vertices recorded by ATLAS in 2017 [64].

3.1.1 Track reconstruction

The trajectory of charged particles crossing the Inner Detector is bent by the magnetic field, resulting in a helix. This helical trajectory can be described by five parameters: the magnitude of the transverse momentum p_{T}, the polar angle θ, the azimuthal angle ϕ, the impact parameter in the transverse plane d_0 and the impact parameter in the longitudinal plane z_0. The impact parameters d_0 and z_0 are defined as the distance of the closest approach between the particle track and the Primary Vertex in the respective planes.

The track reconstruction during Run 2 [65] is performed according to the following steps. First of all, a clustering procedure forms space-points by grouping together the hits left in the Pixel and SCT detectors, which have an associated energy deposit above a certain threshold. Track seeds are produced using groups of three space-points, to which other hits are then associated through an algorithm based on the combinatorial Kalman filter [66]. At this point, an ambiguity-solving algorithm is applied to the track candidates, since the same space-points may be associated with multiple tracks. This algorithm is based on a set of parameters including the momentum of the track, the cluster multiplicity, the χ^2 of the track fit and the number of holes in the track, defined as the number of hits expected in the Inner Detector but not measured. Clusters of hits can be shared by no more than two tracks and each track can have no more than two shared clusters. Track candidates are rejected by the ambiguity solver if they fail to meet any of the following basic quality criteria:

- $p_{\mathrm{T}} > 400\,\mathrm{MeV}$,

- $|\eta| < 2.5$,
- minimum of 7 pixel and SCT clusters,
- maximum of either one shared pixel cluster or two shared SCT clusters on the same layer,
- not more than two holes in the combined pixel and SCT detectors,
- not more than one hole in the pixel detector,
- $|d_0| < 2.0\,\text{mm}$,
- $|z_0 \sin\theta| < 3.0\,\text{mm}$.

If all the requirements listed above are satisfied, a higher-resolution fit of the trajectory is performed to update the track parameters with the information from the TRT and then the track is added to the collection available for the analyses.

3.1.2 Primary Vertices

The reconstructed tracks in the Inner Detector are used also to define the interaction Primary Vertices (PV) [67,68]. The PV identification algorithm looks for a first vertex seed among the intersections between the tracks and the beam line. Tracks are associated with that vertex according to their parameters. If the tracks are incompatible with the vertex seed, are rejected and used to define another vertex seed. This procedure is repeated until all tracks have been associated with a vertex. At this point the Primary Vertex (or Hard Scatter vertex) is identified as the vertex with the highest sum of the squared transverse momenta ($\sum p_{\text{T}}^2$) of the tracks associated with it. All the other vertices are then classified as pileup vertices.

3.2 Electrons and photons

3.2.1 Electron and photon reconstruction

To reconstruct electrons and photons information from the Inner Detector and the calorimeters are used. The main signature left by electrons and photons, indeed, consists in the electromagnetic showers in the calorimeters, but electrons, being charged particles, leave also tracks in the Inner Detector.

The reconstruction algorithm for electrons (and positrons, the electron antiparticles) and photons, described in depth in [69], starts with the identification of the tracks and the clusters to be used. *Proto-clusters* are formed in the EM and hadronic calorimeters, starting from a cell with an energy deposit E^{EM} at least 4 times larger than the cell noise σ^{EM}_{noise}. The proto-cluster is expanded with neighbouring cells with $E^{EM}/\sigma^{EM}_{noise} \geq 2$. Two cells are considered neighbouring if they are adjacent in the (η, ϕ) plane or if they belong to different calorimeter segmentation layers but have at least partial overlap in η or ϕ. Once a cell is added to the

proto-cluster, the algorithm looks for the neighbouring cells next to it and adds them if they satisfy the above requirement. This step is repeated until no neighbouring cells satisfy the condition $E^{EM}/\sigma^{EM}_{noise} \geq 2$. At this point all the cells that are adjacent to the cluster cells and have $E^{EM}/\sigma^{EM}_{noise} \geq 0$ are added to the proto-cluster. If two proto-clusters contain the same cell with $E^{EM}/\sigma^{EM}_{noise} \geq 2$, these proto-clusters are merged. A cell is considered a local maximum when it has $E^{EM} > 500\,\text{MeV}$, at least four neighbours and when none of the neighbours has a larger signal. When proto-clusters have two or more local maxima, they are split into separate clusters. The results of this procedure are called *Topological Calorimeter Clusters* (or *topo-clusters*) [70]. For the reconstruction of electrons and photons, only clusters with EM energy greater than 400 MeV and EM fraction $f_{EM} > 0.5$ are considered, in order to remove most of the pileup clusters. f_{EM} is defined as the ratio between the EM energy, i.e. the energy from cells in the EM calorimeter, and the total cluster energy.

The tracks for the electron candidates are built fitting the hits in the Inner Detector, taking into account also the energy losses due to the interaction with the material. At first the fit is performed assuming that the track originates from a pion, then, if the fit fails but the hits are close in η and ϕ to the cluster candidate, a new fit is done assuming this time a track produced by an electron with possible bremsstrahlung. If several tracks are associated with a cluster, only the one with the largest number of hits is considered. Photon conversion vertices are reconstructed from two tracks with no hits in the innermost pixel detector matching a secondary vertex consistent with a massless particle. Conversion vertices are then matched to the EM topo-clusters.

From the topo-clusters, *superclusters* are constructed as follows. The list of EM topo-clusters is sorted according to their E_{T} and topo-clusters are tested one by one to decide if they have the requirements to become supercluster seeds. To become an electron supercluster seed, a cluster is required to have $E_{\text{T}} \geq 1\,\text{GeV}$ and must be matched to a track with at least four hits in the silicon detectors. For photon supercluster seeds, instead, clusters must have $E_{\text{T}} \geq 1.5\,\text{GeV}$, with no requirement made on any track matching. After the identification of the seed clusters, the algorithm looks for the satellite clusters: a cluster is considered a satellite if it falls within a window of $\Delta\eta \times \Delta\phi = 0.075 \times 0.125$ around the seed cluster barycentre, as these cases tend to represent secondary EM showers originating from the same initial electron or photon. For electrons, a cluster is also considered a satellite if it is within a window of $\Delta\eta \times \Delta\phi = 0.125 \times 0.300$ around the seed cluster barycentre, and its best-matched track is also the best-matched track for the seed cluster. A photon cluster is also classified as satellite if its best-matched track belongs to the conversion vertex matched to the seed cluster. Seed clusters together with their satellite clusters form the superclusters.

After the construction of electron and photon superclusters, an initial energy calibration and position correction is applied to them and tracks are matched to electron superclusters and conversion vertices to photon superclusters, with the same procedure used for EM topo-clusters. At this point, shower shape and other

discriminating variables are used to identify electrons and photons. Since electrons and photon superclusters are built independently, a given supercluster may be identified both as an electron and a photon. These cases are marked explicitly as ambiguous and their final classification is left to each analysis.

3.2.2 Electron identification and isolation

The electron identification working points (WP) are defined through a likelihood discriminant exploiting variables related to the electron track, the lateral and longitudinal development of the electromagnetic shower and the spatial compatibility of the track with the reconstructed cluster. In this way it is possible to separate prompt electrons from all the background sources, like electrons from photon conversions or heavy-flavour hadron decays and misreconstructed calorimeter deposits from hadronic jets. Three mutually inclusive operating points, labelled *Loose*, *Medium* and *Tight*, are defined and optimised in bins of $|\eta|$ and E_{T}. The identification efficiency of the three operating points in the different bins of E_{T} and η is shown in Figure 3.2. The efficiency is measured with the tag and probe (T&P) method using $J/\psi \to e^+e^-$ (in the $5 < E_{\mathrm{T}} < 20\,\mathrm{GeV}$ range) and $Z \to e^+e^-$ events (for $E_{\mathrm{T}} > 15\,\mathrm{GeV}$) from data and MC simulations. The difference between data and MC simulation that can be observed especially at low E_{T} is due to a mismodelling in the variables used in the discriminator. According to this difference, correction factors (called *scale factors*) are derived to correct the MC simulations and make them match the efficiency measured in the data.

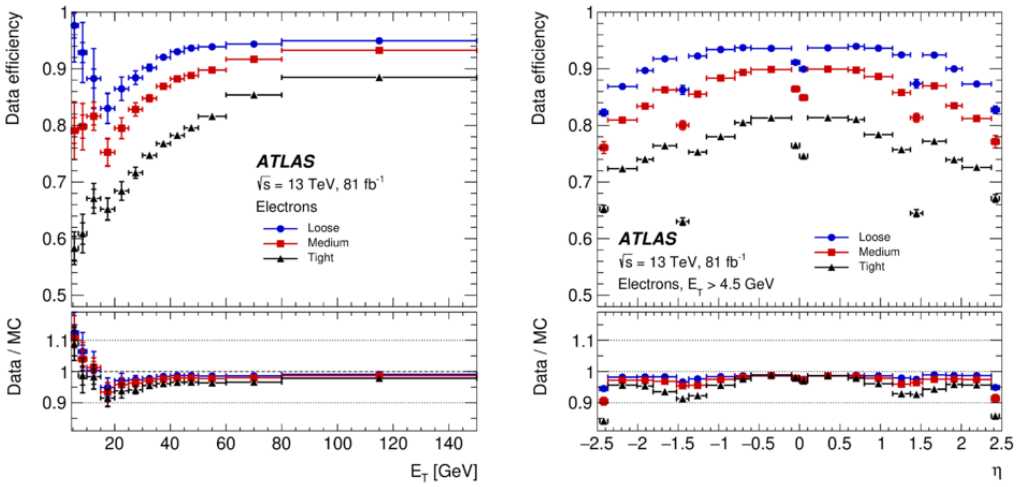

(a) **(b)**

Figure 3.2. Identification efficiencies of electrons from $J/\psi \to ee$ and $Z \to ee$ decays as a function of the electron (a) transverse momentum and (b) pseudorapidity for the different identification working points. [69].

To further discriminate prompt electrons (i.e. from prompt boson decays) from

electrons originating from semi-leptonic or heavy-flavour hadron decays, some isolation criteria are defined and applied to reconstructed electrons. Indeed prompt electrons are in general surrounded by less activity (tracks and energy deposits) with respect to non-prompt electrons. Two isolation variables are defined: the first one, called E_{T}^{cone20}, is based on the calorimeter energy clusters, while the other one, referred to as $p_{\mathrm{T}}^{varcone20}$, on tracks in the Inner Detector. E_{T}^{cone20} is defined as the sum of the E_{T} of topo-clusters in a cone of size $\Delta R = 0.2$ around the electron candidate, after the subtraction of the candidate energy. $p_{\mathrm{T}}^{varcone20}$ instead is defined as the sum of the p_{T} of the tracks with p_{T} above 1 GeV in a cone around the electron candidate with a variable radial opening given by $\Delta R = \min\left(\frac{10}{p_{\mathrm{T}}^{e}[\mathrm{GeV}]}, 0.2\right)$. The isolation working points are defined in two different ways, one having a fixed efficiency value while the other one having fixed cuts on the isolation variables. The definition with fixed efficiency is called *Gradient* working point and it is designed to give an efficiency of 90% at $p_{\mathrm{T}} = 25$ GeV and 99% at $p_{\mathrm{T}} = 60$ GeV, uniform in η. The three fixed cuts working points (*HighPtCaloOnly*, *Loose* and *Tight*) are defined according to the requirements reported in Table 3.1. The isolation efficiency of the different working points (both for the fixed efficiency and the fixed cuts definitions) for electrons from inclusive $Z \to e^+e^-$ events is shown in Figure 3.3.

Table 3.1. Definition of the electron isolation working points with fixed cuts on the isolation variables [69].

Working point	Calorimeter isolation	Track isolation
HighPtCaloOnly	$E_{\mathrm{T}}^{cone20} < \max(0.015 \times p_{\mathrm{T}}^{e}, 3.5\,\mathrm{GeV})$	–
Loose	$E_{\mathrm{T}}^{cone20}/p_{\mathrm{T}}^{e} < 0.20$	$p_{\mathrm{T}}^{varcone20}/p_{\mathrm{T}}^{e} < 0.15$
Tight	$E_{\mathrm{T}}^{cone20}/p_{\mathrm{T}}^{e} < 0.06$	$p_{\mathrm{T}}^{varcone20}/p_{\mathrm{T}}^{e} < 0.06$

The electrons used in the analysis presented in this thesis are selected using the Medium operating point for identification and the HighPtCaloOnly working point for isolation.

3.2.3 Photon identification and isolation

Photons are reconstructed by selecting superclusters with no matched tracks or superclusters matched to a photon conversion vertex in the Inner Detector. The criteria to select prompt and isolated photons and reject the background from hadronic jets are based on shower shape variables, since the electromagnetic showers resulting from photon conversions tend to be wider. Three identification working points (*Loose*, *Medium* and *Tight*) are defined optimising the cuts applied on the discriminant variables in different pseudorapidity bins. Three isolation working points are defined for photons, exploiting the E_{T}^{cone20}, E_{T}^{cone40} and p_{T}^{cone20} variables, where

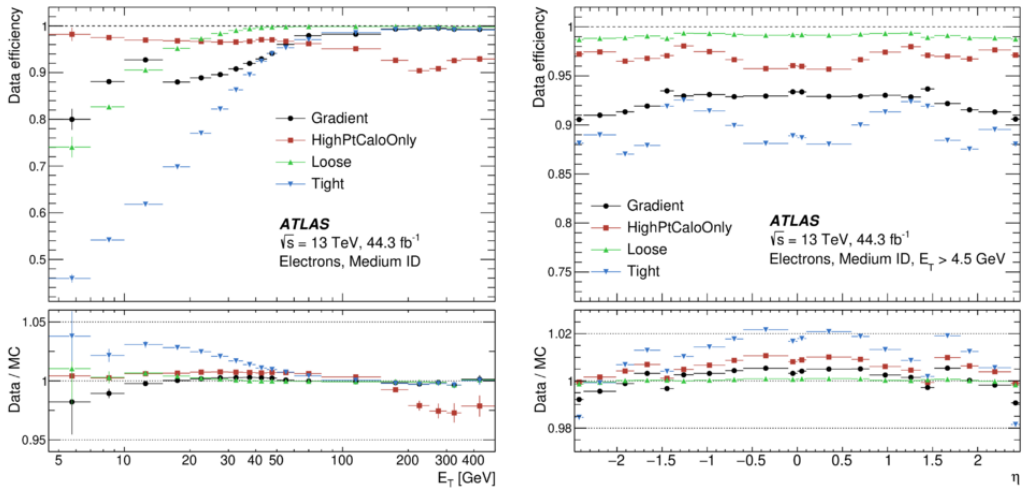

(a) (b)

Figure 3.3. Isolation efficiency of electrons from $Z \to ee$ decays as a function of the electron (a) transverse energy and (b) pseudorapidity for the different working points. [69].

E_{T}^{cone20} is the same variable used for electron isolation, E_{T}^{cone40} is defined as E_{T}^{cone20} but with $\Delta R = 0.4$ and p_{T}^{cone20} is the p_{T} sum of tracks within a cone centred around the photon cluster direction. The three photon isolation working points and the corresponding requirements are reported in Table 3.2.

Photons are not used in the analysis presented in this thesis.

Table 3.2. Definition of the photon isolation working points [69].

Working point	Calorimeter isolation	Track isolation
Loose	$E_{\mathrm{T}}^{cone20} < 0.065 \times E_{\mathrm{T}}$	$p_{\mathrm{T}}^{cone20}/E_{\mathrm{T}} < 0.05$
Tight	$E_{\mathrm{T}}^{cone40} < 0.022 \times E_{\mathrm{T}} + 2.45\,\mathrm{GeV}$	$p_{\mathrm{T}}^{cone20}/E_{\mathrm{T}} < 0.05$
TightCaloOnly	$E_{\mathrm{T}}^{cone40} < 0.022 \times E_{\mathrm{T}} + 2.45\,\mathrm{GeV}$	–

3.3 Muons

3.3.1 Reconstruction

Muons can be reconstructed using the signature of minimum-ionising particles crossing all the ATLAS sub-detectors up to the Muon Spectrometer, with a negligible energy loss in the calorimeters. The MS itself can provide a standalone

reconstruction of muons with $p_{\mathrm{T}} > 7\,\mathrm{GeV}$, but for a more precise measurement and a powerful background rejection the full ATLAS detector is exploited. The muon reconstruction [71] is therefore based mainly on the tracks measured by the ID and the MS, but information on the energy deposits in the calorimeters is also used.

The reconstruction of tracks in the ID is performed as described in Section 3.1, while the tracks in the MS are reconstructed starting from muon segments, short straight-line tracks identified from hits in an individual MS station through a Hough transform [72]. Preliminary track candidates are obtained by combining muon segments in different stations with loose constraints on the IP position and a parabolic trajectory, to approximate the muon bending in the magnetic field. Information on the second coordinate is added to obtain tridimensional track candidates. At this point, a global χ^2 fit of the muon trajectory through the magnetic field is performed, taking into account the effects of the interactions in the detector material as well as the effects of possible misalignments between the different detector chambers. The trajectory obtained by the fit is used to remove outlier hits and add hits along the trajectory that were not included in the previous step. Then the fit is performed again and ambiguities are resolved removing tracks which have a large number of hits in common with higher-quality tracks. These standalone MS tracks are then back-extrapolated to the beam line and their p_{T} is expressed at the IP.

Exploiting the information from the ID, the MS and the calorimeters five types of global muons can be reconstructed: *combined* (CB), *inside-out combined* (IO), *muon-spectrometer extrapolated* (ME), *segment-tagged* (ST) and *calorimeter-tagged* (CT). CB muons are identified by matching MS tracks to ID tracks and performing a combined track fit based on the MS and ID hits. IO muons are reconstructed by extrapolating ID tracks to the MS, searching for at least three loosely aligned MS hits and performing a fit using the ID track, the energy loss in the calorimeters and the MS hits. When no ID track is matched to a MS track, the MS track is extrapolated to the beam line and a ME muon is obtained. In this way the full MS coverage can be exploited, even if the MS track falls outside the ID acceptance. ST muons are built from an ID track matched to at least one MS muon segment with tight angular requirements. CT muons are defined by a match between an ID track and energy deposits in the calorimeters consistent with a minimum-ionising particle. Differently from the previous muon types, which consider ID tracks with p_{T} down to 2 GeV, for the CT muons a threshold of 5 GeV is applied to the track p_{T} to suppress the large background contamination at low p_{T}. All muon types, except for the ME muons, are required to have at least one hit in the pixel detector and at least five hits in the SCT detector. In addition, they are allowed to have in these two detectors at most two missing hits, which are counted when the muon trajectory crosses an active sensor that does not register a hit.

3.3.2 Identification

Several identification working points are defined depending on the number of hits in the different ID sub-detectors and MS stations and on the track fit prop-

erties. The three standard, mutually inclusive, working points are the *Loose*, the *Medium* and the *Tight* working points, with the first one having the highest efficiency but the lowest purity and the last one having the highest purity but the lowest efficiency. Two variables, q/p compatibility and ρ', are introduced to define the selection criteria required by the muon working points. The first variable is defined as

$$q/p\,\text{compatibility} = \frac{|q/p_{ID} - q/p_{MS}|}{\sqrt{\sigma^2(q/p_{ID}) + \sigma^2(q/p_{MS})}}, \tag{3.1}$$

where q/p_{ID} and q/p_{MS} are the ratios of the charge q and the momentum p of the muon measured in the ID and in the MS and $\sigma(q/p_{ID})$ and $\sigma(q/p_{MS})$ are the corresponding uncertainties, while the second one, which is defined only for CB and IO muons, is given by

$$\rho' = \frac{|p_{T,ID} - p_{T,MS}|}{p_{T,CB}}, \tag{3.2}$$

where $p_{T,CB}$ is the p_{T} resulting from the combined track fit.

The Medium selection working point in the region $|\eta| < 2.5$ accepts only CB and IO muons with at least two MS stations that recorded three or more hits in the MDT or CSC detectors. In addition, a q/p compatibility < 7 is required. The acceptance of the Medium working point is extended also to the region $2.5 < |\eta| < 2.7$ with the inclusion of ME muons that registered the hits mentioned before in at least three MS stations. The Tight accepts the same CB and IO muons of the Medium working point, but with more strict requirements on the q/p compatibility and on ρ', applying cuts that have been optimised in bins of p_{T} and η. The Loose working point accepts all the muons passing the Medium working point, plus CT and ST muons in the range $|\eta| < 0.1$. The Loose selection efficiency is further increased by accepting also muons with $p_{\mathrm{T}} < 7\,\text{GeV}$ and $|\eta| < 1.3$ that have been reconstructed both as IO muons and ST muons. In addition to the three standard working points, there are also two working points that have been designed for analyses targeting extreme phase-space regions: the *High-*p_{T} working point is optimal for muons with p_{T} above 100 GeV and has a very good momentum resolution and a powerful rejection low-quality tracks affected by large uncertainties; the *Low-*p_{T} working point is dedicated to muon with extremely low p_{T}, exploiting a set of variables providing a good separation of prompt muons the light-hadron decay background. Further details on the *High-*p_{T} and *Low-*p_{T} working points can be found in [71]. The identification efficiency is measured with the T&P method in $J/\psi \to \mu^+\mu^-$ events for $p_{\mathrm{T}}^{\mu} < 20\,\text{GeV}$ and in $Z \to \mu^+\mu^-$ events for the rest of the p_{T}^{e} spectrum. The efficiency of the three standard working points measured in data and MC simulation is shown in Figure 3.4 for the different p_{T}^{μ} and η bins. A scale factor is derived to take into account the differences from the efficiency measured in data and in MC simulation.

3.3.3 Isolation

As in the case of electrons and photons, also for muons some isolation criteria are defined in order to better discriminate prompt muons from the products of hadronic

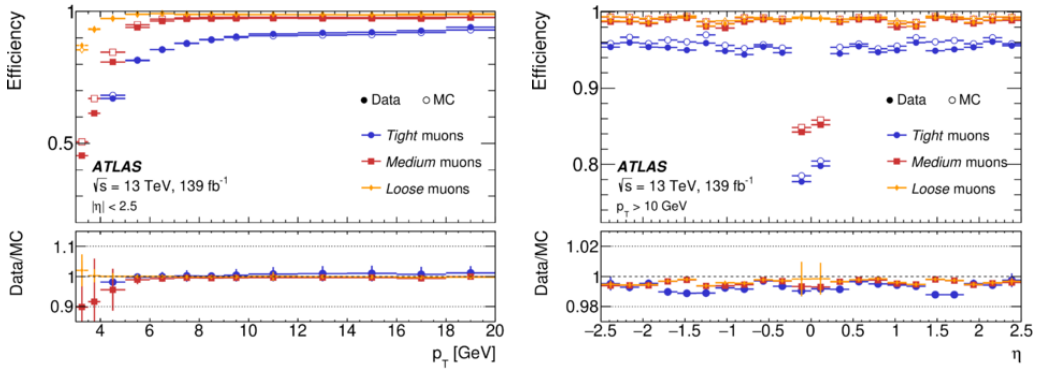

(a) (b)

Figure 3.4. Muon reconstruction and identification efficiency for the Loose, Medium and Tight working points from $J/\psi \to \mu\mu$ events as a function of the transverse momentum (a) and from $Z \to \mu\mu$ events as a function of the pseudorapidity [71].

decays. Similarly to the electron isolation case, variables based on the ID tracks or the calorimeter energy deposits are defined to describe the requirements of the different muon isolation working points. In particular, p_{T}^{cone20} is the scalar sum of the p_{T} of the tracks above 1 GeV in a cone of size $\Delta R = 0.2$ around the muon, excluding the muon track itself; $p_{\mathrm{T}}^{varcone30}$ is similar to p_{T}^{cone20} but in this case the radial opening of the cone is variable and is given by $\Delta R = \min\left(\frac{10}{p_{\mathrm{T}}^{\mu}[\mathrm{GeV}]}, 0.3\right)$; $E_{\mathrm{T}}^{topoetcone20}$ is the sum of the transverse energy of topo-clusters in a cone of size $\Delta R = 0.2$ around the muon position extrapolated to the calorimeters, after the subtraction of the muon energy deposits. The standard muon isolation working points, with the corresponding selection criteria, are listed in Table 3.3. The muon isolation efficiency is measured in $J/\psi \to \mu^+\mu^-$ and $Z \to \mu^+\mu^-$ events analogously as what described for the identification efficiency. Figure 3.5 shows the muon isolation efficiency for the Loose and the Tight working points as a function of the muon transverse momentum

Table 3.3. Definition of the muon isolation working points [71].

Working point	Calorimeter isolation	Track isolation
Loose	$E_{\mathrm{T}}^{topoetcone20} < 0.3 \times p_{\mathrm{T}}^{\mu}$	$p_{\mathrm{T}}^{varcone30} < 0.15 \times p_{\mathrm{T}}^{\mu}$
Tight	$E_{\mathrm{T}}^{topoetcone20} < 0.15 \times p_{\mathrm{T}}^{\mu}$	$p_{\mathrm{T}}^{varcone30} < 0.04 \times p_{\mathrm{T}}^{\mu}$
HighPtTrackOnly	–	$p_{\mathrm{T}}^{cone20} < 1.25\,\mathrm{GeV}$
TightTrackOnly	–	$p_{\mathrm{T}}^{varcone30} < 0.06 \times p_{\mathrm{T}}^{\mu}$

For the analysis presented in this thesis, muons are selected with Medium iden-

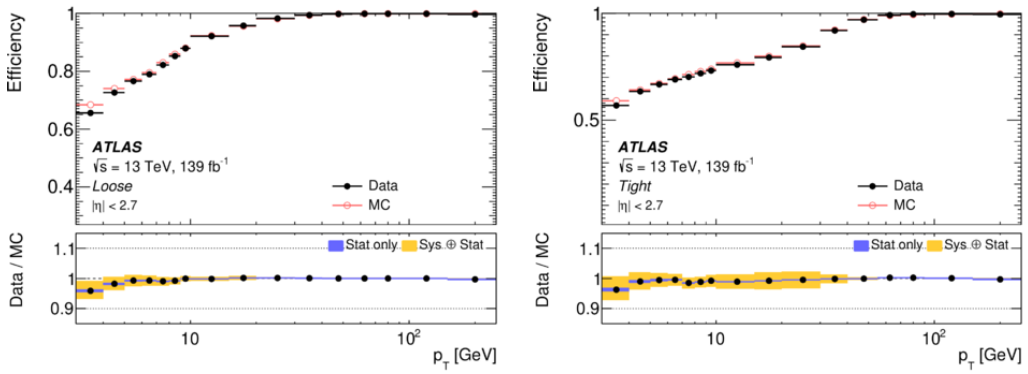

(a) (b)

Figure 3.5. Muon isolation efficiency measured in $Z \to \mu\mu$ events as a function of the transverse momentum for the Loose (a) and the Tight (b) working points [71].

tification and Loose isolation working points.

3.4 Tau leptons

With a mass of 1.777 GeV, tau leptons are the heaviest leptons of the Standard Model. Their proper lifetime is so short ($\tau = 2.9 \times 10^{-13}$ s, corresponding to a decay length $c\tau = 87\,\mu$m) that they decay typically before even entering the active regions of ATLAS detector. The only way to reconstruct and identify tau leptons is therefore through their decay products. 35% of the times tau leptons decay leptonically, through the process $\tau \to \ell\nu_\ell\nu_{tau}$ ($\ell = e, \mu$), while the other 65% decay through the hadronic mode ($\tau \to \nu_\tau +$ hadrons). The decay products of hadronically decaying tau leptons (labelled as τ_{had}) contain one or three charged pions in 72% and 22% of the decays respectively. When there is only one charge pion in the decay, the tau lepton is called *one-prong* ($\tau_{\text{1-prong}}$), while in the case of three charged pions it is called *three-prong* ($\tau_{\text{3-prong}}$). The 68% of the hadronic decays include also a neutral pion. Therefore the signature of the τ_{had} is that of a narrow jet with one or three tracks in the Inner Detector. The neutrino from the hadronic tau lepton decay cannot be reconstructed and the ensemble of all visible τ_{had} decay products is referred to as $\tau_{\text{had-vis}}$. Leptonic tau lepton decays are basically indistinguishable from prompt light leptons (electrons and muons), so they do not have a dedicated reconstruction and identification (they are just reconstructed as electrons or muons with the algorithms described in the previous sections). For this reason, the reconstruction and identification methods presented in this section regard only hadronically decaying tau leptons.

3.4.1 Reconstruction

The τ_{had} reconstruction algorithm used in Run 2 [73, 74] starts looking for jet seeds to be used as tau candidates. Jet seeds are formed using the anti-k_t algorithm [75] with a distance parameter $R = 0.4$ and are required to have $p_{\text{T}} > 10\,\text{GeV}$ and to be within $|\eta| < 2.5$ (excluding the transition region between barrel and forward calorimeters with $1.37 < |\eta| < 1.52$). Among the candidate track vertices, the one with the highest fraction of momentum from the tracks in a cone of $\Delta R = 0.2$ around the jet seed is selected as tau vertex. The tracks around the tau candidate are divided between *core*, if the angular distance from the tau candidate direction is $\Delta R < 0.2$, or *isolation* tracks, if they fall in the region with $0.2 < \Delta R < 0.4$ from the candidate. In order to be considered for this classification, the tracks must have at least two associated hits in the pixel detector, at least seven hits in total in the pixel and the SCT detectors, $p_{\text{T}} > 1\,\text{GeV}$, $|d_0| < 1\,\text{mm}$ and $|\Delta z_0 \sin(\theta)| < 1.5\,\text{mm}$, where $|d_0|$ is the shortest distance from the tau vertex in the transverse plane and z_0 is the point of closest approach along the longitudinal axis. The number of core tracks defines the number of prongs of the tau candidate. The η and ϕ coordinates of the tau candidate, and therefore its direction, are obtained from the vectorial sum of the topo-clusters within $\Delta R < 0.2$ of the seed jet barycenter, using the tau vertex as the origin.

3.4.2 Calibration

An energy calibration procedure is applied to the tau candidate to correct the energy deposit measured in the detector to the values obtained at the generator level in the MC simulation. A baseline correction is computed using the following formula:

$$E_{calib} = \frac{E_{LC} - E_{pileup}}{\mathcal{R}}, \tag{3.3}$$

where E_{LC} is the sum of the energy, calibrated using a local hadronic calibration (LC) [76], of the topo-clusters within $\Delta R < 0.2$ from the tau candidate, E_{pileup} is the energy contribution from multiple interactions occurring in the same bunch crossing The detector response calibration $\mathcal{R}$ is extracted as the Gaussian mean of the $(E_{LC} - E_{pileup})/E^{vis}_{true}$ distribution, with E^{vis}_{true} being the true visible energy (i.e. excluding the contribution of neutrinos) of the tau decay products from MC simulation.

The energy resolution of this baseline method degrades quickly at low p_{T}, therefore an improved energy calibration, based on a multivariate-analysis (MVA) technique, is used to obtain the final energy of the tau candidate. This technique combines the baseline energy correction with information from the Tau Particle Flow method using a boosted regression tree (BRT). The Tau Particle Flow [77] is a method that allows us to reconstruct the individual charged and neutral hadrons in tau decays, significantly improving the tau energy resolution at low p_{T}. Variables related to the topo-cluster constituents, the tau candidate tracks, the primary vertices and the pileup are used as input to the BRT. The full list of the input variables is reported in [74]. A comparison of the resolution obtained with the baseline and

the BRT-based energy calibration as a function of the $\tau_{\text{had-vis}}$ p_{T} is given in Figure 3.6, showing the improvement achieved by the second method at low p_{T}.

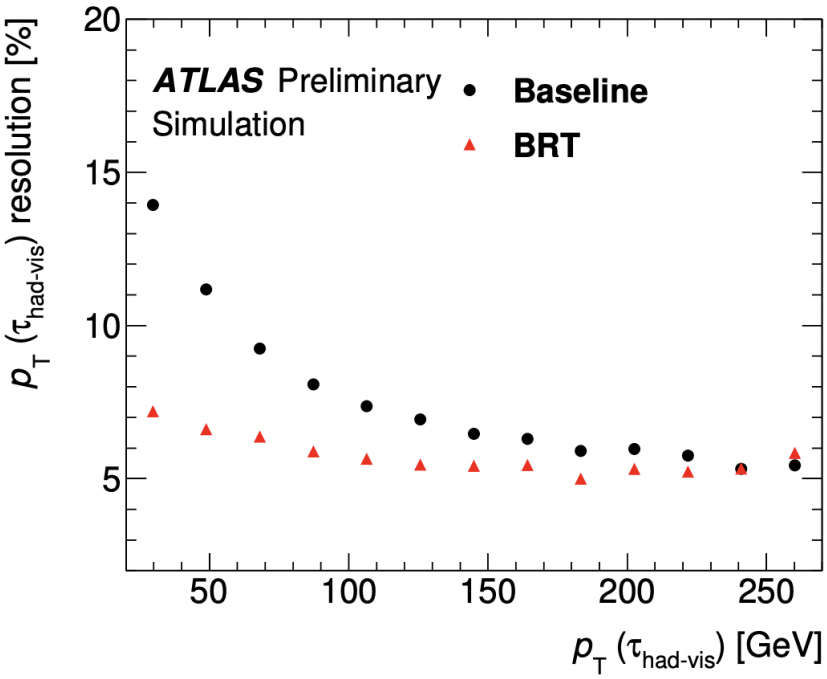

Figure 3.6. Resolution of the baseline and the BRT-based $\tau_{\text{had-vis}}$ energy calibration as a function of the p_{T} [74].

3.4.3 Identification

The main background to hadronic tau lepton decays is constituted by jets of energetic hadrons generated by the fragmentation of quarks and gluons. The tau reconstruction algorithm described above does not provide any discrimination from such background, therefore a dedicated algorithm is introduced to identify the hadronic tau lepton decays. In order to separate hadronic tau leptons from jets, a set of boosted decision trees (BDT) has been developed in Run 1 [78] and has been employed until the first years of the Run 2 data taking. For the rest of Run 2, the BDT has been replaced by a recurrent neural network (RNN) classifier [79], which provides a largely improved jet rejection. The RNN-based identification is used to select the $\tau_{\text{had-vis}}$ objects used in the analysis presented in this thesis.

As input to the RNN a combination of low-level and high-level variables is used. The low-level variables are related to the individual tracks and clusters associated with the $\tau_{\text{had-vis}}$ candidate, while the high-level observables, similar to those used for the BDT-based method, are computed from track and calorimeter quantities. The complete set of input variables is listed in [79]. The architecture of the RNN is depicted in Figure 3.7. The network is split into three separate branches, depending

on the input type (low-level track variables, low-level cluster variables and high-level variables).

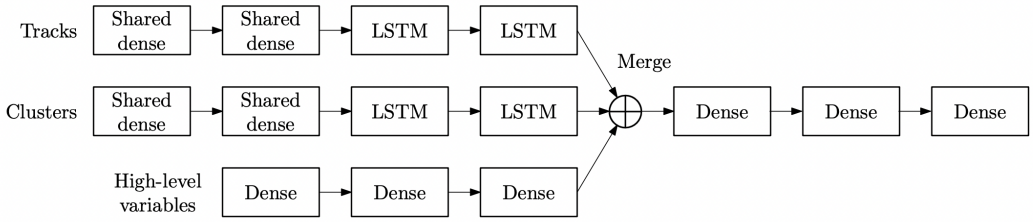

Figure 3.7. Schematic view of the architecture of the RNN used for tau identification [79].

The high-level variables are processed by three fully connected layers of 128, 128 and 16 units. The track and cluster-related variables are instead passed through two fully connected layers of 32 units with shared weights and then through two recurrent layers employing the *long short-term memory* (LSTM) architecture [80]. The first LSTM layer consists of 32 units, while the second one has 32 units for the tracks and 24 for the clusters. To reduce the training and evaluation time, only the ten leading tracks in p_{T} and the six leading clusters in E_{T} are used by the network. The output vectors from the three branches of the network are then concatenated in a *Merge* layer. The result is processed by three consecutive fully connected layers with 64, 32 and 1 units. Through the application of a sigmoid activation function, the tau identification score is obtained. The model has about 56 000 free parameters to be determined via optimisation.

The network is trained using simulated samples of $\tau_{\text{had-vis}}$ candidates. The signal sample is made of $\tau_{\text{had-vis}}$ candidates from the $\gamma^* \to \tau\tau$ process geometrically matched to a true tau lepton at generator level and correctly reconstructed as one-prong or three-prong decays. As background sample, reconstructed $\tau_{\text{had-vis}}$ candidates from simulated dijet samples, reconstructed as one-prong or three-prong decays, are used. Due to the different characteristics of one-prong and three-prong decays, the training of the network is performed separately for the two types of reconstructed $\tau_{\text{had-vis}}$ candidates.

The RNN output score for the $\tau_{\text{had-vis}}$ in the $\gamma^* \to \tau\tau$ sample is transformed to be uniform in $[0, 1]$ in bins of p_{T} and in bins of average number of interactions per bunch crossing. This procedure, called *flattening*, is used to reduce the dependency of the true $\tau_{\text{had-vis}}$ efficiency on the reconstructed p_{T} and pileup. After this transformation, the RNN score corresponds to the fraction of rejected $\tau_{\text{had-vis}}$, independent of p_{T} and pileup. Different cuts on the RNN score are used to define four identification working points with increasing background rejection: *Very Loose*, *Loose*, *Medium* and *Tight*. The corresponding signal selection efficiencies and rejection powers, defined as the reciprocal value of the background selection efficiencies, are reported in Table 3.4.

Figure 3.8 shows the rejection power for misidentified $\tau_{\text{had-vis}}$ as a function of the

Table 3.4. $\tau_{\text{had-vis}}$ identification working points with the corresponding signal efficiencies and background rejection factors for one-prong and three-prong decays [79].

	Signal efficiency		Background rejection	
Working point	**1-prong**	**3-prong**	**1-prong**	**3-prong**
Tight	60%	45%	70	700
Medium	75%	60%	35	240
Loose	85%	75%	21	90
Very Loose	95%	95%	9.9	16

true $\tau_{\text{had-vis}}$ identification efficiency for both the RNN classifier and the BDT-based method used previously by ATLAS, independently for one-prong and three-prong $\tau_{\text{had-vis}}$ candidates. It can be noticed that the RNN classifier has about a two times better background rejection power than the BDT classifier in both cases for any signal selection efficiency.

A non-negligible background source for the $\tau_{\text{had-vis}}$ identification is constituted by electrons misidentified as $\tau_{\text{had-vis}}$. Therefore a separate multivariate discriminant based on a boosted decision tree, labelled eBDT, is constructed to reject such background. The eBDT, originally developed for Run 1 [78], uses information from the calorimeter and the tracking detector, with an important role played by the transition radiation information from the TRT, and is trained on a sample of $\gamma^* \to \tau\tau$ simulated events as signal and a sample of $Z/\gamma^* \to ee$ simulated events as background. The flattened output score of the eBDT discriminant is employed to define three different electron rejection working points, *Loose* WP (95% signal efficiency), *Medium* WP (85% signal efficiency) and *Tight* WP (75% signal efficiency).

All the $\tau_{\text{had-vis}}$ used in the analysis presented in this thesis are selected using the Tight RNN identification working point. Both the Loose and the Medium working points of the eBDT are used depending on the amount of electron background contamination.

3.5 Jets

The hadronisation of quarks and gluons produces sprays of collimated hadrons in the detector, which are called *jets*. Jets leave a signature both in the Inner Detector, with a set of charged tracks, and in the calorimeters, producing the characteristic hadronic showers.

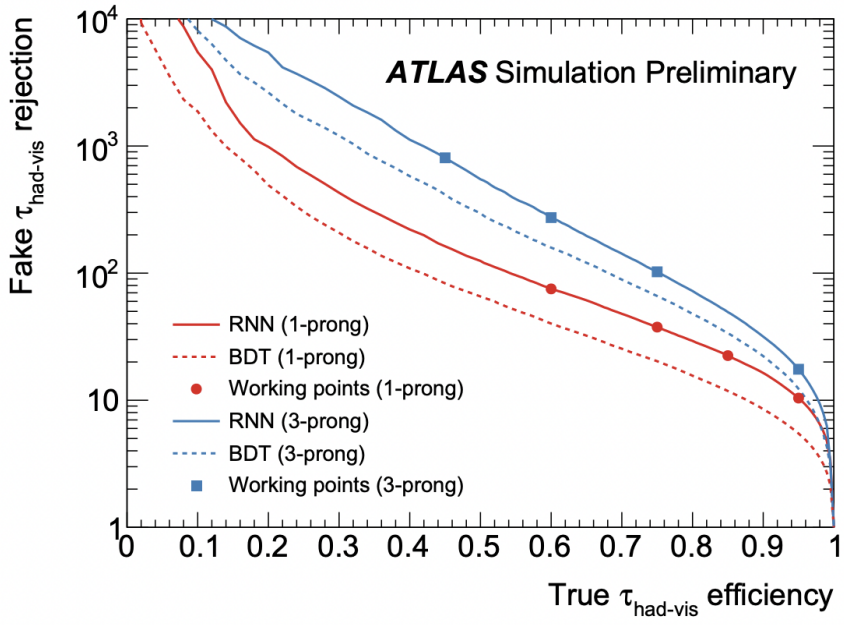

Figure 3.8. Rejection power for misidentified $\tau_{\text{had-vis}}$ depending on the true $\tau_{\text{had-vis}}$ selection efficiency. The curves for one-prong (red) and three-prong (blue) $\tau_{\text{had-vis}}$ candidates using the RNN-based (solid line) and the BDT-based (dashed line) classifiers are shown. The markers indicate the four RNN identification working points [79].

3.5.1 Reconstruction

The jet reconstruction algorithm starts with the formation of topo-clusters in the calorimeters. The reconstruction of the topo-clusters is the same as described in Section 3.2 for electron and photon reconstruction and it is explained in great detail in [70]. To each topo-cluster a four-momentum and a position are associated combining the information of the calorimeter cells that compose the cluster. The topo-cluster four-momenta are used as input to the anti-k_t jet clustering algorithm [75], in which the distance d_{ij} between two constituents considered in the jet clustering process is expressed as

$$d_{ij} = \min\left(\frac{1}{k_i^2}, \frac{1}{k_j^2}\right)\frac{\Delta R_{ij}^2}{R^2}, \tag{3.4}$$

where R is the radius parameter, set in this case to 0.4, ΔR_{ij} is the distance between the two constituents in the (η, ϕ) plane and k_i is the transverse momentum of the i-th constituent. The distance d_{iB} between a constituent and the beam is instead defined by

$$d_{iB} = \frac{1}{k_i^2}. \tag{3.5}$$

The jet clustering algorithm is an iterative procedure which, at each step, evaluates and compares the two metrics for each cluster pair. If $d_{ij} < d_{iB}$ the two clusters are combined to form a single constituent, while if $d_{ij} > d_{iB}$ the i-th cluster

is considered as a jet and removed from the list of constituents. The iterations continue until there are no constituents left in the input list. The jet properties (like four-momentum and position) are computed by combining the information from the constituents clustered with the anti-k_t algorithm. The jets obtained with this algorithm, which exploits only calorimeter information, are referred to as *EMTopo jets*.

The jets used in the analysis presented in this thesis are reconstructed using the *Particle Flow* algorithm [81], which improves the anti-k_t algorithm combining the information from the calorimeter with that from the tracker. In this way it is possible to obtain a better resolution in the low-energy region, since for low-energy charged particles the momentum resolution of the tracker is significantly better than the energy resolution of the calorimeter, and keep as well the superior calorimeter energy resolution at high energies. Before running the anti-k_t algorithm, the Particle Flow algorithm tries to match each track from a list of well-measured tracks in the Inner Detector to the topo-clusters reconstructed in the calorimeters. In order to be considered by the algorithm, the tracks are required to have at least nine hits in the silicon detectors and have no missing hits in the Pixel detector when such hits are expected. In addition they are required to have $|\eta| < 2.5$ and $0.5 < p_{\mathrm{T}} < 40\,\mathrm{GeV}$. In order to match a track to one topo-cluster, the distances $\Delta\phi$ and $\Delta\eta$ between the barycentre of the topo-cluster and the track, extrapolated to the second layer of the EM calorimeter, are computed for each topo-cluster. The topo-clusters are ordered according to the distance $\Delta R'$ defined as

$$\Delta R' = \sqrt{\left(\frac{\Delta\phi}{\sigma_\phi}\right)^2 + \left(\frac{\Delta\eta}{\sigma_\eta}\right)^2}, \tag{3.6}$$

where σ_η and σ_ϕ are angular topo-cluster widths, computed as the standard deviations of the displacement in η and ϕ of the constituent cells with respect to the topo-cluster barycentre. Only the topo-clusters with an energy greater than 0.1 times the track p_{T} are considered for the matching. The topo-cluster with the smallest $\Delta R'$ is taken to be matched to the track. Since a particle may leave its energy in multiple topo-clusters, a procedure based on the significance $S(E^{clus})$ is applied. $S(E^{clus})$ is defined as

$$S(E^{clus}) = \frac{E^{clus} - \langle E_{dep}\rangle}{\sigma(E_{dep})}, \tag{3.7}$$

where $\langle E_{dep}\rangle$ is the expected energy and E^{clus} the energy of the matched topo-cluster. If $S(E^{clus}) < -1$, topo-clusters within a cone of $\Delta R = 0.2$ around the track position, extrapolated to the second EM calorimeter layer, are matched to the track. Once a set of topo-clusters corresponding to the track has been selected, the expected energy deposited in the calorimeter by the particle that produced the track is subtracted cell by cell from the matched topo-clusters. In this way the energy contribution from charged hadrons in the calorimeters is replaced with their p_{T} measured in the tracker, which has a better resolution. After the subtraction, only the energy contribution from neutral hadrons is left. The positive energy topo-clusters surviving the energy subtraction step and the selected tracks are then given

as input to the anti-k_t jet clustering algorithm with radius parameter 0.4. In order to remove a large fraction of the tracks from pileup interactions, the tracks are selected by requiring $|z_0 \sin\theta < 2\,\text{mm}$, with z_0 being the distance of closest approach of the track to the hard-scatter primary vertex along the z-axis.

3.5.2 Calibration

A calibration procedure, made of different steps, is applied to correct the energy of the reconstructed jets in the range $20 < p_\text{T} < 1500\,\text{GeV}$. The reconstructed jets are first corrected for pileup contamination using the jet ghost-area subtraction method. This method, described in [82], applies a subtraction to the jet energy based on the transverse energy density ρ calculated from topo-clusters and the area of the jet. The transverse energy density is computed using charged and neutral particle flow objects to correctly account for the differences in the jet constituents. Since the tracks associated with pileup vertices are removed from particle flow jets, this jet-area subtraction corrects for the impact of charged underlying-event hadrons, charged particles from out-of-time interactions and neutral particles from pileup interactions.

A calibration to the Jet Energy Scale (JES) is then applied to correct the jet energy using particle-level information from the MC simulation [83]. This calibration, called Monte Carlo numerical inversion, corrects in particular the effects of hadronic interactions with the detector passive material and the drops in the jet energy response in the pseudorapidity spectrum due to the transition regions between barrel, end-cap and forward calorimeters, restoring in this way the average reconstructed jet energy to the mean value of the truth jet energy. The correction is derived by matching the jets at reconstructed level with the truth particle-level jets from a MC simulation and evaluating the average jet energy response with a Gaussian fit of the distribution of the E_{reco}/E_{truth} ratio in different E_{truth} and η_{reco} bins.

Further effects related to the jet characteristics and not taken into account by the previous JES calibration, such as the flavour of the originating parton and the composition of the hadrons created in jet fragmentation, may affect the jet energy response. A *global sequential correction* is applied to take into account also these variations and improve the jet response resolution without changing the energy scale. The calibration procedure for particle flow jets is the same described in [84] for EMTopo jets but uses a different set of variables. Corrections corresponding to the following three variables are applied consecutively:

- the fraction of the jet energy measured from the tracks associated with the jet;
- the fraction of jet energy measured in the third EM calorimeter layer;
- the fraction of jet energy measured in the first Tile calorimeter layer.

Finally, a correction factor derived in data events, referred to as *in situ* calibration [83], may be applied to take into account the difference in the jet response

measured in data and MC simulation due to a mismodelling of the hard-scatter interaction, the underlying event or the jet formation process. Well-known processes, like $Z \to \mu\mu$ and $Z \to ee$, are used to correct the p_{T} response for jets in the forward region ($0.8 < |\eta| < 4.5$) as well as for central jets.

Figure 3.9 shows the jet transverse momentum resolution for calibrated particle flow and EMTopo jets as a function of the jet p_{T} and $|\eta|$. It is possible to notice the better performance of the Particle Flow reconstruction algorithm at transverse momenta of up to 90 GeV in the central region, thanks to the improved scale for low-p_{T} hadrons and intrinsic pile-up suppression.

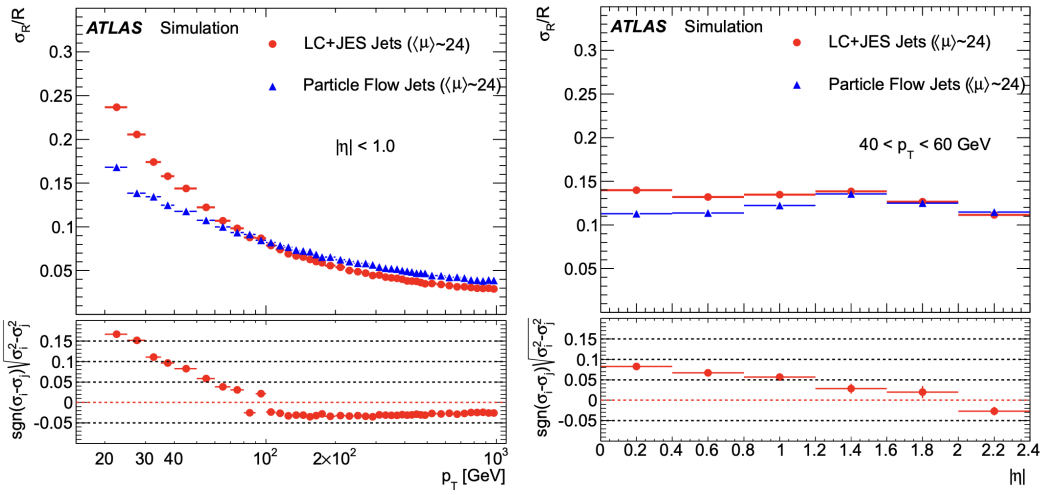

(a) (b)

Figure 3.9. Jet transverse momentum resolution determined in dijet MC events for EMTopo jets and particle flow jets. The lower tab of the plots shows the square root of the difference of the squares of the resolution for the two jet types [81].

3.5.3 Pileup jet tagging

As stated in the previous sections, the energy deposits attributed to pileup interactions are subtracted in order to not be counted in the energy of reconstructed jets from the hard scattering vertex. However, local fluctuations in the pileup activity may lead to the reconstruction of spurious low-p_{T} pileup jets. In order to reject these pileup jets, a multivariate discriminant method, called *Jet Vertex Tagger* (JVT), has been developed [85]. The JVT uses a k-nearest-neighbour algorithm to build a likelihood discriminator based on two variables, corrJVF and R_{pT}. The corrJVF (the *corrected Jet Vertex Fraction*) variable is defined as

$$\mathrm{corrJVF} = \frac{\sum_k p_{\mathrm{T}}^{trk_k}(PV_0)}{\sum_l p_{\mathrm{T}}^{trk_l}(PV_0) + \frac{1}{k \cdot n_{trk}^{PU}} \sum_{n \geq 1} \sum_l p_{\mathrm{T}}^{trk_l}(PV_n)}, \tag{3.8}$$

where $\sum_k p_{\mathrm{T}}^{trk_k}(PV_0)$ is the scalar sum of the transverse momenta of tracks from the hard-scatter vertex associated to the jet, $\sum_{n\geq 1}\sum_l p_{\mathrm{T}}^{trk_l}(PV_n)$ is the scalar sum of the transverse momenta of the tracks associated to the jet originating from any of the pileup interactions, and $k \cdot n_{trk}^{PU}$ (with $k = 0.01$) is a factor depending on the number of pileup tracks (n_{trk}^{PU}) of the event, which is used to correct for the linear increase with n_{trk}^{PU} of the p_{T} sum of the pileup tracks associated to the jet. R_{pT} is instead defined as the scalar p_{T} sum of the tracks that are associated with the jet and originate from the hard-scatter vertex, divided by the calibrated jet p_{T}:

$$R_{pT} = \frac{\sum_k p_{\mathrm{T}}^{trk_k}(PV_0)}{p_{\mathrm{T}}^{jet}}. \tag{3.9}$$

The output score variable of the JVT, whose distributions are shown in Figure 3.10, is such that pileup jets have a peak in 0, while jets originating from the hard-scatter interaction are peaked at 1. A cut on the JVT score is used by the different analyses to suppress the pileup jets.

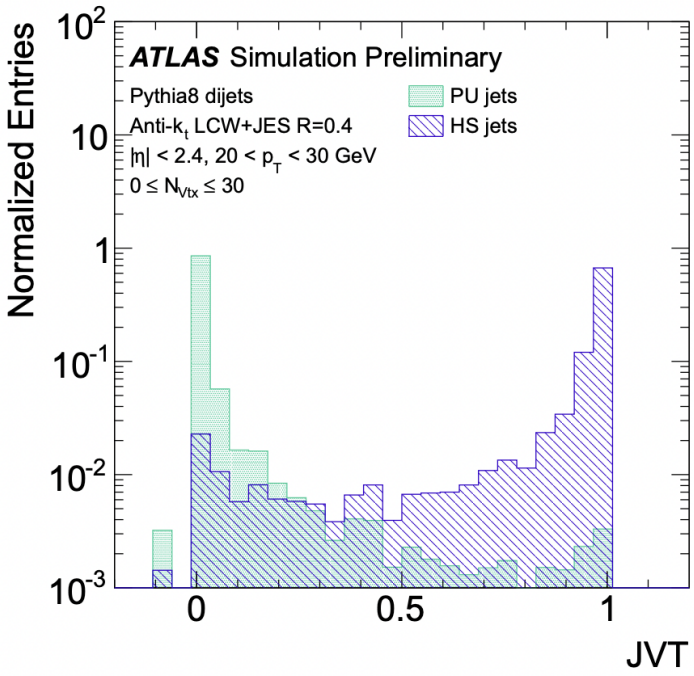

Figure 3.10. Distributions of the JVT output score for pileup and hard-scatter jets from a dijet MC simulation [85].

3.5.4 Heavy-flavour jet tagging

The identification of jets containing b-hadrons or c-hadrons, called b-jets and c-jets respectively, plays an important role in the analysis presented in this thesis as well as in many other ATLAS analyses. Various algorithms are used by ATLAS

for the identification of heavy-flavour jets (namely b-jets and c-jets) exploiting some peculiar properties that make them differ from the *light* jets, i.e. jets originating from u, d, s quarks and gluons [86,87]. Indeed b-hadrons have a lifetime of the order of 1.5 ps ($\langle c\tau \rangle \approx 450\,\mu$m), therefore their mean flight length is sufficiently long to make them produce during the decay a displaced secondary vertex. The algorithms dedicated to b-tagging, i.e. the identification of b-hadrons, are based on a two-stage approach, with low-level algorithms, which reconstruct the b-jet characteristic features using the tracks associated with the jet and the displaced vertices, followed by high-level algorithms, which combine the results from low-level ones with multivariate selection techniques.

The following low-level taggers are defined:

- The IP2D and IP3D taggers [88] are two complementary algorithms that use the impact parameter information to construct a discriminating variable. The IP2D tagger makes use of the signed transverse impact parameter significance of the tracks, while IP3D uses both the signed transverse and longitudinal impact parameter significance. Probability density functions derived from MC simulation are used to compute ratios of the b-jet, c-jet and light-flavour jet probabilities for each track. Three log-likelihood ratio (LLR) discriminants are constructed by summing the per-track probability ratios for each jet-flavour hypothesis: one separating b-jets from light-flavour jets, one to separate b-jets from c-jets and the last one to discriminate between c-jets and light-flavour jets. These three discriminants are given as input to the high-level taggers.

- The secondary vertex tagging algorithm (SV1) [89] is based on the reconstruction of displaced secondary vertices. The algorithm starts looking for a possible two-track displaced vertex. Then it runs iteratively on all the tracks associated with the jet and, according to the result of a χ^2 test, which evaluates the track-to-vertex association, matches the track to the secondary vertex. The tracks are discarded if, after the matching with the vertex, the vertex invariant mass is above 6 GeV. With this approach, the decay products of b- and c-hadrons are assigned to a single common secondary vertex. The SV1 algorithm produces eight discriminating variables, such as the number of tracks and the invariant mass of the secondary vertex and its energy fraction, to be used as inputs to the high-level taggers.

- The topological multi-vertex algorithm (JetFitter) [90] tries to reconstruct the full b- and c-hadron decay chain by the identification of the b- and c-hadron flight direction, on which the primary and secondary vertices lie. With this approach it is possible to resolve the b- and c-hadron vertices even when a single track is assigned to them. Eight discriminating variables are used as inputs to the high-level taggers, including the track multiplicity of the displaced vertices, the invariant mass and the energy fraction of the tracks associated to them.

- The RNN-based b-tagging algorithm (RNNIP) [91] uses a recurrent neural network to process the set of tracks associated with the jet to produce the

probability of the jet to belong to each of the following four classes: light jets, b-jets, c-jets and tau jets. The RNN takes as inputs the signed impact parameter significance of each track, the fraction of the jet p_{T} carried by the track and the angular distance between the track and jet axis. The four output probabilities are combined to obtain a single score for the jet to be used by the high-level taggers.

Three high-level taggers are available by ATLAS analyses for b-jet identification. The MV2c10 algorithm [88] uses a BDT to combine the outputs of the IP2D, IP3D, SV1 and JetFitter algorithms, with the exception of the JetFitter c-tagging variables. The BDT is trained on a hybrid $t\bar{t} + Z'$ sample to separate b-jets from c-jets and light jets. The DL1 algorithm [88] is based on a deep feed-forward neural network with a multidimensional output corresponding to the probabilities for a jet to be a b-jet (p_b), a c-jet (p_c) or a light jet (p_l). The input variables to DL1 are the same used for the MV2c10 algorithm with the addition of the JetFitter c-tagging variables, which are related to the properties of secondary and tertiary vertices. The training parameters of the neural network are optimised in order to maximise the b-tagging performance. Since all flavours are treated equally during training, the trained network can be used for both b-jet and c-jet tagging. The three output probabilities, (p_b, p_c and p_l), are combined to obtain the final DL1 discriminant. In the b-tagging case, the discriminant D_{DL1} is given by

$$D_{\mathrm{DL1}} = \ln\left(\frac{p_b}{f \cdot p_c + (1-f) \cdot p_l}\right), \tag{3.10}$$

where f is the effective c-jet fraction in the background training sample. The c-jet fraction in the background is chosen a posteriori in order to optimise the performance of the algorithm. A c-tagger can be obtained by swapping p_b and p_c and re-tuning the parameter f. The background jet rejections versus the b-jet tagging efficiency for the different b-tagging algorithms mentioned before are shown in Figure 3.11.

The last b-jet tagger, which is the one used to identify b-jets in the analysis presented in this thesis, is the DL1r algorithm [92]. The DL1r tagger is an extension of the DL1, because, in addition to the DL1 input variables, it uses also the RNNIP output. The DL1r tagger outperforms both the MV2c10 and the DL1 algorithms, as shown in Figure 3.12, which reports the light-jet and c-jet rejection versus the b-jet efficiency for the three high-level b-taggers.

3.6 Missing transverse momentum

Momentum conservation in the transverse plane with respect to the beam axis implies that the vectorial sum of the transverse momenta of all the particles in the final state should be null. Any momentum imbalance may indicate that particles invisible to the detector systems were produced in the collision, like neutrinos. However, this momentum imbalance, called missing transverse momentum[1] ($\vec{p}_{\mathrm{T}}^{\,\mathrm{miss}}$)

[1] The missing transverse momentum is often (improperly) called missing transverse energy.

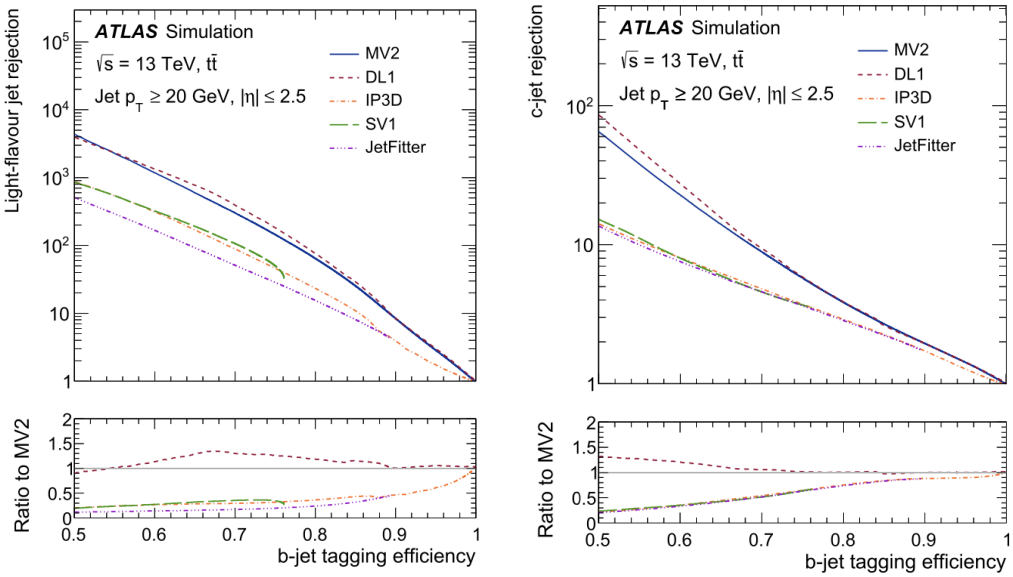

Figure 3.11. The light jet (a) and c-jet (b) rejection versus the b-jet tagging efficiency for the IP3D, SV1, JetFitter, MV2 c10 and DL1 b-tagging algorithms evaluated on a $t\bar{t}$ sample from MC simulation [87].

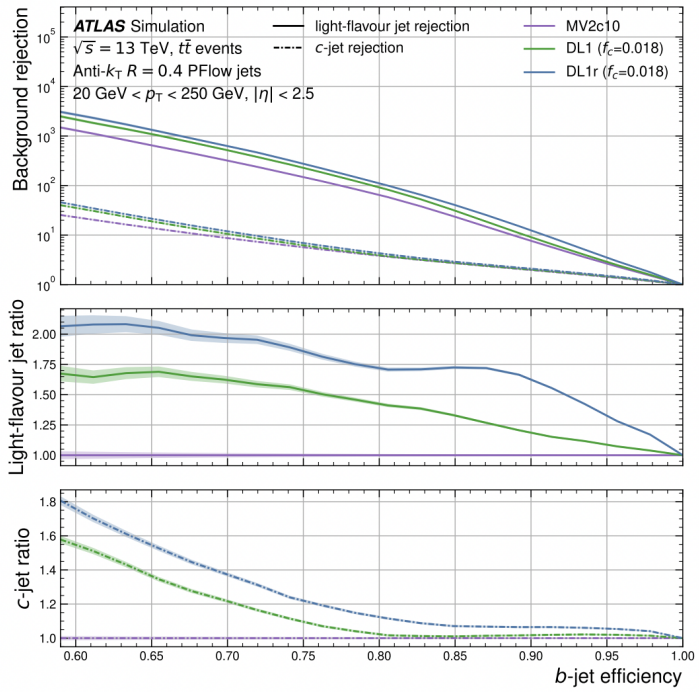

Figure 3.12. Light-flavour jet and c-jet rejection factors as a function of the b-jet efficiency for the high-level b-taggers MV2c10, DL1 and DL1r. The lower two panels show the ratio of the light-flavour jet rejection and the c-jet rejection of the algorithms to MV2c10 [92].

plays also a very important role in searches for new particles introduced by beyond Standard Model theories. For this reason, the evaluation of the missing transverse momentum, and of its magnitude ($E_{\mathrm{T}}^{\mathrm{miss}}$), in the most precise way possible is a crucial aspect in many ATLAS analyses.

The computation of the $\vec{p}_{\mathrm{T}}^{\,\mathrm{miss}}$ [93, 94] is performed using the signals of all the reconstructed and calibrated particles in the final state: electrons, photons, muons, hadronically decaying τ-leptons and jets. The contribution to $\vec{p}_{\mathrm{T}}^{\,\mathrm{miss}}$ of such objects is called *hard term*. To the hard term, a *soft term* is added, which includes all the signals, like tracks and topo-clusters, that were not associated with reconstructed objects. The missing transverse momentum, defined as a 2D vector with an x and a y component, is computed through the following equation:

$$\vec{p}_{\mathrm{T}}^{\,\mathrm{miss}} = -\left(\sum_{\substack{\text{reco.} \\ \text{obj. } i}} \vec{p}_{\mathrm{T}}^{\,i} + \sum_{\substack{\text{soft} \\ \text{signals } j}} \vec{p}_{\mathrm{T}}^{\,j} \right), \tag{3.11}$$

where the first term is the hard term and the second one is the soft term. The standard ATLAS choice is to consider only a track soft term (TST), which, even not taking into account neutral particles, is insensitive to pileup since only tracks originating from the hard-scatter vertex are considered.

The objects used in the $\vec{p}_{\mathrm{T}}^{\,\mathrm{miss}}$ definition are independent of each other. Anyway, double-countings may occur if the same detector signals are used by the reconstruction algorithms to reconstruct different objects. An overlap removal procedure [94] is therefore applied to avoid such situations. In case of overlaps between different objects, the overlap removal algorithm tells which object has to be kept and which instead has to be discarded. To each object a priority is associated, which corresponds to the order used to construct the hard-term of the $\vec{p}_{\mathrm{T}}^{\,\mathrm{miss}}$. The first objects considered for the computation are electrons, followed by photons, then hadronically decaying τ-leptons and finally jets. Muons are reconstructed mainly from ID and MS signals, so usually they do not present overlap with other reconstructed objects in the calorimeters. If a lower-priority object shares the calorimeter signal with a higher-priority object, the lower-priority object is fully rejected. In the case of partial overlaps instead, the selection of the object to keep is based on some requirements. Partial overlaps of jets with electrons or photons are resolved using the ratio $k_E = E_{e/\gamma}^{\mathrm{EM}}/E_{jet}^{\mathrm{EM}}$. If $k_E < 0.5$, the jet is included in the $\vec{p}_{\mathrm{T}}^{\,\mathrm{miss}}$ calculation with its p_{T} scaled by $1-k_E$, otherwise it is discarded and the tracks associated only to the jet are used in the TST computation. In case of overlap between jets and muons, the transverse momentum ratio and the multiplicity of tracks matched to the hard-scatter vertex are used to determine if the jet is due to pileup and therefore needs to be discarded. Photons radiated by muons at small angles may be reconstructed as jets in the calorimeter. Such jets, identified by requirements on track multiplicity and energy deposit characteristics, are kept for the $\vec{p}_{\mathrm{T}}^{\,\mathrm{miss}}$ computation. All the reconstructed tracks associated with the Primary Vertex and that are close to the direction of other hard objects are not considered for the TST evaluation.

Chapter 4

Search for third-generation leptoquarks in the non-resonant production

Although hadronically decaying tau leptons present lower reconstruction and identification efficiencies with respect to light leptons (electrons and muons), the study of processes involving tau leptons can be extremely useful to test lepton universality and look for new physics. Tau leptons play for instance a crucial role in searches for leptoquarks with preferential couplings to third-generation fermions [20]. Several measurements and searches have been already performed by the LHC experiments of processes with a couple of tau leptons in the final state. For example, the ATLAS Collaboration has performed measurements of the $Z \to \tau\tau$ cross-sections [95], studied the properties of the $H \to \tau\tau$ decay [96,97] and searched for new heavy resonances decaying to $\tau^+\tau^-$ pairs [29]. Searches for single- and pair-production of third-generation leptoquarks have been performed as well by both the ATLAS [22–25] and CMS experiments [26–28].

The analysis presented in this thesis contributes to completing the picture of leptoquark searches in ATLAS with a search for heavy vector leptoquarks with strong coupling to third-generation fermions, focusing on final states with tau leptons. The innovative aspect of this analysis, if compared to the previous ATLAS analyses searching for leptoquarks, is that, while those analyses are focused on the leptoquark resonant production, the analysis presented here focuses on the non-resonant production, which allows it to gain high sensitivity from the large interference term between the leptoquark and the SM Drell-Yan process. Moreover, the $\tau\tau$ final state is the preferential channel to look for leptoquarks, since an analogous search with the $pp \to \mu\tau$ or $pp \to \mu\mu$ processes, for instance, would not be competitive because of the flavour suppression of the light-lepton couplings. So far, the only result of a leptoquark search in the non-resonant production has been provided by the CMS experiment [31], setting the state-of-the-art exclusion limits on the leptoquark coupling strength λ for this production channel. The 95% CL[1] upper limits as a function of the leptoquark mass observed by the CMS Collaboration, assuming

[1] Confidence Level

the simplified U_1 vector leptoquark model (introduced in Section 1.6.2), are shown in Figure 4.1, together with the expected limits and the region preferred by the B anomalies. The CMS results show a 2.8 σ discrepancy between the expected and observed limits.

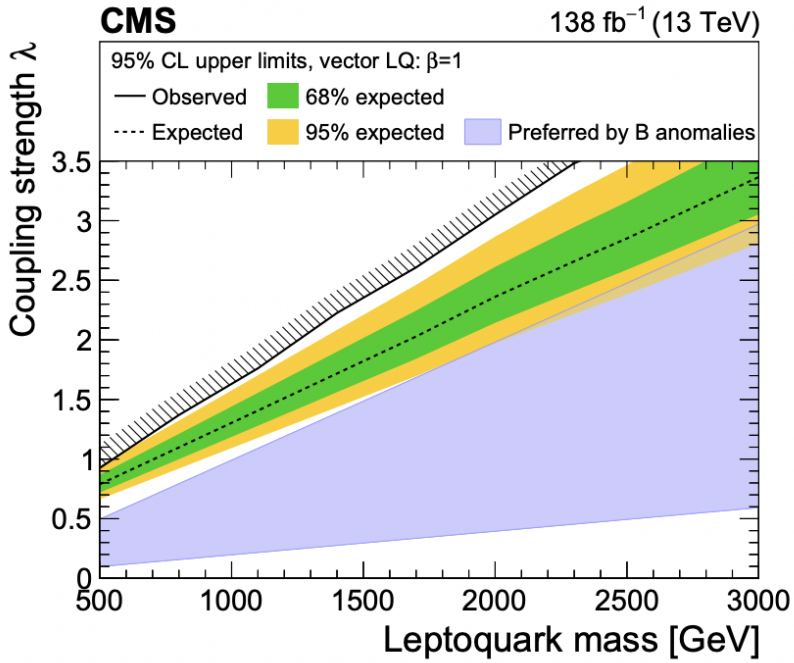

Figure 4.1. Observed and expected upper limits measured by the CMS Collaboration at the 95% CL on the coupling strength λ of a vector leptoquark model determined by considering only the non-resonant production of two τ leptons through t-channel leptoquark exchange [31]. Exclusive leptoquark couplings to b quarks and τ leptons are assumed. The region with blue shading shows the parameter space preferred by the B anomalies [20].

My personal contribution to this analysis has been substantial. I have participated in the analysis activities since its start, developing a framework to analyse the data collected by the ATLAS detector in the LHC Run 2, playing an active role in the choice of the analysis regions, triggers and selections to apply, validating the background estimate in the validation regions, contributing to the drafting of the analysis documentation and producing the preliminary results presented in this thesis.

This Chapter is dedicated to the presentation of the analysis searching for third-generation leptoquarks in the non-resonant production channel. The analysis target and the processes under study are presented in Section 4.1, followed by the description of the analysis regions in Section 4.2 and the samples used in Section 4.3. Section 4.4 describes the selections applied to the physics objects and to the events in each region. Section 4.5 is dedicated to the presentation of the data-driven

technique applied for the estimation of the fake-tau background, while Section 4.6 illustrates the different uncertainties considered by the analysis. Finally, the event yields in the signal regions are reported in Section 4.7, while the preliminary analysis results and their interpretation are discussed in Section 4.8.

4.1 Measurement purpose

The leptoquark search is performed through a precision measurement of the detector-level distribution of the visible invariant mass of the di-tau system ($m_{\tau\tau}^{\text{vis}}$), where the tau-leptons can decay hadronically or leptonically. This will allow the results of this analysis to be used also to produce a precision measurement of the differential Drell-Yan $\tau\tau$ cross-section with respect to the $\tau\tau$ invariant mass. In general, the visible mass of a di-lepton system, $m_{\ell\ell}^{\text{vis}}$, is the invariant mass of the visible components of the momenta of the two leptons in the detector. For a light lepton (electron or muon), the visible momentum $\vec{p}^{\,\text{vis}}$ is merely the measured momentum, while for a tau-lepton it is the total momentum of its visible decay products. In addition to the visible invariant mass, different variables representing the mass of the di-tau system were also considered. Among the candidates considered as the discriminant variable for the leptoquark search, there are the total transverse mass[2], the mass reconstructed through the $\sqrt{s}_{\text{min}}$ method [98] and the mass obtained from a Dense Neural Network (DNN). All these other observables, however, were found to have less sensitivity for the exclusion limits reported in Section 4.8.3, if compared to the visible invariant mass, and therefore were discarded.

The $\tau\tau$ visible invariant mass spectrum is investigated in the high-mass region, namely above the Z boson resonance, where the highest yield from the non-resonant production of heavy leptoquarks with strong couplings to third-generation fermions is expected. According to the simplified U_1 leptoquark model [20], the possible processes involving leptoquarks are the pair-production, single-production and Drell-Yan t-channel exchange, whose corresponding Feynman diagrams are shown in Figure 4.2.

For high-mass leptoquarks, the single and pair-production are suppressed and the t-channel exchange becomes the dominant leptoquark process. The leptoquark t-channel exchange contributes to the Drell-Yan $pp \to \tau^+\tau^- + X$ cross-section with a pure BSM term and a term accounting for the interference between the leptoquark exchange and the SM Drell-Yan $\tau\tau$ process, where a couple of tau-leptons is generated from the interaction of same-flavour quarks through the s-channel mediated by a Z or γ^* boson. The Feynman diagram of the SM Drell-Yan $\tau\tau$ process is

[2]The total transverse mass of a di-lepton system is given by

$$m_{\text{T}}^{\text{total}} = \sqrt{m_T^2(\vec{p}_1^{\,\text{vis}}, \vec{p}_2^{\,\text{vis}}) + m_T^2(\vec{p}_1^{\,\text{vis}}, \vec{p}_{\text{T}}^{\,\text{miss}}) + m_T^2(\vec{p}_2^{\,\text{vis}}, \vec{p}_{\text{T}}^{\,\text{miss}})},$$

where

$$m_T(\vec{p}_1^{\,\text{vis}}, \vec{p}_2^{\,\text{vis}}) = \sqrt{2|\vec{p}_1^{\,\text{vis}}||\vec{p}_2^{\,\text{vis}}|(1 - \cos\Delta\phi(\vec{p}_1^{\,\text{vis}}, \vec{p}_2^{\,\text{vis}}))}.$$

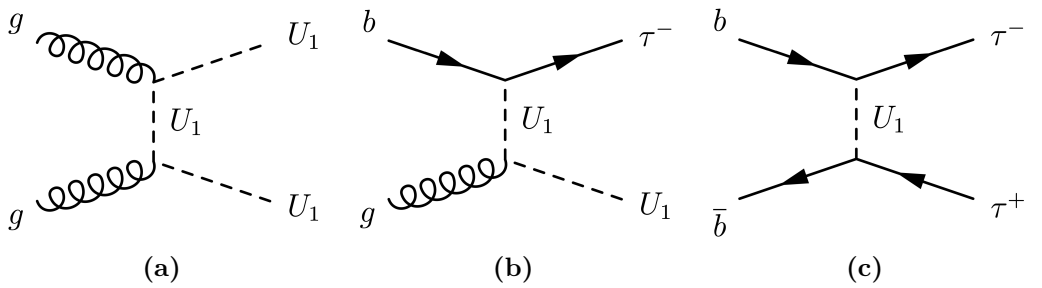

Figure 4.2. Feynman diagrams of the pair-production (a), single-production (b) and t-channel exchange (c) of leptoquarks with strong couplings to third-generation fermions.

reported in Figure 4.3. The pure BSM term scales like g_U^4/m_U^4, with g_U the leptoquark coupling and m_U the leptoquark mass, while the interference term scales like g_U^2/m_U^2. For weakly-coupled high-mass leptoquarks, at low $\tau\tau$ invariant masses the pure BSM term is suppressed and the interference term has the dominant impact on the Drell-Yan $\tau\tau$ cross-section, while at high $\tau\tau$ invariant masses the pure BSM term dominates over the interference term.

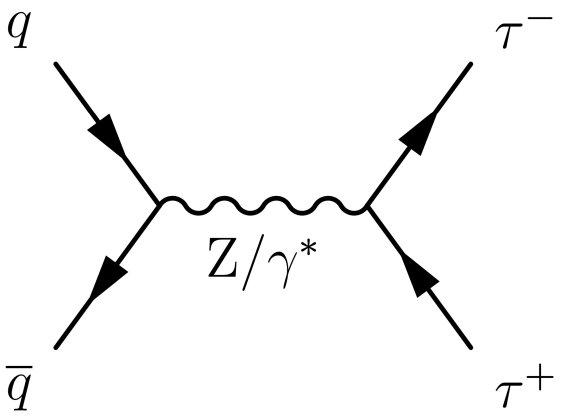

Figure 4.3. Feynman diagram of the SM Drell-Yan process with two tau-leptons in the final state.

The main production mechanism for the leptoquark t-channel exchange is via a $b\bar{b}$ initial state (contributions from $b\bar{s}$- and $s\bar{s}$-initiated processes are small due to the flavour structure of the leptoquark couplings of this model). The process studied by this analysis is represented by the Feynman diagram in Figure 4.4, in which the final state is composed of two tau-leptons, which may decay through either hadrons or leptons, and two b-jets. The hatched blob, from which the $\tau^+\tau^-$ couple originates, represents both the SM Drell-Yan process and the leptoquark t-channel exchange.

The search for third-generation leptoquarks is therefore performed by measuring the distribution of the $\tau\tau$ visible invariant mass and looking for deviations from the SM prediction in the high-mass region of the distribution, where a strong impact on

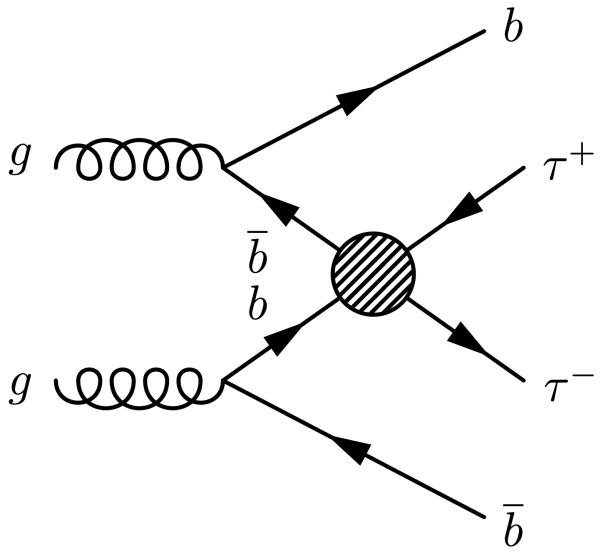

Figure 4.4. Feynman diagram of the process with the $bb\tau\tau$ final state. The hatched blob may represent both the SM Drell-Yan $\tau\tau$ process and the leptoquark t-channel exchange.

the $bb\tau\tau$ cross-section from the leptoquark production is expected. In the ideal case of 100% b-tagging efficiency, the measurement would be performed selecting only final states with two opposite-sign tau-leptons and two b-jets. However, for practical use, the choice of the working point of the b-tagging algorithm has to make a trade-off between the b-jet tagging efficiency and the light-jet rejection (see Section 3.5.4). For this reason, a relevant fraction of the $bb\tau\tau$ events may end up having only one reconstructed b-jet or even no reconstructed b-jets. To avoid losing such events, no requirements on the number of reconstructed b-jets are applied by the analysis in the event selection. The measurement, however, is performed by dividing the visible $\tau\tau$ invariant mass distribution into regions defined by the b-jet multiplicity, since each of them presents a different signal sensitivity and background composition.

4.2 Analysis regions

Several analysis regions are defined according to the flavour of the reconstructed leptons, their charge and the number of reconstructed b-jets. All regions require exactly two reconstructed and identified leptons (electrons, muons or tau-leptons) with the reconstruction and identification criteria defined in Section 4.4. Moreover, all the analysis regions require a visible invariant mass of the two leptons $m_{\ell\ell}^{\text{vis}} > 100\,\text{GeV}$ (for which they are labelled *high-mass* regions), since this is the region of the di-lepton invariant mass spectrum where most of the sensitivity to the leptoquark t-channel exchange is expected. The 100 GeV threshold has been chosen to remove the hadron resonances and the large $Z \to \ell\ell$ contribution at lower invariant mass.

A first division between the analysis regions is based on the flavours of the two leptons in the selected events. Six flavour regions are thus defined according to the six different ways of combining the three lepton flavours to form a lepton pair: $\tau_{\text{had}}\tau_{\text{had}}$, $e\tau_{\text{had}}$, $\mu\tau_{\text{had}}$, ee, $\mu\mu$, $e\mu$. In this way, all the possible outcomes of the $\tau\tau$ decay are taken into account. Another region definition criterium is based on the sign of the electric charges of the di-lepton pair. Two regions are identified in this sense: an opposite-sign region, in which the two leptons have opposite electric charges, and a same-sign region, where the two leptons have the same charge. Finally, regions are also identified by the b-jet multiplicity (namely the number of reconstructed b-jets in the event): three regions are defined in this way, one without any reconstructed b-jet, one with only one reconstructed b-jet and the last one with two or more reconstructed b-jets.

Combining the previous criteria on the lepton flavour, charge and b-jet multiplicity, the signal and validation regions of the analysis are obtained. The signal regions, which are used in the detector-level fits, are constituted by the opposite-sign $\tau_{\text{had}}\tau_{\text{had}}$, $e\tau_{\text{had}}$ and $\mu\tau_{\text{had}}$ regions. The opposite-sign ee, $\mu\mu$ and $e\mu$ regions instead are not included in the fits since they are expected to have a very low signal sensitivity due to the huge background contribution from di-boson, $t\bar{t}$ and $Z \to \ell\ell$ processes. These regions are therefore used to validate the SM MC predictions of such processes. Different validation regions are obtained from the same-sign $\tau_{\text{had}}\tau_{\text{had}}$, $e\tau_{\text{had}}$ and $\mu\tau_{\text{had}}$ regions: here no leptoquark signal is expected and most of the events populating them come from multi-jet QCD events in which the jets are misreconstructed as hadronic tau-leptons (referred to as *fakes*). These same-sign regions are thus used as validation regions for the data-driven estimate of the fakes background. The signal and validation regions used by the analysis are summarised in the scheme shown in Figure 4.5.

4.3 Data and MC samples

In order to perform a search for new physics it is of primary importance to have a prediction of the involved SM processes as accurate as possible. A prediction of the BSM signal expected according to a certain theoretical model is needed as well. MC simulations are used to produce the distributions of interest for the most important SM processes and for the BSM signal, which are then compared with the data collected by the detector. To assess the uncertainty related to the predictions, for each SM process several samples are produced with different combinations of MC generators and sets of parameters. The data and MC samples used for the leptoquark search are described in the following paragraphs.

4.3.1 Data

The analysis presented here makes use of the full LHC Run 2 proton-proton collision dataset collected by the ATLAS detector between 2015 and 2018 at $\sqrt{s} = 13\,\text{TeV}$. Only events recorded under stable beam conditions and for which all relevant detector subsystems were known to be in a good operating condition are used.

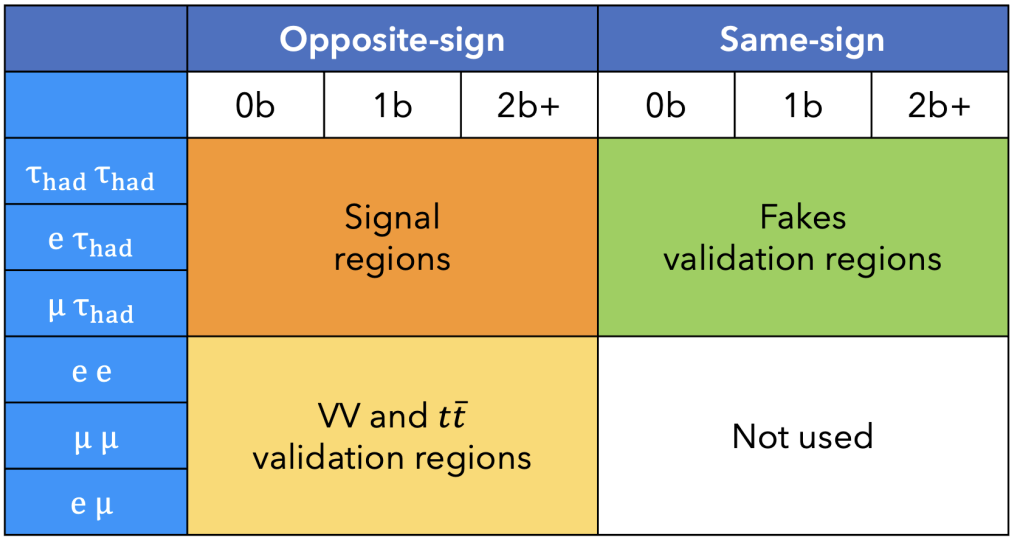

Figure 4.5. Signal and validation regions used by the analysis. The regions are defined by lepton flavours, lepton charges and b-jet multiplicity.

This dataset corresponds to an integrated luminosity of $140\,\text{fb}^{-1}$.

4.3.2 MC predictions

Drell-Yan predictions

The production of the Drell-Yan $Z/\gamma^* \to \ell\ell$+jets process was simulated with the Sherpa 2.2.11 [60] generator using next-to-leading-order (NLO) matrix elements (ME) for up to two partons, and leading-order (LO) matrix elements for up to five partons calculated with the Comix [99] and OpenLoops [100] libraries. They were matched with the Sherpa parton shower [101] using the MEPS@NLO prescription [102] and the NNPDF3.0nnlo set of PDFs [103].

As an alternative to Sherpa, the Powheg Box v1 generator [61] was used for the simulation at NLO accuracy of the hard-scattering processes of Z boson production and decay in the electron, muon, and tau-lepton channels. It was interfaced to Pythia 8.186 [59] for the modelling of the parton shower, hadronisation, and underlying event, with parameters set according to the AZNLO tune [104]. The CT10nlo PDF set [105] was used for the hard-scattering processes, whereas the CTEQ6L1 PDF set [106] was used for the parton shower. The effect of QED final-state radiation was simulated with Photos++ 3.52 [107]. The EvtGen 1.2.0 program [108] was used to decay bottom and charm hadrons.

In order to extend the statistical power of these predictions in the high $m_{\ell\ell}$ region, a dedicated high-statistics Sherpa sample was produced for the $Z \to \tau\tau$, $Z \to ee$ and $Z \to \mu\mu$ processes with $m_{\ell\ell} > 120\,\text{GeV}$, using otherwise identical settings to the inclusive samples described above. The inclusive samples described

previously are therefore used exclusively for the $m_{\ell\ell} < 120\,\text{GeV}$ prediction, while the high-statistics samples are used in the remaining invariant mass spectrum. Similarly, but only for the $Z \to \tau\tau$ process, a series of POWHEG BOX + PYTHIA samples were produced in exclusive bins of $m_{\tau\tau}$, starting from 120 GeV.

W+jets predictions

No predictions for the $W \to \ell\nu$+jets process were taken from MC simulations. This is because this process cannot produce a lepton pair in the final state at particle level. Anyway, events from the $W \to \ell\nu$+jets process may end up with a couple of reconstructed leptons in the final state, but in that case at least one of the two leptons is a *fake* and the contribution of such events is estimated through a data-driven technique, as explained in Section 4.5.

$t\bar{t}$ predictions

The production of $t\bar{t}$ events was modelled using the POWHEG BOX v2 [61] generator at NLO with the NNPDF3.0NLO [103] PDF set and the h_{damp} parameter, which regulates the high-p_{T} radiation against which the $t\bar{t}$ system recoils, set to 1.5 m_{top}. The events were interfaced to PYTHIA 8.230 [109] to model the parton shower, hadronisation, and underlying event, with parameters set according to the A14 tune [110] and using the NNPDF2.3LO set of PDFs [111]. The decays of bottom and charm hadrons were performed by EVTGEN 1.6.0 [108].

The impact of using a different parton shower and hadronisation model is evaluated by comparing the above $t\bar{t}$ sample with another event sample produced with the POWHEG BOX v2 [61] generator using the NNPDF3.0NLO [103] PDFs. Events in the latter sample were interfaced with HERWIG 7.04 [112], using the H7UE set of tuned parameters [113] and the MMHT2014LO PDF set [114]. The decays of bottom and charm hadrons were simulated using the EVTGEN 1.6.0 program [108].

Single top-quark predictions

The main production channels for the single-top processes are the associated production with the W boson (Wt), the s-channel production and the t-channel production.

The associated production of top quarks with the W bosons was modelled by the POWHEG BOX v2 [61] generator at NLO in QCD using the five-flavour scheme and the NNPDF3.0NLO set of PDFs [103]. The diagram removal scheme [115] was used to remove interference and overlap with $t\bar{t}$ production. The related uncertainty is estimated by comparison with an alternative sample generated using the diagram subtraction scheme [115, 116]. The events were interfaced to PYTHIA.8.230 [109] using the NNPDF2.3LO set of PDFs [111] and the A14 tune [110].

Single-top t-channel and s-channel productions were modelled using the POWHEG BOX v2 [61] generator at NLO in QCD using the four-flavour and five-flavour schemes respectively and the corresponding NNPDF3.0NLO set of PDFs [103]. The events were interfaced with PYTHIA 8.230 [109] using the A14 tune and the NNPDF2.3LO set of PDFs [111].

The uncertainty due to the parton shower and hadronisation model is evaluated by comparing the nominal sample of events with a sample where the events generated with the POWHEG BOX v2 [61] generator were interfaced to HERWIG 7.04 [112], using the H7UE set of tuned parameters [113] and the MMHT2014LO PDF set [114].

Multi-boson predictions

Samples of di-boson final states (VV) were simulated with the SHERPA 2.2.11 [60] generator. Fully leptonic final states and semileptonic final states, where one boson decays leptonically and the other hadronically, were generated using matrix elements at NLO accuracy in QCD for up to one additional parton and at LO accuracy for up to three additional parton emissions. Samples for the loop-induced processes $gg \to VV$ were generated using LO-accurate matrix elements for up to one additional parton emission for both the cases of fully leptonic and semileptonic final states. The matrix element calculations were matched and merged with the SHERPA parton shower based on Catani–Seymour dipole factorisation [101] using the MEPS@NLO prescription [102]. The virtual QCD corrections were provided by the OPENLOOPS library [100]. The NNPDF3.0NNLO set of PDFs was used [111], along with the dedicated set of tuned parton-shower parameters developed by the SHERPA authors.

Leptoquark predictions

Potential off-shell leptoquark contributions to high-mass Drell-Yan production were simulated with MADGRAPH5_AMC@NLO 2.2.2 [117], using LO-accurate matrix elements (ME) with up to two final-state partons in addition to the leptoquark-mediated interaction. The ME calculation employed the NNPDF3.0NLO set of PDFs [103] (H_{T}-sliced) / NNPDF2.3LO set of PDFs [111] (N_{parton}-sliced). Events were interfaced to PYTHIA 8.186 [59] for the modelling of the parton shower, hadronisation, and underlying event. The overlap between matrix element and parton shower emissions was removed using the CKKW-L merging procedure [118]. The A14 tune [110] of PYTHIA 8 was used with the NNPDF2.3LO PDF set [111]. The decays of bottom and charm hadrons were performed by EVTGEN 1.2.0 [108].

The signal contribution is simulated assuming the vector leptoquark of the simplified U_1 model [20] with strong coupling to third-generation fermions. The vector leptoquark samples are generated using the Universal FeynRules Output (UFO) model [119] with the couplings $g_U = 1$, $\beta_L^{33} = 1$, $\beta_L^{23} = 0$ and $\beta_R^{33} = 0$[3], meaning that

[3]The indices refer to the fermion generations and therefore $\beta_L^{33} = \beta_L^{b\tau} = 1$, $\beta_L^{23} = \beta_L^{b\mu} = \beta_L^{s\tau} = 0$.

the leptoquark is coupled only to left-handed fermion fields of the third-generation. Samples for the contribution of both the pure BSM term and the interference term between BSM and SM amplitude, which is negative, are produced. The shape of the differential cross-section with respect to the di-lepton invariant mass for the pure BSM term and for the interference term does not have a strong dependence on the leptoquark mass, as shown in Figure 4.6. Therefore the signal samples for the different leptoquark mass points are generated simply by reweighting the leptoquark template. In this way the signal samples for the pure BSM and interference term are produced for the following leptoquark masses: 1.5 TeV, 2.0 TeV, 2.5 TeV and 3.0 TeV.

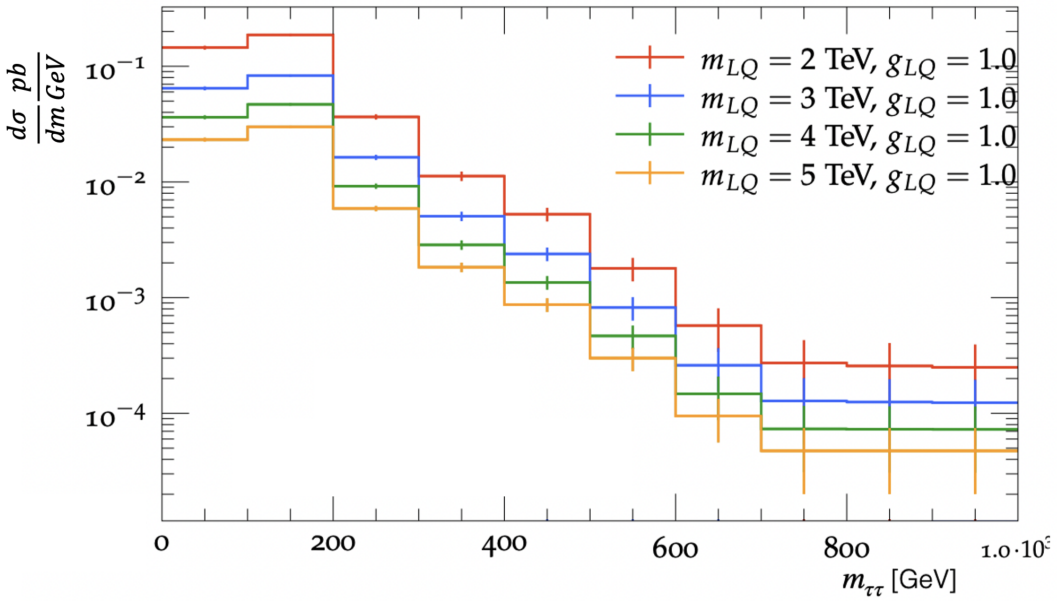

Figure 4.6. Predicted particle-level differential cross-sections of the interference between SM Drell-Yan $\tau\tau$ production and leptoquark t-channel exchange for different leptoquark masses. In all cases, the predicted interference term reduces the SM Drell-Yan cross-section, so in this plot its absolute value is reported.

4.4 Selections

The selections applied to the reconstructed objects (tau-leptons, muons, electrons and jets) are identical for all the analysis regions. They mostly follow the standard ATLAS prescriptions already defined in detail in Chapter 3 and are briefly summarised in Section 4.4.1. The reconstructed objects passing these selections are then used to categorise the events among the different analysis regions, according to the criteria explained in Section 4.4.2.

4.4.1 Object selection

Hadronic tau-leptons

Hadronically decaying tau-leptons (τ_{had}) are seeded by jets built from locally calibrated TopoClusters, as described in Section 3.4. For this analysis, the FastJet implementation [120] of the anti-k_t jet reconstruction algorithm is used with a radius parameter $R = 0.4$. The τ_{had} candidates are required to be in the pseudorapidity region defined by $|\eta| < 2.47$, excluding the calorimeter transition region ($1.37 < |\eta| < 1.52$), have one or three associated charged tracks and have $p_{\text{T}} > 25\,\text{GeV}$ after the application of the Tau Energy Scale (TES) correction. The identification of the τ_{had} candidates is then performed through the application of the Tight RNN working point.

Moreover, in order to enhance the rejection of electrons, which are easily misidentified as one-prong hadronic taus, the τ_{had} candidates are required to pass the Loose working point of the eBDT discriminator. Further requirements are also applied to remove the calorimeter-tagged muons that have a particularly high misidentification rate in the central η region ($|\eta| < 0.1$) due to poor coverage of the muon system: therefore, in this region, τ_{had} candidates within $\Delta R = 0.1$ from a calorimeter-tagged muon are removed.

The application in the object selection of classifiers like the RNN used in the τ_{had} identification may result in different selection efficiencies in data and MC simulation. For tau-leptons, these differences are evaluated from Z boson decay samples and translated into correction factors (called *scale factors*) to be applied to MC events to achieve closure with the observed data. In this analysis, scale factors for the TES correction, the RNN identification and the eBDT selection are applied.

Electrons and muons

In this analysis, both light leptons originating directly from prompt tau-lepton decays and prompt light leptons from other sources are considered. Since electrons and muons from tau-lepton decays tend to carry a rather small fraction of the original tau-lepton momentum, candidate light leptons are required to have $p_{\text{T}} > 7\,\text{GeV}$. Electrons are required to be in the fiducial region of the inner tracker and electromagnetic calorimeter ($|\eta| < 2.47$, excluding the calorimeter transition region), to pass the Medium identification working point and the HighPtCaloOnly isolation working point. Muon candidates, instead, must be combined or segment-tagged, have $|\eta| < 2.5$ and pass the Medium identification working point and the Loose isolation working point.

Differences in reconstruction, identification and isolation efficiencies between data and MC simulation are accounted for by scale factors derived in the Z and J/ψ mass regions.

Jets

Jets are built from Particle Flow objects using the anti-k_t algorithm with radius parameter $R = 0.4$, as described in Section 3.5. The transverse momentum of the reconstructed jets is then corrected with Jet Energy Scale (JES) calibrations. After these calibrations, jets with $p_{\mathrm{T}} < 25\,\mathrm{GeV}$ are removed. The JVT multi-variate discriminant method is used to remove jets with $p_{\mathrm{T}} < 60\,\mathrm{GeV}$ and $|\eta| < 2.4$ that have large estimated energy fractions from pileup collision vertices (above this p_{T} scale, the requirement becomes unnecessary). Simulated jets are corrected for their JVT efficiencies and p_{T} scale and resolution by applying scale factors derived from measurements in multi-jet, γ+jets and Z+jets data.

To identify hadronic jets containing b-hadrons, the DL1r b-tagging algorithm described in Section 3.5.4 is used. The tagger operating point with a b-jet identification efficiency of 77% in an inclusive sample of b-jets from $t\bar{t}$ events is chosen. The b-jet and c-jet tagging probabilities are measured in a $t\bar{t}$-enriched sample in collision data. The light-jet misidentification rate, instead, is measured in Z+jets events. Simulated tagging rates are corrected with scale factors derived from these measurements.

Overlap removal

It may occur that the same set of tracks and calorimeter clusters is associated with more than one reconstructed object. An overlap removal algorithm is therefore applied in order to remove objects corresponding to the same detector signals. The criteria applied to perform the overlap removal are reported in Table 4.1 and are based on the angular separation $\Delta R = \sqrt{(\Delta\eta)^2 + (\Delta\phi)^2}$ between the two reconstructed objects.

4.4.2 Event selection

The reconstructed objects passing the selections described in the previous section are then used to classify the events at the detector level among the different regions of the analysis introduced in Section 4.2. Each of the six flavour categories ($\tau_{\mathrm{had}}\tau_{\mathrm{had}}$, $e\tau_{\mathrm{had}}$, $\mu\tau_{\mathrm{had}}$, ee, $\mu\mu$, $e\mu$) applies some specific selections and cuts to the events. The selections applied for the event categorisation in the analysis regions are mutually exclusive, so that an event can never be accepted by two different regions. If an event does not fulfil the requirements of any region, it is discarded.

In all regions, exactly two leptons, reconstructed and identified according to the criteria laid out in the previous section, must be present in an accepted event. Moreover, the visible invariant mass of the di-lepton system is always required to be in the high-mass region, defined by $m_{\ell\ell}^{\mathrm{vis}} > 100\,\mathrm{GeV}$.

To be classified in the $\tau_{\mathrm{had}}\tau_{\mathrm{had}}$ category, an event is required in first place to pass the $\tau_{\mathrm{had}}\tau_{\mathrm{had}}$ trigger selection reported in Section 4.4.3. The event must then have

Table 4.1. Criteria applied to perform the overlap removal between reconstructed objects. The criteria are listed following the order of application.

Object to remove	Object to keep	Criteria
tau	electron	The tau is removed if $\Delta R < 0.2$.
tau	muon	The tau is removed if $\Delta R < 0.2$.
electron	muon	If they share a track, the electron is removed if the muon is associated with a signature in the muon spectrometer, otherwise the muon is removed.
jet	electron	Any jet within $\Delta R = 0.2$ of an electron is removed.
jet	muon	Any jet within $\Delta R = 0.2$ of a muon is removed.
electron	jet	Any electron within $\Delta R = 0.4$ of a jet is removed.
muon	jet	Any muon within $\Delta R = 0.4$ of a jet is removed.
jet	tau	Any jet within $\Delta R = 0.2$ of a tau is removed.

exactly two τ_{had} objects, with the leading τ_{had} having $p_{\text{T}} > 90\,\text{GeV}$ and the subleading τ_{had} having $p_{\text{T}} > 60\,\text{GeV}$. These requirements on the τ_{had} p_{T} are introduced to ensure that the τ_{had} objects are in the plateau region of the trigger efficiency curve (considering the thresholds of the most relevant triggers of the $\tau_{\text{had}}\tau_{\text{had}}$ trigger list), to avoid the large systematic uncertainty related to the turn-on region. The offline reconstructed τ_{had} objects are then required to be matched[4] to the trigger objects (namely the objects reconstructed by the HLT to perform the trigger decision) which fired the trigger and have a p_{T} above the nominal threshold of the fired trigger. In addition, a veto is imposed on events with light leptons.

For the $\mu\tau_{\text{had}}$ and $e\tau_{\text{had}}$ flavour categories, the events have to pass the respective trigger selection described in Section 4.4.3. Then, exactly one τ_{had} object must be present in the event as well as exactly one muon or electron (for the $\mu\tau_{\text{had}}$ and $e\tau_{\text{had}}$ regions respectively), reconstructed and identified as illustrated in the previous section. If there are additional light leptons, the event is vetoed. The muon or electron p_{T} is required to be above 27 GeV. Finally, the reconstructed muon or electron of the event has to match with the trigger object that fired the trigger and have a p_{T} above the nominal threshold of the fired trigger. Only in the $e\tau_{\text{had}}$ category, in which the contribution from the $Z \to ee$ background is larger, the τ_{had} objects are required to pass also the Medium working point of the eBDT discriminator, which provides a greater rejection of electrons misidentified as τ_{had} candidates, without a relevant loss in the tau-lepton identification efficiency, as shown by the studies reported in Section 4.4.4.

[4] A reconstructed object and a trigger object are matched if their angular separation is $\Delta R < 0.4$.

For the ee, $\mu\mu$ and $e\mu$ categories, exactly two electrons, two muons and one electron and one muon must be present in the event, respectively, all of them required having $p_{\mathrm{T}} > 27\,\mathrm{GeV}$. For the trigger selection, the ee category applies the same triggers used by the $e\tau_{\mathrm{had}}$ region, the $\mu\mu$ category the same triggers used by the $\mu\tau_{\mathrm{had}}$ region and the $e\mu$ category the triggers used by both the $e\tau_{\mathrm{had}}$ and $\mu\tau_{\mathrm{had}}$ regions. The matching between the reconstructed objects and the trigger objects is required as well.

After the flavour categorisation, the events are classified between the opposite-sign and same-sign regions according to the charges of the two leptons and then between the 0 b-jet, 1 b-jet and 2 or more b-jets regions according to the b-jet multiplicity.

4.4.3 Triggers

The triggers used by this analysis in the event selection are chosen among the unprescaled triggers with the loosest selection criteria available in each data-taking period. For the $e\tau_{\mathrm{had}}$ and $\mu\tau_{\mathrm{had}}$ regions, single-electron and single-muon triggers are used, respectively. Three single-electron triggers for the $e\tau_{\mathrm{had}}$ region and two single-muons triggers for the $\mu\tau_{\mathrm{had}}$ region are used in logical OR in each data-taking period, according to the standard ATLAS prescriptions. The use of different triggers with increasing p_{T} thresholds and decreasing strictness in the identification and isolation criteria allows the analyses to cover with high efficiency and reasonable trigger rates a wide range of the p_{T} spectrum of the triggering objects. Unprescaled electron-tau and muon-tau triggers are available as well, but are not included in the analysis trigger lists, since their addition does not lead to a relevant improvement of the overall trigger efficiency and acceptance[5], as shown by Figure 4.7 and 4.8, which report the trigger efficiency times acceptance for different single-object and di-object triggers, highlighting the contribution added specifically by each trigger. The list of triggers used by the analysis in the $e\tau_{\mathrm{had}}$ and $\mu\tau_{\mathrm{had}}$ regions for each data-taking period is reported in Table 4.2.

The lowest unprescaled single-tau triggers have nominal thresholds which are much higher than the thresholds of single-electron and single-muon triggers, because at low p_{T} the contribution of fake taus from multi-jet events would bring the trigger rate over an acceptable level. Therefore, in the $\tau_{\mathrm{had}}\tau_{\mathrm{had}}$ region, the exclusive use of single-tau triggers would result in a relevant loss of events in the first bins of the $m_{\tau\tau}$ distribution. To increase the trigger acceptance in this invariant mass region, di-tau trigger chains can be used in logical OR with single-tau triggers. Anyway, to lower the trigger rate, the di-tau triggers with the lowest thresholds in all years except 2015 apply additional L1 jet requests which reduce the trigger acceptance, as shown in Figure 4.9. Thus, only the di-tau triggers without additional

[5]This is because the tau triggers have in general a worse efficiency with respect to electron and muon triggers and the electron-tau and muon-tau triggers may have L1 requests, like additional jets, which reduce the phase-space covered by the trigger.

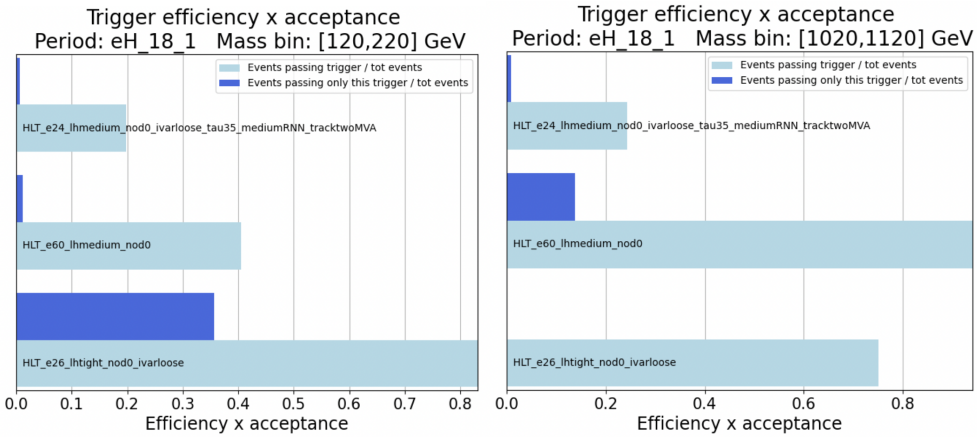

Figure 4.7. Efficiency times acceptance of possible trigger chains for the $e\tau_{\text{had}}$ region in a low (a) and a high (b) $m_{e\tau}$ bin for an example data-taking period of 2018. The light blue bars represent the absolute efficiency times acceptance of each trigger chain, while the dark blue bars the specific contribution that each trigger chain would add to the others.

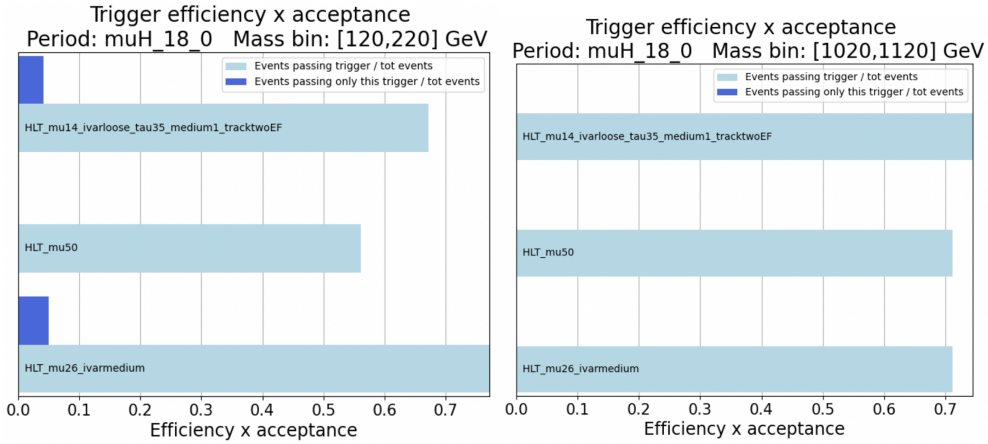

Figure 4.8. Efficiency times acceptance of possible trigger chains for the $\mu\tau_{\text{had}}$ region in a low (a) and a high (b) $m_{\mu\tau}$ bin for an example data-taking period of 2018. The light blue bars represent the absolute efficiency times acceptance of each trigger chain, while the dark blue bars the specific contribution that each trigger chain would add to the others.

L1 jet requests are used in the analysis. The full list of trigger chains used in the $\tau_{\text{had}}\tau_{\text{had}}$ region, divided per data-taking period, is reported in Table 4.3.

In simulated events, a trigger efficiency scale factor is applied to account for differences between the predicted and measured trigger efficiencies [121–123].

Table 4.2. List of the trigger chains applied in the $e\tau_{\text{had}}$ and $\mu\tau_{\text{had}}$ regions. The triggers are divided per year of the Run 2 and data-taking period.

Year	Period	Trigger name ($e\tau_{\text{had}}$ region)	Trigger name ($\mu\tau_{\text{had}}$ region)
2015	all	HLT_e24_lhmedium_L1EM20VH	HLT_mu20_iloose_L1MU15
		HLT_e60_lhmedium	HLT_mu40
		HLT_e120_lhloose	
2016	A-D3	HLT_e26_lhtight_nod0_ivarloose	HLT_mu24_ivarmedium
		HLT_e60_lhmedium_nod0	HLT_mu50
		HLT_e140_lhloose_nod0	
	D4-end	HLT_e26_lhtight_nod0_ivarloose	HLT_mu26_ivarmedium
		HLT_e60_lhmedium_nod0	HLT_mu50
		HLT_e140_lhloose_nod0	
2017	All	HLT_e26_lhtight_nod0_ivarloose	HLT_mu26_ivarmedium
		HLT_e60_lhmedium_nod0	HLT_mu50
		HLT_e140_lhloose_nod0	
2018	All	HLT_e26_lhtight_nod0_ivarloose	HLT_mu26_ivarmedium
		HLT_e60_lhmedium_nod0	HLT_mu50
		HLT_e140_lhloose_nod0	

Table 4.3. List of the trigger chains applied in the $\tau_{\text{had}}\tau_{\text{had}}$ region. The triggers are divided per year of the Run 2 and data-taking period.

Year	Period	Trigger name ($\tau_{\text{had}}\tau_{\text{had}}$ region)
2015	All	HLT_tau80_medium1_tracktwo_L1TAU60
		HLT_tau35_medium1_tracktwo_tau25_medium1_tracktwo_L1TAU20IM_2TAU12IM
2016	A	HLT_tau80_medium1_tracktwo_L1TAU60
		HLT_tau80_medium1_tracktwo_L1TAU60_tau50_medium1_tracktwo_L1TAU12
	B-D3	HLT_tau125_medium1_tracktwo
		HLT_tau80_medium1_tracktwo_L1TAU60_tau50_medium1_tracktwo_L1TAU12
	D4-end	HLT_tau160_medium1_tracktwo
		HLT_tau80_medium1_tracktwo_L1TAU60_tau50_medium1_tracktwo_L1TAU12
2017	B1-B7	HLT_tau160_medium1_tracktwo
		HLT_tau80_medium1_tracktwo_L1TAU60_tau50_medium1_tracktwo_L1TAU12
	B8-end	HLT_tau160_medium1_tracktwo_L1TAU100
		HLT_tau80_medium1_tracktwo_L1TAU60_tau60_medium1_tracktwo_L1TAU40
2018	B-J	HLT_tau160_medium1_tracktwoEF_L1TAU100
		HLT_tau80_medium1_tracktwoEF_L1TAU60_tau60_medium1_tracktwoEF_L1TAU40
	K-end	HLT_tau160_medium1_tracktwoEF_L1TAU100
		HLT_tau160_mediumRNN_tracktwoMVA_L1TAU100
		HLT_tau80_medium1_tracktwoEF_L1TAU60_tau60_medium1_tracktwoEF_L1TAU40
		HLT_tau80_mediumRNN_tracktwoMVA_L1TAU60_tau60_mediumRNN_tracktwoMVA_L1TAU40

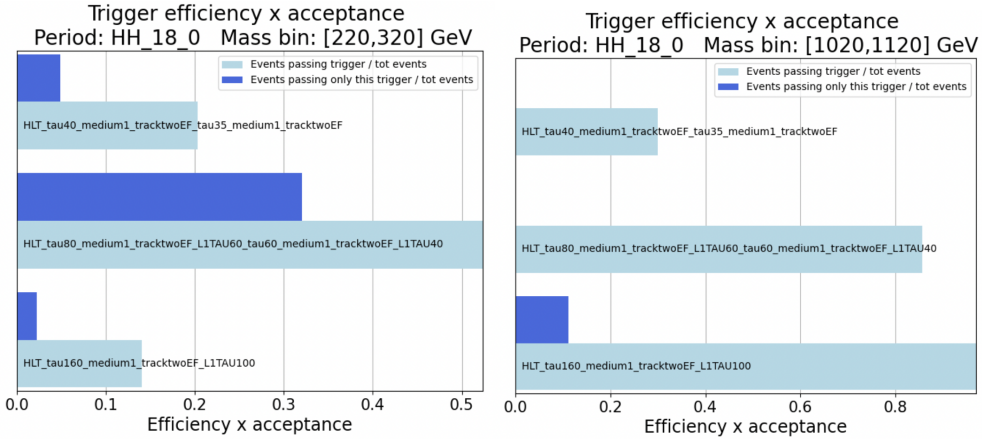

Figure 4.9. Efficiency times acceptance of possible trigger chains for the $\tau_{\text{had}}\tau_{\text{had}}$ region in a low (a) and a high (b) $m_{\tau\tau}$ bin for an example data-taking period of 2018. The light blue bars represent the absolute efficiency times acceptance of each trigger chain, while the dark blue bars the specific contribution that each trigger chain would add to the others.

4.4.4 $Z \to ee$ background rejection

One of the main background sources in the $e\tau_{\text{had}}$ region is constituted by the $Z \to ee$ process. Events from the $Z \to ee$ process may indeed be categorised in the $e\tau_{\text{had}}$ region if an electron is misreconstructed as a hadronic tau-lepton. In order to reduce the $Z \to ee$ background, a cut on the output variable of the eBDT discriminator can be applied when selecting the τ_{had} candidates. Three working points (*Loose*, *Medium* and *Tight*) are defined for the eBDT discriminator, providing an increasing background rejection but at the same time a decreasing signal efficiency, where in this case the signal is made of true hadronically decaying tau-leptons and the background consists of electrons identified as τ_{had} objects.

Since the $Z \to ee$ background has a relevant contribution only in the $e\tau_{\text{had}}$ region, the reconstructed τ_{had} candidates in this region are required to pass the Medium working point of the eBDT algorithm, to obtain a good rejection of events from the $Z \to ee$ process. In the $\mu\tau_{\text{had}}$ and $\tau_{\text{had}}\tau_{\text{had}}$ regions, instead, even if the $Z \to ee$ background has a small contribution, the τ_{had} candidates are required to pass the Loose eBDT working point, so that a fraction of the electrons faking hadronic tau-leptons is discarded anyway, but the signal loss is kept as small as possible.

The signal efficiency and the background rejection of the eBDT working points applied to the τ_{had} selections in the $e\tau_{\text{had}}$, $\mu\tau_{\text{had}}$ and $\tau_{\text{had}}\tau_{\text{had}}$ regions are evaluated using a simulated sample of $Z \to \tau\tau$ events as signal and a simulated sample of $Z \to ee$ events as background. In the $e\tau_{\text{had}}$ region, the application of the Medium working point results in a 90% signal efficiency and a 69% background rejection. Signal efficiency and background rejection do not depend on the τ_{had} p_{T} nor on the

invariant mass $m_{e\tau}$ and remain constant even at high p_{T} and $m_{e\tau}$ values, as shown by Figures 4.10 and 4.11, which report the $m_{e\tau}$ and τ_{had} p_{T} distributions before and after the Medium eBDT working point selection on τ_{had} candidates, obtained from a $Z \to ee$ MC sample and a $Z \to \tau\tau$ MC sample respectively. The efficiency of the Loose eBDT working point in a $Z \to \tau\tau$ MC sample is measured to be 99.4% in the $\mu\tau_{\mathrm{had}}$ region and 99.2% in the $\tau_{\mathrm{had}}\tau_{\mathrm{had}}$ region, as shown by Figure 4.12 and 4.13, which report the $m_{\ell\ell}$ and τ_{had} p_{T} distributions before and after the Loose eBDT working point selection on τ_{had} candidates from a $Z \to \tau\tau$ MC sample in the $\mu\tau_{\mathrm{had}}$ and $\tau_{\mathrm{had}}\tau_{\mathrm{had}}$ regions respectively. Therefore, applying the Loose eBDT working point has almost no effect on the signal.

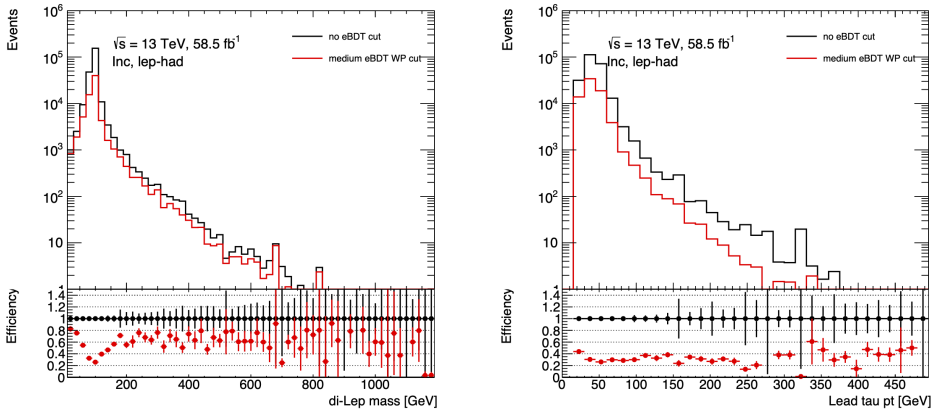

(a) **(b)**

Figure 4.10. The upper pad reports the $m_{e\tau}$ (a) and the τ_{had} p_{T} (b) distributions before (black) and after (red) the application of the Medium eBDT working point to τ_{had} candidates in the $e\tau_{\mathrm{had}}$ region for a $Z \to ee$ MC sample. The lower pad shows the ratios to the black distribution. No invariant mass cut has been applied to produce these plots.

4.5 Background estimate

The background contribution to the Drell-Yan process studied by this analysis is largely dependent on the considered region. The relative contributions of the different background processes vary depending on the flavour categorisation and the b-jet multiplicity. In the 0 b-jet region of the $e\tau_{\mathrm{had}}$ and $\mu\tau_{\mathrm{had}}$ categories, the main sources of background events are constituted of $W \to \ell\nu$+jets and multi-jet events, in which a jet is misidentified as a τ_{had}, $t\bar{t}$ and di-boson events with a real τ_{had} and a light lepton and $Z \to \ell\ell$ events, in which a light lepton is misidentified as a τ_{had}. In the 1 and 2 or more b-jet regions, instead, the dominant background is made of $t\bar{t}$ and single-top events with real τ_{had} candidates and light leptons. The $\tau_{\mathrm{had}}\tau_{\mathrm{had}}$ 0 b-jet region is dominated by multi-jet events, with two jets faking hadronic tau-leptons, while in the $\tau_{\mathrm{had}}\tau_{\mathrm{had}}$ 1 and 2 or more b-jet regions the dominant background is represented by the $t\bar{t}$ process.

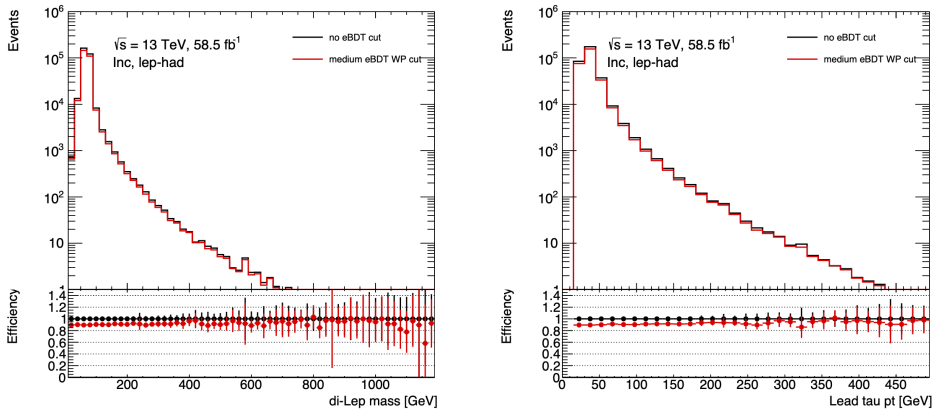

(a) **(b)**

Figure 4.11. The upper pad reports the $m_{e\tau}$ (a) and the τ_{had} p_{T} (b) distributions before (black) and after (red) the application of the Medium eBDT working point to τ_{had} candidates in the $e\tau_{\text{had}}$ region for a $Z \to \tau\tau$ MC sample. The lower pad shows the ratios to the black distribution. No invariant mass cut has been applied to produce these plots.

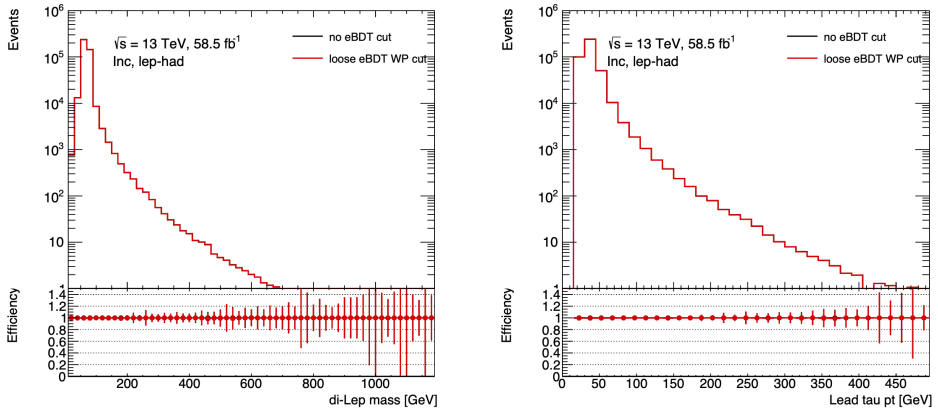

(a) **(b)**

Figure 4.12. The upper pad reports the $m_{\mu\tau}$ (a) and the τ_{had} p_{T} (b) distributions before (black) and after (red) the application of the Loose eBDT working point to τ_{had} candidates in the $\mu\tau_{\text{had}}$ region for a $Z \to \tau\tau$ MC sample. The lower pad shows the ratios to the black distribution. No invariant mass cut has been applied to produce this plot.

In this analysis, the contribution from all the background sources with two leptons at the particle level in the final state is estimated through MC simulation, while the fake-tau background contribution, made of all the events in which one or more of the reconstructed hadronically decaying tau-leptons are not a true tau-lepton, is derived from a data-driven technique. The need to use a data-driven method to estimate the *fakes'* contribution is due to the large uncertainties in modelling multi-jet events, which make the MC simulation not reliable in this case. The method

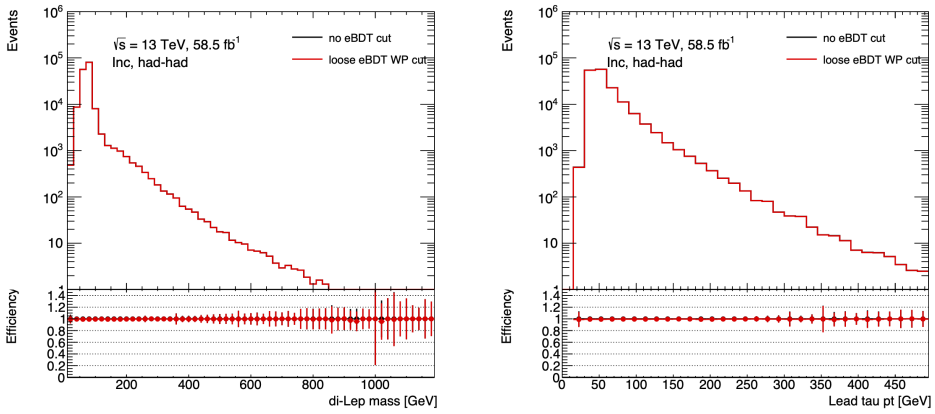

(a) **(b)**

Figure 4.13. The upper pad reports the $m_{\tau\tau}$ (a) and the leading τ_{had} p_{T} (b) distributions before (black) and after (red) the application of the Loose eBDT working point to τ_{had} candidates in the $\tau_{\text{had}}\tau_{\text{had}}$ region for a $Z \to \tau\tau$ MC sample. The lower pad shows the ratios to the black distribution. No invariant mass cut has been applied to produce this plot.

adopted to estimate this background is called *Universal Fake Factors* method [124]. This method uses events in data which pass the signal region selections, but with the τ_{had} identification criteria inverted (anti-ID), to estimate the fake-tau contribution in the signal regions. The events with anti-ID taus are then extrapolated into the signal regions using transfer factors, which represent the probability for a hadronic object to be reconstructed as a τ_{had}. These transfer factors are known as *fake factors*. The following sections describe in detail the Fake Factor method and its application to the analysis.

4.5.1 The Fake Factor method

The Fake Factor method, used to estimate the fake-tau background in this analysis, is based on the definition of anti-ID regions (one per signal region) which share with the signal regions all the selection criteria except for the tau identification requirement, which is instead reversed. Therefore, to be accepted by the anti-ID regions, the τ_{had} candidates, which in the signal regions are required to pass the Tight RNN working point (corresponding to an RNN score > 0.8), must have an RNN score < 0.8[6]. The fake factors (FFs) are defined as the transfer factors from an anti-ID region to the corresponding ID region and are measured in data from dedicated control regions (CRs) enriched in fake-taus. The fake factor is therefore given by

$$\text{FF} = \frac{N_{\text{ID}}^{\text{CR}}}{N_{\text{anti-ID}}^{\text{CR}}} \,, \tag{4.1}$$

[6] A minimum requirement of RNN score > 0.01 is applied anyway.

where $N_{\text{ID}}^{\text{CR}}$ is the number of events with jets reconstructed as hadronic taus according to the defined identification criteria and $N_{\text{anti-ID}}^{\text{CR}}$ the number of jets reconstructed as hadronic taus with reversed RNN score requirement, measured in the control region. The fake-tau contribution in the signal region ($N_{\text{ID}}^{\text{SR}}$) is then obtained by multiplying the number of events with anti-ID taus in the signal region ($N_{\text{anti-ID}}^{\text{SR}}$) by the corresponding fake factor:

$$N_{\text{ID}}^{\text{SR}} = N_{\text{anti-ID}}^{\text{SR}} \times \text{FF} \ . \tag{4.2}$$

The jets producing fake taus present different characteristics depending on their origin. Fake-taus generated from gluons tend to have a larger width, while fake-taus from quarks usually present a smaller width. The estimate of the fakes' contribution in the signal region is more accurate the more similar the jet composition is between control and signal regions. Since finding a control region with the same jet composition as the signal region is not trivial, different fake factors are measured in different control regions, each enriched in jets originating from a specific source, and then a fit is performed to find the fractions of the various contributions in the signal region. Three *primitive* fake factors are used in this analysis, measured respectively in a region enriched in quark jets (FF_{q}), one enriched in gluon jets with low JVT score ($\text{FF}_{\text{g}}^{\text{ljvt}}$) and one enriched in gluon jets with high JVT score ($\text{FF}_{\text{g}}^{\text{hjvt}}$):

$$\text{FF}_{\text{q}} = \frac{N_{\text{ID}}^{\text{CR}_{\text{q}}}}{N_{\text{anti-ID}}^{\text{CR}_{\text{q}}}} \ , \qquad \text{FF}_{\text{g}}^{\text{ljvt}} = \frac{N_{\text{ID}}^{\text{CR}_{\text{g}}^{\text{ljvt}}}}{N_{\text{anti-ID}}^{\text{CR}_{\text{g}}^{\text{ljvt}}}} \ , \qquad \text{FF}_{\text{g}}^{\text{hjvt}} = \frac{N_{\text{ID}}^{\text{CR}_{\text{g}}^{\text{hjvt}}}}{N_{\text{anti-ID}}^{\text{CR}_{\text{g}}^{\text{hjvt}}}} \ . \tag{4.3}$$

The relative fractions of the three jet components in the signal region are evaluated by performing a fit on the tau width using template distributions. The measured fractions are then used as coefficients in a linear combination of the three primitive fake factors to obtain the signal region transfer factor.

The template tau width distributions and the primitive fake factors are provided by the ATLAS Fake Tau Task Force (FTTF). The primitive fake factors are measured using the full Run 2 dataset collected by the ATLAS detector constructing regions which are enriched in a specific fake-tau source. FF_{q} is extracted from $Z \to \mu\mu$ events while $\text{FF}_{\text{g}}^{\text{ljvt}}$ and $\text{FF}_{\text{g}}^{\text{hjvt}}$ are obtained from multi-jet events with at least two hadronic jets (requiring a JVT score < 0.8 for the former and a JVT score > 0.8 for the latter). In each of these control regions, the primitive fake factor is measured in the following way:

$$\text{FF} = \frac{N_{\text{ID}}^{\text{Data}} - N_{\text{ID}}^{\text{MC}}}{N_{\text{anti-ID}}^{\text{Data}} - N_{\text{anti-ID}}^{\text{MC}}} \ , \tag{4.4}$$

where N_{ID} and $N_{\text{anti-ID}}$ are the number of events with the reconstructed hadronic taus passing or failing the tau identification criteria, respectively. In Equation 4.4, to the number of events measured in data, the number of events with true leptons is subtracted to ensure that only events with fake-taus originating from hadronic jets are considered in the fake factor evaluation. The component of true-lepton events is obtained from the MC simulation of the most relevant processes, selecting

events with detector-level leptons matched to particle-level leptons. In this way, the fake factor method can be used only to estimate the fakes' contribution from quark jets or gluon jets and does not take into account the contribution from electrons or muons misidentified as tau-leptons.

4.5.2 Tau width template fit

To obtain the coefficients for the three primitive fake factors to be used in the construction of the combined fake factors suitable for this analysis, distributions of the tau width are produced from data events in the anti-ID signal regions and then fit with the template distributions from the FTTF. The tau width variable used in the fit is defined as

$$\text{width} = \frac{\sum_i \Delta R^i p_{\mathrm{T}}^i}{\sum_i p_{\mathrm{T}}^i}, \tag{4.5}$$

where the sum runs over all the constituents of the jet-seed of the τ_{had} object with $p_{\mathrm{T}} > 500\,\text{MeV}$ and ΔR is the angular distance of the constituent direction from the jet-seed axis. The distributions used in the fit are binned with respect to the p_{T} and η of the tau candidates, decay mode (one-prong or three-prongs) and trigger selection (separating taus which fired a trigger from those which did not). The binning has been optimised to avoid having bins with too poor statistics. The distributions are also divided between same-sign events, used to validate the fakes' background estimate, and opposite-sign events, used to obtain the fake factors for the signal regions.

A fit is therefore performed on the tau width distributions of the anti-ID signal regions with the tau width templates provided by the FTTF and the coefficients α_{q}, $\alpha_{\mathrm{g}}^{\mathrm{ljvt}}$ and $\alpha_{\mathrm{g}}^{\mathrm{hjvt}}$, which represent the relative fractions of quark-jet, low-JVT gluon-jet and high-JVT gluon-jet components in the anti-ID signal regions, are obtained. In the fit, the constraint $\alpha_{\mathrm{q}} + \alpha_{\mathrm{g}}^{\mathrm{ljvt}} + \alpha_{\mathrm{g}}^{\mathrm{hjvt}} = 1$ is applied. Examples of the fit results in some representative bins for the $\tau_{\text{had}}\tau_{\text{had}}$ region are given in Figure 4.14, while for the $e\tau_{\text{had}}$ and $\mu\tau_{\text{had}}$ regions are given in Figure 4.15.

4.5.3 Evaluation of combined fake factors

The values of the coefficients extracted from the tau width fit described in the previous section are used to construct a linear combination of the primitive fake factors, from which the combined fake factors suitable for the analysis are obtained:

$$\mathrm{FF}_{\mathrm{comb}} = \alpha_{\mathrm{q}}\mathrm{FF}_{\mathrm{q}} + \alpha_{\mathrm{g}}^{\mathrm{ljvt}}\mathrm{FF}_{\mathrm{g}}^{\mathrm{ljvt}} + \alpha_{\mathrm{g}}^{\mathrm{hjvt}}\mathrm{FF}_{\mathrm{g}}^{\mathrm{hjvt}}, \tag{4.6}$$

where FF_{q}, $\mathrm{FF}_{\mathrm{g}}^{\mathrm{ljvt}}$ and $\mathrm{FF}_{\mathrm{g}}^{\mathrm{hjvt}}$ are the primitive FFs for the quark-jet, the low-JVT gluon-jet and the high-JVT gluon-jet components provided by the FTTF. The combined fake factors are produced with the same binning of the tau-width distributions. Examples of combined fake factors in some representative bins are given in Figure 4.16 for the $\tau_{\text{had}}\tau_{\text{had}}$ region and in Figure 4.17 for the $e\tau_{\text{had}}$ and $\mu\tau_{\text{had}}$ regions.

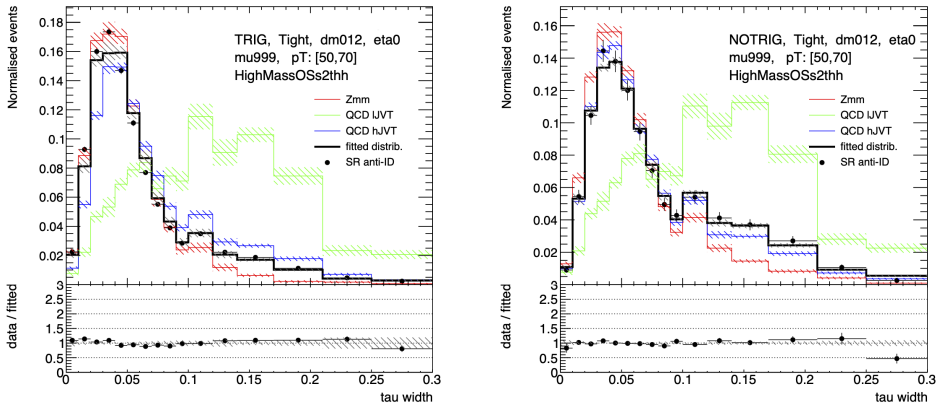

(a) **(b)**

Figure 4.14. Examples of the tau width fit for the $\tau_{\text{had}}\tau_{\text{had}}$ region in the $(50, 70)$ GeV p_{T} bin for the case in which the tau candidate fires a trigger (a) and the case in which no trigger is fired by the tau (b). The red, green and blue distributions represent respectively the quark-jet template, the low-JVT gluon-jet template and the high-JVT gluon-jet template. The points represent the data in the anti-ID signal region and the black line is the distribution obtained from the combination of the template distributions with the best-fit values of the corresponding coefficients.

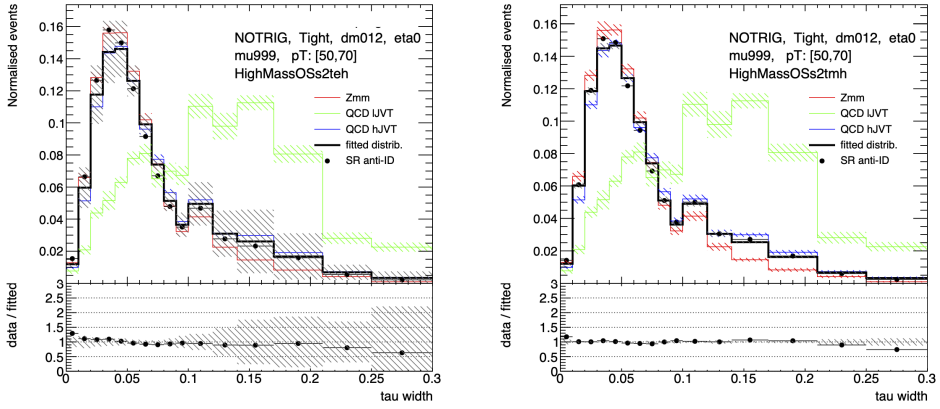

(a) **(b)**

Figure 4.15. Examples of the tau width fit for the $e\tau_{\text{had}}$ (a) and $\mu\tau_{\text{had}}$ (b) regions in the $(50, 70)$ GeV p_{T} bin. The red, green and blue distributions represent respectively the quark-jet template, the low-JVT gluon-jet template and the high-JVT gluon-jet template. The points represent the data in the anti-ID signal region and the black line is the distribution obtained from the combination of the template distributions with the best-fit values of the corresponding coefficients.

An uncertainty is associated with the combined fake factors, given by the sum in quadrature of three different components: the first component represents the statistical uncertainty on the tau width templates, propagated into the combined fake factor computation; the second component accounts for the statistical uncertainty

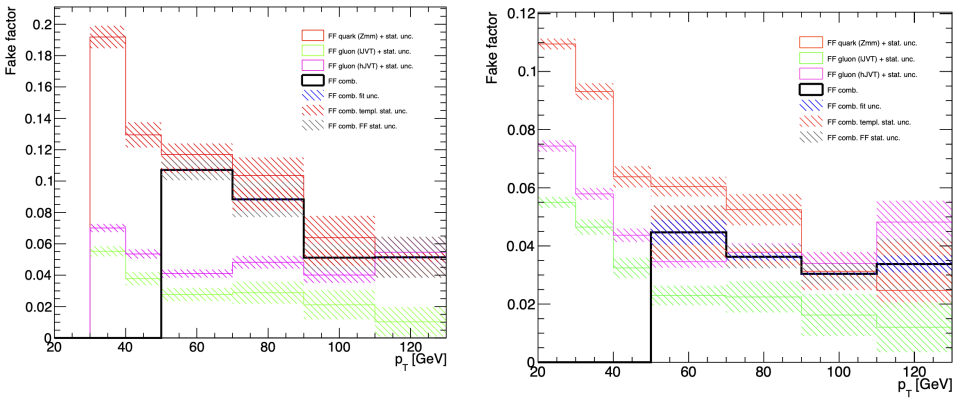

(a) **(b)**

Figure 4.16. Examples of fake factors for the $\tau_{\text{had}}\tau_{\text{had}}$ region for the case in which the tau candidate fires a trigger (a) and the case in which no trigger is fired by the tau (b). The red, green and purple lines represent respectively the quark-jet, the low-JVT gluon-jet and the high-JVT gluon-jet fake factors provided by the FTTF. The black line represents the combined fake factor. The combined fake factor in the first p_{T} bins is zero because the analysis selections do not accept τ_{had} candidates in that p_{T} region.

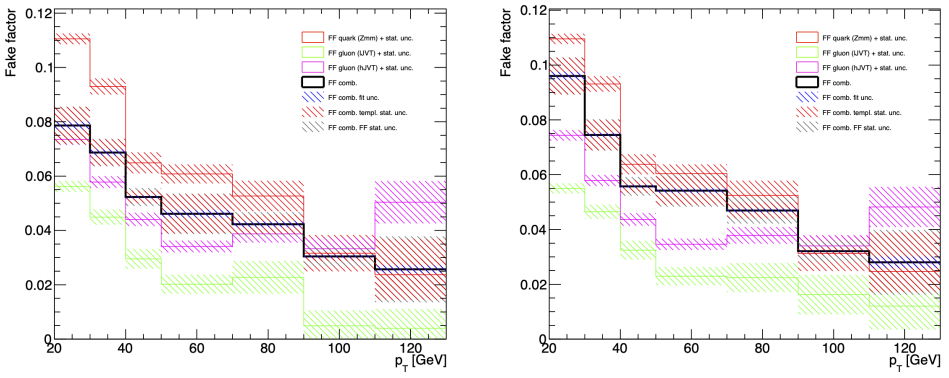

(a) **(b)**

Figure 4.17. Examples of fake factors for the $e\tau_{\text{had}}$ (a) and $\mu\tau_{\text{had}}$ (b) regions. The red, green and purple lines represent respectively the quark-jet, the low-JVT gluon-jet and the high-JVT gluon-jet fake factors provided by the FTTF. The black line represents the combined fake factor.

of the primitive fake factors; the third component considers the uncertainty on the coefficients of the linear combination obtained from the tau width fit.

4.5.4 Fake-tau background extrapolation

The combined fake factors are used to extrapolate the fakes' background from the anti-ID signal regions to the corresponding ID signal regions. The procedure

to extrapolate the fakes' background in the $\tau_{\text{had}}\tau_{\text{had}}$ region is slightly different than that used in the $e\tau_{\text{had}}$ and $\mu\tau_{\text{had}}$ regions. The difference is due to the fact that in the $e\tau_{\text{had}}$ and $\mu\tau_{\text{had}}$ regions the fakes' background contains only events with one fake tau, while in the $\tau_{\text{had}}\tau_{\text{had}}$ region the fakes' background can contain events with one or two fake taus and therefore a specific procedure is needed to avoid double counting. In the ee, $\mu\mu$ and $e\mu$ regions, instead, the fakes' background has no contribution and therefore no extrapolation is needed.

In the $\tau_{\text{had}}\tau_{\text{had}}$ region the fakes' background can be obtained from the sum of three components:

$$N_{fakes} = N(\tau_{fake}, \tau_{true}) + N(\tau_{true}, \tau_{fake}) + N(\tau_{fake}, \tau_{fake}), \tag{4.7}$$

where the first term considers the events in which the leading tau is fake and the subleading is true, the second term the events in which the leading tau is true and the subleading is fake and the last term the events in which both taus are fake. However, in data there is no way to know if a tau is true or fake and therefore the previous categorisation cannot be applied. A classification based on the tau RNN quality score is used instead. Three categories of events are defined, labelled B, C and D, depending on which of the two hadronic taus of the $\tau_{\text{had}}\tau_{\text{had}}$ event fails the identification criteria of the analysis (anti-ID tau):

- category B, in which the leading tau is anti-ID and the subleading tau is ID;
- category C, in which the leading tau is ID and the subleading tau is anti-ID;
- category D, in which both taus are anti-ID.

It can be shown that the fakes' background contribution in the signal region (category A) can be obtained through the following combinatorial formula:

$$\begin{aligned} N_{fakes} = & [\underbrace{N(\tau_{\text{anti-ID}}, \tau_{\text{ID}})}_{\text{Cat. B}} - \underbrace{N(\tau^t_{\text{anti-ID}}, \tau^t_{\text{ID}})}_{\text{Cat. B (MC)}}] \cdot \text{FF}_1 \\ & + [\underbrace{N(\tau_{\text{ID}}, \tau_{\text{anti-ID}})}_{\text{Cat. C}} - \underbrace{N(\tau^t_{\text{ID}}, \tau^t_{\text{anti-ID}})}_{\text{Cat. C (MC)}}] \cdot \text{FF}_2 \\ & - [\underbrace{N(\tau_{\text{anti-ID}}, \tau_{\text{anti-ID}})}_{\text{Cat. D}} - \underbrace{N(\tau^t_{\text{anti-ID}}, \tau^t_{\text{anti-ID}})}_{\text{Cat. D (MC)}}] \cdot (\text{FF}_1 \cdot \text{FF}_2), \end{aligned} \tag{4.8}$$

where $N(\tau_{\text{anti-ID}}, \tau_{\text{ID}})$, $N(\tau_{\text{ID}}, \tau_{\text{anti-ID}})$, $N(\tau_{\text{anti-ID}}, \tau_{\text{anti-ID}})$ are the number of events measured in data in the B, C and D categories respectively, while $N(\tau^t_{\text{anti-ID}}, \tau^t_{\text{ID}})$ $N(\tau^t_{\text{ID}}, \tau^t_{\text{anti-ID}})$, $N(\tau^t_{\text{anti-ID}}, \tau^t_{\text{anti-ID}})$ are the number of events in the B, C and D categories measured in MC simulation with the additional requirement for taus to be matched with particle-level leptons (either taus, electrons or muons). FF_1 and FF_2 in Equation 4.8 are the fake factors associated with the leading and the subleading τ_{had} of the event respectively (extracted from the appropriate p_{T}, η and decay-mode bin). The subtraction of the events from the MC simulation ensures that only the component of fake taus originating from jets is used in the extrapolation.

In the $e\tau_{\text{had}}$ and $\mu\tau_{\text{had}}$ regions, the extrapolation is more immediate, since there is only one hadronic tau. The number of fakes' background events in the signal region in this case can be computed as

$$N_{fakes} = [\underbrace{N(\tau_{\text{anti-ID}}, \ell)}_{\text{from Data}} - \underbrace{N(\tau^{t}_{\text{anti-ID}}, \ell^{t})}_{\text{from MC}}] \cdot \text{FF}, \tag{4.9}$$

where $N(\tau_{\text{anti-ID}}, \ell)$ is the number of events with an anti-ID τ_{had} measured in data, FF is the fake factor related to the anti-ID τ_{had} and $N(\tau_{\text{anti-ID}},^{t} \ell^{t})$ is the number of events with an anti-ID τ_{had} measured in the MC simulation with the requirement that the hadronic tau and the light lepton are matched to particle-level leptons.

4.5.5 Uncertainty on the fakes' background estimate

The sources contributing to the uncertainty on the fakes' background estimate can be grouped into two main categories, which will be referred to as *systematic* and *statistical* uncertainties. In the systematic uncertainty contribution, all the uncertainties related to the fake factors (and mentioned in Section 4.5.3) are considered. These uncertainties comprise the following contributions:

- the uncertainty related to the statistics of the tau width templates provided by the FTTF,
- the uncertainty related to the statistics of the primitive fake factors,
- the uncertainty on the tau width fit parameters.

These three components are summed in quadrature to obtain the systematic uncertainty associated with the combined fake factors, which is then propagated to obtain the systematic uncertainty on the fakes' estimate.

Another important source of uncertainty for the fakes' estimate, which is independent of the ones mentioned above, is represented by the statistical uncertainty on the number of events in the anti-ID signal region, which are used in Equations 4.8 and 4.9 to extrapolate the fakes' background. The statistical uncertainty on data and MC events appearing in those equations is propagated to obtain the statistical uncertainty on the estimated number of events of the fakes' background in the signal region. Figure 4.18 shows the absolute (upper pad) and relative (lower pad) uncertainty bands on the extrapolated fakes' estimate for the opposite-sign (OS) regions. Analogous plots for the same-sign (SS) regions can be found in Appendix C. It can be noticed that in the $e\tau_{\text{had}}$ and $\mu\tau_{\text{had}}$ regions the main contribution to the fakes' uncertainty is the systematic one, while in the $\tau_{\text{had}}\tau_{\text{had}}$ region statistical and systematic uncertainties are comparable.

A further source of uncertainty for the fakes' estimate may come from the modelling uncertainties of the MC predictions in the anti-ID regions used for the MC subtraction in Equations 4.8 and 4.9 (especially for the $Z \to \ell\ell$ and $t\bar{t}$ samples). The MC contribution to be subtracted is small compared to the data, as shown in

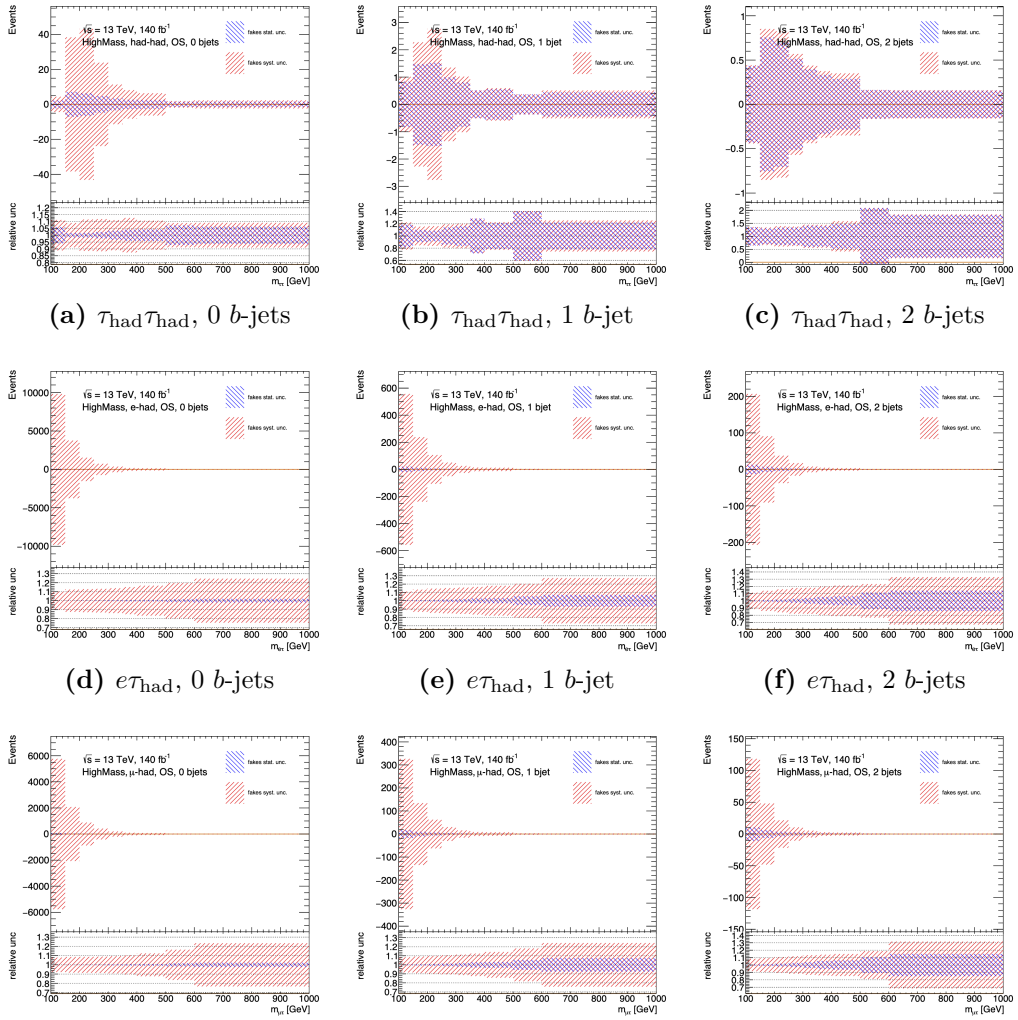

(a) $\tau_{\text{had}}\tau_{\text{had}}$, 0 b-jets **(b)** $\tau_{\text{had}}\tau_{\text{had}}$, 1 b-jet **(c)** $\tau_{\text{had}}\tau_{\text{had}}$, 2 b-jets

(d) $e\tau_{\text{had}}$, 0 b-jets **(e)** $e\tau_{\text{had}}$, 1 b-jet **(f)** $e\tau_{\text{had}}$, 2 b-jets

(g) $\mu\tau_{\text{had}}$, 0 b-jets **(h)** $\mu\tau_{\text{had}}$, 1 b-jet **(i)** $\mu\tau_{\text{had}}$, 2 b-jets

Figure 4.18. Absolute (upper pad) and relative (lower pad) uncertainties on the extrapolated fakes estimate in the opposite-sign regions. (a)-(c) show the $\tau_{\text{had}}\tau_{\text{had}}$ region, (d)-(f) show the $e\tau_{\text{had}}$ region, (g)-(i) show the $\mu\tau_{\text{had}}$ region, all of them divided per b-jet multiplicity.

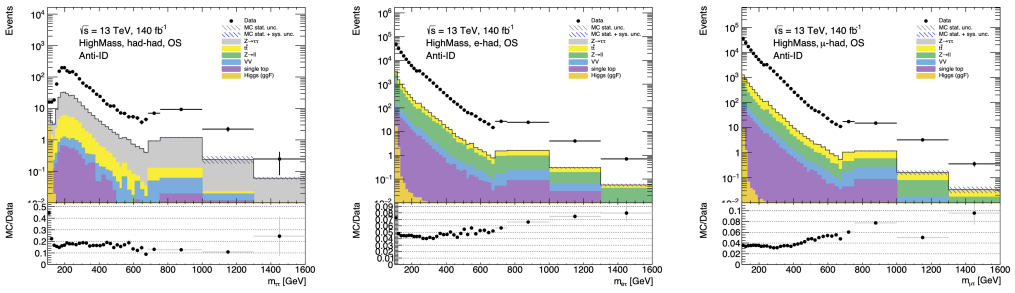

(a) $\tau_{\text{had}}\tau_{\text{had}}$ **(b)** $e\tau_{\text{had}}$ **(c)** $\mu\tau_{\text{had}}$

Figure 4.19. The upper pad shows data and MC distributions of $m_{\ell\ell}^{\text{vis}}$ in the opposite-sign anti-ID region for the $\tau_{\text{had}}\tau_{\text{had}}$ (a), the $e\tau_{\text{had}}$ (b) and the $\mu\tau_{\text{had}}$ (c) regions. The lower pad shows the ratio between MC predictions and data.

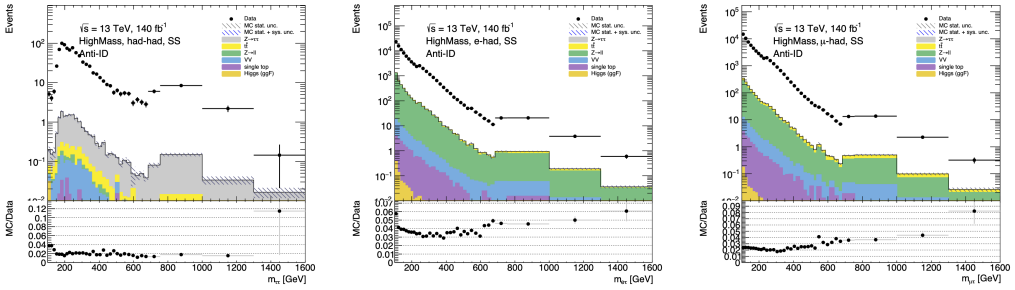

(a) $\tau_{\text{had}}\tau_{\text{had}}$ **(b)** $e\tau_{\text{had}}$ **(c)** $\mu\tau_{\text{had}}$

Figure 4.20. The upper pad shows data and MC distributions of $m_{\ell\ell}^{\text{vis}}$ in the same-sign anti-ID region for the $\tau_{\text{had}}\tau_{\text{had}}$ (a), the $e\tau_{\text{had}}$ (b) and the $\mu\tau_{\text{had}}$ (c) regions. The lower pad shows the ratio between MC predictions and data.

Figures 4.19 and 4.20. Therefore, assuming an uncertainty on the MC predictions in the anti-ID regions similar to the corresponding ones in the tau ID regions, the overall effect on the total fakes' estimate uncertainty is negligible.

4.5.6 Validation of the fakes' background estimate

The reliability of the fakes' background estimate obtained with the Fake Factor method is checked in the same-sign (SS) validation regions, where the two final state leptons are required to satisfy the same requirements as for the analysis signal regions, but to have the same charge. Since the signal process is characterised by the presence of two opposite-sign leptons, the same-sign regions are expected to be enriched in fake-taus.

Figure 4.21 shows the comparison between data and SM prediction of the invariant mass distribution for the same-sign $\tau_{\text{had}}\tau_{\text{had}}$ region. The fakes' contribution to the SM prediction is derived as described in the previous sections. An acceptable closure between the data points and the data-driven background from fakes

(complemented with the other MC-derived background components) can be seen. Some localised discrepancy in events with b-jets can be noticed, but the addition of a non-closure uncertainty is considered not necessary since in the signal regions with 1 or more b-jets the background from fakes has a small contribution.

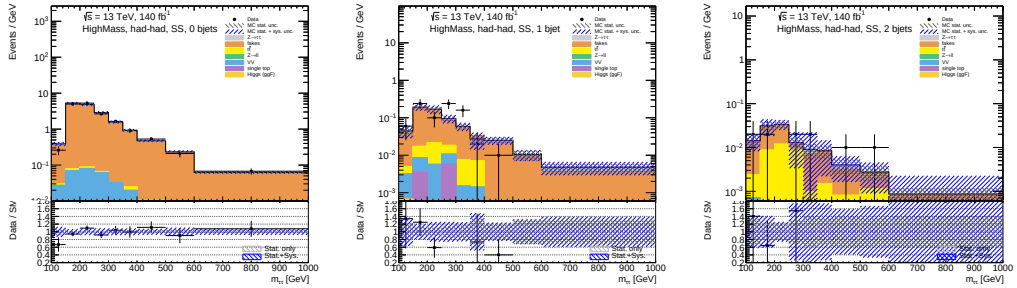

(a) $\tau_{\text{had}}\tau_{\text{had}}$, 0 b-jets **(b)** $\tau_{\text{had}}\tau_{\text{had}}$, 1 b-jet **(c)** $\tau_{\text{had}}\tau_{\text{had}}$, 2 b-jets

Figure 4.21. Validation kinematic plots in the same-sign $\tau_{\text{had}}\tau_{\text{had}}$ region for the visible invariant mass distribution for events with 0 b-jets (a), 1 b-jet (b) and 2 b-jets (c).

The invariant mass distributions in the same-sign $e\tau_{\text{had}}$ and $\mu\tau_{\text{had}}$ regions are reported in Figures 4.22 and 4.23, respectively. Some discrepancy is observed in the $e\tau_{\text{had}}$ region, which seems to lead to a systematic over-estimate of the fakes' background, which is anyway within the uncertainty band. For the $\mu\tau_{\text{had}}$ channel, instead, the fakes' background prediction shows good agreement with the data points.

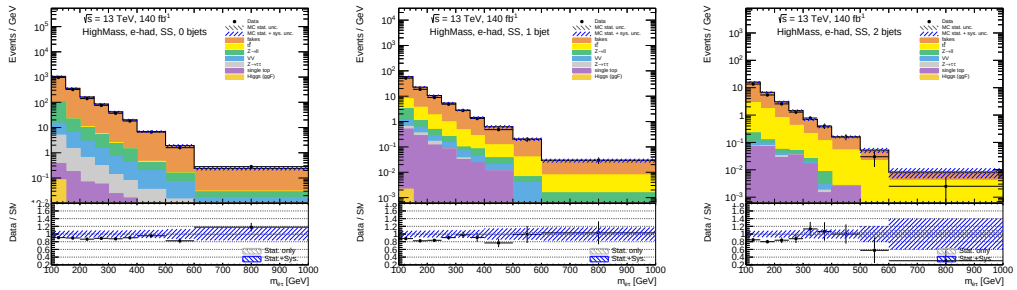

(a) $e\tau_{\text{had}}$, 0 b-jets **(b)** $e\tau_{\text{had}}$, 1 b-jet **(c)** $e\tau_{\text{had}}$, 2 b-jets

Figure 4.22. Validation kinematic plots in the same-sign $e\tau_{\text{had}}$ region for the visible invariant mass distribution for events with 0 b-jets (a), 1 b-jet (b) and 2 b-jets (c).

In all the same-sign regions, a reasonable closure is achieved between the data and the background predictions, including the fakes' estimate, and therefore this technique can be assumed to be reliable for the derivation of the background from fake taus in the analysis signal regions.

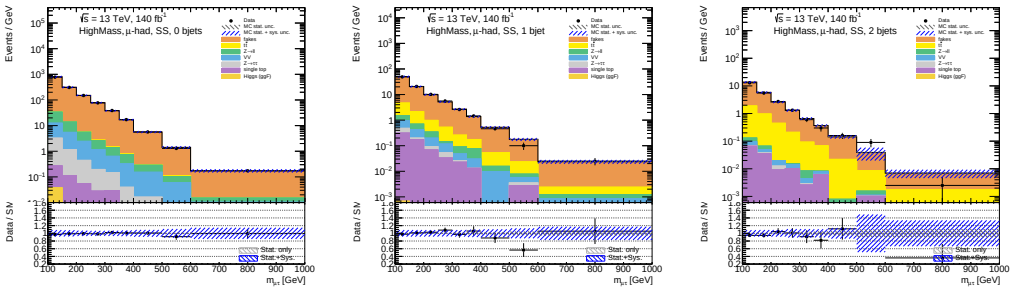

(a) $\mu\tau_{\text{had}}$, 0 b-jets **(b)** $\mu\tau_{\text{had}}$, 1 b-jet **(c)** $\mu\tau_{\text{had}}$, 2 b-jets

Figure 4.23. Validation kinematic plots in the same-sign $\mu\tau_{\text{had}}$ region for the visible invariant mass distribution for events with 0 b-jets (a), 1 b-jet (b) and 2 b-jets (c).

4.5.7 Validation of the MC-derived background

The contribution from the background processes involving two true leptons is derived from the MC simulation. The reliability of the MC prediction for the $t\bar{t}$, di-boson (VV), $Z \to \ell\ell$ and single-top processes is checked by comparing the distributions of some kinematic variables of interest obtained from data and MC simulation in the light-lepton regions (ee, $\mu\mu$ and $e\mu$). In these regions, indeed, these are the dominant processes, while the background from jets misidentified as tau-leptons is absent. Moreover, the signal is completely negligible if compared to the huge background contributions. Figure 4.24 reports the $m_{\ell\ell}$ distribution divided per b-jet multiplicity obtained from data and MC simulation for the ee, $\mu\mu$ and $e\mu$ regions. The distributions of additional kinematic variables can be found in Appendix B. In all distributions, the MC predictions are in agreement with the data points within the uncertainty band.

4.6 Uncertainties

Several sources of uncertainty are considered in this analysis, in addition to the statistical uncertainty related to the event counting in data and the statistics of MC simulations. The different systematic uncertainty contributions can be classified into *modelling* uncertainties, which derive from variations of the theoretical predictions of the SM processes, *experimental* uncertainties, which arise from imperfect knowledge of the ATLAS detector, the LHC beam conditions or the reconstruction and identification of final-state objects, *fakes'* uncertainties, which come from the data-driven technique used to estimate the fake-tau background. The fakes' uncertainties, which include also a statistical component from the event counting in the anti-ID regions, have been already discussed in Section 4.5.5. A description of the various modelling and experimental uncertainty sources and their impact on the analysis measurements is given below.

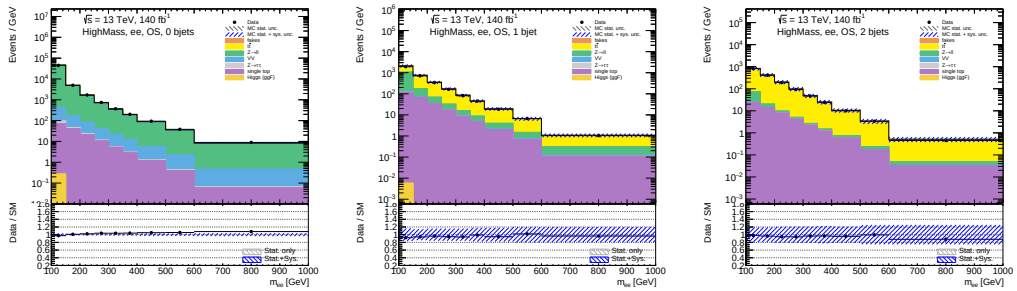

(a) ee region, 0 b-jets **(b)** ee region, 1 b-jets **(c)** ee region, 2 b-jets

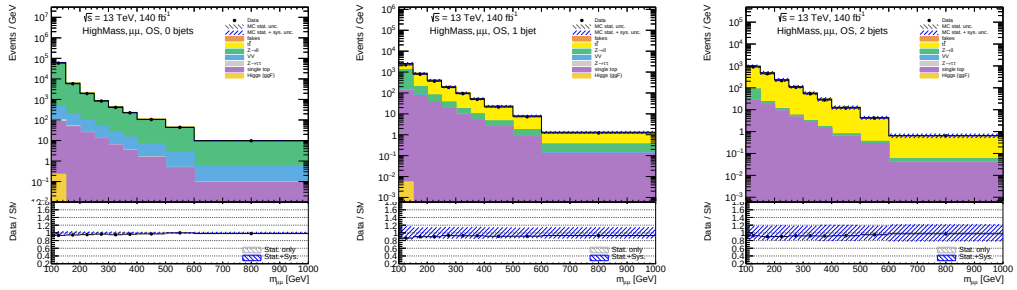

(d) $\mu\mu$ region, 0 b-jets **(e)** $\mu\mu$ region, 1 b-jets **(f)** $\mu\mu$ region, 2 b-jets

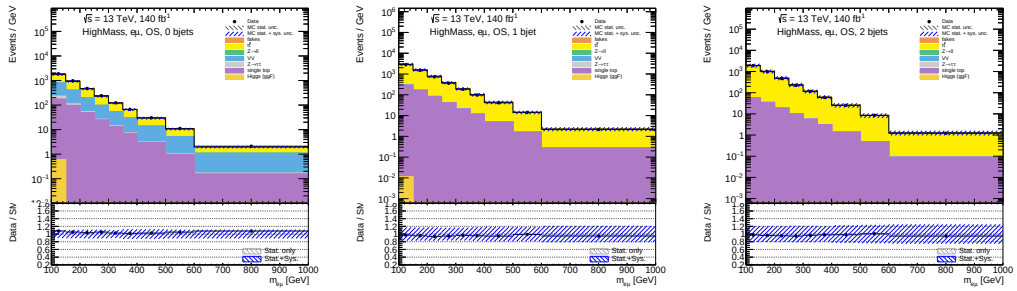

(g) $e\mu$ region, 0 b-jets **(h)** $e\mu$ region, 1 b-jets **(i)** $e\mu$ region, 2 b-jets

Figure 4.24. Invariant mass distributions divided per b-jet multiplicity for the ee, $\mu\mu$ and $e\mu$ regions.

4.6.1 Modelling uncertainties

The uncertainty on the theoretical predictions of the most relevant SM processes is derived by variating the MC generator configurations used to generate the predictions of those processes. The SM processes with the highest relevance in this analysis are the Drell-Yan, the $t\bar{t}$ and the single-top. The modelling uncertainties associated with these processes are obtained from the symmetrised difference between the distributions produced with the nominal and the variated MC generator. The list of the modelling systematic variations considered in this analysis is given below:

- $t\bar{t}$ matching/merging scheme: the uncertainty on the $t\bar{t}$ MC matching and merging schemes is obtained by comparing a sample simulated using Powheg Box + Pythia 8 with $p_{\mathrm{T}}(hard) = 1$ with the nominal sample generated using Powheg Box + Pythia 8;
- $t\bar{t}$ parton-shower model: the uncertainty on $t\bar{t}$ parton-shower MC models is obtained by comparing a sample simulated using Powheg Box + Herwig 7 with the nominal sample generated using Powheg Box + Pythia 8;
- $t\bar{t}$ scale variations: the uncertainty on the NLO $t\bar{t}$ MC scale choices is obtained by comparing a sample with $h_{\mathrm{damp}} = 3 \cdot m_t = 517.5\,\mathrm{GeV}$ and the nominal sample with $h_{\mathrm{damp}} = 1.5 \cdot m_t = 258.75\,\mathrm{GeV}$;
- single-top interference scheme: the uncertainty to take into account the differences between the diagram removal (DR) and diagram subtraction (DS) approaches in the single-top Wt production is obtained by comparing a sample with the DS scheme with the nominal sample, which uses the DR scheme;
- single-top parton-shower model: the uncertainty on the single top parton-shower MC models for the s-channel and t-channel productions is obtained by comparing a sample simulated using Powheg Box + Herwig 7 with the nominal sample generated using Powheg Box + Pythia 8;
- Drell-Yan production modelling: the uncertainty on the Matrix Element and Parton Shower for the Drell-Yan di-lepton processes is obtained by comparing a sample produced with Powheg Box + Pythia 8 with the nominal sample produced with Sherpa 2.2.11.

More information on the MC generator parameters employed to produce the nominal and the variated samples can be found in Section 4.3. The impact of the modelling uncertainties on the visible invariant mass distribution for the $Z \to \tau\tau$, $Z \to \ell\ell$, $t\bar{t}$ and single-top processes is reported in Figures 4.25, 4.26, 4.27 and 4.28, respectively.

4.6.2 Experimental uncertainties

In order to take into account the imperfect knowledge of the ATLAS detector and of the object reconstruction and identification methods, a set of experimental

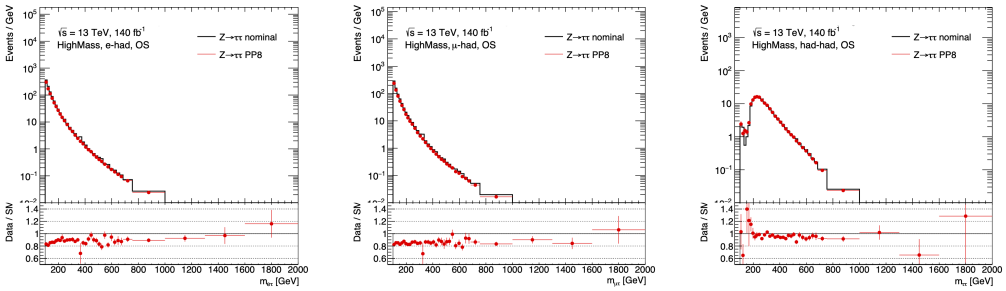

(a) **(b)** **(c)**

Figure 4.25. Impact of the modelling systematics of the $Z \to \tau\tau$ process on the visible invariant mass distribution for the $e\tau_{\text{had}}$ (a), $\mu\tau_{\text{had}}$ (b) and $\tau_{\text{had}}\tau_{\text{had}}$ (c) regions.

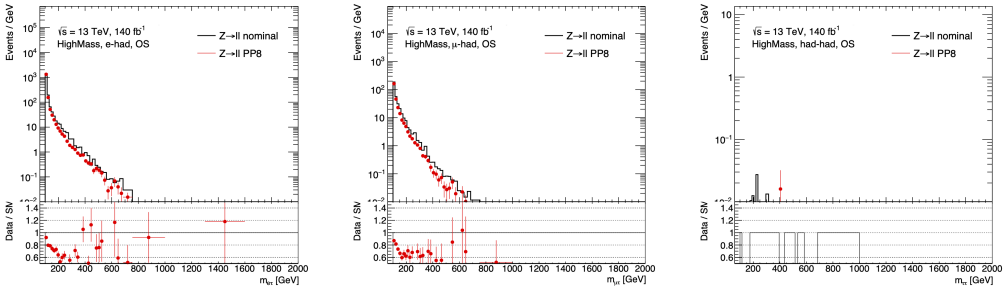

(a) **(b)** **(c)**

Figure 4.26. Impact of the modelling systematics of the $Z \to \ell\ell$ process (with $\ell = e, \mu$) on the visible invariant mass distribution for the $e\tau_{\text{had}}$ (a), $\mu\tau_{\text{had}}$ (b) and $\tau_{\text{had}}\tau_{\text{had}}$ (c) regions.

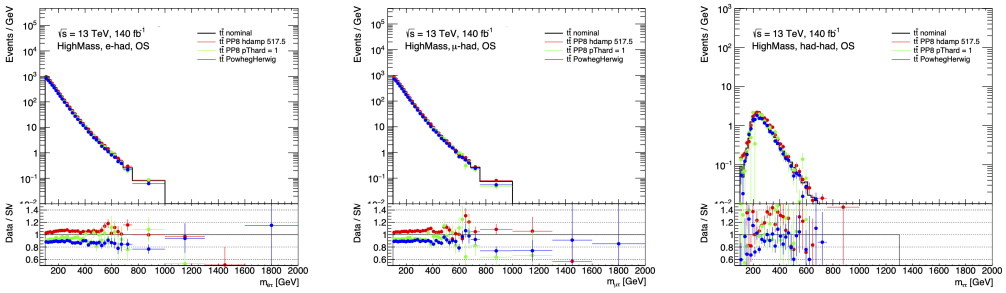

(a) **(b)** **(c)**

Figure 4.27. Impact of the modelling systematics of the $t\bar{t}$ process on the visible invariant mass distribution for the $e\tau_{\text{had}}$ (a), $\mu\tau_{\text{had}}$ (b) and $\tau_{\text{had}}\tau_{\text{had}}$ (c) regions.

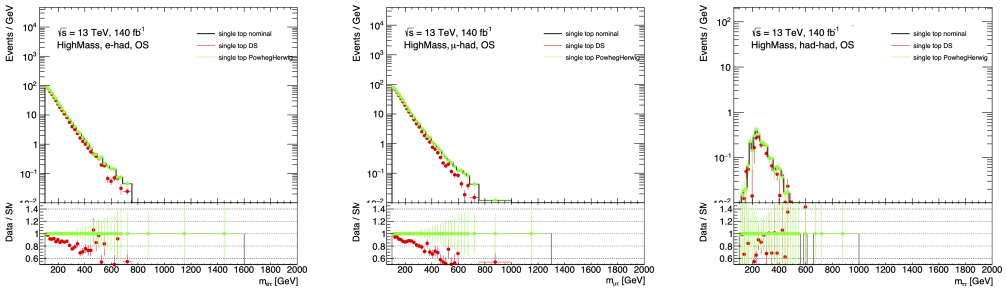

(a) (b) (c)

Figure 4.28. Impact of the modelling systematics of the single-top process on the visible invariant mass distribution for the $e\tau_{\text{had}}$ (a), $\mu\tau_{\text{had}}$ (b) and $\tau_{\text{had}}\tau_{\text{had}}$ (c) regions.

systematic uncertainties is considered in this analysis. For each of the physics objects used to define the analysis regions, specific uncertainties are included. These experimental uncertainties can be assessed by applying some variations during the selection, identification and reconstruction process of the analysis objects and evaluating the difference between the nominal and the variated distributions of the variables of interest. The variations applied to assess the experimental uncertainties can be broadly divided into resolution variations, which affect the kinematics of the physics objects, and scale variations, which alter the weight associated with each event.

The following experimental uncertainties, which are provided by the various ATLAS Combined Performance (CP) groups, are taken into account:

- luminosity: the uncertainty in the luminosity affecting the background predictions and total extracted cross-sections;
- hadronically decaying tau-leptons: uncertainties on the TES and τ_{had} identification efficiency corrections;
- electron reconstruction and identification: uncertainties on the electron momentum and identification efficiency corrections;
- muon reconstruction and identification: uncertainties on the muon momentum and identification efficiency corrections;
- jet reconstruction: uncertainties on the jet energy scale, resolution, and JVT efficiency corrections;
- b-jet identification: uncertainties on the b-, c-, and light-jet tagging rate corrections;
- trigger: uncertainty on the trigger efficiency corrections.

The luminosity uncertainty, obtained using the LUCID-2 detector [125], is 1.7% and equally affects all regions. The impact of the most important experimental

systematic uncertainties on the $m_{\ell\ell}$ distribution in the signal regions is reported in Appendix C.

Experimental uncertainty pruning

A total of about 260 recommended experimental systematic uncertainties are provided by the CP groups for the objects considered in this analysis. Anyway, most of them do not have a significant impact on the measurement performed by the analysis and can be safely neglected. A pruning procedure is therefore carried out to evaluate which uncertainties play a relevant role and which instead can be ignored. The selection of the systematic uncertainties to be neglected is based on the di-lepton invariant mass variable in the $\tau_{\text{had}}\tau_{\text{had}}$ and $e\mu$ regions divided per b-jet multiplicity. In this way, the effects of the uncertainties affecting the relevant objects of the signal regions (hadronic taus, electrons, muons and b-jets) are considered. The impact of each uncertainty is evaluated by variating the nominal MC distribution of $m_{\ell\ell}$ at $\pm 1\sigma$ (considering a Gaussian distribution of the parameter affected by the variation) according to the prescriptions given by the CP groups.

The pruning criterium proceeds as follows. For each experimental systematic uncertainty, the relative variation[7] at $\pm 1\sigma$ with respect to the nominal value is computed in each bin of the $m_{\ell\ell}$ distribution. To each bin, the relative statistical uncertainty on the expected number of events (given by the Poissonian approximation $1/\sqrt{N}$, with N the number of MC events in the bin) is associated. The experimental uncertainty is then neglected if its relative variation is smaller than 10% of the relative statistical uncertainty in every bin. In order to avoid large fluctuations between adjacent bins due to low statistics, a Gaussian filter with $\sigma = 2$ is applied to the histograms of both the statistical and the experimental uncertainties.

Among the 260 experimental uncertainties considered by this study, only 69 appear to have a non-negligible impact and are therefore included in the fit described in Section 4.8. The complete list of the experimental systematic uncertainties which are not discarded by the pruning procedure is reported in Appendix C, grouped according to the reconstructed objects they are related to. The pruning impact on each experimental uncertainty group is lower than 1% in each bin of the $m_{\ell\ell}$ distribution divided per b-jet multiplicity in all the signal regions.

4.6.3 Uncertainty impact

Figures 4.29, 4.30 and 4.31 show the impact of the different uncertainties on the $m_{\ell\ell}$ distribution for the $\tau_{\text{had}}\tau_{\text{had}}$, $e\tau_{\text{had}}$ and $\mu\tau_{\text{had}}$ signal regions, respectively. The relative total uncertainty is reported together with the contribution from the statistical, the modelling, the experimental and the fakes' uncertainties. The experimental uncertainties are divided according to the reconstructed objects they are

[7] The relative variation in a $m_{\ell\ell}$ bin is the difference between the variated and the nominal bin content divided by the nominal one.

related to: TAUS uncertainties are related to hadronically decaying tau-leptons, MUON uncertainties to muons, EGAMMA uncertainties to electrons and photons, JET uncertainties to hadronic-jets, FTAG uncertainties to b-tagged and c-tagged jets. Each relative experimental uncertainty is evaluated as half the difference between the $+1\sigma$ and -1σ variations of the $m_{\ell\ell}$ distribution normalised to the nominal distribution.

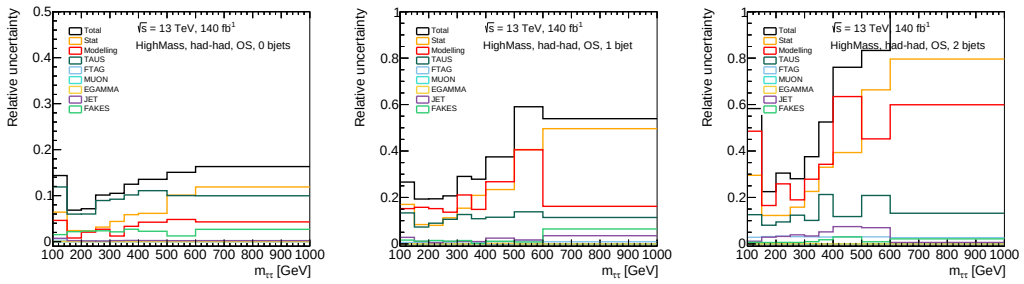

(a) **(b)** **(c)**

Figure 4.29. Relative uncertainties on the SM prediction of the $m_{\ell\ell}$ distribution in the $\tau_{\text{had}}\tau_{\text{had}}$ region with 0 b-jets (a), 1 b-jet (b) and 2 b-jets The experimental uncertainties are divided according to the objects they are related to.

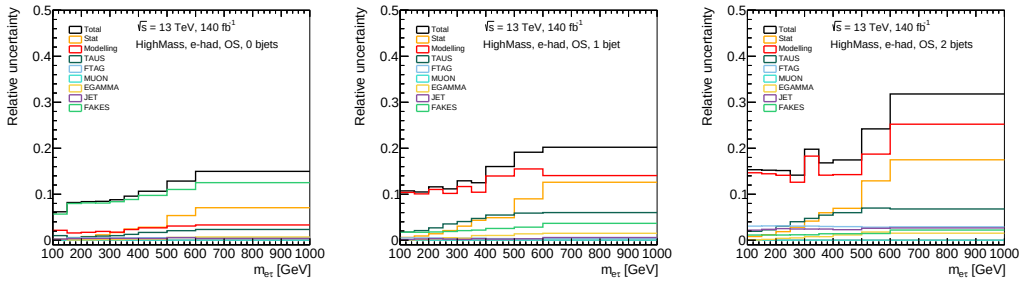

(a) **(b)** **(c)**

Figure 4.30. Relative uncertainties on the SM prediction of the $m_{\ell\ell}$ distribution in the $e\tau_{\text{had}}$ region with 0 b-jets (a), 1 b-jet (b) and 2 b-jets The experimental uncertainties are divided according to the objects they are related to.

The impact of the different uncertainty sources on the $m_{\ell\ell}$ distribution is largely dependent on the lepton flavour and the b-jet multiplicity. In. the $\tau_{\text{had}}\tau_{\text{had}}$ region with 0 b-jets, the main contribution to the total uncertainty comes from the tau-related experimental uncertainties (which are dominated by the Tau Energy Scale systematics), while in the $e\tau_{\text{had}}$ and $\mu\tau_{\text{had}}$ regions with 0 b-jets the most relevant uncertainty source is the systematic uncertainty on the fakes' background estimate. In the 1 and 2 b-jet regions, instead, the most important contributions come from the modelling and the statistical uncertainties

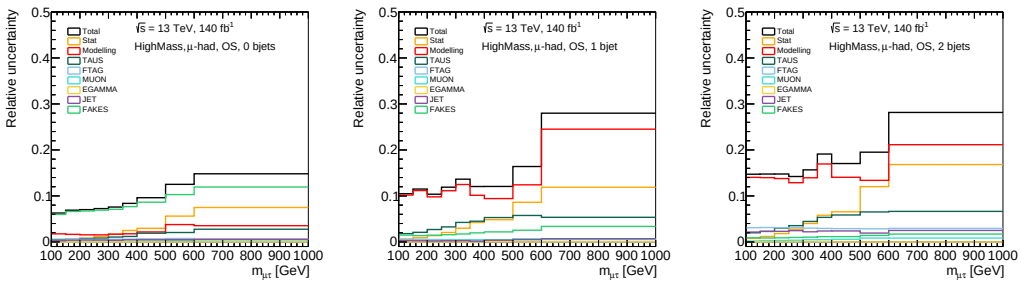

(a) **(b)** **(c)**

Figure 4.31. Relative uncertainties on the SM prediction of the $m_{\ell\ell}$ distribution in the $\mu\tau_{\text{had}}$ region with 0 b-jets (a), 1 b-jet (b) and 2 b-jets The experimental uncertainties are divided according to the objects they are related to.

4.7 Event yields in signal regions

Tables 4.4, 4.5 and 4.6 report the expected event yields in the signal regions for the SM processes considered by the analysis, together with the observed event yield from the Run 2 dataset collected by ATLAS.

Table 4.4. Event yields in the $\tau_{\text{had}}\tau_{\text{had}}$ region divided per b-jet multiplicity from the MC predictions of the SM processes and from the observed Run 2 data.

Process	0 b-jets	1 b-jet	2 b-jets
$Z \to \ell\ell$	1.93 ± 0.07	0.15 ± 0.02	0.00 ± 0.00
$Z \to \tau\tau$	4462.02 ± 363.43	97.11 ± 10.62	7.61 ± 1.12
Fakes	1326.39 ± 135.36	56.42 ± 6.77	9.91 ± 1.70
$H \to \tau\tau$	46.67 ± 1.18	3.53 ± 0.11	0.45 ± 0.02
Multi-boson	109.13 ± 8.77	3.95 ± 0.38	0.14 ± 0.04
Single-top	26.59 ± 2.45	40.96 ± 3.92	7.49 ± 0.89
$t\bar{t}$	118.87 ± 11.67	293.24 ± 27.18	195.82 ± 19.81
Total	6083.04 ± 408.74	489.71 ± 42.20	227.37 ± 23.32
Data	5759	427	193

Figures 4.32, 4.33 and 4.33 show the comparison between data and SM prediction distributions for the visible invariant mass in the signal regions ($\tau_{\text{had}}\tau_{\text{had}}$, $e\tau_{\text{had}}$ and $\mu\tau_{\text{had}}$ respectively, divided per b-jet multiplicity). The BSM+SM distributions

Table 4.5. Event yields in the $e\tau_{\text{had}}$ region divided per b-jet multiplicity from the MC predictions of the SM processes and from the observed Run 2 data.

Process	0 b-jets	1 b-jet	2 b-jets
$Z \to \ell\ell$	27203.72 ± 1386.95	603.80 ± 48.72	27.84 ± 2.24
$Z \to \tau\tau$	15211.82 ± 473.83	267.00 ± 19.91	10.40 ± 2.03
Fakes	149826.61 ± 14023.48	8244.85 ± 866.63	2888.35 ± 313.59
$H \to \tau\tau$	473.83 ± 4.00	10.32 ± 0.09	0.57 ± 0.00
Multi-boson	8253.17 ± 204.73	179.02 ± 7.61	8.22 ± 0.74
Single-top	2420.04 ± 83.92	3903.08 ± 103.28	708.99 ± 34.82
$t\bar{t}$	12708.01 ± 538.67	34608.28 ± 839.06	24304.35 ± 833.91
Total	216070.43 ± 14144.58	47786.80 ± 1274.10	27946.10 ± 923.64
Data	210699	44498	25868

Table 4.6. Event yields in the $\mu\tau_{\text{had}}$ region divided per b-jet multiplicity from the MC predictions of the SM processes and from the observed Run 2 data.

Process	0 b-jets	1 b-jet	2 b-jets
$Z \to \ell\ell$	6257.77 ± 36.53	135.38 ± 5.88	8.24 ± 0.76
$Z \to \tau\tau$	14175.43 ± 453.06	261.08 ± 16.14	18.38 ± 1.14
Fakes	143018.61 ± 11879.06	8007.02 ± 738.93	2798.63 ± 261.65
$H \to \tau\tau$	461.33 ± 3.84	9.64 ± 0.08	0.65 ± 0.01
Multi-boson	8875.14 ± 226.83	182.76 ± 9.44	7.30 ± 0.57
Single-top	2546.29 ± 89.82	4087.84 ± 108.30	730.82 ± 36.11
$t\bar{t}$	13465.94 ± 560.57	36709.52 ± 885.30	25778.36 ± 869.59
Total	188771.68 ± 11937.83	49370.13 ± 1231.30	29341.39 ± 942.71
Data	199643	47440	28104

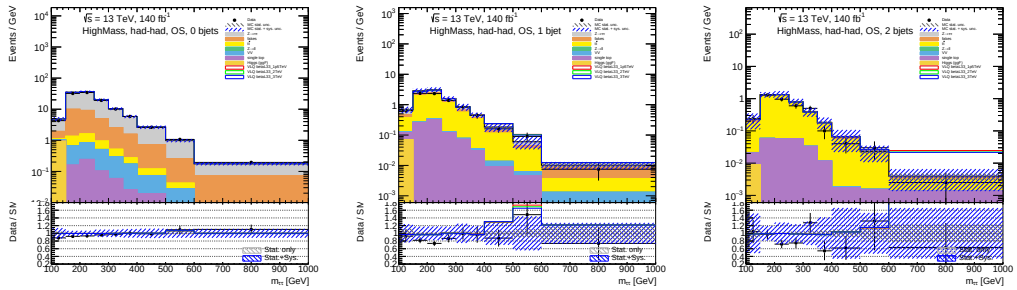

(a) (b) (c)

Figure 4.32. Data and MC distributions in the $\tau_{\text{had}}\tau_{\text{had}}$ signal region for the visible invariant mass for events with 0 b-jets (a), 1 b-jet (b) and 2 b-jets (c).

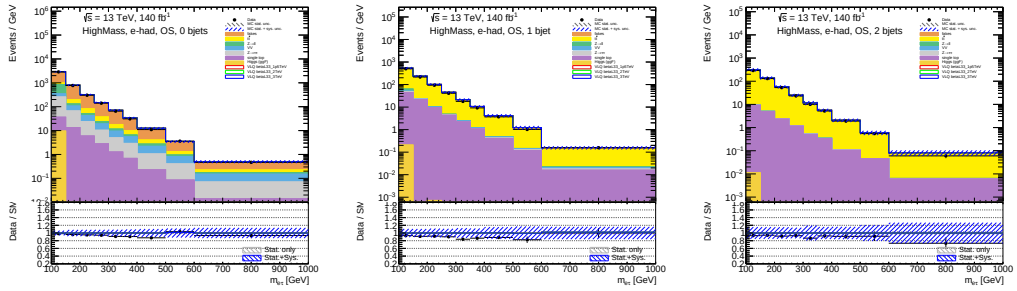

(a) (b) (c)

Figure 4.33. Data and MC distributions in the $e\tau_{\text{had}}$ signal region for the visible invariant mass for events with 0 b-jets (a), 1 b-jet (b) and 2 b-jets (c).

for different leptoquark masses are shown as well[8]. Distributions for further kinematic variables are reported in Appendix D.

4.8 Results and interpretation

The search for leptoquarks with preferential couplings to third-generation fermions is performed through a binned profile-likelihood fit to the detector-level observed data. The visible di-lepton invariant mass is used as the discriminant variable. In order to constrain the SM background predictions and to cover the full range of possible experimental signatures of leptoquark-like new physics, the analysis aims to perform the fit in the multiple signal regions defined by the flavour of the reconstructed leptons and the multiplicity of b-tagged jets.

Hypotheses with leptoquarks of several different masses are tested. The leptoquark coupling parameter $g_U^2 = 2\lambda^2$ to third-generation fermions is the parameter of the fit model. The leptoquark impact on the prediction is taken into account both

[8]The values of the leptoquark coupling used to add the interference and the pure BSM terms to the SM prediction correspond to the best-fit values obtained from the fit described in Section 4.8.

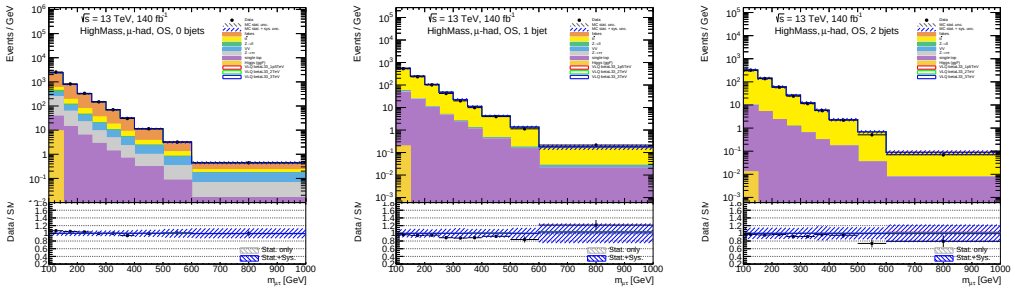

(a) (b) (c)

Figure 4.34. Data and MC distributions in the $\mu\tau_{\text{had}}$ signal region for the visible invariant mass for events with 0 b-jets (a), 1 b-jet (b) and 2 b-jets (c).

through production processes involving only BSM interaction vertices (pure BSM term) and via interference with SM processes (interference term). Systematic uncertainties are included in the fit as nuisance parameters with Gaussian constraint terms in the likelihood function. A linear approximation based on the nominal model and the available $\pm 1\sigma$ systematic variation points is used to smoothly interpolate over the parameter space.

In the absence of a significant deviation from the SM prediction, exclusion limits for leptoquark couplings are determined for each mass hypothesis using a modified CLs technique [126] with the maximum profile-likelihood ratio as the test statistic, using the asymptotic approximation [127]. The *pyhf* framework [128] is employed to find the maximum-likelihood point in the parameter space and to approximate the likelihood function's shape around its optimum. The *cabinetry* toolkit [129] is used to steer the likelihood fit and to produce control plots.

4.8.1 Expected results

Before performing the likelihood fit with the Run 2 data, several studies have been carried out using instead an Asimov dataset constructed from the SM predictions. These studies were focused on the optimisation of the fitting strategy and on the evaluation of the expected sensitivity in the different signal regions. The optimal binning of the $m_{\ell\ell}$ distribution for the fit consists of only three bins given by $[100, 250]$ GeV, $[250, 400]$ GeV and $[400, 1000]$ GeV. The sensitivity to the leptoquark signal has been evaluated according to this binning, comparing the SM expectation with the BSM+SM yields. Figure 4.35 shows, for the three analysis flavour signal regions, the expected yield for the SM-only scenario and for a BSM scenario adopting the simplified U_1 model with $\beta_L^{33} = 1$, $\beta_R^{33} = 0$, $m_{LQ} = 1.5\,\text{TeV}$ and $g_U^2 = 4$. The BSM significance, evaluated as the difference between the BSM yield and the SM yield divided by the square root of the SM yield, is also reported. The $e\tau_{\text{had}}$ and $\mu\tau_{\text{had}}$ regions appear to have almost no sensitivity to the BSM scenario, while the $\tau_{\text{had}}\tau_{\text{had}}$ region has almost a 2σ sensitivity.

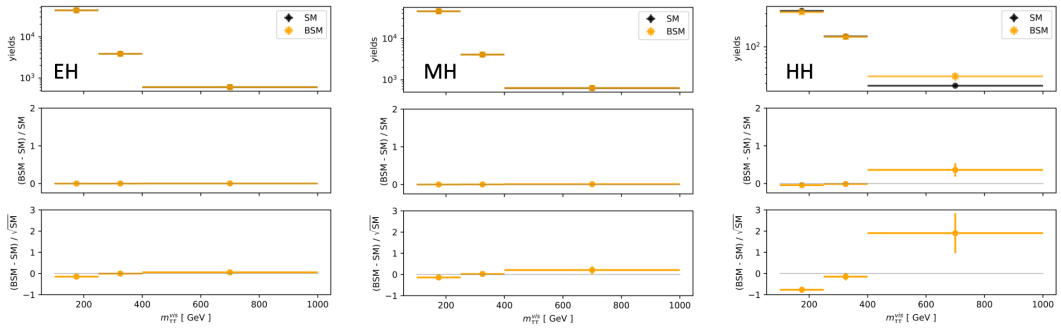

Figure 4.35. The upper pad shows the expected signal yields in the $e\tau_{\text{had}}$ (a), $\mu\tau_{\text{had}}$ (b) and $\tau_{\text{had}}\tau_{\text{had}}$ (c) signal regions for the SM prediction and the BSM+SM prediction, considering the simplified U_1 leptoquark model with $\beta_L^{33} = 1$, $\beta_R^{33} = 0$, $m_{LQ} = 1.5\,\text{TeV}$ and $g_U^2 = 4$. The middle pad shows the signal to background ratios and the lower pad the signal significance.

The very poor sensitivity in the $e\tau_{\text{had}}$ and $\mu\tau_{\text{had}}$ regions is due to the large $t\bar{t}$ background which dominates over the entire invariant mass spectrum, in particular in the 1 b-jet and 2 b-jet regions, where the leptoquark process most contributes to the Drell-Yan cross-section. The expected 95% CL upper limits on the g_U^2 coupling for the $m_{LQ} = 1.5\,\text{TeV}$ model, reported in Table 4.7, reflect this situation. The exclusion limit obtained by fitting independently the $m_{\ell\ell}$ distribution in the $e\tau_{\text{had}}$ and $\mu\tau_{\text{had}}$ regions is much higher than the limit obtained in the $\tau_{\text{had}}\tau_{\text{had}}$ region. Moreover, a combined fit performed in the three signal regions seems to bring no considerable improvement to the $\tau_{\text{had}}\tau_{\text{had}}$-only limit. For this reason, the preliminary results reported in this thesis are obtained considering only the $\tau_{\text{had}}\tau_{\text{had}}$ region. Studies are ongoing to optimise a cut on a variable related to the $E_{\text{T}}^{\text{miss}}$ which should reduce the $t\bar{t}$ background and enhance the signal sensitivity in the $e\tau_{\text{had}}$ and $\mu\tau_{\text{had}}$ regions.

Table 4.7. Expected 95% upper limits on the g_U^2 coupling for the $m_{LQ} = 1.5\,\text{TeV}$ model obtained from independent fits in the $\tau_{\text{had}}\tau_{\text{had}}$, $e\tau_{\text{had}}$ and $\mu\tau_{\text{had}}$ regions and from a combined fit in the three regions. For these fits, only the statistical uncertainties are included as nuisance parameters.

Region	$g_U^2 - 1\sigma$	g_U^2	$g_U^2 + 1\sigma$
$e\tau_{\text{had}}$	12.6	15.3	19.1
$\mu\tau_{\text{had}}$	11.1	14.1	18.2
$\tau_{\text{had}}\tau_{\text{had}}$	3.1	3.9	5.0
$e\tau_{\text{had}}$ $+\mu\tau_{\text{had}}$ $+\tau_{\text{had}}\tau_{\text{had}}$	3.0	3.8	5.0

4.8.2 Profile-likelihood fit

For a preliminary result, only the $\tau_{\text{had}}\tau_{\text{had}}$ region is considered in the profile-likelihood fit, since the $e\tau_{\text{had}}$ and $\mu\tau_{\text{had}}$ regions are expected to add almost no signal sensitivity. The fit is performed with the $m_{\ell\ell}$ distribution in the two regions defined by the presence of 0 b-tagged jets and 1 b-tagged jet, each composed of three bins. The region with 2 or more b-jets is not included in the preliminary result since it makes the fit unstable and therefore it needs further investigation. The systematic uncertainties are included as nuisance parameters (NPs) with a Gaussian probability density function. Normalisation factors on the $t\bar{t}$ and $Z \to \ell\ell$ +jets processes are included as free-floating parameters. The modelling uncertainties are treated as shape and normalisation parameters, except for the ones related to the $t\bar{t}$ and $Z \to \ell\ell$ +jets processes, which are instead considered shape-only parameters. The statistical uncertainty on the signal and background MC events is implemented as additional nuisance parameters with Poisson priors. The statistical uncertainty on the signal is decorrelated from the statistical uncertainty on the background. The parameter of interest (POI) of the fit is the leptoquark coupling g_U^2. The binned profile likelihood function with g_U^2 as POI and $\boldsymbol{\theta}$ as NPs can be expressed in the following way:

$$\mathcal{L}(\boldsymbol{n}, \boldsymbol{\theta^0}|g_U^2, \boldsymbol{\theta}) = \prod_{i\in\text{bins}} \mathcal{P}\left(n_i|S_i(\boldsymbol{\theta}|g_U^2) + B_i(\boldsymbol{\theta})\right) \times \prod_{j\in\text{syst}} \mathcal{G}\left(\theta_j^0|\theta_j, \Delta\theta_j\right), \tag{4.10}$$

where $\boldsymbol{n}$ are the observed bin contents, the first factor in the product is the Poisson probability of observing in the ith bin n_i events and the second factor is the Gaussian constraint on the nuisance parameters $\boldsymbol{\theta}$ (assuming an *a priory* knowledge from auxiliary measurements given by $\theta_j = \theta_j^0 \pm \Delta\theta_j$). The expected number of events in each bin is parameterised by the sum of the SM prediction $B_i(\boldsymbol{\theta})$ and the BSM contribution $S_i(\boldsymbol{\theta}|g_U^2) = g_U^2 \cdot S_i^{\text{INT}}(\boldsymbol{\theta}) + g_U^4 \cdot S_i^{\text{BSM}}(\boldsymbol{\theta})$, which includes both the pure BSM term and term of interference with the SM.

Tables 4.8 and 4.9 report the post-fit event yields in each $m_{\ell\ell}$ bin of the 0 and 1 b-jet $\tau_{\text{had}}\tau_{\text{had}}$ regions respectively in the $m_{LQ} = 1.5\,\text{TeV}$ case, while Figure 4.36 shows the post-fit $m_{\ell\ell}$ distributions. The results from the fit show no significant deviation from the SM predictions in any of the four leptoquark mass points considered, as confirmed by the p-values[9] obtained for the SM-only hypothesis, which are equal to 0.28 in all the cases.

The nuisance parameter pulls in Figure 4.37, given by $(\hat{\theta} - \theta_0)/\Delta\theta$, with $\hat{\theta}$ the post-fit NP value and θ_0 the pre-fit NP value, show that the fit performed considering only the 0 and 1 b-jet $\tau_{\text{had}}\tau_{\text{had}}$ regions is stable. No anomalous constraints are obtained for any NP, except for the tau TES systematic uncertainty for low-p_{T} tau-leptons, which was expected since it derives from a rough extrapolation uncertainty on the single-particle calorimeter response from Run 1. Figure 4.38 reports instead the pre-fit and post-fit impact of the highest-ranked NPs on the determination of

[9] In a statistical hypothesis test, the p-value is the probability for the null hypothesis (SM-only in this case) of obtaining results equally or less compatible with such hypothesis with respect to the ones observed.

Table 4.8. Post-fit event yields in each bin of the 0 b-jet $\tau_{\text{had}}\tau_{\text{had}}$ signal region from the MC predictions of the SM processes, the observed Run 2 data and the pure BSM and interference contributions from the simplified U_1 vector leptoquark model with $m_{LQ} = 1.5\,\text{TeV}$.

Process	bin 1 ([100, 250] GeV)	bin 2 ([250, 400] GeV)	bin 3 ([400, 1000] GeV)
LQ BSM	3.37 ± 4.31	5.49 ± 7.04	5.34 ± 7.03
LQ Int	-13.22 ± 8.45	-10.37 ± 6.62	-3.13 ± 2.00
$Z \to \ell\ell$	1.08 ± 0.08	0.61 ± 0.05	0.00 ± 0.00
$Z \to \tau\tau$	2535.54 ± 88.64	1317.67 ± 48.75	303.22 ± 12.72
Fakes	844.98 ± 66.13	370.47 ± 33.72	107.37 ± 7.46
$H \to \tau\tau$	46.60 ± 1.17	0.03 ± 0.00	0.00 ± 0.00
Multi-boson	61.83 ± 3.27	42.12 ± 2.65	11.74 ± 1.07
Single-top	16.75 ± 1.03	10.14 ± 0.90	1.39 ± 0.20
$t\bar{t}$	60.19 ± 6.38	32.70 ± 3.40	5.82 ± 0.65
Total	3557.13 ± 56.65	1768.87 ± 35.35	431.74 ± 10.64
Data	3549	1763	447

Table 4.9. Post-fit event yields in each bin of the 1 b-jet $\tau_{\text{had}}\tau_{\text{had}}$ signal region from the MC predictions of the SM processes, the observed Run 2 data and the pure BSM and interference contributions from the simplified U_1 vector leptoquark model with $m_{LQ} = 1.5\,\text{TeV}$.

Process	bin 1 ([100, 250] GeV)	bin 2 ([250, 400] GeV)	bin 3 ([400, 1000] GeV)
LQ BSM	4.19 ± 5.35	7.63 ± 9.80	7.48 ± 8.79
LQ Int	-15.58 ± 9.95	-12.46 ± 7.96	-4.69 ± 3.00
$Z \to \ell\ell$	0.13 ± 0.02	0.00 ± 0.00	0.00 ± 0.00
$Z \to \tau\tau$	61.72 ± 3.90	24.97 ± 1.63	5.54 ± 0.66
Fakes	36.60 ± 3.71	14.04 ± 1.34	5.54 ± 0.46
$H \to \tau\tau$	3.50 ± 0.11	0.01 ± 0.00	0.00 ± 0.00
Multi-boson	2.10 ± 0.20	1.02 ± 0.10	1.08 ± 0.09
Single-top	29.04 ± 1.81	12.78 ± 0.99	1.81 ± 0.24
$t\bar{t}$	150.14 ± 14.10	78.62 ± 7.51	12.88 ± 1.54
Total	271.84 ± 14.18	126.61 ± 7.58	29.64 ± 5.50
Data	266	133	28

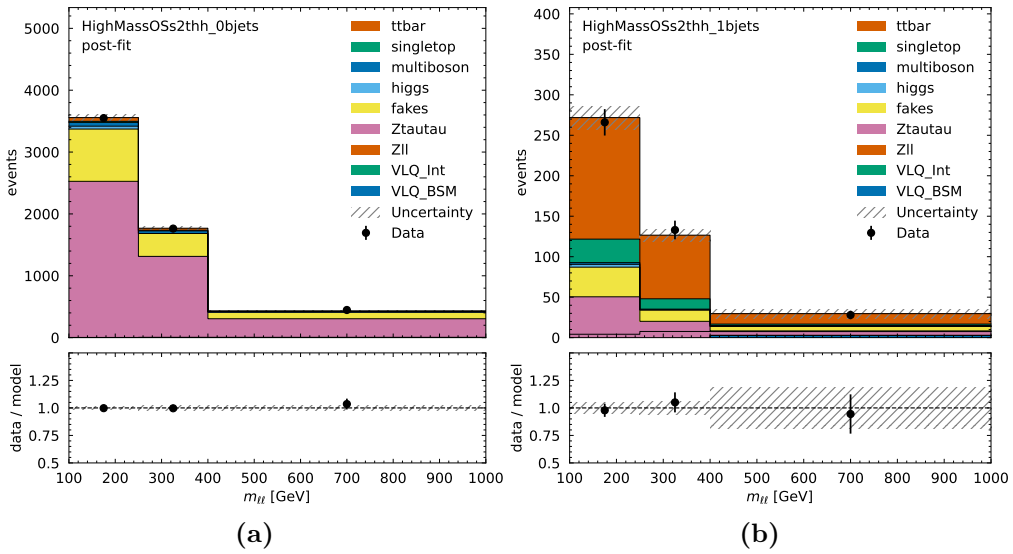

Figure 4.36. Post-fit distributions of the visible invariant mass in the 0 b-jet (a) and 1 b-jet (b) $\tau_{\text{had}}\tau_{\text{had}}$ signal regions obtained with $m_{LQ} = 1.5\,\text{TeV}$.

the POI.

4.8.3 Exclusion limits

Since no evidence of leptoquark contributions is found in the results from the profile-likelihood fit, upper exclusion limits are derived for the leptoquark coupling in the different leptoquark mass scenarios using the CLs method. The variable obtained from the ratio of the profile-likelihoods in the BSM signal hypothesis and in the SM-only hypothesis is used as the test statistic. The distribution of the test statistic is determined using the asymptotic approximation. The 95% CL upper limits on the g_U^2 parameter obtained with the CLs technique for the four leptoquark mass hypotheses are reported in Figure 4.39. All limits are placed under the assumption of vector leptoquarks coupling exclusively to left-handed b quarks and tau-leptons ($\beta_L^{33} = 1$, $\beta_R^{33} = 0$).

The expected and observed upper limits at 95% CL on the coupling strength λ, given by $\lambda = \sqrt{g_U^2/2}$, are shown in Figure 4.40 as a function of the leptoquark mass. The same plot reports also the expected and observed upper limits obtained by the CMS Collaboration under the same assumptions used in this analysis. The result reported in this thesis, although being only a preliminary result obtained from a subset of the analysis signal regions, does not seem to confirm the discrepancy between expected and observed limits found by the CMS experiment and excludes a wider region of the parameter space. The plot displays also the region preferred by the B anomalies.

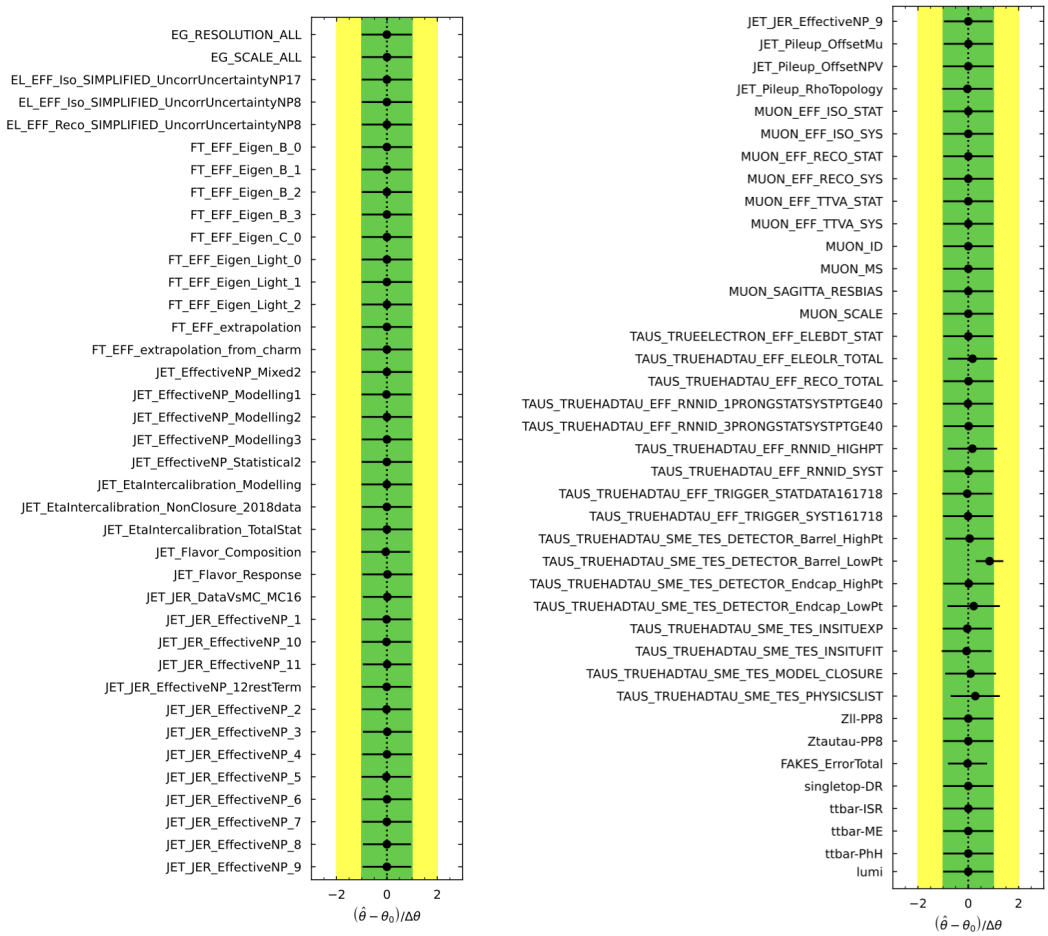

Figure 4.37. Nuisance parameter pulls.

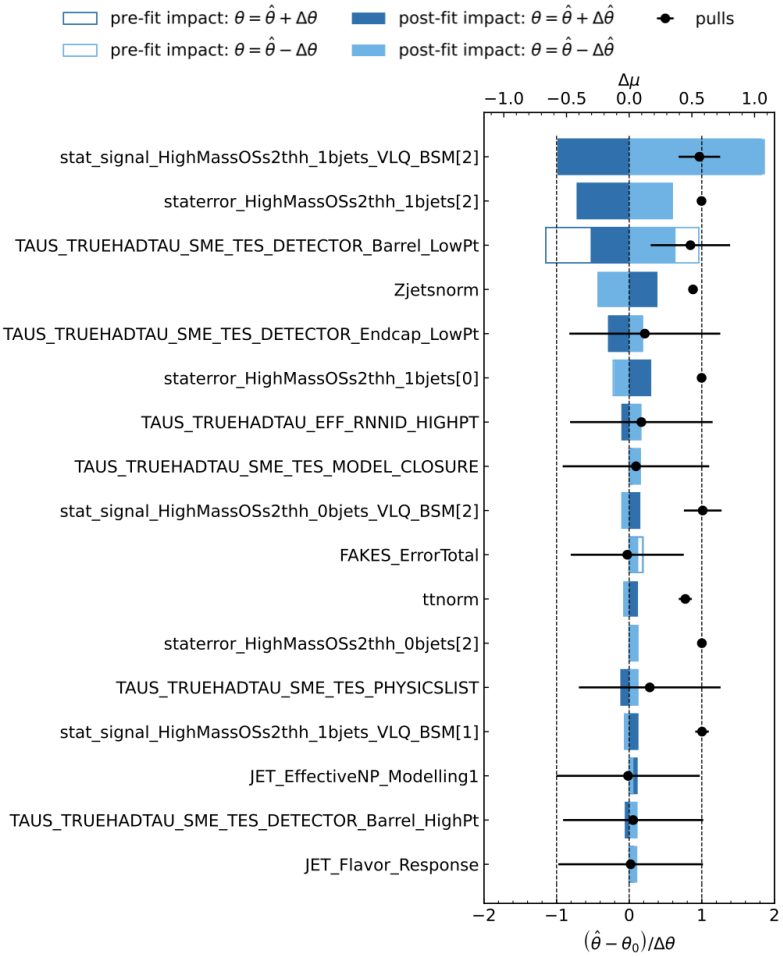

Figure 4.38. Pre-fit and post-fit impacts of the highest-ranked NPs on the determination of the POI.

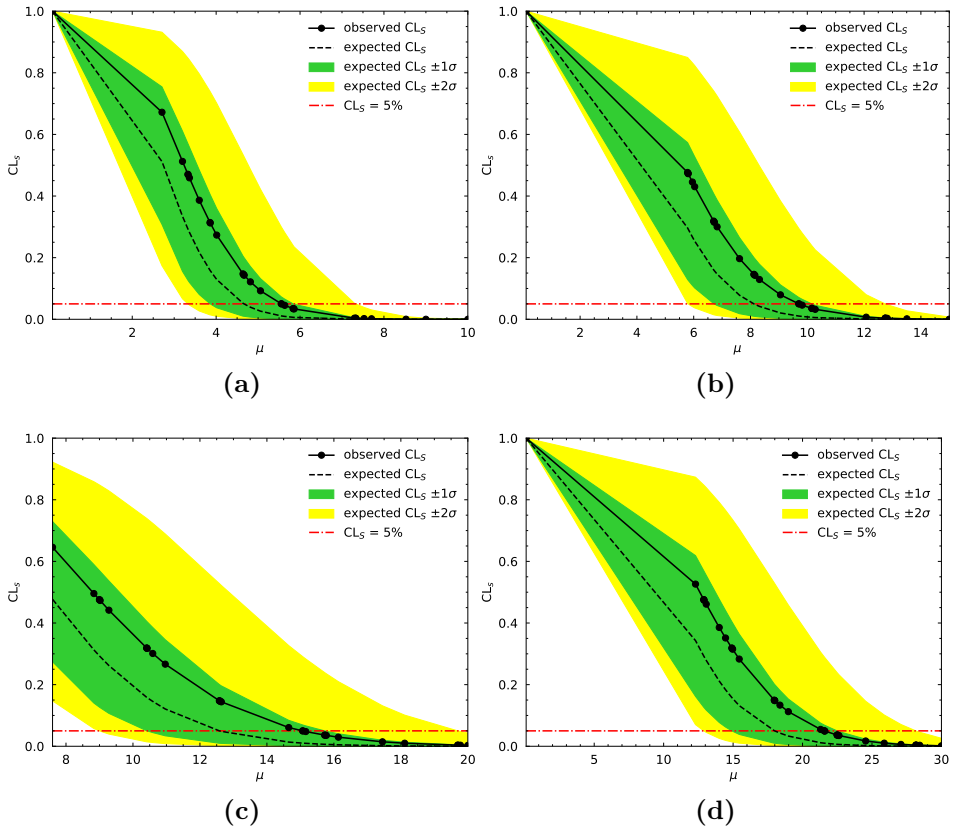

Figure 4.39. Expected (dashed black line) and observed (continuous black line) CLs values for different values of the parameter of interest of the fit μ (namely g_U^2) for the $m_{LQ} = 1.5\,\text{TeV}$ (a), $m_{LQ} = 2.0\,\text{TeV}$ (b), $m_{LQ} = 2.5\,\text{TeV}$ (c) and $m_{LQ} = 3.0\,\text{TeV}$ (d) hypotheses. The intersection with the dashed red line gives the 95% CL upper exclusion limits.

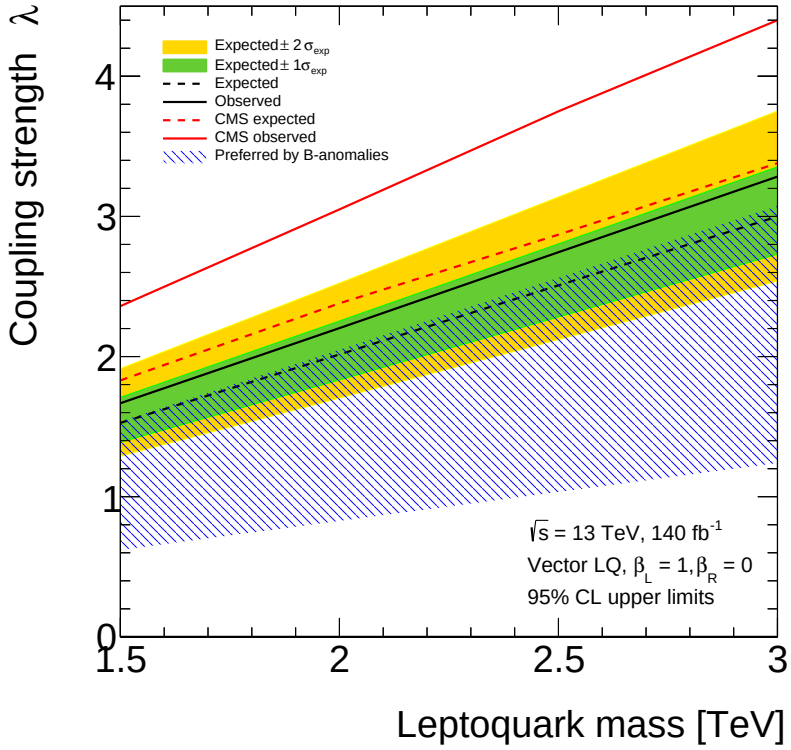

Figure 4.40. Observed and expected upper limits at the 95% CL on the coupling strength λ of a vector leptoquark model determined by considering only the non-resonant production of two τ leptons through t-channel leptoquark exchange. Exclusive leptoquark left-handed couplings to b quarks and τ leptons are assumed. The hatched region shows the parameter space preferred by the B anomalies [20]. The observed and expected upper limits measured by the CMS Collaboration [31] are reported for reference.

Chapter 5

The L0 Muon Barrel trigger for the HL-LHC

Run 3, started in 2022 and foreseen to last until the end of 2025, is the last run of operation of the LHC machine as it was designed. However, the life cycle of the collider will not conclude with Run 3, since a new phase of operation is planned to start after an upgrade of the collider machine and of the detectors placed along its ring. The upgraded machine will allow the experiments to collect ten times the amount of data recorded so far, largely enhancing the sensitivity to rare processes and beyond Standard Model signatures.

This Chapter presents a brief overview of the changes that will be applied to the LHC machine (Section 5.1) and to the ATLAS sub-systems (Section 5.2) during the upgrade stage that will follow the end of Run 3. Then a more detailed description of the upgraded Level-0 Muon Barrel TDAQ system, in whose development activity I was extensively involved, is given (Section 5.3), followed by the presentation of a hardware test performed to validate the encoding protocol to be used to transmit data between the electronic boards of the Level-0 Muon Barrel TDAQ system (Sections 5.4 and 5.5).

5.1 The High-Luminosity LHC

After the end of Run 3, the LHC machine will undergo a major upgrade which will extend its operability by another decade or more and will largely enhance its performance. The new configuration of the LHC, which has been given the name of *High-Luminosity LHC* (HL-LHC) [130], is foreseen to start its operation with Run 4 at the beginning of 2029. During the Long Shutdown 3 many outdated components of the LHC machine will be substituted by new ones designed with innovative technologies, like 11 to 12 T superconducting magnets, very compact superconducting RF cavities with ultra-precise phase control, new technologies and materials for beam collimation and high-current superconducting links with almost zero dissipation.

Thanks to this cutting-edge technologies, the HL-LHC is expected to achieve a peak instantaneous luminosity of $5 \times 10^{34}\,\mathrm{cm}^{-2}\mathrm{s}^{-1}$, which may be pushed up to $7.5 \times 10^{34}\,\mathrm{cm}^{-2}\mathrm{s}^{-1}$, with the goal of collecting an integrated luminosity between $3000\,\mathrm{fb}^{-1}$ and $4000\,\mathrm{fb}^{-1}$ in 12 years of operation, about 10 times larger than the integrated luminosity delivered by the LHC in its three runs. The much harsher conditions of HL-LHC for radiation levels and pileup, which will have a nominal value of 140 but may go up to 200 in the highest performance scenario, will challenge the experiments placed along the accelerator ring, which plan to upgrade their detectors to cope with the new conditions and improve their performance.

5.2 The ATLAS Phase-II Upgrade

With the Phase-II Upgrade, which will take place during the LHC Long Shutdown 3, many ATLAS sub-systems will be improved or replaced in order to maintain their excellent performance even in the much higher pileup conditions of the HL-LHC. The sub-systems that will be affected by the Phase-II Upgrade are listed in this section together with a brief description of the related changes. A complete overview of all the changes that the ATLAS detector will undergo during the Phase-II Upgrade can be found in [131].

5.2.1 The Inner Tracker

During the Phase-II Upgrade the entire ATLAS tracking system, which currently includes the pixel detector, the strip detector and the TRT, will be replaced by a new tracker, the Inner Tracker (ITk), completely based on semiconductor technology. The ITk will consist of a pixel detector at small radius close to the beam pipe and a large area strip tracker surrounding it. It will largely increase the granularity with respect to the Inner Detector (passing from the current 100 million channels to more than 5 billion) and will extend the pseudorapidity coverage (from $|\eta| < 2.5$ to $|\eta| < 4$). A display of the ITk layout is shown in Figure 5.1.

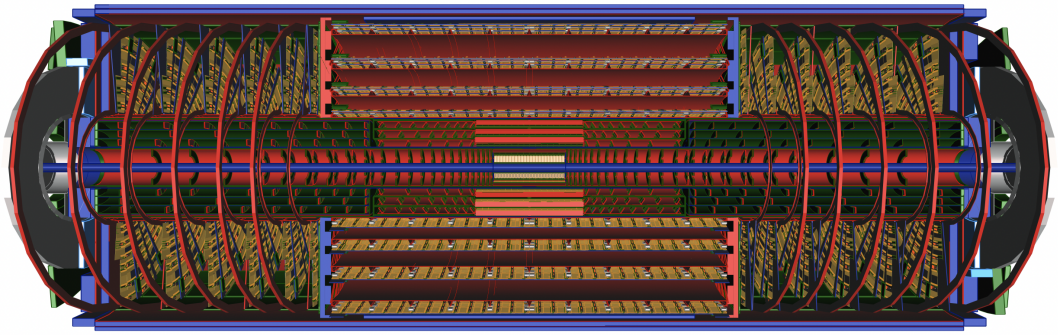

Figure 5.1. Display of the ITk layout [132].

The pixel detector [133] is made of flat barrel layers and multiple inclined or vertical ring-shaped end-cap disks, which cover a pseudorapidity region up to $|\eta| = 4$.

It is divided into three separate mechanical areas: the two-layer Inner System (IS), with the innermost layer placed at a distance of 34 mm from the beam pipe, the Outer Barrel (OB) system, covering the central detector region with three flat layers and three rings, and the Outer End-cap (OE), made of three sets of rings installed on each side of the OB. The pixels in the barrel rings are tilted in order to decrease the amount of material crossed by the particles in the forward regions. 3D sensors are used in the innermost layer and set of rings, with a $25 \times 100\,\mu m$ and $50 \times 50\,\mu m$ pixel size for the barrel and the disks respectively, while the other layers and rings have a pixel size of $50 \times 50\,\mu m$.

The ITk strip detector [134] is made of a barrel region and two identical end-cap regions. The active elements of the detector, which are modules made of a sensor, circuits and a power board, are mounted on the two sides of local support structures with a small stereo angle to provide the second coordinate measurement. A schematic view of the layout of the ITk, showing the displacement of the layers and modules of the pixel and strip detectors, is reported in Figure 5.2.

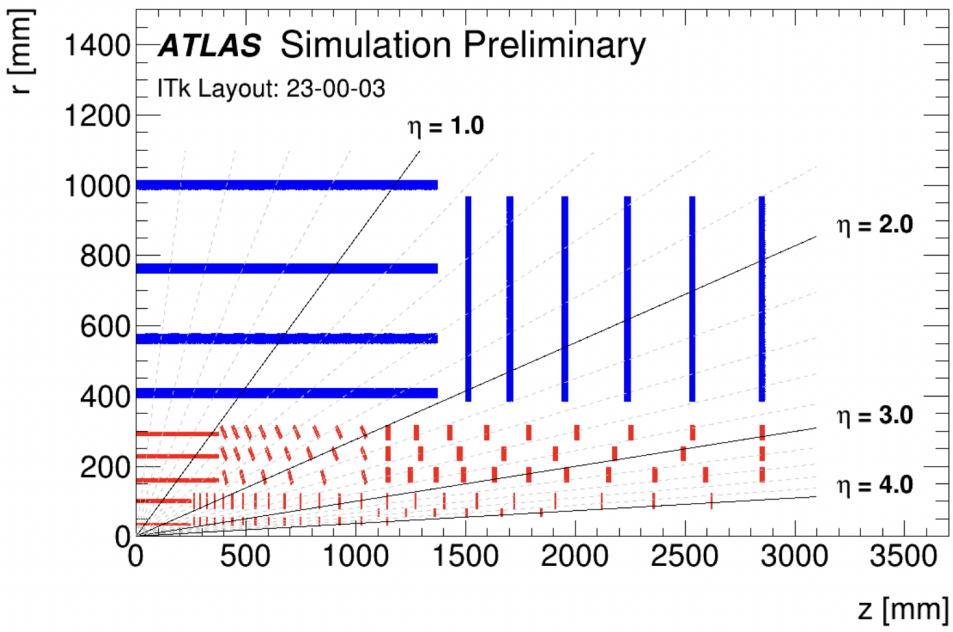

Figure 5.2. Schematic view of one quadrant of the ITk [132]. Only active detector elements are shown, in red for the pixel detector and in blue for the strip detector.

5.2.2 The High-Granularity Timing Detector

Due to the extremely high-pileup conditions, the separation of pileup tracks from those originating from the hard-scatter interaction will become particularly challenging in the forward regions of the ITk. A novel precision-timing silicon detector, the High-Granularity Timing Detector (HGTD) [135], will be installed in the gap region between the barrel and end-cap calorimeters, at a distance in z of $\pm 3.5\,m$

from the nominal interaction point. The HGTD will consist of many silicon-based Low Gain Avalanche Detectors covering the pseudorapidity interval $2.4 < |\eta| < 4$. It will complement the ITk spatial resolution with precise timing information (30 to 50 ps time resolution) on the charged particles in the forward regions. With this extremely fine timing resolution, it will be possible to distinguish tracks originating from interactions occurring very close in space but well separated in time.

5.2.3 The calorimeter system

The electromagnetic and hadronic calorimeters will maintain their required performance in the HL-LHC conditions, even though a signal degradation is expected in the forward calorimeters, and therefore they will not need to be replaced in the Phase-II Upgrade. What will be replaced instead is the readout electronics and the low-voltage powering system due to the limited radiation tolerance of the currently installed front-end components [136, 137]. The replacement of the entire readout electronics is also demanded by the new trigger system proposed for the HL-LHC.

For the LAr calorimeter, new readout Front-end Boards and Calibration Boards will be installed on-detector. The Front-end Boards will receive the signals from the calorimeter cells and perform analog processing and digitisation. The Calibration Boards will inject calibrated signals directly into the calorimeter cells. The new off-detector LAr Signal Processor Boards will receive the full digitised data stream from the Front-end boards, apply digital filtering to the signals of each cell, buffer the data and send them to the data acquisition system when a trigger accept signal is received.

The new schema will allow the full calorimeter granularity and the three-dimensional information on the shower development to be exploited, with a consequent increase in the performance of the first-level trigger algorithms.

5.2.4 The muon system

The upgrade of the muon system in preparation for the HL-LHC has been divided into two steps. The first one, the Phase-I Upgrade, took place during the Long Shutdown 2, when the two end-cap Small Wheels were replaced by the New Small Wheels (NSWs), based on small Thin Gap Chambers (sTGC) and Micromegas chambers [138]. The NSWs started taking data in Run 3 but their full potential will be exploited starting from Run 4, in which they will be used both for trigger and precision measurements, allowing ATLAS to reduce the high trigger rate in the MS end-caps and improve the trigger efficiency. Moreover, in the LS2 the BIS7 and BIS8 MDT chambers, which are the BI MDT chambers in the small sector at the highest $|\eta|$, have been replaced by the integrated BIS78 stations of new RPC and small-diameter MDT (sMDT) chambers to enhance the trigger coverage in this region [139].

The second step of the upgrade is represented by the Phase-II Upgrade in the

LS3, which foresees the installation of new chambers, the substitution of some existing ones and the replacement of almost the entire front-end, trigger and readout electronics [140]. New RPC triplet chambers will be installed in the inner region of the barrel (BI), to compensate for the reduced efficiency of legacy RPCs due to ageing and to close most of the acceptance holes in the current barrel muon trigger due to toroid coils and support structures. With the new requirements for muon trigger candidates allowed by the additional RPC station, the product of the efficiency and the acceptance of the barrel muon trigger is foreseen to reach 92% in the worst-case scenario. In order to allow the installation of the BI RPCs, the BI MDT chambers, which currently occupy all the available space, will be replaced with sMDT chambers, so that the overall thickness of RPC and sMDT chambers will equal the current MDT one. For the end-cap muon trigger, the current EIL4 TGC doublet chambers will be replaced by TGC triplets with finer granularity, which will allow the use of a more robust 2/3 majority trigger requirement and smaller coincidence windows. To reduce the fake trigger rate from low-p_{T} charged particles generated inside the end-cap toroid cryostats, a coincidence of hits in the Big Wheel TGCs and in the chambers in front of the cryostats (NSW TGCs, EIL4 TGCs and BIS78 RPCs) will be required. The EIL4 TGC will cover the region around the NSW at $1.05 < |\eta| < 1.3$ in the large sectors, while the BIS78 RPCs will cover the same region in the small sectors. The layout of the muon spectrometer for the Phase-II Upgrade is represented in Figure 5.3.

The trigger and readout chain of the muon system will be entirely redefined in order to meet the rate and latency requirements of the Phase-II TDAQ scheme. All the TGC and RPC electronics will be replaced, except for the front-end one. An important difference with respect to the current design is that all the TGC and RPC data from each bunch crossing will be transferred to the counting room (USA15) where they will be used by more complex algorithms to perform the trigger decision. Also the MDT electronics will be redesigned, since all the MDT data will be transmitted to the counting room to be used both for muon tracking and to improve the quality of the trigger candidates. Finally, also the low-voltage and high-voltage power system of the muon spectrometer will be replaced during the Phase-II Upgrade, in order to guarantee a reliable power supply for the entire operation period of the HL-LHC.

5.2.5 The TDAQ system

The Phase-II trigger and data acquisition system must be able to cope with the conditions imposed by the *ultimate* configuration of HL-LHC ($\mathscr{L} = 7.5 \times 10^{34}\,\mathrm{cm}^{-2}\mathrm{s}^{-1}$ and up to 200 interactions per bunch crossing). The design of the Phase-II TDAQ system is based on a two-level trigger architecture, similar to the present one, with a hardware-based Level-0 (L0) trigger and a high-level trigger (Event Filter) [141].

The L0 trigger system, which has to satisfy the requirements of 1 MHz maximum rate and 10 µs latency, is composed by the Level-0 Calorimeter Trigger (L0Calo),

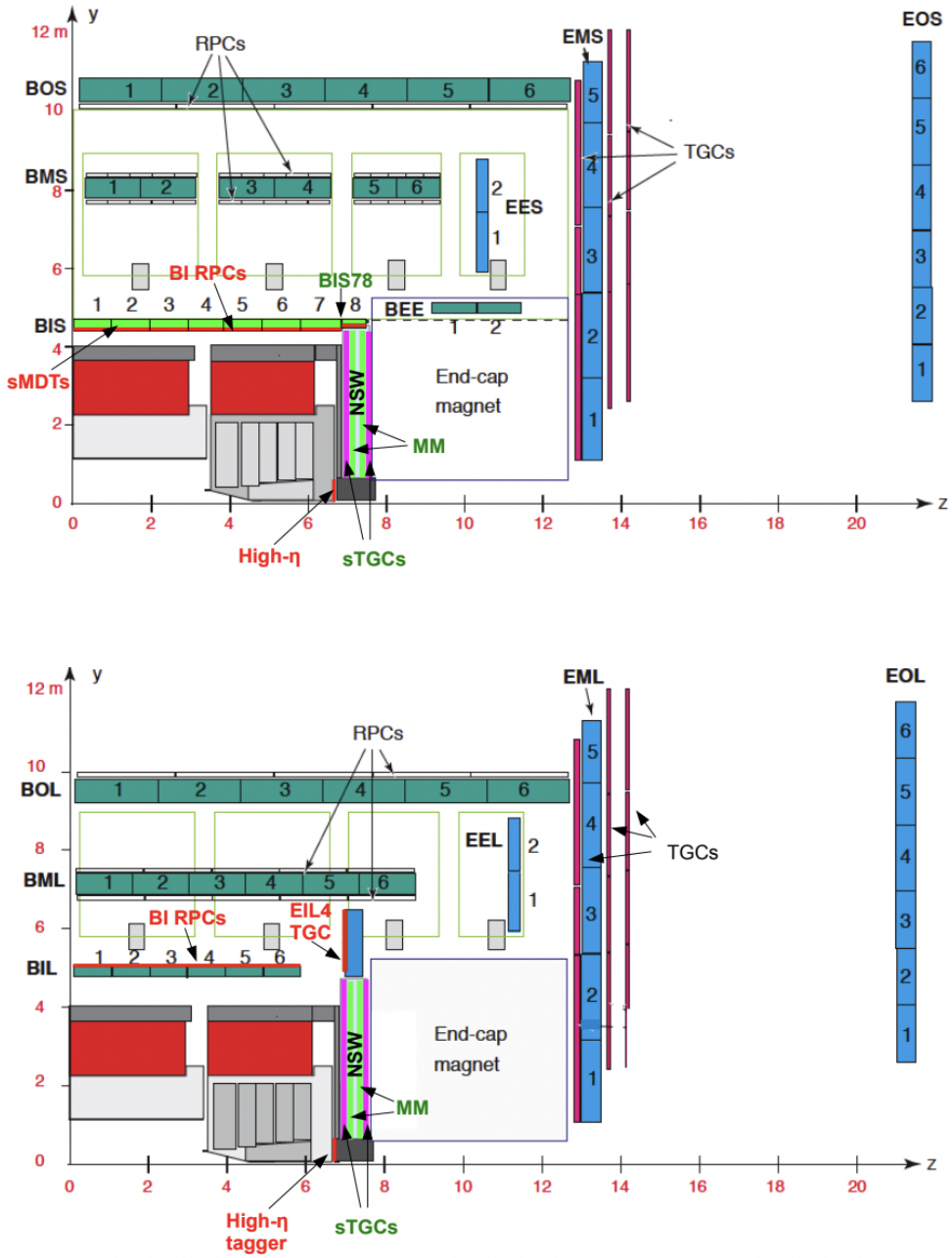

Figure 5.3. Views in the *R-z* plane of the muon spectrometer layout for the Phase-II Upgrade, showing a small sector (top) and a large sector (bottom) [140].

which will make use also of forward jets and electrons, the Level-0 Muon Trigger (L0Muon), which will employ upgraded Barrel and End-cap Sector Logic and NSW trigger processors using information from the RPC, TGC, NSW and even MDT detectors, and the Global Trigger, which will replace the current Topological Trigger with more complex algorithms based on full-granularity detector information and event-level quantities. The final trigger decision will be made by the Central Trigger Processor (CTP), which will have the possibility to apply prescales and deadtime and start the readout process of the detectors through the Trigger, Timing and Control (TTC) system.

After receiving the L0-accept trigger decision, all the detectors will transmit their data to the Data Acquisition (DAQ) system, which is composed of the Readout and Dataflow sub-systems, at 1 MHz. Such a high rate bandwidth (ten times larger than the one of the Run 2 first-level trigger) will allow low p_{T} thresholds on trigger objects to be maintained despite the increase in the instantaneous luminosity and as a consequence a good acceptance for the most important physics processes. The Readout sub-system will contain the Front-End LInk eXchange (FELIX) and Data Handler components, while the Dataflow sub-system will consist of the Event Builder, Storage Handler and Event Aggregator components.

The Event Filter system will perform the high-level trigger functionalities, refining the trigger objects and making a trigger decision using information from all the sub-detectors with an output rate of 10 kHz. The Event Filter system consists of a CPU-based processing farm and the Hardware-based Tracking for the Trigger co-processors. The Event Filter trigger decision will enable the transfer of the data corresponding to the accepted events from the DAQ system to permanent storage. A schematic design of the TDAQ architecture for the Phase-II Upgrade is illustrated in Figure 5.4.

5.3 The Level-0 Muon Barrel TDAQ system

The L0 Muon Barrel TDAQ system for the Phase-II Upgrade is in charge of selecting L0 muon trigger candidates using information from the RPC and MDT detectors and from the Tile Calorimeter and of performing the readout of RPC data. The L0 muon barrel trigger algorithm and the RPC readout logic are executed by 32 ATCA[1] boards, one for each MS barrel sector. These boards, called barrel Sector Logic (SL) boards, are placed in the USA15[2] experimental hall and are based on an FPGA which hosts the trigger and readout logic. An FPGA (Field Programmable Gate Array) is a semiconductor device made of a matrix of configurable logic blocks (CLBs) connected via programmable interconnections. The main advantage of an FPGA with respect to an ASIC (Application Specific Integrated Circuit) is that the former can be reprogrammed according to the desired functionality as many times

[1] ATCA (Advanced Telecommunications Computing Architecture) is an open industry standard for communication equipment.

[2] Underground Service ATLAS, commonly referred to as ATLAS counting room.

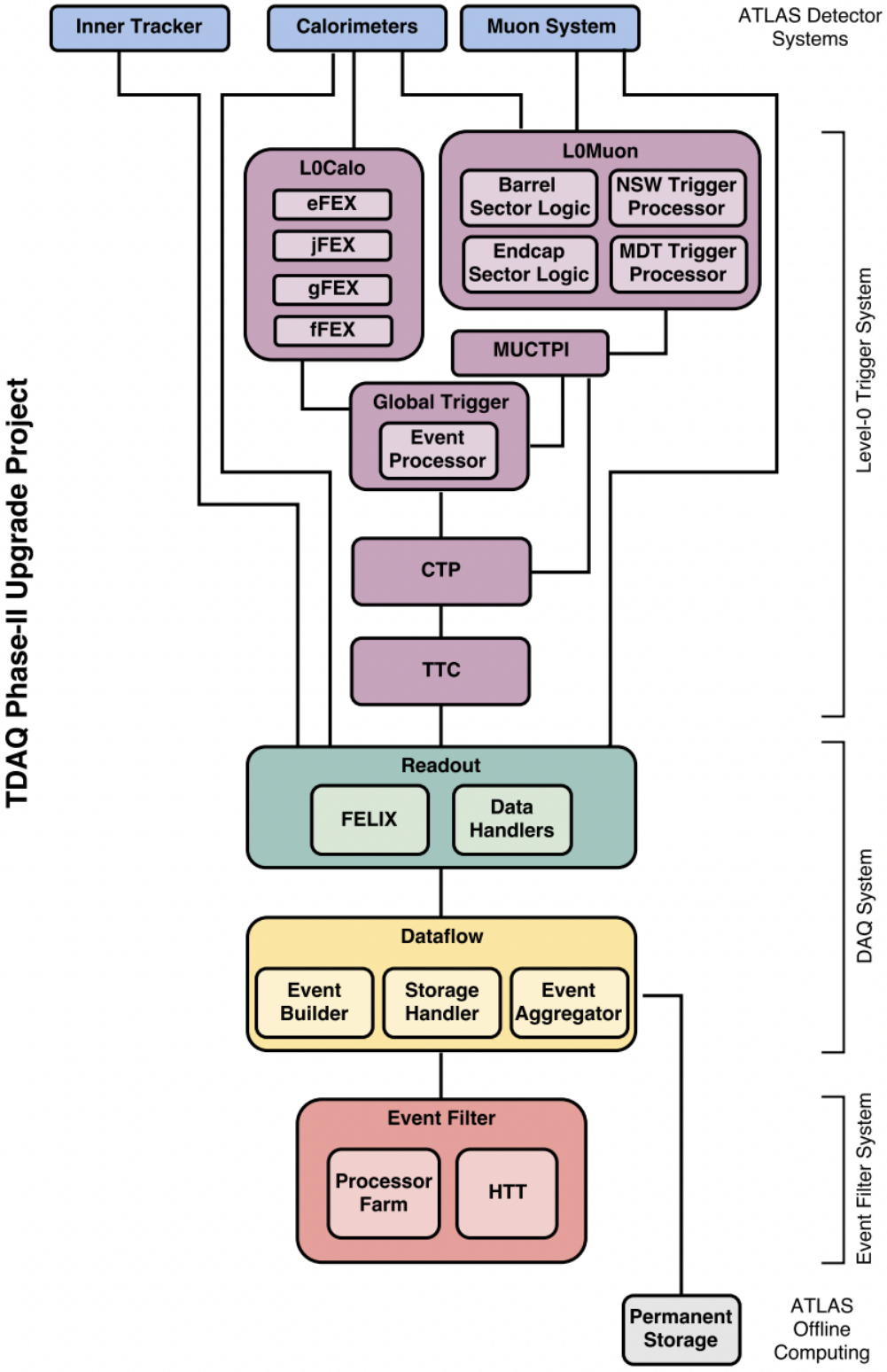

Figure 5.4. Design of the TDAQ architecture for the Phase-II Upgrade, highlighting the division in three main systems: the Level-0 Trigger, the DAQ and the Event Filter [141].

as needed after manufacturing, whereas the latter can be used only for the specific task it was designed for. The barrel SL boards receive all the RPC data from the Data Collector and Transmitter (DCT) boards, which are FPGA-based boards installed on-detector to collect the signals coming from the front-end (FE) boards. The DCT boards replace the Pad boxes used to digitise the data and implement the lower-level trigger logic in Runs 1-3. The total number of DCT boards foreseen for the installation is 1546, of which 338 for the BI RPC stations and 1208 for the BM and BO ones. Two versions of the DCT board have been designed with slightly different architecture and functionality, due to the different front-end electronics of the BI RPCs with respect to the BM and BO RPCs (see Chapter 6). Indeed in the BM and BO case the front-end boards used in Runs 1-3, which implement the ASD (Amplifier Shaper Discriminator) functionality generating a unipolar analog signal, are kept also for the LHC high-luminosity phase, while for the BI region novel FE boards have been developed which include a TDC (Time-to-Digital converter) and provide digitised data to the DCTs through serial links.

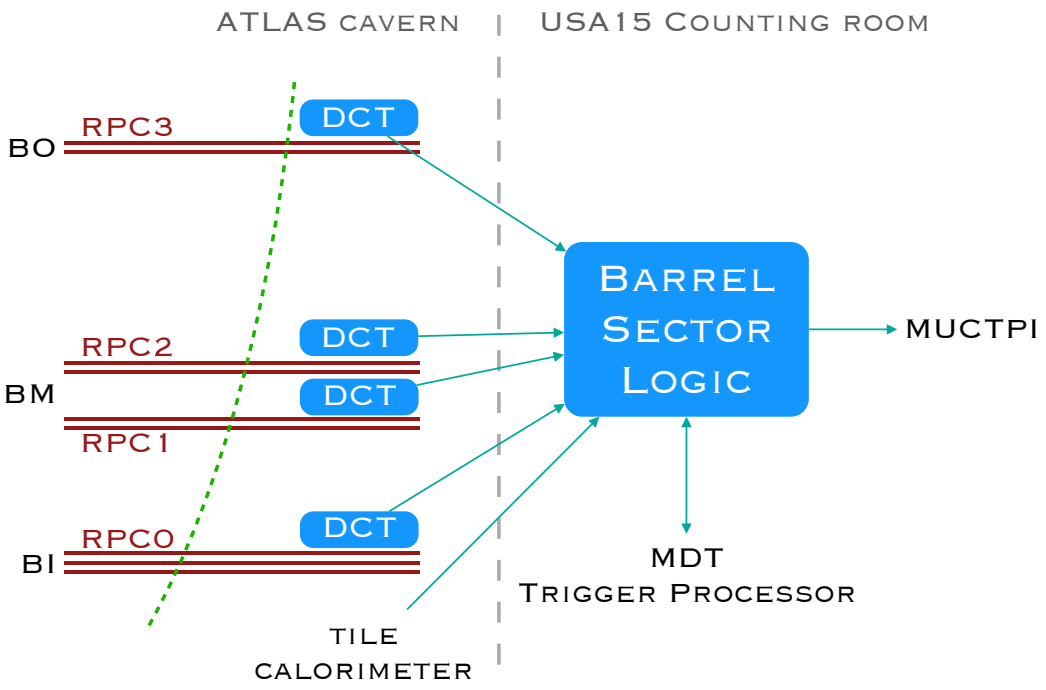

Figure 5.5. The Level-0 Muon Barrel trigger schema.

A scheme of the L0 Muon Barrel trigger system is depicted in Figure 5.5. On each RPC station two DCT boards are installed in the BO region, four in the BM region and one or two in the BI region. One BI RPC station is made of a triple gas gap RPC chamber, a BM station of two double gas gap chambers (BM1 and BM2) and a BO station of one double gas gap chamber. Each barrel sector has in total up to 50 DCT boards, all of them connected to a single SL board. The trigger algorithm executed by the SL board is based on coincidences of hits in the four RPC

layers (1 BI, 2 BM and 1 BO). A muon candidate is generated if a coincidence of hits is recorded in at least three RPC layers or alternatively if there is a hit coincidence between BI and BO stations. In some specific regions information from the outer layers of the Tile Calorimeter is included in the trigger decision as well. The SL board sends the muon candidates to the MDT Trigger Processor (MDTTP), which sends back a confirmation or a rejection decision based on a more precise estimation of the muon p_{T}. The final muon candidates are then sent from the SL to the Muon Central Trigger Processor Interface (MUCTPI).

5.4 DCT-SL interface

Each DCT is connected to the SL board of its sector through a bidirectional optical fibre. The fibre is used to send all the RPC data collected by the DCT and some DCT monitoring parameters (like voltage and temperature) to the SL board in the counting room and through the SL to the TDAQ system. At the same time the optical fibre is also used to transmit control data, TTC signals and the FPGA firmware bitstream to the DCT. The data transmission that proceeds from the DCT towards the SL is called *uplink*, while the transmission that occurs in the opposite direction is called *downlink*. The communication between DCT and SL is handled by the Low Power GigaBit Transceiver (lpGBT) ASIC [142], a radiation tolerant serialiser/deserialiser device included in the DCT design. The lpGBT is a highly flexible device, developed for the use in several systems of the ATLAS and CMS experiments for the Phase-II Upgrade, since it offers several encoding and decoding schemes suitable for the specific needs in terms of radiation-hardness and data bandwidth imposed by the HL-LHC conditions.

For the DCT-SL communication purpose, the lpGBT is configured as a transceiver (therefore both as a transmitter and a receiver) providing an uplink bandwidth of 10.24 Gb/s and a downlink bandwidth of 2.56 Gb/s. In order to correct possible transmission errors due to noise without the need to transmit the data again, the lpGBT uses a Forward Error Correction (FEC) encoding based on Reed-Solomon techniques [143]. The FEC encoding assumes the use of a certain part of the bandwidth to transmit parity bits which are then used to correct the errors. Two different encoding schemes, FEC5 and FEC12, are provided by the lpGBT, which differ in transmission robustness but also in the bandwidth fraction used for the FEC data. The FEC12 encoding, adopted for the downlink, is the most robust, being able to correct up to 12 consecutive errors at the cost of half the bandwidth: therefore only 1.28 Gb/s of the downlink bandwidth can be used for user data. For the uplink instead, in which maximising the available bandwidth is essential, the FEC5 encoding is used, which leaves 8.96 Gb/s out of 10.24 Gb/s for the user data but at the same time offers good performance against transmission errors.

On the SL side, the transmitted data have to be decoded and corrected according to the scheme adopted by the lpGBT. On this purpose, the lpGBT-FPGA project [144] provides a back-end counterpart to the lpGBT ASIC, called lpGBT-

FPGA core, to be implemented in the FPGA of the device that interfaces with the lpGBT. A logic block scheme of the lpGBT-FPGA core firmware is represented in Figure 5.6. The lpGBT-FPGA core consists of a downlink logic block, composed by Scrambler, Encoder, Interleaver and TX Gearbox, to prepare the data to be sent to the lpGBT according to the lpGBT protocol, and an uplink block, made of Frame Aligner, RX Gearbox, Deinterleaver, Decoder and Descrambler, to decode the data arriving from the lpGBT.

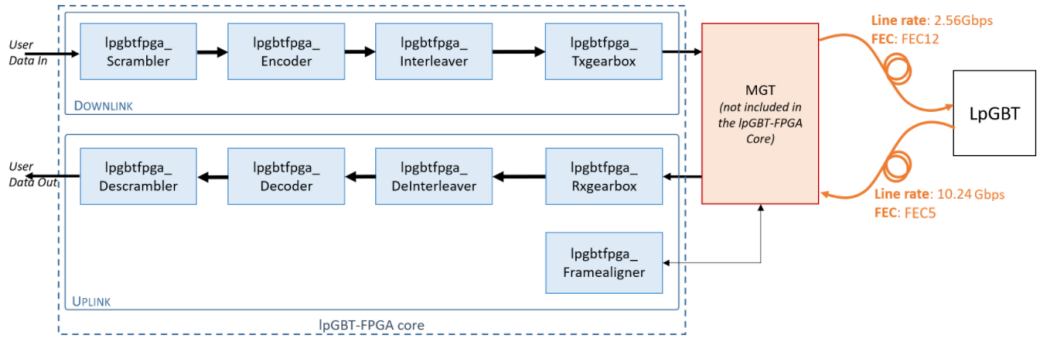

Figure 5.6. Logic block schema of the lpGBT-FPGA core [144].

The downlink logic arranges the data to be sent to the lpGBT into 64-bit frames which are transmitted as 32-bit frames at 80 MHz, for a total downlink bandwidth of 2.56 Gb/s. The original lpGBT-FPGA downlink logic is actually designed to work with a bandwidth of 10.24 Gb/s by upsampling the downlink frames, so that uplink and downlink have the same line rate. For the L0 Muon Barrel project, however, the original design has been modified to obtain a 2.56 Gb/s bandwidth in order to avoid wasting resources. The downlink logic block generates the 64-bit frame starting from an input frame of 36 bits, in which 2 bits represent the IC-field (for internal slow control of the lpGBT), 2 bits the EC-field (for external slow control) and 32 bits are reserved for the user data. Using an 80 MHz clock, with valid data every two clock cycles, this input frame is sent to the Scrambler, which performs a scrambling operation to ensure a high density of 0/1 transitions. The scrambled word is passed to the Encoder, which generates a 24-bit FEC code using a Reed-Solomon scheme. The FEC code is sent, together with the scrambled word, to the Interleaver, which applies an interleaving operation to obtain an error correction capability of up to 12 consecutive wrong bits. The Interleaver arranges the interleaved data word and the FEC code in a single frame and adds the downlink header, a 4-bit word needed by the lpGBT to realign the downlink frames after the serial transmission. The resulting 64-bit word is received every 25 ns by the TX Gearbox, which divides it into two 32-bit words to be sent at 80 MHz to a multi-gigabit transceiver (MGT). The MGT, which serialises the downlink frames and transmits them to the lpGBT via an optical fibre, is not part of the lpGBT-FPGA core.

For the uplink transmission, the lpGBT scrambles, encodes and interleaves the data to be sent to the lpGBT-FPGA core using the FEC5 encoding. The data are

arranged by the lpGBT into 256-bit frames and transmitted as a serial stream at 10.24 Gb/s. The 256-bit uplink frame consists of 224 bits of user data, a 2-bit uplink header used to re-align the frames, a 2-bit IC-field and a 2-bit EC-field for the slow controls, 20 bits for the FEC code and 6 unconnected bits. The uplink frame, after being deserialised by an MGT, enters the uplink logic block of the lpGBT-FPGA core divided into 32-bit words at 320 MHz. The first two bits of these words are sent to the Frame Aligner, which aligns the incoming frames by looking for the uplink header and sending an RX slide signal to the MGT until the first two bits of the input frames coincide with the uplink header. Once the header is locked, the 32-bit words are passed at 320 MHz to the RX Gearbox, which outputs a 256-bit frame every 25 ns. This frame is sent to the Deinterleaver, which discards the header, performs the opposite operation with respect to the Interleaver and separates the data from the FEC code. The data frame and the FEC code obtained in this way are then passed to the Decoder, which uses the latter to decode the data. The 234-bit decoded word is sent to the Descrambler, which descrambles it and separates the 224-bit user data from the slow control and unconnected bits.

5.5 lpGBT protocol communication test

One of the first tests to be carried out related to the development of the L0 Muon Barrel trigger and readout electronics for the Phase-II Upgrade certainly deals with the interface between the DCT and the SL board. It is indeed of primary importance to make sure that the communication between the two boards can be performed successfully using the lpGBT protocol. Therefore, in order to test the lpGBT protocol with the configuration demanded by the L0 Muon Barrel design, a test bench employing two Xilinx KC705 evaluation boards [145] has been set up [146]. The KC705 evaluation board is a very versatile device provided with an FPGA of the Kintex-7 family (the XC7K325T-2FFG900C FPGA), a fixed oscillator with differential 200 MHz output, a programmable oscillator, differential SMA input and output pins and user LEDs. The purpose of the test was to transmit data between the FPGAs of the two boards using the lpGBT protocol and check if the signal reception and decoding work properly. For the communication test, two different boards are needed, since the asymmetric architecture for uplink and downlink logic of the lpGBT-FPGA core prevents a loopback mode. Therefore two separate firmwares have been developed to be implemented in the FPGAs of the two boards.

The first firmware implements the logic of the SL side and therefore it includes an instance of the lpGBT-FPGA core, an instance of an MGT (which for Kintex-7 FPGAs is called GTX) and the logic to wrap them up. All the clocks used by the firmware are obtained from the board-embedded 200 MHz oscillator. This differential clock is driven internally to the FPGA and used by a clock multiplier (MMCM) to generate two differential 160 MHz clocks, which are driven to output SMA pins. The GTX is configured with an RX line rate of 10.24 Gb/s and a TX line rate of 2.56 Gb/s and uses as reference clock one of the two 160 MHz clocks generated by the

MMCM and driven to the GTX through SMA pins. As free-running GTX clock, the same 160 MHz clock is employed, driven in this case internally to the FPGA. The uplink and downlink logic blocks work with the RX and TX reconstructed clocks produced by the GTX, with a frequency of 320 MHz and 80 MHz respectively. A scheme of this firmware, showing the signals and clocks used by each logic block, is depicted in Figure 5.7.

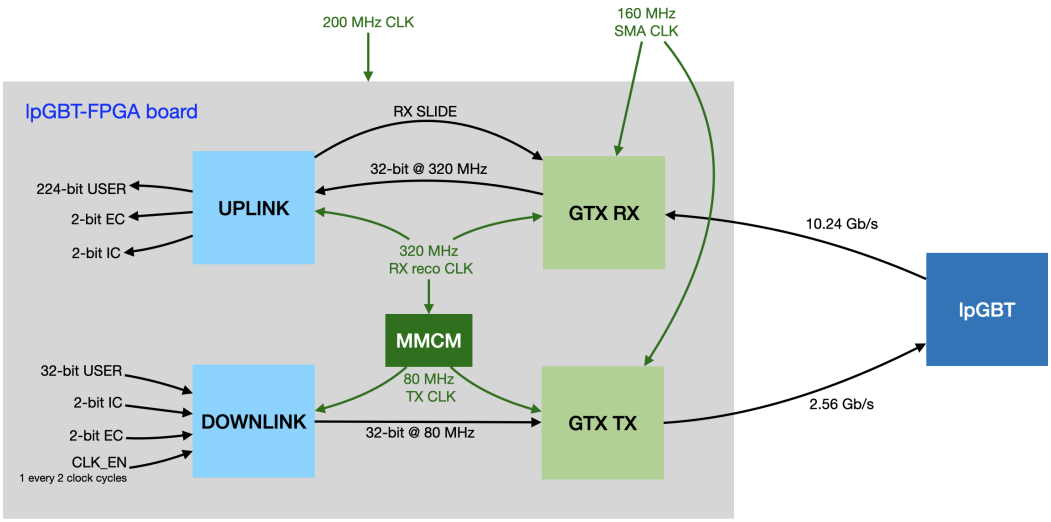

Figure 5.7. Logic block scheme of the firmware implementing the lpGBT-FPGA core.

The firmware of the second board has to perform the functions of the lpGBT. For this purpose, this firmware implements the logic of the lpGBT-Emulator [147], provided by the lpGBT project, together with a GTX instance and wrapping logic. The clock scheme is the same of the first firmware, except for the fact that the GTX reference clock is driven from one of the two 160 MHz clocks generated by the MMCM of the first firmware. For the hardware test, in order to make the transceivers lock the input signals, it is necessary that the GTX reference clocks originate from the same source (so that both frequency and phase are the same in the two boards). The line rates of the GTX of this firmware have the values exchanged with respect to the previous one, with an RX and a TX line rates of 2.56 Gb/s and 10.24 Gb/s respectively.

In addition to the logic described above, each firmware includes also some logic dedicated specifically to the evaluation of the data transmission performance. This logic, which is the same for the two FPGAs, generates a counter (made of 32 bits for the firmware with the lpGBT-FPGA core and 224 bits for the firmware with the lpGBT-Emulator), which is incremented every 25 ns. The counter is used as input user data for the downlink logic for the first firmware and for the uplink logic for the second one. Both these logic blocks encode the counter using the lpGBT protocol and pass it to the respective GTX, which transmits the data to the other board.

Both firmwares are also provided with a logic block which takes the decoded data (from the uplink chain for the first firmware and from the downlink chain for the second one) and checks if their content is incremented every 25 ns, as expected. If this is the case, a signal driven to one of the user LEDs makes the LED blink with 1 Hz frequency. Otherwise another LED is lit up.

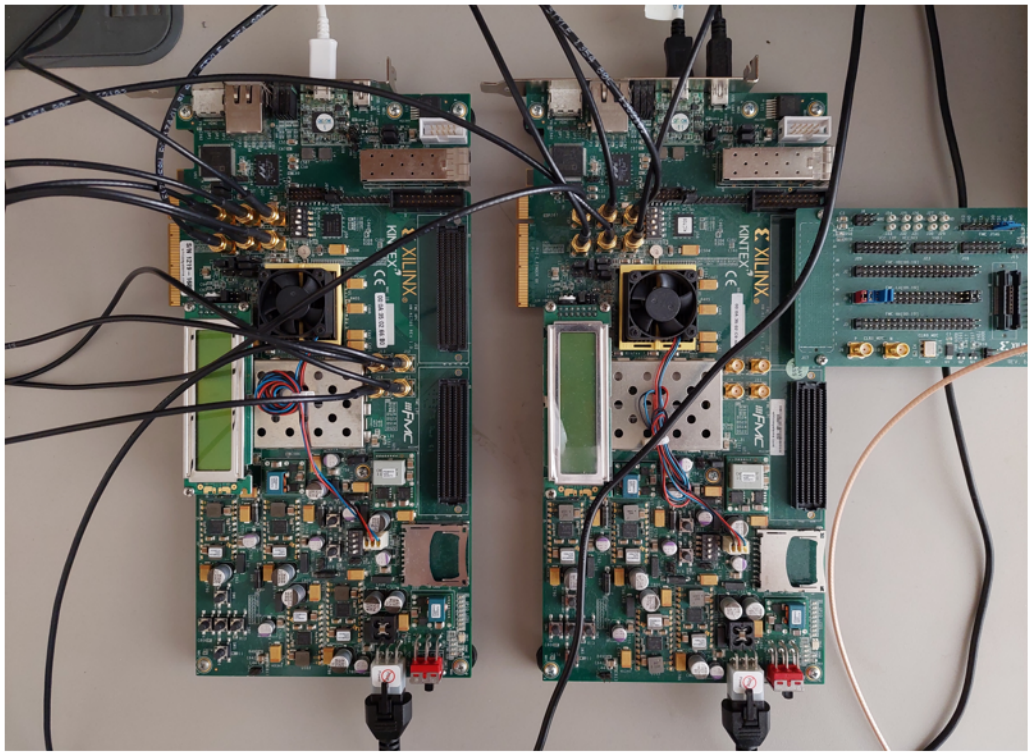

Figure 5.8. Hardware setup of the lpGBT protocol communication test using two KC705 evaluation boards.

Before the preparation of the hardware setup, a software simulation of the data communication between the two firmwares had been performed using the Xilinx-AMD Vivado Design Suite [148] (with version 2020.2). After checking with the simulation that all the signals are propagated as expected, the hardware test has been set up with the two KC705 evaluation boards as shown in Figure 5.8. The boards are powered by 12 V power adapters and the firmware bitstream is uploaded into the FPGA through a USB-JTAG connector from a PC. Coaxial cables are used to connect the input and output SMA pins: four cables are used to send the differential 160 MHz clocks from the FPGA of the board with the lpGBT-FPGA core (left board in the figure) to the GTX reference clock pins of both boards, two cables drive the differential TX signal of the GTX of the first board to the pins of the differential RX signal of the GTX of the second board and other two cables connect the GTX TX pins of the second board with the GTX RX pins of the first one. The outcome of the transmission and decoding of the counter signal during the hardware

test could be monitored through two user LEDs as described above. During a 48 hour long test, one LED on both boards kept blinking while the other LED never lit up[3], meaning that no transmission errors occurred and that the measured bit error rate is lower than $6 \times 10^{-6}\,\mathrm{s}^{-1}$. This test shows that the lpGBT protocol is a valid protocol for the data transmission between DCT and SL boards.

[3]When a transmission error is detected, the second led lights up and stays on until the board is switched off, so that it can tell only if at least one error occurred.

Chapter 6

Development of the DCT firmware

During the Phase-II Upgrade the entire trigger and readout electronics of the RPC-based muon system, except for the front-end boards, will be replaced. In place of the Pad and Splitter boxes, which perform the current low-level RPC trigger algorithm, novel DCT boards will be installed to collect all the RPC data and transmit them to the counting room. The innovative characteristic of the DCT board is the presence of an FPGA which can perform a fast processing of the RPC data before the off-detector transmission. One of the main tasks for the Phase-II Upgrade of the RPC system is the development of the firmware to be implemented in the DCT FPGA. Several challenges are encountered for the DCT firmware development, due to the high number of front-end channels collected by each board, the low latency allocated for the firmware operations and the different logic that the two DCT versions (BMBO and BI) have to implement.

Section 6.1 of this Chapter describes in detail the design and functionality of the DCT board, highlighting the common aspects and the differences between the two DCT versions. The subsequent sections present the development of the DCT firmware, for which I have given a substantial contribution: the firmware for the BMBO DCT is presented in Section 6.2 while the version for the BI DCT in Section 6.3.

6.1 The Data Collector and Transmitter board

The DCT is an FPGA-based board specifically designed for the L0 Muon Barrel trigger and readout system to operate in the highly challenging conditions of the HL-LHC [149]. Two versions of the DCT board have been developed, one to collect the RPC data from the BM and BO stations (BMBO DCT) and another one to collect the RPC data from the BI stations (BI DCT). Although being based on a common layout design and sharing most of the components, the two DCT versions differ in input signals, cabling and functionality of the FPGA logic. This is due to the RPC front-end electronics, which in the BI region will be different with respect

to the BM and BO regions. Indeed, while for the BM and BO RPC chambers the current front-end boards will be kept also for the HL-LHC runs, for the new BI RPCs a novel front-end board has been designed to achieve a better time resolution. The block scheme of the DCT board is illustrated in Figure 6.1, in which the components shared between the two versions are coloured in blue, while the different components are represented in green.

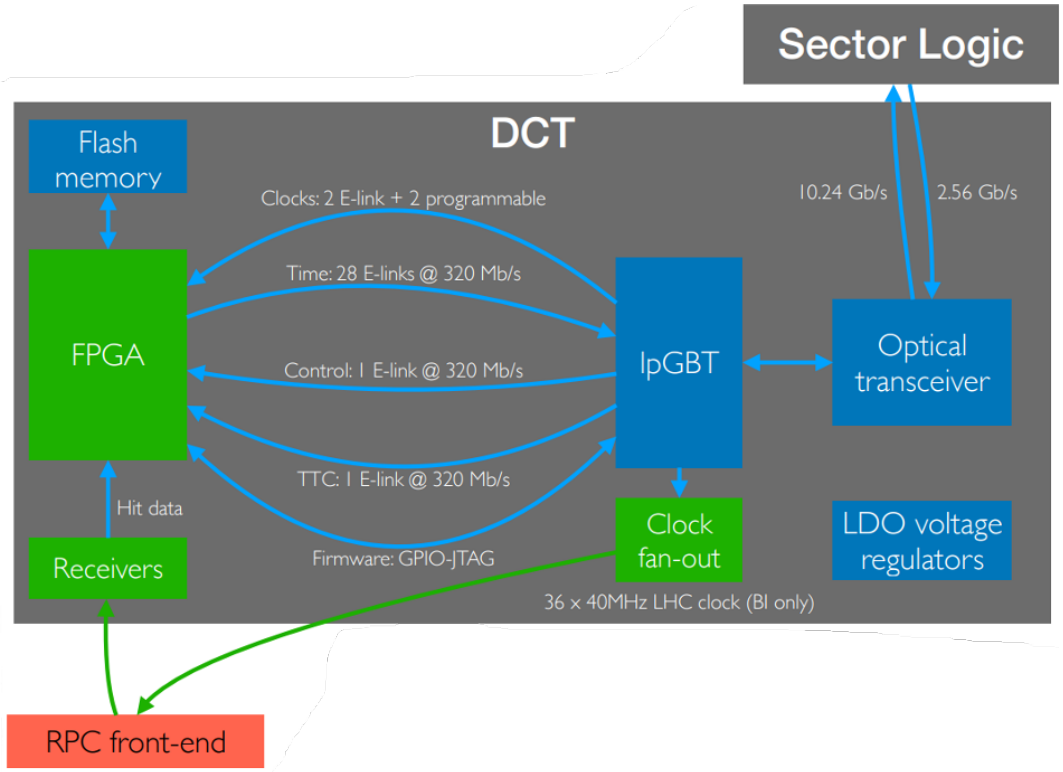

Figure 6.1. Block scheme of the DCT board. The components that are shared between the BI and the BMBO versions are represented by blue blocks, while the components that are different for the two versions are represented by green blocks.

Two DCT boards will be installed to read out the RPC doublet on one BO station, four DCTs will collect the signals of the two RPC doublets on one BM station and one DCT per triplet chamber will be installed in the BI region. The number of DCTs per RPC sector depends on the sector itself, ranging from 45 DCTs in a standard small sector to a maximum of 50 in the feet sectors. The maximum number of BI DCTs per sector is 10 while for the BMBO DCTs the maximum number is 40 per sector. Considering the 32 RPC sectors, 16 per barrel side, the total amount of DCTs that will be installed on-detector is 1546. Taking into account also an additional 10% of boards as spares, the total number of DCTs that will be produced is about 1700.

6.1.1 Front-end electronics and receivers

The legacy front-end boards in the BM and BO regions implement the ASD (Amplifier Shaper Discriminator) functionality. The output stage of the ASD chip is driven by a PNP transistor which acts as a switch. When an RPC hit signal is detected by the ASD chip, the transistor is activated generating a pulse signal whose width is between 11 ns and 12.5 ns depending on the amplitude of the avalanche. The analog pulse is received by the DCT board, which is in charge of performing the digitisation. The new BI front-end boards, instead, are provided with a TDC (Time-to-Digital Converter) with a 100 ps time resolution. The BI DCT boards, therefore, receive differential digital signals from the BI front-end.

Different front-end signals imply the use of different types of receivers in the two DCT versions: the BI DCT uses LVDS (Low Voltage Differential Signaling) receivers, while the BMBO DCT employs the legacy front-end receiving schema of the Pad boards (shown in Figure 6.2). In this schema, the unipolar front-end signal is AC coupled on the Pad or the DCT board and the circuit represented in the figure translates it to a LVDS compatible signal. An LVDS receiver chip (TI DS90LV048) receives this differential signal and produces a TTL (Transistor-Transistor Logic) 3.3 V signal, which is then sent to the FPGA.

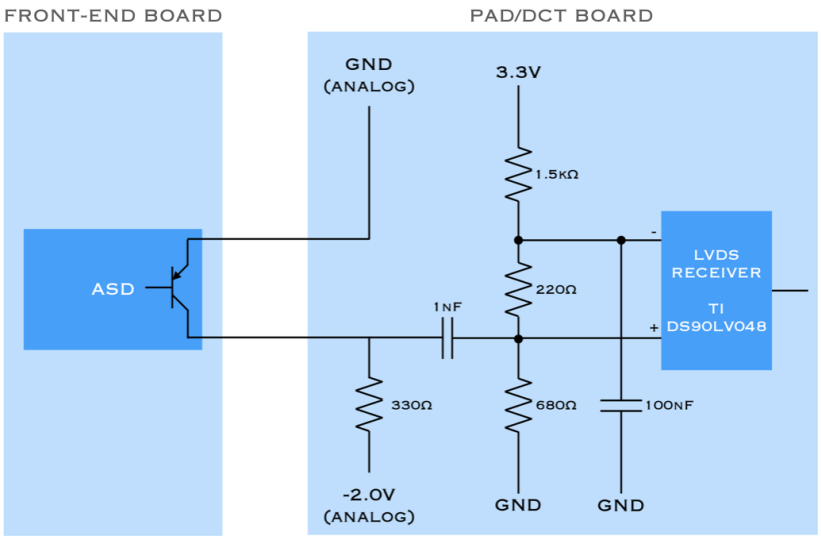

Figure 6.2. BMBO legacy front-end receiving schema.

6.1.2 FPGA

The FPGA of the DCT has the task of processing the RPC front-end hits, digitising them (only in the BMBO version), performing the zero-suppression logic and sending them to the lpGBT. The FPGA device chosen for the BMBO DCT is the XC7A200T FFG1156 from the Xilinx Artix-7 family [150]. With a total of 500 I/O

user pins, 33 650 CLBs (each CLB contains four lookup tables and eight flip-flops) and a maximum data rate of 6.26 Gb/s, this device is perfectly suitable for the needs of the BMBO DCT firmware, as shown in Section 6.2.

For the BI DCT, instead, the resources of the Artix-7 FPGA are not sufficient for the implementation of the firmware, which in this case has to perform a more complex processing of the RPC hits, as described in Section 6.2. Therefore, for the BI DCT, the XC7K325T FBG900 device from the Xilinx Kintex-7 family [151] has been chosen, which has the same number of user pins and similar data rate with respect to the Artix-7 device of the BMBO DCT but a larger number of CLBs (50 950) and routing resources.

6.1.3 FPGA-lpGBT interface

The lpGBT ASIC, configured in the same way in both DCT versions, handles the serial data communication with the SL board, performing the encoding of the data to be sent to the off-detector SL board using the lpGBT protocol and the decoding of the data transmitted from the SL to the DCT FPGA. The output data bandwidth, used to send RPC hits and control and monitoring data, is 10.24 Gb/s, with a user bandwidth of 8.96 Gb/s, while the input bandwidth, used for configuration and control commands and the FPGA firmware, is 2.56 Gb/s, with a user bandwidth of 1.28 Gb/s. Further details on the lpGBT configuration for the data transmission between the DCT and the SL boards can be found in Section 5.4.

Several connections, summarised in Table 6.1, allow the transfer of data between the FPGA and the lpGBT. In particular, 28 E-links are used to transmit data from the FPGA to the lpGBT at a speed of 320 Mb/s: these data include both the RPC hits and board monitoring parameters like temperature, voltage and hit rate. On the opposite direction, namely from the lpGBT to the FPGA, one E-link is dedicated to TTC (Time, Trigger and Control) signals and another one to configuration and control data. The speed of both E-links is 320 Mb/s. The lpGBT delivers the clocks to the FPGA through four clock lines: two clocks (E-link clocks) have a fixed phase while the other two are fully programmable. Lastly, 5 general purpose (GPIO) pins of the lpGBT are connected to the JTAG pins of the FPGA and are used for FPGA programming and debugging. 4 further GPIO pins of the lpGBT are connected to standard FPGA pins and can be used to transmit other bidirectional signals like reset and monitoring signals.

6.1.4 Other components

The other components that complete the DCT board design, and that are common between the two DCT versions, are a flash memory, to store the FPGA firmware sent from the SL board via the lpGBT and loaded into the memory using the GPIO pins, voltage regulators, to provide the power supply voltage to the various chips of the board, and a radiation tolerant SFP+ optical transceiver, which is connected

Table 6.1. Connections between DCT FPGA and lpGBT. The direction is relative to the FPGA (OUT = FPGA to lpGBT, IN = lpGBT to FPGA).

Type	Number	Direction	Speed	Description
E-link	28	OUT	320 Mb/s	RPC hit time and monitoring data
E-link	1	IN	320 Mb/s	configuration and control data
E-link	1	IN	320 Mb/s	TTC data
GPIO	5 pins	INOUT	TBD	general purpose
Clocks	4	IN	40 MHz	2 programmable + 2 E-link clocks

to the serial input/output port and the bidirectional optical fibre going to the SL board. The voltage regulators are commercial LDO (Low Drop-Out) regulators which provide the five voltage levels (1.0 V, 1.2 V, 1.8 V, 2.5 V and 3.3 V) needed by the board components. In particular, the 1.2 V power supply is used to power the lpGBT, 1.0 V for the FPGA core logic, 1.8 V for the FPGA auxiliary power, 2.5 V for the optical transceiver and 3.3 V for the LVDS receivers and the flash memory.

In addition, the BI DCT FPGA sends 36 clocks with the LHC collision frequency to the front-end boards, which need it to perform the TDC functionality.

6.1.5 Cabling and connectors

To connect the front-end boards to the DCT in the BM and BO regions, the legacy cables currently connecting the front-end boards to the Pads will be used. Therefore, the connectors of the BMBO DCT have to be compatible with the current cabling scheme. The interface with the BM and BO legacy front-end electronics depends on the detector region. The BM and BO RPCs have both η and ϕ strips. The η signals are transmitted to the DCT from four 8-channel front-end boards, whose connectors are grouped together into one copper wire cable, through 68-pin connectors, 32 of which carry the single-ended signals, 32 are used for the ground reference and 4 are unconnected. The ϕ signals are transmitted through either 68-pin or 80-pin connectors, depending on the RPC chamber size. The 80-pin connectors carry 40 single-ended signals and 40 ground references from five 8-channel front-end boards. Each BMBO DCT receives RPC hit signals from up to 36 front-end boards through 4×68-pin connectors for the η signals and 4×68-pin (for BM2 RPCs) or 4×80-pin connectors (for BM1 and BO RPCs) for the ϕ signals. Even though the ϕ connectors are different in these two cases, there is no need to develop two separate board designs: indeed for the ϕ connectors, the BMBO DCT has four 80-pin PCB footprints, on which both the 68-pin and the 80-pin connectors can be mounted. Thus, the maximum number of RPC strips connected to one BMBO DCT is 288.

In the BI region, the front-end boards are connected to the DCT through 12×68-pin connectors. Each 68-pin connector is connected to 3 front-end boards, each sending out 8 differential LVDS signals for the RPC hits, 1 single-ended discriminator OR signal, 1 differential clock and 3 ground references.

6.1.6 The DCT board prototypes

The prototype of the first version of the BMBO DCT board, shown in Figure 6.3, was produced in 2021 and, since then, it has been extensively tested both for its functionalities and its performance. The basic functionality of all the different DCT components (optical transceiver, LVDS receivers, lpGBT, flash memory and connectors) has been tested and no issues have been detected. The measured power consumption of the DCT board prototype, powered with a supply of 3.5 V, is 9.7 W after the upload of the FPGA firmware, including also the optical transceiver consumption. The total power consumption of the current RPC on-detector electronics (Pads and Splitters) is 26 kW, which, if divided by the total number of DCTs that will be installed in the Phase-II Upgrade (1546), gives an estimate of the maximum power consumption allocated per DCT, which corresponds to about 16.8 W. The value measured with the prototype is therefore within this estimate, leaving even an abundant margin.

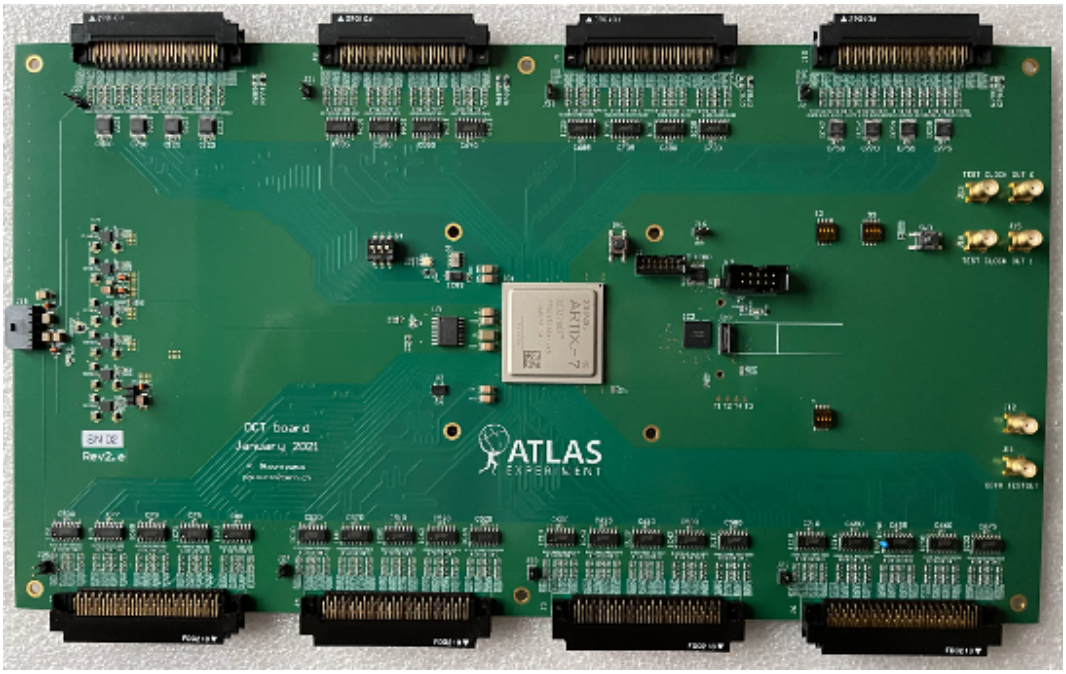

Figure 6.3. First version of the BMBO DCT board prototype.

Radiation tests have also been carried out to validate the radiation tolerance of the DCT components individually and of the board in its entirety. No deterioration

of the performance of the board and of its components has been observed after the irradiation with the doses required by the Radiation Tolerance Criterion (RTC). The RTC is obtained as the radiation level expected from ten years of operation of the HL-LHC multiplied by a safety factor [152]. Three main types of damage can affect semiconductor devices in the high radiation level environment of the LHC experiments:

- The Total Ionising Dose (TID) is the energy deposition due to ionising particles that create hole-electron pairs when crossing the semiconductor. The charge accumulated in the device can degrade its performance or damage it.
- Damage to the semiconductor may originate from atom displacements due to the elastic scattering of a particle on the nuclei of the lattice. To test this type of damage, the Non-Ionising Energy Loss (NIEL) is used.
- Single Event Effects (SEE) are radiation effects due to a large energy deposit left by the ionisation of a high-energy particle. These events are classified as non-destructive, like Single Event Upset (SEU) and Single Event Transient (SET), and destructive effects, like Single Event Latchup (SEL) and Single Event Burnout (SEB).

The radiation levels expected in the MS for ten years of HL-LHC operation, obtained from a GEANT4 simulation, are reported in Table 6.2 together with the corresponding RTC values.

Table 6.2. Simulated radiation level (SRL) on DCT for $4000\,\mathrm{fb}^{-1}$ and the corresponding Radiation Tolerance Criterion (RTC) requirement for the three types of radiation damage.

Type	Unit	SRL	RTC
TID	Gy	18.4	82.6
NIEL	$\mathrm{n/cm^2}$	7.20×10^{11}	4.21×10^{12}
SEE	$\mathrm{h/cm^2}$	1.38×10^{11}	1.24×10^{12}

Tests to evaluate the performance of the BMBO DCT firmware described in Section 6.2 have been performed too. A testbench has been set up using the BMBO DCT prototype to read out the cosmic muon hits detected by two legacy RPC chambers. The main goal was the test of the TDC performance and to measure the time resolution. The measured resolution was $\sigma_T = 0.36\,\mathrm{ns}$, which is compatible with the expected RPC resolution.

On the basis of the tests performed on the first BMBO DCT prototype, a second version has been designed with a few changes with respect to the first one.

The most relevant change is the replacement of the optical transceiver. Indeed, in the first prototype, the VTRX+ transceiver was used, which is a radiation-tolerant optical transceiver based on the Versatile Link Plus architecture [153] developed specifically for the HL-LHC upgrade projects. However, considering that there exist commercial SFP+ transceivers which are perfectly compatible with the needs of the Phase-II RPC-based trigger and readout system and are also radiation tolerant, for the second version of the BMBO DCT the VTRX+ module has been replaced by a less expensive commercial SFP+ transceiver. Moreover, an additional LDO voltage regulator for the 1.0 V power supply has been included in the design to avoid excessive heating. Finally, some other minor modifications have been introduced to the DCT design, like the movement of the lpGBT and the transceiver to the border of the board and the addition of holes to allow the mounting of passive cooling bars, if necessary. The prototype of the second version of the BMBO DCT was delivered at the beginning of 2024 and it is currently undergoing a series of validation tests.

For the BI DCT instead, there is still no prototype available. The BI DCT design, mainly based on the BMBO DCT, is almost complete and the prototype production is foreseen during the course of 2024.

6.2 The BMBO DCT firmware

The core of the DCT functionalities lies inside the FPGA, where a large number of logic ports is interconnected to execute complex operations. The task of activating the basic logic ports, routing the connections between them and concatenating them to form composite structures able to perform elaborate logic functions is assigned to the FPGA firmware. The main functions of the BMBO DCT firmware are the measurement of the rising time of the RPC hit signals, the suppression of the null data and the transmission of the hits to the SL board via the lpGBT. The functional logic block diagram of the BMBO DCT firmware is shown in Figure 6.4. The firmware is designed to receive up to 288 front-end signals, which can be masked out in case the DCT reads out a smaller number of front-end channels or if some channels appear to be particularly noisy. The 288 input channels are divided in the following way: a maximum of 64 channels for the η strips and 80 channels for the ϕ strips for each of the two gas gaps that compose one RPC doublet chamber. The input signals are sampled by 288 deserialisers, which are followed by the TDC logic which measures the rising edge time of the RPC hits. After zero-suppression, the RPC data are buffered by two stages of FIFO memories before being sent out to the lpGBT.

The entire logic that composes the BMBO DCT firmware, which is described in more detail in the following sections, has been simulated with the Vivado Design Suite software [148] (with version 2023.2). A simulation testbench has been set up which sends as input to the DCT firmware the hits expected in a BM RPC station with the instantaneous luminosity of the HL-LHC. More information on the simulated RPC hits is given in Section 6.2.6.

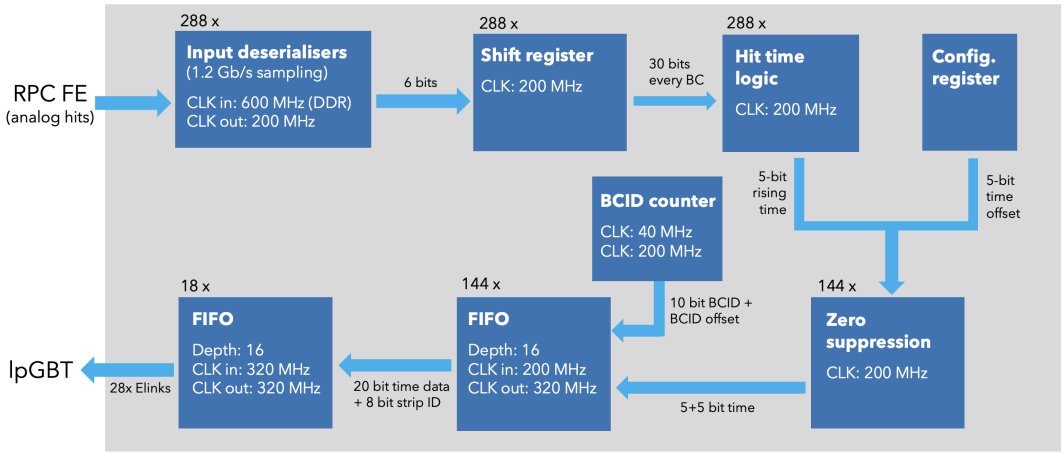

Figure 6.4. Logic block scheme of the BMBO DCT firmware.

6.2.1 Clocks

Even though the lpGBT can deliver up to four different clocks to the FPGA, the firmware design is based only on one differential input clock, expected to have the LHC collision frequency[1]. Two clock multipliers are used to generate the 200 MHz, 320 MHz and 600 MHz clocks needed by the firmware internal logic starting from the input 40 MHz clock. The generated clocks are routed to the firmware logic blocks as shown in Figure 6.5. The 200 MHz clock is used by the input deserialisers, the TDC and zero-suppression logic and the first stage of FIFO memories, the 320 MHz clock is needed by both stages of FIFO memories and the 600 MHz clock is used only by the deserialiser to perform the input sampling. Finally, both the 40 MHz and the 200 MHz clocks are needed by a logic block that generates the bunch crossing ID (BCID) to identify the current LHC collision (the BCID ranges from 0 to 3562).

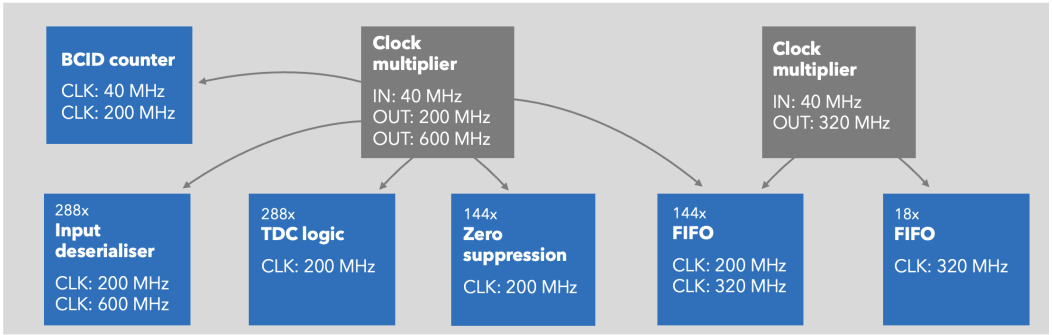

Figure 6.5. Clock scheme of the BMBO DCT firmware.

[1]The actual LHC collision frequency is 40.079 MHz, but in the development of the firmware, for simplicity, the rounded value of 40 MHz has been used since it makes no difference for simulation and implementation purposes. The same approximation also applies to the multiples of the LHC frequency.

6.2.2 TDC logic

The firmware input signals are 288 analog pulses whose time duration is correlated to the charge collected by the RPC chambers. A set of input deserialisers embedded in the FPGA I/O logic, one for each front-end channel, receives the RPC signals and uses the 600 MHz clock with double data rate (DDR) to sample them at 1.2 Gb/s. The deserialiser output is a 6-bit word synchronous with the 200 MHz clock. 288 shift registers assemble the 6-bit words to form a 30-bit frame. Each deserialiser output word is stacked on top of the 30-bit shift register every 5 ns, so that the least significant bit (LSB) is always the oldest bit. Once every 25 ns the 30-bit frames are passed to 288 hit time logic blocks, which have the task of performing the TDC operation. Working with the 200 MHz clock, the hit time logic measures the rising edge time (namely the position of the 0-1 transition) in the 30-bit frame, providing this information as a 5-bit word. Since there are 30 possible positions for the 0-1 transition, the content of the 5-bit word representing the rising edge time can range from 1 to 30. The value 0 is used instead if no transition is found. In this way, the resolution of the TDC, given by the inverse of the sampling frequency, is 833 ps. Figure 6.6 shows the output of the different logic blocks described in this section, starting from an RPC hit signal to the measured 5-bit rising edge time, obtained through the firmware simulation.

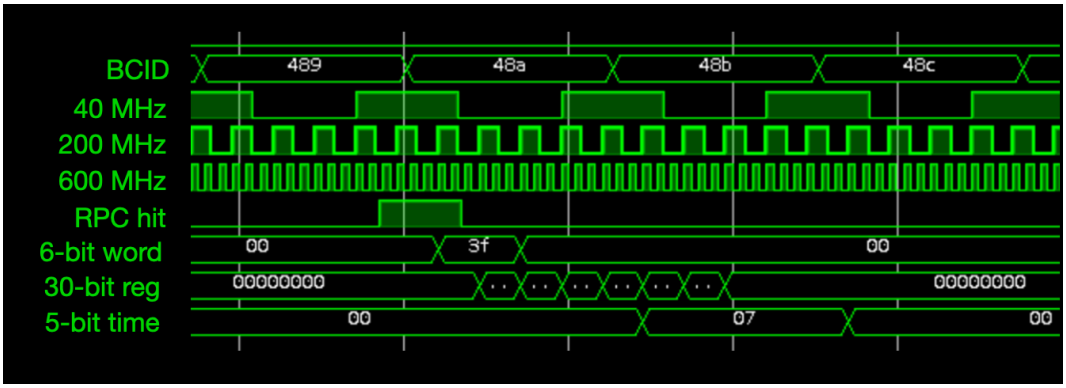

Figure 6.6. Snapshot of the BMBO DCT firmware simulation showing the BCID counter, the 40 MHz, 200 MHz and 600 MHz clocks, one RPC hit pulse signal, the relative 6-bit word produced by the deserialiser, the 30-bit shift register and the 5-bit rising edge time measured by the TDC.

A first version of the firmware included also the measurement of the falling edge time of the RPC hits. However, since the falling edge time is not needed for trigger or object reconstruction purposes, it has been chosen to remove its measurement from the firmware, saving in this way half of the bandwidth used to transmit RPC data to the SL and reducing the occupancy and the latency of the firmware. If needed for calibration, the falling edge time can be anyway measured and transmitted with low priority to the SL board.

Going back to the version of the firmware with only rising time measurement, after the TDC logic the two 5-bit words representing the rising time for the cor-

responding RPC strips of the two gas gaps of the same RPC doublet chamber are assembled to be transmitted together to the SL. In this way, the same strip number has to be transmitted only one time, allowing us to save bandwidth, contrarily to what would happen if the time measurements of the two gas gaps were sent separately. At this point, the 10-bit words carrying the two rising times have to be buffered by FIFO memories before they can be sent to the lpGBT. In order to avoid transmitting the words containing no time measurement, a zero-suppression logic block is implemented: this logic allows the 10-bit words to be written into the FIFOs only if they are different from 0, that is only if they contain a hit time measurement for a specific strip (on at least one of the two gas gaps).

6.2.3 FIFO pipeline

RPC hit data cannot be transmitted to the lpGBT as soon as the time measurement is performed, since the output bandwidth is limited. The words containing the time information are therefore queued into the FPGA buffer memories waiting for their turn to be transmitted. For this purpose a two-stage pipeline of RAM memories configured with the FIFO (First In First Out) mode is implemented.

The first stage consists of 144 FIFO memories, one for each strip number, having a width of 20 bits and a depth of 16 words. After the zero-suppression, by combining the hit time word with the 10 least significant bits of the corresponding 12-bit BCID, a 20-bit word is formed, which is written into the FIFOs using the 200 MHz clock. A maximum of 16 hits for each strip index can be stored in the FIFOs at the same time. If a larger number of hits per strip arrives before the old hits are read out, the new hits get lost. Anyway, the simulation shows that this first stage of memories is never filled completely.

The second stage of FIFOs is made of 18 memories with a width of 28 bits and a depth of 16 words. Each memory of the second stage reads data from 8 memories of the first stage at 320 MHz, to allow serialisation of the incoming hit data towards the lpGBT. Together with the time information and the BCID read out from the first stage of memories, also the strip number is stored in the second FIFO stage, obtaining a 28-bit word. The E-links that connect the FPGA to the lpGBT allow the transmission of one 28-bit word at a time at 320 MHz. So the 18 memories of the second stage are read out one at a time according to a priority given by their index. Contrarily to the case of the first FIFO stage, the memories of the second stage, which also in this case can store up to 16 words, may be completely filled in case of events with high hit multiplicity, with the consequent loss of some hits.

The fraction of lost hits can be estimated through simulation using simulated hit data for one of the BM RPC chambers with the highest hit rate. Two simulations have been performed, one with RPC hits simulated assuming an instantaneous luminosity of about $7 \times 10^{34}\,\mathrm{cm^{-2}s^{-1}}$, a value close to the maximum value reached by the HL-LHC in the highest performance conditions, and another one assuming an instantaneous luminosity of about $11 \times 10^{34}\,\mathrm{cm^{-2}s^{-1}}$, to take into account also

a safety factor. In the first case, on more than 112 000 hits only the 0.002% is lost, with none of the lost hits associated with a true muon, while in the second case the percentage of lost hits is 0.003% on a total of 166 000, including this time also some muon hits (0.03% of the total hits associated with a true muon). From the simulation results, it can be therefore concluded that the fraction of lost hits due to the complete filling of the memories is negligible. Figure 6.7 shows the occupancy distributions of each second stage FIFO obtained from simulation.

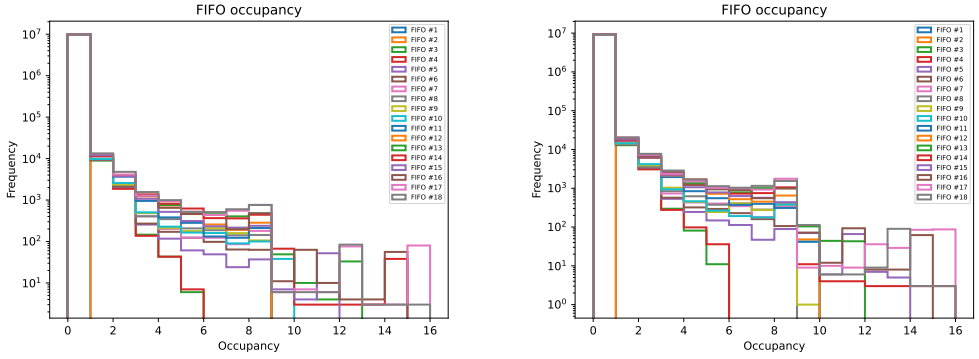

(a) (b)

Figure 6.7. Distributions of the occupancy of the second stage FIFO memories of the BMBO DCT firmware obtained from simulation assuming an instantaneous luminosity of $7.2 \times 10^{34}\,\mathrm{cm^{-2}s^{-1}}$ (a) and $10.8 \times 10^{34}\,\mathrm{cm^{-2}s^{-1}}$. The frequency on the vertical axis refers to the number of clock cycles at 320 MHz the memories had a certain occupancy level.

6.2.4 Output data format

As stated in Section 6.1.3, data can be transmitted from the FPGA to the lpGBT via 28 E-links. In order to optimise the data transmission, the DCT firmware has been developed considering an output data format of 28-bit words. In this way, the 28 E-links can be used in parallel to transmit one bit of the output word each at 320 MHz. The same 28 E-links are used to send both RPC hit time data and monitoring data and therefore they need to be formatted in such a way that the SL firmware can distinguish them. The output data format that has been chosen is reported in Figure 6.8. The 28 bits forming the RPC hit time word are organised in the following way: the 8 most significant bits are used for the strip index, which is a number lower than 144 (the indices from 0 to 63 refer to the η strips, while the indices from 64 to 143 to the ϕ strips), the following 10 bits represent the least significant bits of the BC in which the hit occurred and the last ten bits carry the rising edge time measurements of the two layers (namely the gas gaps) of the RPC doublet. The 28 bits of the monitoring data are instead divided between an 8-bit identifier, which is a number greater than 144 so that monitoring words cannot be confused with RPC time data, and 20 bits for the actual content (like temperatures,

SEU monitoring, hit rates).

RPC hit time data format

8-bit strip ID (<144)								10-bit BCID										5-bit rising time layer 0					5-bit rising time layer 1				
27	26	25	24	23	22	21	20	19	18	17	16	15	14	13	12	11	10	9	8	7	6	5	4	3	2	1	0

Monitoring data format

8-bit ID (>=144)								Monitoring data																			
27	26	25	24	23	22	21	20	19	18	17	16	15	14	13	12	11	10	9	8	7	6	5	4	3	2	1	0

Figure 6.8. Output data format for RPC hit time data and monitoring data of the BMBO DCT firmware.

6.2.5 Configuration and monitoring

The DCT configuration commands arrive at the FPGA from the lpGBT through one E-link with a speed of 320 Mb/s. The SL board sends the configuration data as 32-bit words with a 12-bit header. A logic block in the DCT firmware, working with the 320 MHz clock, deserialises the serial stream coming from the configuration E-link using the 12-bit header to align the 32-bit words. The content of these data is used to program the following configuration registers:

- Input channel mask: a 288-bit register used to mask the 288 input front-end channels. This mask may be useful in case some particularly noisy channels need to be switched off or in case less than 288 channels are connected to the DCT.
- Time calibration registers: one 5-bit register every 16 front-end channels containing time calibration data. These data are summed to the measured hit time after the TDC logic in order to have the rising edge at the centre of the BC.
- Coarse timing offset registers: a 4-bit register every 16 front-end channels to be summed to the BCID to calibrate the BCID with respect to the SL.
- BC offset register: a 6-bit register used by the BCID counter logic to take into account the length of the fibre connecting the DCT to the SL.
- Dead-time register: a 3-bit register containing the dead-time to be applied to the input channels.

Aside from the RPC hit time data, the DCT FPGA sends to the SL information on the status of the FPGA. These monitoring data are transmitted to the lpGBT through the same 28 E-links used for the RPC data. Therefore a priority logic has

been developed to handle the output data flow, assigning high priority to the RPC data and low priority to monitoring words. The following information has to be sent to the SL:

- FIFO occupancy: in case a FIFO is almost full, a monitoring word with a busy signal has to be sent out.
- SEU monitoring: in the case of SEU, which is automatically corrected by an SEM (Soft Error Mitigation) block, a monitoring word has to be sent out.
- FPGA temperature.
- RPC hit rates: 288 counters to measure the RPC hit rate for the 288 input front-end channels, to be sent to the SL with lower priority with respect to the previous monitoring data.
- The busy signal from FIFO occupancy and the SEU monitoring can be also sent in real-time using the 2-bit EC-field of the uplink frame.

The logic related to the monitoring data is still not included in the current version of the BMBO DCT firmware. In the current version, the monitoring words carry the content of the configuration registers. Also the decoding logic for the TTC data received by the FPGA through the dedicated E-link is still to be implemented (the only TTC signal used by the DCT firmware is the BC reset needed by the BCID counter logic).

6.2.6 Latency

A very important characteristic of the DCT FPGA firmware that can be evaluated through the simulation is certainly its latency, that is the time that passes between the reception on the FPGA of the front-end RPC hit signal and the transmission of the corresponding hit time word to the lpGBT. The firmware logic of the BMBO DCT FPGA has no fixed latency, since the RPC data are buffered in the FPGA memories and then sent out sequentially. A distribution of the latency can be obtained by the subtraction of the BCID of the output data from the number of the BC in which those data are sent out.

The simulation is performed with three sets of input RPC hit signals, representing different RPC chambers and different pileup conditions. The RPC signals used for the simulation of the BMBO DCT firmware are data collected by the RPC detector during the LHC Run 2 (with $\mathscr{L} = 1.8 \times 10^{34}\,\mathrm{cm^{-2}s^{-1}}$) and extrapolated to the HL-LHC instantaneous luminosity. The extrapolation is performed by superimposing the data collected in multiple BCs to obtain the signals corresponding to one HL-LHC BC. Two pileup conditions are considered: in the first case the superimposition includes 4 BCs for a total simulated instantaneous luminosity of $7.2 \times 10^{34}\,\mathrm{cm^{-2}s^{-1}}$, a value similar to the one of the HL-LHC highest performance scenario, while in the second case data from 6 BCs are superimposed, obtaining an instantaneous luminosity of $10.8 \times 10^{34}\,\mathrm{cm^{-2}s^{-1}}$, well above the maximum HL-LHC value. The three sets of RPC signals used for the simulation are the following:

- one set of RPC signals of the BML3 station with 4 superimposed BCs;
- one set of RPC signals of the BML3 station with 6 superimposed BCs;
- one set of RPC signals of the BML6 station with 6 superimposed BCs;

The RPC stations chosen for the simulation are among the stations with the highest hit rate and geometric acceptance. Figure 6.9 shows the BMBO DCT firmware latency distribution obtained from simulation with the three sets of input signals mentioned above.

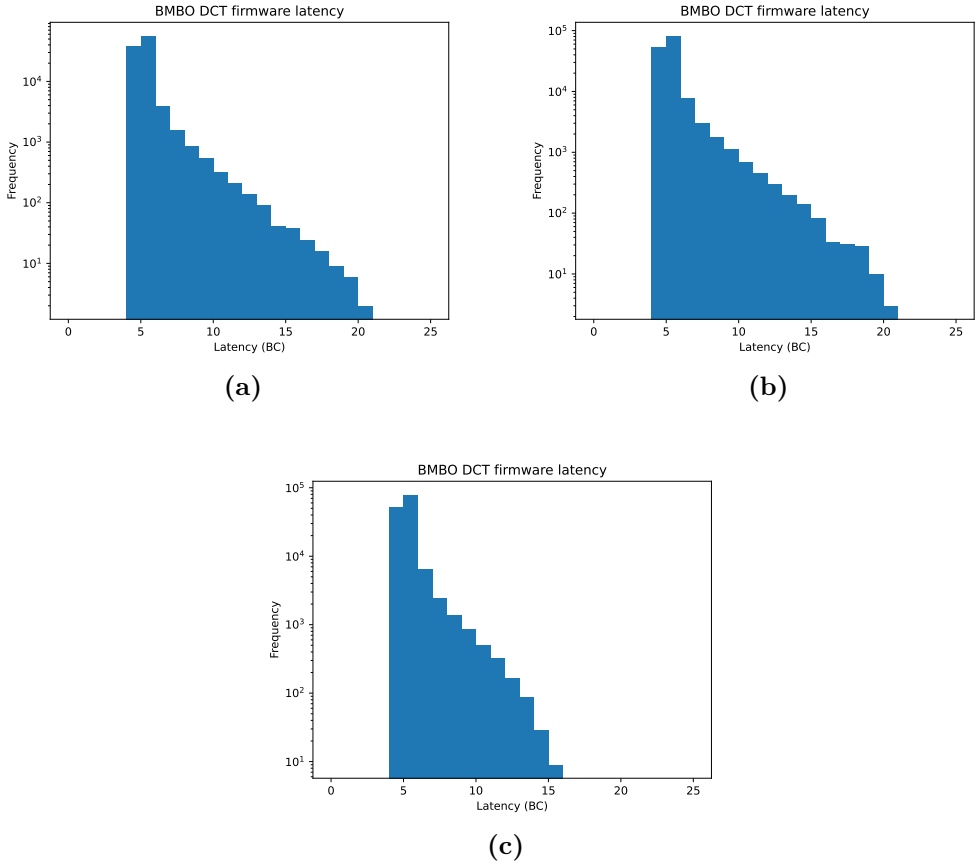

Figure 6.9. BMBO DCT firmware latency measured from simulation with three sets of input RPC signals: BML3 station signals with 4 superimposed BCs (a), BML3 station signals with 6 superimposed BCs (b) and BML6 station signals with 6 superimposed BCs (c).

From the simulation, a minimum latency of 4 BCs is obtained, while the maximum latency depends on the η sector. The distributions with the BML3 station signals show a maximum latency of 20 BCs in both the simulated pileup conditions, while in the BML6 case there are no hits with a latency larger than 15. The maximum latency allocated for the DCT by the Phase-II Muon TDAQ design is 548 ns [154], corresponding to about 22 BCs. This latency has to include both the

latency of the FPGA firmware and the latency of the lpGBT and other contributions external to the FPGA. The lpGBT latency can be estimated from hardware DCT tests and has still to be measured, but it is expected to be within a few BCs. The FPGA latency estimated from the BMBO DCT firmware simulation with the BML6 station is therefore compatible with the Phase-II FPGA latency requirement. The latency obtained from the simulations with the BML3 instead is a bit larger than the FPGA latency requirement: in the overestimated hypothesis of an lpGBT latency of 4 BCs (and a consequent FPGA allocated latency of 18 BCs), the percentage of hits exceeding the FPGA allocated latency would be 0.008% in the highest pileup scenario. Anyway, even if the allocated FPGA latency is exceeded, the data are still delivered to the SL board, which will not use them for the trigger algorithm but will send them to the readout system.

6.2.7 FPGA resource occupancy

The BMBO DCT firmware has been implemented using the Vivado Design Suite software without incurring timing closure issues. The total amount of resources of the BMBO DCT FPGA occupied by the firmware, divided per resource type, is reported in Table 6.3.

Table 6.3. FPGA resource utilisation of the BMBO DCT firmware.

Resource	Available	Utilisation	Utilisation %
LUT	133800	27249	20.37
LUTRAM	46200	2396	5.19
FF	269200	37693	14.00
IO	500	348	69.60
BUFG	32	8	25.00
MMCM	10	2	20.00

For all the resource types, a low utilisation level is obtained, indicating that the Artix-7 FPGA chosen for the BMBO DCT is perfectly suitable for the implementation of its firmware. No occupancy issues are expected from a small amount of additional logic that is still missing from the current implemented version of the firmware, which comprises the TTC signal decoding logic and monitoring logic. The missing logic is foreseen to increase the utilisation of lookup tables (LUT) and flip-flops (FF), whose current utilised fraction is quite low (20.37% for LUT and 14.00% for FF). Figure 6.10 shows the Artix-7 device, highlighting the positions of the CLBs used to implement the logic of the BMBO DCT firmware.

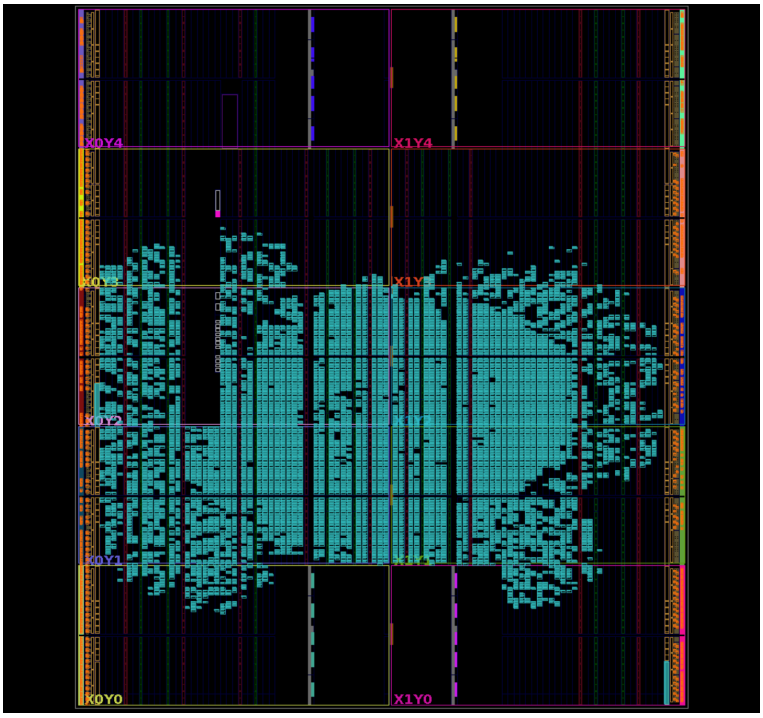

Figure 6.10. FPGA device after the implementation of the BMBO DCT firmware. The logic cells used to implement the firmware are highlighted.

6.3 The BI DCT firmware

The baseline structure of the BI DCT firmware is inherited from the BMBO version. Among the common aspects between the two versions, there are the number of input channels, the connections with the lpGBT (which determine the output word length), the clock scheme, the two-stage FIFO pipeline to read out the data and the configuration and monitoring logic. However, the firmware logic is profoundly different in the two versions, since the BI RPC characteristics and the BI front-end design require a very specific processing of the RPC time data by the DCT before they can be sent to the SL board. Figure 6.11 shows the functional logic block diagram of the BI DCT firmware. A first relevant difference from the BMBO version is constituted by the input signals, which in the BI case contain the rising and falling edge time of the RPC hits, previously digitised by the front-end boards. The BI RPC chambers do not have ϕ strips and so the BI DCT input channels represent only η strips. Each of the three gas gaps of the BI RPC triplet has two layers of 48 η strips, one read out on the left side and the other one on the right side, for a total of 288 channels. Another aspect that distinguishes the BI DCT firmware from the BMBO version is a logic block that decodes the front-end data, which are sent from the front-end boards using the Manchester encoding protocol. Finally, a large difference resides in the main logic blocks of the firmware, which in the BI case have to perform more complex operations to extract the ϕ coordinate from the time measurements of the η strips.

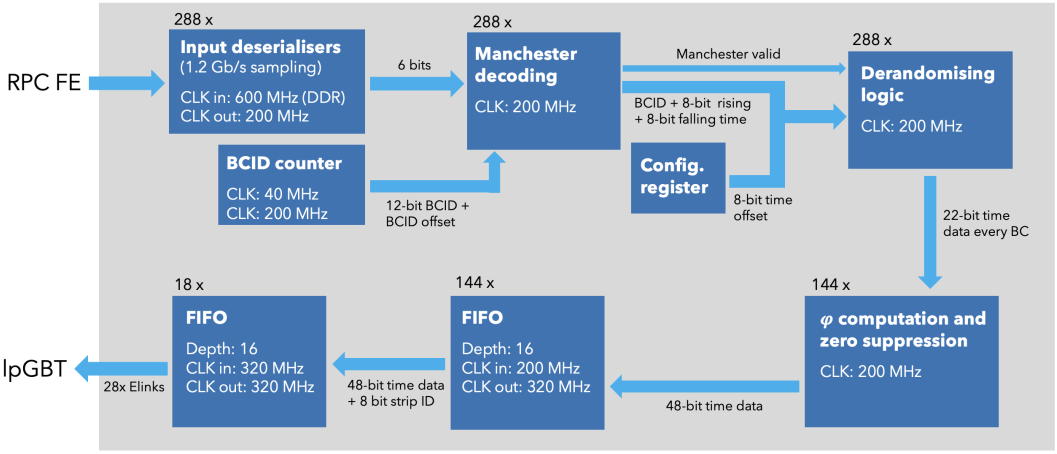

Figure 6.11. Logic block scheme of the BI DCT firmware.

The clock scheme used in the BI DCT firmware is analogous to the BMBO DCT one, with two clock multipliers that use the 40 MHz input clock to generate the 200 MHz, 320 MHz and 600 MHz clocks, with the 600 MHz clock used only by the deserialisers, the 320 MHz clock used by the FIFO memories and the 200 MHz clock by the rest of the logic.

As in the case of the BMBO DCT firmware, also the logic of the BI DCT firmware has been simulated with the Vivado Design Suite software (with version 2023.2). The BI RPC hits given as input to the firmware by the simulation testbench have been obtained starting from the hits collected in Run 2 by the RPC detectors in the BM region (from a large sector at $|\eta| = 3$) and then extrapolated to rate expected in the BI region. The high pileup condition has been obtained superimposing the hits collected in 6 different BCs, for a total simulated instantaneous luminosity of $10.8 \times 10^{34}\,\mathrm{cm}^{-2}\mathrm{s}^{-1}$, much higher with respect to the highest value foreseen in the LHC high luminosity phase.

6.3.1 Decoding

For the BI RPCs the TDC is performed by the front-end boards, which measure both the rising and falling edge time of the RPC hits (with a 100 ps time resolution), encode them using the Manchester encoding protocol and send them to the DCT board. The Manchester protocol encodes the data performing a XOR logic operation between the unencoded data and the transmission clock, as illustrated in Figure 6.12. In this way there is always a signal transition in the middle of one encoded bit, with the type of transition (0 to 1 or 1 to 0) indicating the bit content (0 or 1). The advantage of this encoding protocol resides in the fact that it does not need an external synchronization signal. RPC hit time data are transmitted from the front-end boards as groups of 16 bits (8 for the rising edge and 8 for the falling edge time) preceded by a specific signal sequence to indicate the start of the hit transmission. Zero idles are transmitted in case of no TDC data.

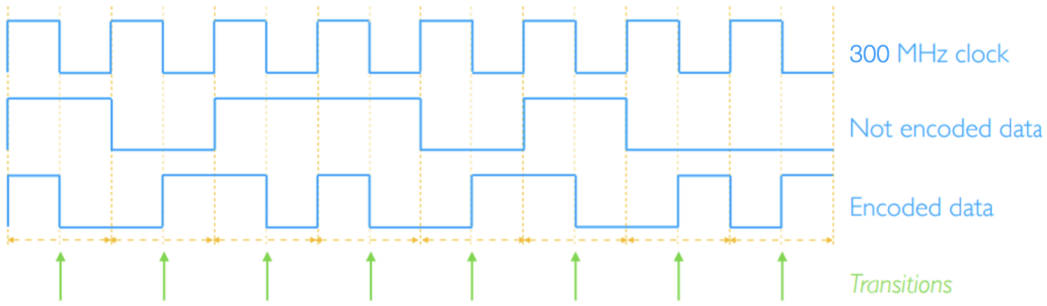

Figure 6.12. Manchester encoding protocol.

As for the BMBO version, the front-end input data are deserialised by 288 embedded deserialiser working with the 600 MHz DDR clock for a sampling rate of 1.2Gb/s. Each deserialiser produces 6 bits at 200 MHz which are passed to the decoding logic block. This logic block adds the deserialised bits to a 72-bit shift register, which is decoded if a hit transmission start sequence is found. To the 16-bit time data output, also the BCID is associated. An additional signal from the decoding logic block tells if the decoded data are valid. Figure 6.13 is a snapshot of the BI DCT firmware simulation showing the signal carrying the encoded time data of a BI RPC hit, together with the deserialised bits and the decoded data produced by the Manchester decoding logic block.

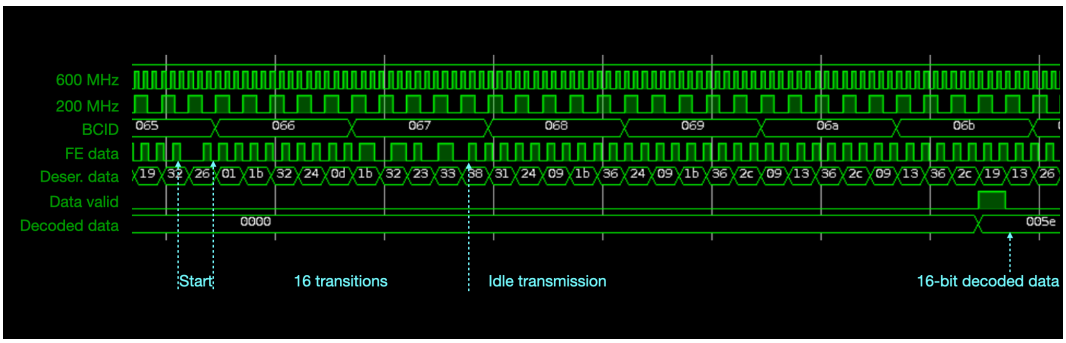

Figure 6.13. Snapshot of the BI DCT firmware simulation showing the 600 MHz and 200 MHz clocks, the BCID counter, the signal of one front-end channel, the data after deserialisation and the decoded hit time data together with the Manchester valid signal.

6.3.2 Estimate of the ϕ coordinate

The BI RPC detectors do not have ϕ strips and therefore cannot provide directly information on this coordinate for the muon hits. However, differently from the BMBO RPCs, the BI RPC strips, which measure only the η coordinate, have readings on both sides (which will be referred to as left and right readings). Exploiting the very good time resolution of the left and right rising edge time measurements of the η strips, it is possible to obtain a decent estimate of the other coordinate. Before the computation of the ϕ coordinate of a hit, however, it is necessary to be sure that both left and right time data have arrived at the DCT. Indeed, since the time data arrive at the DCT with a non-fixed latency and left and right measurements of the same η strip are sent from different front-end channels, it is very likely that the two measurements required by the ϕ estimate are not available at the same time. Hence a derandomising logic block per front-end channel is introduced in the firmware with the task of storing into registers the rising and falling time information for a few[2] BCs, so that left and right data for a certain BC can be provided together to the subsequent logic block. The position x along the ϕ coordinate is given by

$$x = \frac{v}{2}(t_2 - t_1) + const, \tag{6.1}$$

where t_1 and t_2 are the signal arrival times from the left and right readings and v the signal propagation velocity, measured to be $v = 20\,\text{cm/ns}$. With a time resolution[3] $\sigma_t = 0.2\,\text{ns}$, the resolution on the position is

$$\sigma_x = \frac{v}{2}\sqrt{2}\sigma_t = 2.8\,\text{cm}. \tag{6.2}$$

The ϕ coordinate estimation is performed by 144 logic blocks (since each of them uses the data from two front-end channels), which compute the difference between the left rising time and the right rising time of the same η strip and apply the calibration factor $(v/2)$ and the offset, obtaining in this way an 8-bit estimate of position along the ϕ coordinate for that hit.

At this point, all the information related to a specific strip index, namely BCID, ϕ coordinate, rising and falling edge time of left and right readings, is combined to form a 48-bit word which is sent to the FIFO memories. Only data with at least one measurement[4] different from 0 are written into the FIFOs (zero-suppression). The same two-stage FIFO pipeline of the BMBO DCT firmware is used to organise and assign a priority to the data before sending them to the lpGBT. The only difference is in the FIFO width, which is 48 bits for the first stage and 56 bits for the second stage (due to the addition of the strip index to the data from the previous stage memories). An RPC hit is therefore represented by a 56-bit word, as

[2] In the current version of the BI firmware the incoming data are stored for the time duration of 5 BCs. This is an overestimation of the latency difference between the various front-end channels and will be reduced when a more precise value will be available, with a consequent reduction of resource occupancy and firmware latency.

[3] The nominal TDC time resolution is 100 ps, but, due to noise and other effects, it is likely that the actual time resolution available for the ϕ estimate will not be lower than 200 ps.

[4] One measurement between rising and falling time of left and right readings.

described with more details in Section 6.3.3, which is divided into two 28-bit words and sent to the lpGBT through the 28 E-links with two cycles of the 320 MHz clock.

6.3.3 Output data format

The output data format for the BI RPC hit data and the monitoring data is shown in Figure 6.14. The information related to one RPC hit is transmitted with two consecutive 28-bit words, identified by their two most significant bits. The first word includes an 8-bit BCID, the 8 bits of the η strip index (which is a number lower than 144) and the 8 bits of the estimated ϕ coordinate. The second word, instead, contains the left and right time measurements. For the rising time, the full 8-bit information provided by the front-end TDC is transmitted, while for the falling time, due to the limits imposed by the 28-bit format, only the 6 most significant bits are carried, with a consequent degradation of the falling time resolution. For space reasons, the right falling time measurement has been divided between the first and the second word. This RPC hit data format has been chosen to facilitate the data processing by the SL firmware: indeed all the information needed for the trigger algorithm is contained in the first word, while the second word is sent directly to the readout logic.

The configuration registers and the monitoring data of the BI DCT firmware are the same as described in Section 6.2.5 for the BMBO DCT firmware. For the BI monitoring data, the two most significant bits are reserved as the identifier, while the remaining 26 bits can be used to carry the monitoring information.

BI DCT time data

Word ID ("01")	8-bit BCID								8-bit strip ID (<144)								8-bit ϕ coordinate								2-bit (MSB) right fall time	
27	26	25	24	23	22	21	20	19	18	17	16	15	14	13	12	11	10	9	8	7	6	5	4	3	2	1	0

Word ID ("10")	8-bit left rising time								6-bit left falling time						8-bit right rising time								4-bit right falling time			
27	26	25	24	23	22	21	20	19	18	17	16	15	14	13	12	11	10	9	8	7	6	5	4	3	2	1	0

BI monitoring data

Word ID ("11")	Monitoring data																									
27	26	25	24	23	22	21	20	19	18	17	16	15	14	13	12	11	10	9	8	7	6	5	4	3	2	1	0

Figure 6.14. Output data format for RPC hit time data and monitoring data of the BI DCT firmware.

6.3.4 Latency

The latency of the BI DCT firmware is estimated from the simulation analogously to the BMBO case. The distribution of the latency, shown in Figure 6.15 is

obtained by subtracting the BCID of the output RPC hit data from the current BC number. The minimum latency is 7 BCs while the maximum measured latency is 21 BCs. The maximum allocated latency for the BI DCT by the Phase-II latency document is about 16 BCs (including both FPGA and lpGBT latency), a value lower than the one allocated for the BMBO DCT. This is because the BI front-end board, which performs the TDC, has a higher latency than the BMBO legacy front-end board. Considering an overestimate of 4 BCs for the lpGBT latency, the maximum allocated latency for the FPGA is thus 12 BCs. From the BI DCT firmware simulation, the fraction of hits reporting a latency larger than 12 BCs is 0.016, which will be reduced after the adoption in the derandomising logic block of a more accurate estimate of the latency difference between the various front-end channels. However, any hit word exceeding the maximum latency would be sent anyway to the SL, which would use it in the readout but not in the trigger logic.

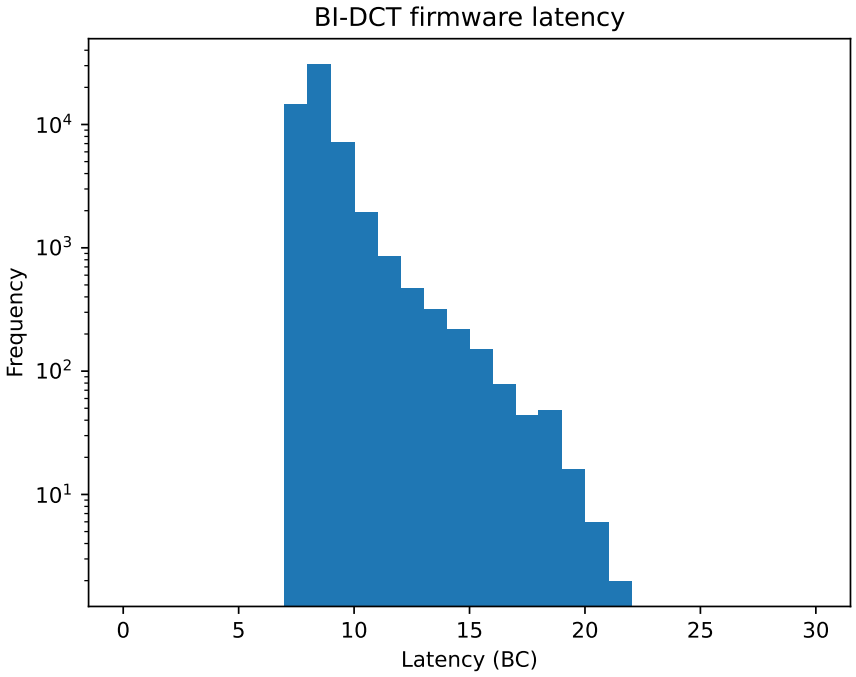

Figure 6.15. BI DCT firmware latency distribution obtained from simulation.

6.3.5 FPGA resource occupancy

The BI DCT firmware has been implemented using the Vivado Design Suite software. A first implementation has been attempted using the same Artix-7 FPGA of the BMBO DCT, but due to the limited routing resources of this FPGA timing closure could not be achieved. The Kintex-7 device instead turns out to be optimal for a successful implementation of the BI DCT firmware. The amount of resources available in the Kintex-7 FPGA and the fraction occupied by the BI DCT firmware

are reported in Table 6.4.

Table 6.4. FPGA resource utilisation of the BI DCT firmware.

Resource	Available	Utilisation	Utilisation %
LUT	203800	145694	71.49
LUTRAM	64000	6484	10.13
FF	407600	114334	28.05
IO	500	348	69.60
BUFG	32	6	18.75
MMCM	10	2	20.00

The fraction of resources used by the implemented firmware is not excessive and does not cause issues with timing closure. As in the case of the BMBO DCT firmware, a small amount of logic is still missing from the current version of the BI DCT firmware (TTC decoding and monitoring logic), but the amount of resources foreseen for this logic is very small and no issues are expected from its addition. Figure 6.16 shows the Kintex-7 device after the BI DCT firmware implementation, highlighting the positions of the logic cells used to implement the firmware logic.

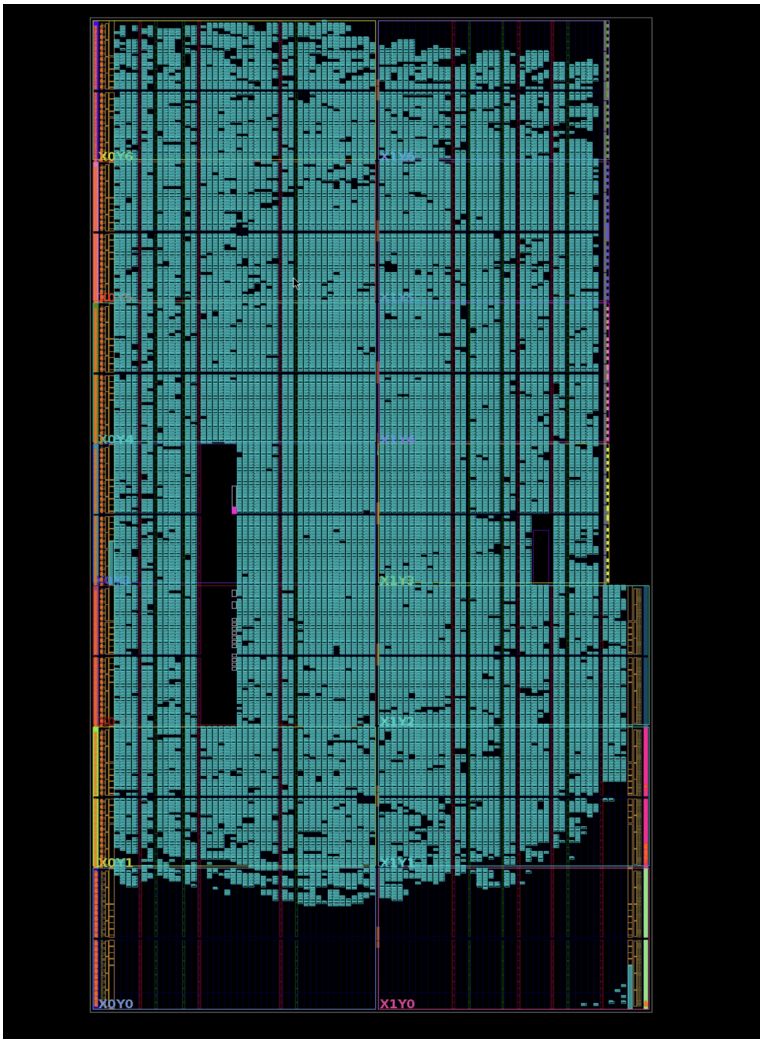

Figure 6.16. FPGA device after the implementation of the BI DCT firmware. The logic cells used to implement the firmware are highlighted.

Chapter 7

Development of the Barrel Sector Logic firmware

While the DCT board represents the novel aspect introduced by the Phase-II Upgrade for the on-detector electronics of the L0 Muon Barrel trigger and data acquisition system, on the off-detector side the novelty is constituted by the adoption of a sophisticated FPGA-based board, called Barrel Sector Logic (SL), which will have to collect all the data recorded by the RPC detectors, perform the L0 Muon trigger algorithm and execute the readout logic. The SL board is based on a much more complex design with respect to the DCT and has to interface with a large number of sub-systems and handle a huge amount of data. The SL board is also the only way to control and configure the on-detector RPC electronics and plays a fundamental role in the ATLAS low-level trigger scheme foreseen for the high luminosity phase of the LHC.

A particularly delicate task lies in the design and development of the firmware that will be implemented in the FPGA to perform the complex operations demanded to the SL board. This task is extremely challenging due to the large amount of resources needed to process all the RPC data, the constraints imposed by the resource location in the FPGA device and the very strict timing constraints required by the L0 Muon trigger scheme. I have contributed greatly to the design of the SL firmware, developing the entire logic dedicated to interfacing with the external systems and processing the RPC data before sending them to the trigger and readout logic and managing the assembly of the various logic blocks which compose the SL firmware, performing the simulation of the logic and solving the implementation issues.

This Chapter is dedicated to the description of the development of the SL FPGA firmware. Section 7.1 introduces the SL board, with a description of its functionality, components and interfaces with the external systems. Section 7.2 presents the SL FPGA firmware, describing in detail the firmware logic, the challenges encountered during its implementation and the strategy adopted to solve the issues.

7.1 The Barrel Sector Logic board

The Phase-II Upgrade foresees the installation of 32 off-detector Barrel SL boards in USA15, one per RPC sector (16 sectors in side A and 16 sectors in side C of the ATLAS barrel). The SL board design is shared between the Barrel and the End-cap L0 Muon TDAQ systems, thus the board layout and components are the same, but the functionalities and interfaces are completely different. The Barrel Sector Logic plays a central role in the L0 Muon Barrel trigger and data acquisition schema and consequently has to interface with a large number of sub-systems, to receive detector data and configuration commands and to transmit readout data and trigger candidates.

The main task of the Barrel SL board, hereinafter simply referred to as SL board, is the execution of the trigger and readout algorithm [155]. This board indeed has to perform the L0 Muon barrel trigger algorithm, selecting muon candidates according to the requirements described in Section 5.3 in less than 390 ns. The selected candidates are then sent to the MDT-TP board which uses the MDT hit information to perform an improved measurement of the muon momentum and confirm or reject the Barrel SL candidates. After the reception of the confirmation, the SL board transmits the trigger candidates to the MUCTPI. At the same time the SL board has to store all the RPC hit data received from the DCTs for 10 µs (the Phase-II L0 trigger latency) and send them to the readout system through the FELIX modules upon a L0-Accept signal from the Central Trigger Processor.

The first SL board prototype, shown in Figure 7.1, is available and all its components have been extensively tested, showing no evidence of anomalies in their functionality. The second prototype, expected to be also the final prototype, is under production. With respect to the first version, the second prototype introduces a few modifications to the SL board schematics regarding the power sequence circuit, the clock distribution and the DC/DC converter.

7.1.1 Physical components

The SL board is an FPGA-based board developed as an ATCA blade. The SL FPGA is the XCVU13P-FLGA2577-1-E from the Xilinx Virtex UltraScale+ family [156]. This device is made of four die slices called Super Logic Regions (SLRs) connected by dedicated routes named Super Long Lines (SLLs) placed mostly in the central part of the die. With about 3.5×10^6 flip-flops, 1.7×10^6 lookup tables and 128 high-speed transceivers (named GTY transceivers) supporting line rates up to 32.75 Gb/s, the XCVU13P FPGA has the type and amount of resources needed to implement a highly-complex firmware like the one of the L0 Muon Barrel SL.

The SL board is provided of a Mercury XU5 MPSoC[1] (Multiprocessor system-on-chip) [157], which is a mezzanine board used for the interface with the Detector Control System (DCS) and the L0 barrel TDAQ server. The MPSoC mezzanine

[1] ME-XU5-5EV-2I-D12E part number

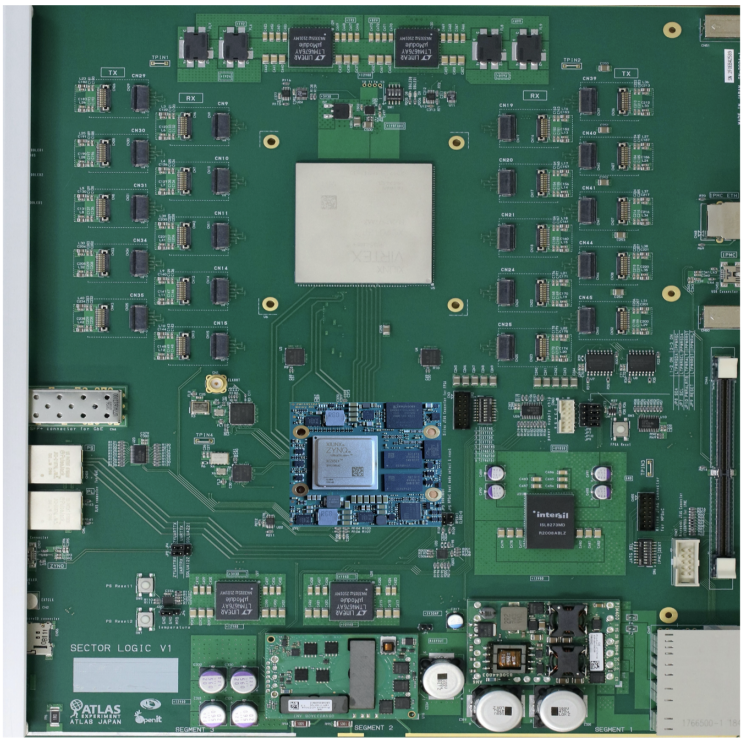

Figure 7.1. First SL board prototype.

communicates with the XCVU13P FPGA through an AXI Chip2Chip (C2C) serial bus and it is used for the following functionalities:

- implementing the ethernet protocol with the L0 barrel TDAQ server;
- receiving the SL and DCT firmwares from the L0 barrel TDAQ server and uploading them on the SL and DCT FPGAs respectively;
- transmitting the configuration and control commands received from the L0 barrel TDAQ server to the SL and DCT;
- sending the DCT and SL monitoring data to the L0 barrel TDAQ server;
- interfacing with the external DCS clients.

The other components that constitute the SL board design are the optical transceivers for the input/output fibres, power modules (DC/DC converters) for supplying the required voltages to the SL chips and temperature and voltage sensors. The optical transceivers are grouped into 20 Samtec FireFly modules connected to the FPGA GTYs, each module providing 12 TX or 12 RX optical fibres. Finally, one IPMC (Intelligent Platform Management Controller) module is used to interface with the ATCA shelf manager, control the power of the SL board and monitor voltages from voltage sensors, current from DC/DC converters and temperatures of FPGA and MPSoC. The maximum power consumption of the SL board is 350 W. A block scheme of the SL board physical components is shown in Figure 7.2.

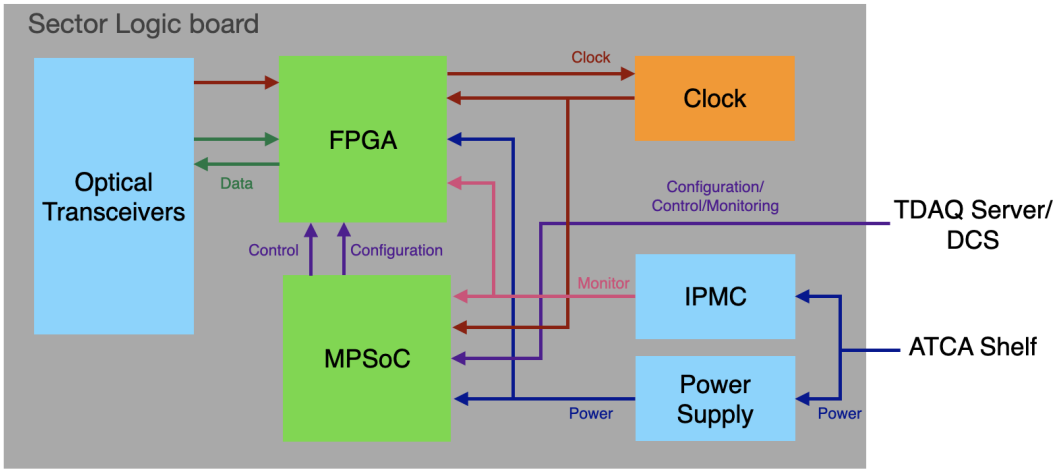

Figure 7.2. Block scheme of the SL board.

7.1.2 Interfaces

Figure 7.3 illustrates the L0 Muon TDAQ system, showing the interfaces of the Barrel SL board with the other sub-systems.

Each SL board can communicate with up to 50 on-detector DCT boards through bidirectional optical fibres. The DCTs send to the SL the RPC hit data and information on the status of the DCTs and the front-end electronics. The SL, instead, transmits to the DCTs configuration commands and the TTC signals needed by the DCT firmware. The SL receives the Tile Calorimeter hit data, which are used by the trigger algorithm for the selection of muon candidates, from 3 TileTDAQi boards through 6 fibres.

The SL board is connected also with one MDTTP board through 8 fibres, used to send up to 8 muon trigger candidates per BC and receive back confirmation, with the MUCTPI through 4 fibres, used to send up to 4 final muon trigger candidates per BC, with 3 End-cap SL boards through 3 fibres, used to send the BIS78 trigger candidates, and with the FELIX modules, with 1 fibre used to receive TTC signals and 4 fibres to transmit the readout data.

A bidirectional ethernet connection allows the SL to communicate with the L0 barrel TDAQ server to transfer configuration and monitoring data. The SL communicates with the ATCA shelf manager through the IPMC and with the SL and DCT DCS clients through the MPSoC (by implementing an OPC-UA server).

The data transmission between SL and DCTs occurs according to the lpGBT configuration described in Section 5.4: the data are encoded using the lpGBT protocol and are transmitted with a bandwidth of 10.24 Gb/s from the DCTs to the SL and with a bandwidth of 2.56 Gb/s from the SL to the DCTs. The communication

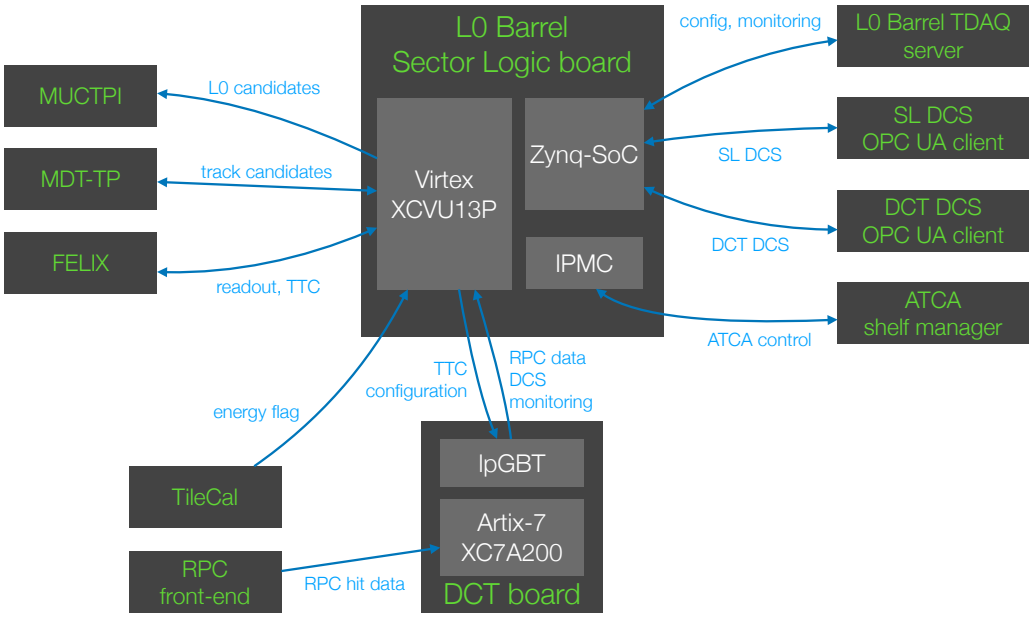

Figure 7.3. The Barrel Sector Logic board and its interfaces with the other systems.

with the TileTDAQi boards, the MDTTP, the MUCTPI, the End-cap SL boards and the FELIX modules exploits the 8B/10B encoding protocol and a bandwidth of 9.6 Gb/s. A summary of the SL input/output connections, the corresponding number of fibres, the data content and the transmission bandwidth and protocol is given in Table 7.1.

7.2 The SL FPGA firmware

The design and development of the SL FPGA firmware have been particularly challenging due to the complex operations that the firmware logic has to perform, the very large amount of data to be handled and the very strict timing and spatial constraints to be respected. The timing constraints come from the high frequency of the clocks used by the firmware logic (mainly 240 MHz and 320 MHz) while the spatial constraints arise from the multi-die structure of the XCVU13P device and the disposition of input/output connections and resources inside the FPGA. A careful floorplanning logic has been conceived to divide the firmware logic among the four die-slices of the FPGA in such a way as to optimise the resource utilisation and minimise the distances travelled by the internal signals [158].

7.2.1 Logic floorplanning

As mentioned previously, the SL FPGA is made of four SLRs (labelled SLR0, SLR1, SLR2 and SLR3), each having one fourth of the total FPGA resources. In particular, each SLR is provided with 32 GTY transceivers, having a transmitting

Table 7.1. SL input/output connections with the external systems, the number of fibres used for the communication, the bandwidth and the protocol of the transmission and the data content.

External system	SL IN/OUT	Fibres	Bandwidth (Gb/s)	Protocol	Data content
DCT	IN	50	10.24	lpGBT	RPC data, monitoring data
DCT	OUT	50	2.56	lpGBT	TTC, commands, configuration
TileCal	IN	6	9.6	8B/10B	Tile Calorimeter data
End-cap SL	OUT	3	9.6	8B/10B	BIS78 trigger candidates
MDTTP	IN	8	9.6	8B/10B	trigger candidate confirmation
MDTTP	OUT	8	9.6	8B/10B	SL trigger candidates
MUCTPI	OUT	4	9.6	8B/10B	L0 barrel trigger candidates
FELIX	IN	1	9.6	8B/10B	TTC signals
FELIX	OUT	4	9.6	8B/10B	Readout data
TDAQ server	IN	1	TBD	ethernet	SL/DCT configuration
TDAQ server	OUT	1	TBD	ethernet	SL/DCT monitoring
DCS clients	IN	1	TBD	ethernet	SL/DCT DCS commands
DCS clients	OUT	1	TBD	ethernet	SL/DCT DCS data
Shelf manager	IN	1	TBD	IPMI	ATCA commands
Shelf manager	OUT	1	TBD	IPMI	ATCA data

and a receiving fibre each. Therefore a firmware design with all the DCT data arriving to the same SLR is not allowed, since it would require at least 50 transceivers in a single SLR. On the other hand, the firmware design should avoid spreading the transceivers used for the same function among the different SLRs. It is indeed a good idea to group the transceivers depending on their connection type, so that the logic blocks processing their data can be implemented using the resources as close as possible to them, to avoid long routing of the signals internally to the FPGA, which are very likely to lead to timing closure issues, given the high-frequency clock constraints. The routing of the signals is particularly delicate when they need to be passed between different SLRs: indeed the transfer of signals between two adjacent SLRs can be performed only through the SLLs routes, which have a higher delay if compared to regular interconnects.

The floorplanning of the SL firmware logic has been conceived to optimise the FPGA resource utilisation and to minimise the number of signals crossing different SLRs. The active transceivers have been grouped accordingly, taking into account the differences between BMBO and BI DCT data. The length of the RPC η strips in the BM and BO regions covers half detector chamber, so that, at least for what concerns BM and BO RPCs, one entire sector can be logically divided into two independent trigger sectors (each of them corresponding to half RPC sector). In the BI region, instead, the length of the η strips covers the entire chamber and such a division is therefore not possible and the trigger algorithm requires the data of the BI RPCs of the entire sector. Thus, the SL firmware design foresees all the BI DCT data to be received in the SLR0, where they are decoded and processed to make them compatible with the data format expected by the trigger algorithm. The SLR0 hosts also the logic which performs the trigger algorithm for the BIS78 RPCs, whose candidates are not part of the barrel muon candidates but are instead sent to the End-cap SL boards, which use them for the L0 end-cap muon trigger. The SLR1 and SLR2 receive the data of the BMBO DCTs, each of the two from half RPC sector, decode them and prepare them for the trigger logic. Two instances of the trigger algorithm are implemented, one placed in the SLR1 and the other one in the SLR2. The two

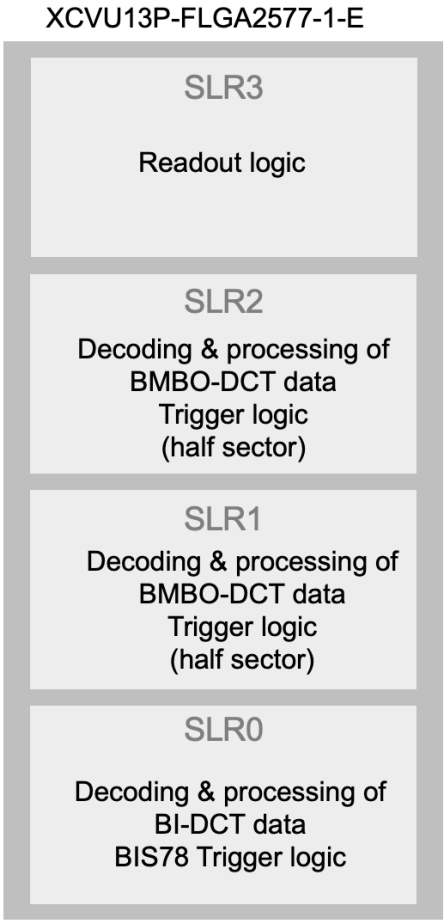

Figure 7.4. Floorplanning of the SL firmware logic.

trigger logic blocks are the same, but each of them takes as input only the BMBO DCT data of half RPC sector. Both trigger logic instances need as well all the BI DCT data, which are then passed from the SLR0 to both the SLR1 and SLR2. Each trigger logic block can produce up to four muon trigger candidates to be sent to the MDTTP. Finally, all the readout logic, which is highly resource-demanding, is placed in the SLR3. The other three SLRs, therefore, have to pass all the received DCT data, after the decoding, to the SLR3, which stores them into local memories before sending them out to the readout system. A schematic summary of the floorplanning of the SL firmware logic is reported in Figure 7.4.

From a practical point of view, such a floorplanning is obtained by constraining the resources needed for the implementation of each logic block to be placed on a specific SLR. For this purpose, four Pblocks are created (a Pblock is a selected region of the device that constrains the logic assigned to it during the placement process). For the SL firmware design, each Pblock is defined so as to cover entirely a different SLR. The various logic blocks composing the SL firmware are thus assigned to the four Pblocks according to the floorplanning described above.

7.2.2 FPGA transceiver usage

Most of the SL connections with the external systems described in Section 7.1.2 (DCTs, MDTTP, MUCTPI, End-cap SL, FELIX, TileCal) are handled by the FPGA-embedded high-speed GTY transceivers, which are connected with the SL board FireFly modules. The 128 GTY transceivers of the SL FPGA are organised in groups of four, called Quads, for a total of 32 Quads, with 8 Quads per SLR. The Quads are numbered from 120 to 135 on the left bank of the FPGA and from 220 to 235 on the right bank.

Of the 128 GTY transceivers available on the SL FPGA, the SL firmware employs 76. The FPGA transceiver usage, bandwidth and connectivity with the external systems are shown in the scheme reported in Figure 7.5. In the SLR0, 10 GTYs are used (both with RX and TX connection) to communicate with the BI DCTs, 6 GTYs are used to receive the Tile Calorimeter data (RX only), 3 GTYs are used to send the BIS78 trigger candidates to the End-cap SL boards (TX only) and 1 GTY is employed to receive the TTC signals (RX only). In the SLR1 and SLR2, the same number of transceivers is used, with 20 GTYs to communicate with the BMBO DCTs (both RX and TX enabled), 4 GTYs to send the trigger candidates to the MDTTP and receive back confirmation (both TX and RX enabled) and 2 GTYs to transmit the final L0 barrel trigger candidates to the MUCTPI. In the SLR3, only 4 transceivers are used to send to FELIX the readout data (TX only).

The configuration of the transceivers depends on the system they are used to interface with. All the GTYs used for the DCT communication are configured with an RX bandwidth of 10.24 Gb/s, a TX bandwidth of 2.56 Gb/s and no encoding (the firmware is provided of a separate logic block to decode the DCT data according to the lpGBT encoding protocol). The GTYs used to interface with the remaining

external systems are configured, instead, with a bandwidth of 9.6 Gb/s both for RX and TX and with the 8B/10B encoding protocol.

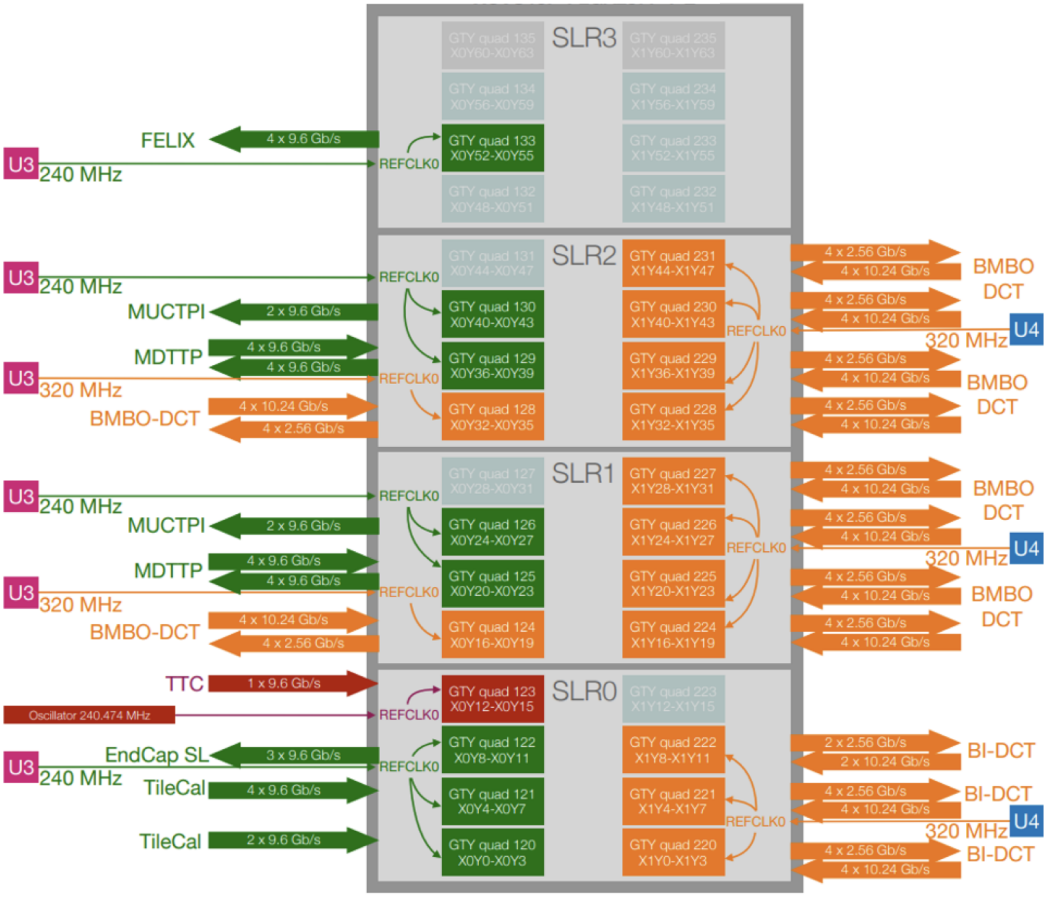

Figure 7.5. FPGA transceiver usage and reference clocks scheme.

7.2.3 Clock scheme

The SL board is provided with several embedded oscillators able to supply clocks with a wide range of frequencies. Anyway, the clocks used for the firmware logic as well as for the GTY operation are all derived from the same clock, reconstructed in the FPGA from the TTC signals received in the SLR0 from one transceiver. The only transceiver using a reference clock not derived from the TTC reconstructed clock is precisely this one, which works instead with the clock provided by an oscillator of the board with a 240 MHz frequency. The clock reconstructed from the TTC signal has the LHC collision frequency (40 MHz[2]) and is used by a clock multiplier to generate the clocks needed by the firmware internal logic, namely a 80 MHz, a 240 MHz and a 320 MHz clock. The 80 MHz clock is used by the logic

[2]Even if the LHC collision frequency is 40.079 MHz, in this Chapter its value is approximated to 40 MHz for simplicity. The same holds for its multiples and for the frequency of the board oscillators.

that encodes the data to be sent to the DCTs, the 240 MHz clock is used by the readout logic and the 320 MHz by the logic performing the decoding of the DCT data, the logic executing the trigger algorithm and all the logic between these two blocks.

The GTY reference clocks are routed from the jitter cleaners of the board. The SL board is provided with four jitter cleaners Si5395 (labelled U1, U2, U3 and U4), which remove the noise from clock signals. The 40 MHz TTC reconstructed clock is sent to a pin of the FPGA which is driven to one of the input ports of the U1 jitter cleaner. The U1 jitter cleaner uses the clock from a board oscillator (with a 40 MHz frequency) to clean the input clock signal. The output clock is sent as input to both the U3 and U4 jitter cleaners. The U3 jitter cleaner generates the 240 MHz and 320 MHz reference clocks for the transceivers of the left bank of the FPGA, while the U4 jitter cleaner produces the 320 MHz reference clock for the transceivers of the right bank. Figure 7.6 reports a scheme of the connections of the input and output ports of the four jitter cleaners of the SL board.

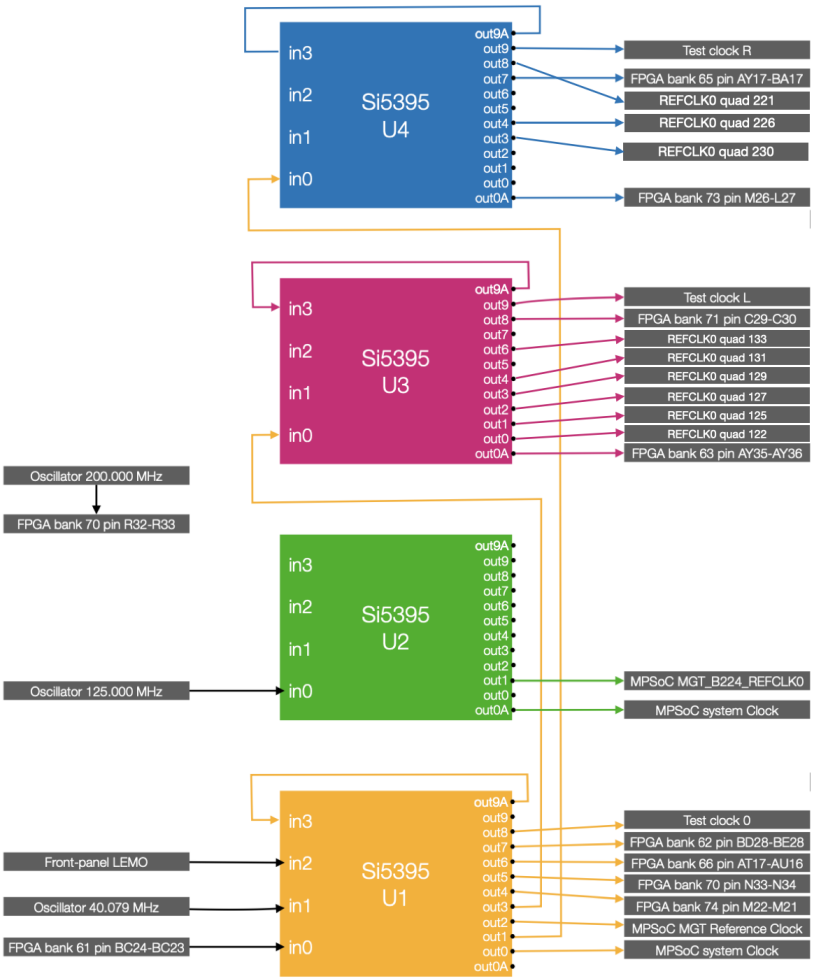

Figure 7.6. Configuration of the jitter cleaners of the SL board.

7.2.4 DCT interface logic

As stated in the previous sections, the SL FPGA can interface with up to 50 DCT boards, connected with the transceivers of the different SLRs of the FPGA in the following way: 10 BI DCTs are connected to the GTYs of the SLR0, 20 BMBO DCTs to the GTYs of the SLR1 and the remaining 20 BMBO DCTs to the GTYs of the SLR1. For each connected DCT, a DCT interface logic block is instantiated by the SL firmware (therefore 10 DCT interface logic blocks in the SLR0, 20 in the SLR1 and 20 in the SLR2). Although sharing most of the logic, the logic blocks used to interface with the BI and the BMBO DCTs present some differences, due to the different data format of the two DCT versions (refer to Sections 6.2.4 and 6.3.3 for the DCT data formats). The decoding/encoding logic is common to both blocks: the data transmission for both DCT versions, indeed, uses the lpGBT encoding protocol and thus, for each DCT transceiver, the SL firmware has to instantiate an lpGBT-FPGA core to decode the data received from the DCTs and encode the data to be sent towards the DCTs. The lpGBT-FPGA core is made of a downlink block, which passes to the transceiver the decoded data as 32-bit words at 80 MHz, and an uplink block, which receives the encoded DCT data from the transceiver as 32-bit words at 320 MHz, decodes them and outputs a 224-bit frame every 25 ns. A detailed description of the functioning and composition of the downlink and uplink blocks can be found in Section 5.4. After the decoding by the uplink block, a logic block referred to as *data divider* divides the 224-bit uplink frames producing 28-bit words at 320 MHz, which correspond to the words generated by the DCT firmware before being sent to the lpGBT.

The 28-bit DCT words obtained in this way have a double fate: on one hand they are sent directly to the readout logic in the SLR3, on the other hand they are used by the trigger algorithm instances in the SLR1 and SLR2. Before being sent to the trigger logic, however, the DCT data have to be processed to arrange them in a format suitable for the trigger algorithm and from here the BMBO and BI interface logic blocks diverge. The processing of the 28-bit words is performed by a *derandomising* logic block, which has the task of ordering the DCT data according to the BC information they carry. This derandomisation is necessary since the RPC hit data arrive to the SL board from the 50 DCTs with a non-fixed latency ranging from 5 to 20 BCs with respect to the one the hit occurred in. For both BI and BMBO data, the derandomising logic block consists of 17 blocks (indexed from 0 to 16), each storing into registers the data corresponding to a specific BC. The incoming DCT word is passed to the block whose index is equal to the BCID of the word modulo 17. At each Bunch Crossing, only 16 out of 17 blocks can receive the hit data, due to the finite range of the latency, and the remaining block is reset. Each logic block receives the hit data corresponding to a specific BC for up to 16 consecutive BCs. The DCT data are stored only if they carry information about the hit strip index: in the BMBO case the separation of RPC hit data from monitoring data is based on the strip index, since only the hit data carry a strip index below 144; in the BI case, instead, the word identifier is carried by the first two bits and only the first word of the RPC hit data format is stored, since the trigger algorithm needs only information on the η strip index and the ϕ coordinate. The stored data

are arranged to form frames in which each bit corresponds to an RPC strip index and its value tells if the strip recorded a hit in that specific BC. Therefore, in the BMBO case, the data are arranged to form a 64-bit frame for the η strips and an 80-bit frame for the ϕ strips, while, in the BI case, a 48-bit frame is formed for the η strips and a 128-bit frame for the ϕ coordinate (which is extracted by the BI DCT firmware from the timing measurements of the η strips). When constructing these frames, a hit coincidence in two layers out of the three composing the BI RPC triplet is required, while for the BM and BO RPCs a hit in at least one of the two layers of the RPC doublet is required.

The derandomising logic block produces in this way a frame representing the hits on the η strips and another for the hits in the ϕ strips every 25 ns. The output frames of the SLR0 derandomising logic are passed to the trigger logic instances of the SLR1 and SLR2. The output frames of the derandomising logic of the SLR1 and SLR2 are instead sent to the respective trigger logic blocks. A schematic block diagram of the DCT interface logic is represented in Figure 7.7.

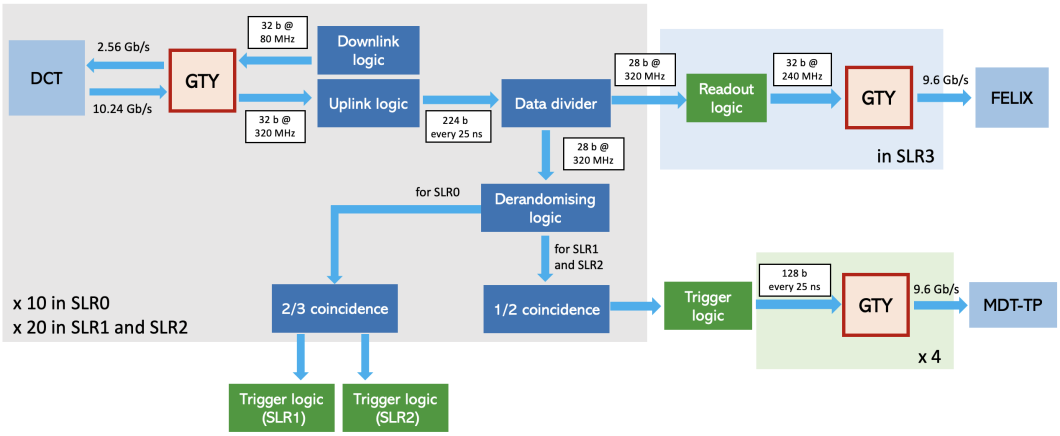

Figure 7.7. Functional block scheme of the SL firmware interface logic.

7.2.5 Trigger logic

The SL firmware implements two instances of the trigger algorithm, one placed in the SLR1 and the other one in the SLR2, each generating the trigger candidates for half RPC sector and working with the 320 MHz clock. The trigger logic receives the hit data corresponding to the four RPC stations (BI, BM1, BM2 and BO) and searches for muon candidates applying a hit coincidence between the RPC stations within windows opened around the BM2 station, which is chosen as pivot station. The algorithm runs in parallel four p_{T} thresholds, corresponding to 5, 10, 15 and 20 GeV, which determine the window opening (a larger window corresponds to a lower p_{T} trigger threshold). A coincidence of hits inside the window is requested in at least three out of the four stations both for the η and the ϕ coordinates. A SL trigger candidate is then formed if there is a simultaneous coincidence both for the

η and for the ϕ coordinate.

Then, an overlap removal procedure is applied to avoid double-countings of the candidates. Indeed hits in close-by strips may lead to the generation of multiple candidates which actually refer to the same muon. For this purpose, a lookup table is built to select a single candidate among a set of neighbouring candidates. At this point, a priority encoder is employed to select up to two candidates per trigger logic instance. Higher priority is assigned to candidates with higher p_{T} threshold and, in the case the threshold is the same, with lower η. The baseline trigger scheme foresees the generation of up to four SL trigger candidates per RPC sector to be sent to the MDTTP, however, if needed, the number of candidates can be increased to up to 8 per sector (since SL and MDTTP are connected through 8 fibres).

7.2.6 Readout logic

The readout logic, placed entirely on the SLR3 and working with the 240 MHz clock, receives all the DCT data from the SLR0, SLR1 and SLR2 and the trigger candidates from the SLR1 and SLR2 and stores them in local memories waiting for a L0-Accept signal. If the data are selected by a L0-Accept signal before the maximum L0 trigger latency (10 µs), they are sent to the readout system through the FELIX modules, otherwise they are deleted.

The readout logic for the DCT data is made of three blocks, each managing the data coming from a different SLR. These three blocks instantiate one *memory block* per DCT (therefore 10 memory blocks for the logic managing DCT data from the SLR0, 20 for the DCT data from the SLR1 and 20 for the DCT data from the SLR2). A memory block is based on a standard dual-port RAM memory. The depth of the RAM is 8192, so that it can store up to 16 words per BC for a maximum of 512 different BCIDs, and the width is 32 bits. As the DCT data arrive to the memory block, they are written into the RAM using as writing address the BCID information carried by them. Before being stored, the 28-bit DCT data are padded to obtain a 32-bit word with the most significant bits of the 12-bit SL BC counter (since the DCT words carry only the 10 or 8 least significant bits of the BCID in the BMBO and BI cases respectively) and with additional empty bits. When a L0-Accept signal is received by the SL for a given BCID, all the corresponding hit data stored in the RAM memory are read consecutively and sent to the transceiver connected to FELIX.

A separate logic block is in charge of storing the L0 muon trigger candidates arriving from the two trigger logic instances. For this purpose, a RAM memory with a depth of 512 words (corresponding to 512 different BCIDs) and a width of 512 bits (to store up to four 128-bit candidates) is instantiated. The writing and reading procedure is analogous to the DCT data one. Of the four fibres connecting the SL with the FELIX modules, three are used to send the DCT data and one is dedicated to trigger candidates.

7.2.7 Simulation

The entire SL firmware logic has been simulated with the Vivado Design Suite software [148]. A testbench has been set up to simulate the transmission of DCT data from three RPC stations in order to check the decoding and interface logic and the SL muon candidate generation by the trigger algorithm. The testbench instantiates three logic blocks, one to simulate the data transmission from a BI DCT, one from a BM2 DCT and the last one from a BO DCT. Each logic block generates every 200 ns a packet of 28-bit words with the DCT output format. The content of the generated DCT words is conceived to represent RPC hits forming a coincidence in the three RPC stations both for the η and the ϕ strips. In the time between the generation of two hit data packets, words with the DCT monitoring data format are generated. For each logic block, the lpGBT-Emulator logic [147] is instantiated to emulate the functions of the DCT lpGBT. The encoded DCT data from the three lpGBT-Emulator blocks are sent to three transceivers, whose TX ports are connected with the RX ports of three GTY transceivers of the SL firmware. The simulated BI DCT data are sent to a GTY of the SLR0, while the simulated BMBO DCT data are sent to two GTYs of the SLR1. The propagation of the simulated DCT data through the different SL firmware logic blocks has been checked through the simulation. The decoding by the uplink logic blocks is performed properly and the original DCT words generated in the testbench are correctly reconstructed. Then, the derandomising logic arranges the incoming hit data into frames representing the η and ϕ hits of an entire BC. These frames are correctly transmitted to the SLR1, where the trigger algorithm instance generates the trigger candidate as expected.

Figure 7.8 reports the snapshot of some relevant signals from the SL firmware simulation described above. For the three simulated DCT connections (BI, BM2 and BO) the following signals are shown: the serial RX signals received by the transceivers, the 224-bit frames coming from the uplink decoding logic, the 28-bit DCT words obtained from the division of the decoded frames, the frames storing the η and ϕ hits produced by the derandomising logic and the 128-bit trigger candidate word generated by the trigger logic together with a valid candidate signal. The trigger algorithm is executed with a fixed latency which from the simulation is measured to be 62.6 ns (temporal separation between blue and yellow cursors in Figure 7.8), which corresponds to 20 clock cycles at 320 MHz.

7.2.8 Implementation and resource occupancy

The SL firmware implementation has been performed using the Vivado Design Suite software. Achieving timing closure (that is the fulfilment of all the timing constraints imposed by the high-frequency clocks used for the signal propagation) has been particularly challenging. The first issue was finding a way to arrange all the firmware logic among the four SLRs of the SL FPGA so that each logic block had a sufficient amount of resources available. On this topic, spatial constraints to the logic placement derive from the input/output connections: indeed, the logic

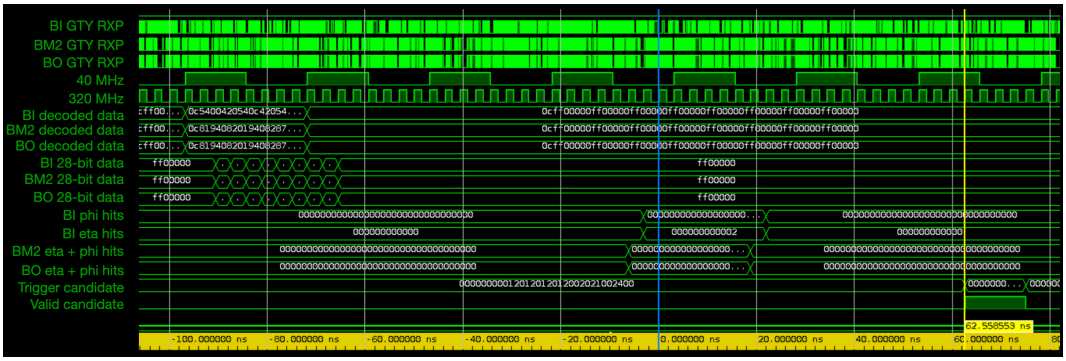

Figure 7.8. Snapshot of the SL firmware simulation showing the GTY RX signals, the 40 MHz and 320 MHz clocks, the decoded data, the 28-bit DCT data, the hit frames and the valid trigger candidate. The blue cursor indicates the time the hit frames are received by the trigger logic, while the yellow cursor the time a trigger candidate is generated.

blocks operating on the data received by a specific transceiver should be kept as close as possible to the transceiver location, in order to prevent the signals from travelling long distances. A second issue, even more delicate than the first one, is keeping the number of signals crossing different SLRs as low as possible. Indeed the number of connections between SLRs is limited and a high flow of data across different SLRs may slow down significantly their transmission, inevitably incurring in a timing failure. After several trials, the floorplanning that optimises the FPGA resource utilisation and at the same time minimises the number of signals transmitted between different SLRs is the one described in Section 7.2.1.

However, such a firmware logic placement was still giving rise to timing closure issues. Indeed, even if the number of signals crossing different SLRs is not high, the transmission along the SLLs connecting adjacent SLRs is slower than the regular interconnects and cannot be performed in one clock cycle (the data are transmitted between the SLRs at 240 MHz or 320 MHz). In order to solve this issue, pipeline registers have been added to the firmware to facilitate the SLR crossings and ease the timing constraints (by the introduction of additional clock cycles in the data transmission). Specifically, for each SLR crossing a register has been added. Therefore one register is used for signals making one SLR crossing (namely BI DCT data from the SLR0 to the SLR1 and BMBO DCT data from the SLR2 to the SLR3), two registers for signals making two SLR crossings (BI DCT data from the SLR0 to the SLR2 and BMBO DCT data from the SLR1 to the SLR3) and three registers for signals making three crossings (BI DCT data from the SLR0 to the SLR3).

With the adoption of the measures exposed above, all the timing constraints were eventually fulfilled and a successful implementation of the firmware was obtained. The overall FPGA resource utilisation, reported in Table 7.2, shows no critical issues, even if the resource occupancy is not equally distributed among the four SLRs of the FPGA, as shown in Table 7.3, due to the different demands in terms of resources of the firmware logic blocks. Figure 7.9 shows the XCVU13P

device after the SL firmware implementation, highlighting the positions of the logic cells used to implement the logic.

Table 7.2. Overall FPGA resource utilisation of the SL firmware.

Resource	Available	Utilisation	Utilisation %
LUT	1728000	605645	35.05
LUTRAM	791040	1341	0.17
FF	3456000	471106	13.63
BRAM	2688	498	18.51
IO	448	227	50.67
GT	128	78	60.94
BUFG	1344	18	1.34
MMCM	16	1	6.25

Table 7.3. Percentage of the resources of each SLR occupied by the SL firmware.

Resource	SLR0	SLR1	SLR2	SLR3
LUT	24%	29%	29%	58%
FF	12%	15%	15%	13%
BRAM	1%	2%	2%	55%
CLB	44%	55%	52%	77%

The FPGA has anyway still enough available resources for some pieces of logic which are missing from the current SL firmware version. This additional logic, expected to require a small amount of resources, consists mainly of monitoring logic, BIS78 trigger logic (to be placed entirely in the SLR0) and input/output interface logic with the MUCTPI, the Tile Calorimeter and the End-cap SL. Moreover, the trigger algorithm has to be completed with the estimate of the p_{T} and the charge of the candidate and the introduction of hit coincidence in the BI and BO stations as a sufficient condition for the generation of a candidate (as foreseen by the Phase-II L0 Muon trigger scheme).

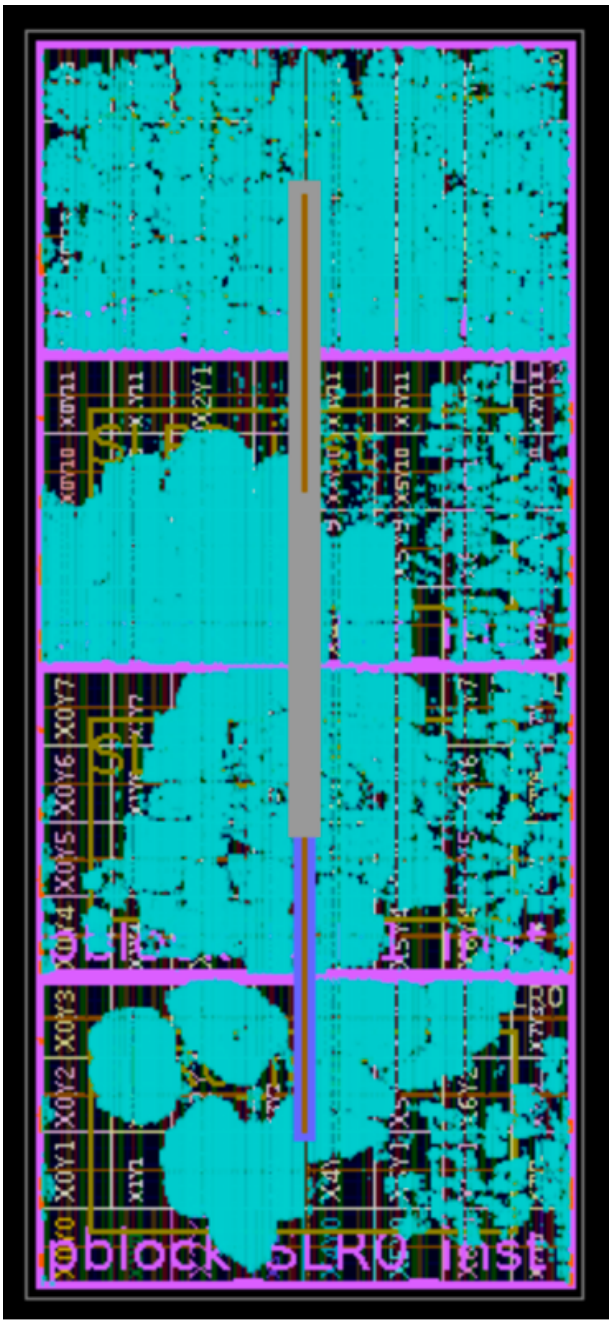

Figure 7.9. FPGA device after the implementation of the SL firmware. The logic cells used to implement the firmware are highlighted.

Conclusion

An analysis searching for third-generation leptoquark in the non-resonant production has been presented in this thesis. This analysis plays an important role in the framework of leptoquark searches performed at collider experiments. Indeed it investigates a process which has not been covered by the previous ATLAS results and in which a high signal sensitivity is expected. The analysis focuses on events with at least one hadronic tau in the final states. Obtaining a reliable prediction of the SM processes has been challenging, due to the large fake-tau background which cannot be modelled with MC simulations. The data-driven technique adopted, based on the innovative Fake Factor method, proved to be effective in modelling such background, as demonstrated by the very good closure between data and SM predictions achieved in the validation regions. The distributions of the visible invariant mass of the di-lepton system in the final state have been used to compare the expectation from the SM prediction with the measurement obtained with the full dataset collected by the ATLAS detector during the Run 2 of the LHC. No significant deviations from the SM prediction have been observed. The results of a profile-likelihood fit have been then used to compute exclusion limits on the leptoquark coupling at 95% CL through the CLs technique for different values of the leptoquark mass parameter. The results obtained in this work have been compared with the ones from a measurement performed by the CMS Collaboration, which investigated the same process under the same leptoquark model assumptions adopted here. The discrepancy between expected and observed upper limits found by the CMS experiment is not confirmed by the result presented in this thesis, which instead sets a more stringent limit in the leptoquark parameter space. However, the result presented here is still a preliminary result, obtained with only a few of the available signal regions of the analysis. Some work is still necessary to include in the result also the 2 b-jet $\tau_{\text{had}}\tau_{\text{had}}$ region, in which the fit is not stable, and the $e\tau_{\text{had}}$ and $\mu\tau_{\text{had}}$ regions, for which studies are ongoing to reduce the large $t\bar{t}$ background and enhance the signal sensitivity.

The work regarding the upgrade of the ATLAS Muon Spectrometer for the High-Luminosity LHC has also been reported in this thesis. The development of the firmware of the DCT boards and of the SL board has been presented, together with the related challenges, which were successfully overcome. All the firmware logic described in this thesis has been validated through a software simulation, using samples with the expected HL-LHC RPC signals as input data in the DCT case and patterns of DCT data generating a muon trigger candidate in the SL case. While the BMBO DCT firmware has been validated also through a test performed

with the DCT board prototype and legacy RPC detectors, the BI DCT firmware and the SL firmware still need to be validated with a hardware testbench employing the respective prototypes.

Appendices

Appendix A

Kinematic distributions in the same-sign regions

The following plots show the distributions for some kinematic variables for data and SM prediction in the same-sign $\tau_{\text{had}}\tau_{\text{had}}$ (Figure A.1), $e\tau_{\text{had}}$ (Figure A.2) and $\mu\tau_{\text{had}}$ (Figure A.3) regions. All the distributions presented here are inclusive with respect to the b-jet multiplicity. The same-sign regions are used to validate the data-driven estimate of the fake-tau background.

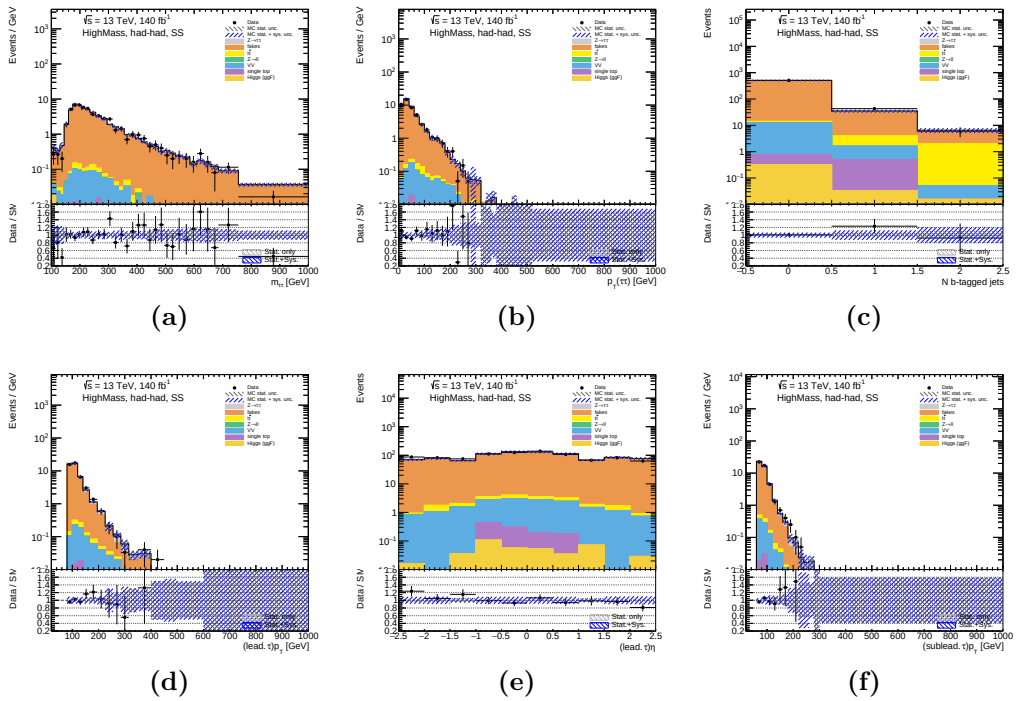

Figure A.1. Validation kinematic plots in the same-sign $\tau_{\text{had}}\tau_{\text{had}}$ region for the $m_{\tau\tau}$ (a), $p_T^{\tau\tau}$ (b), b-jet multiplicity (c), leading tau p_T (d) and subleading tau p_T (e).

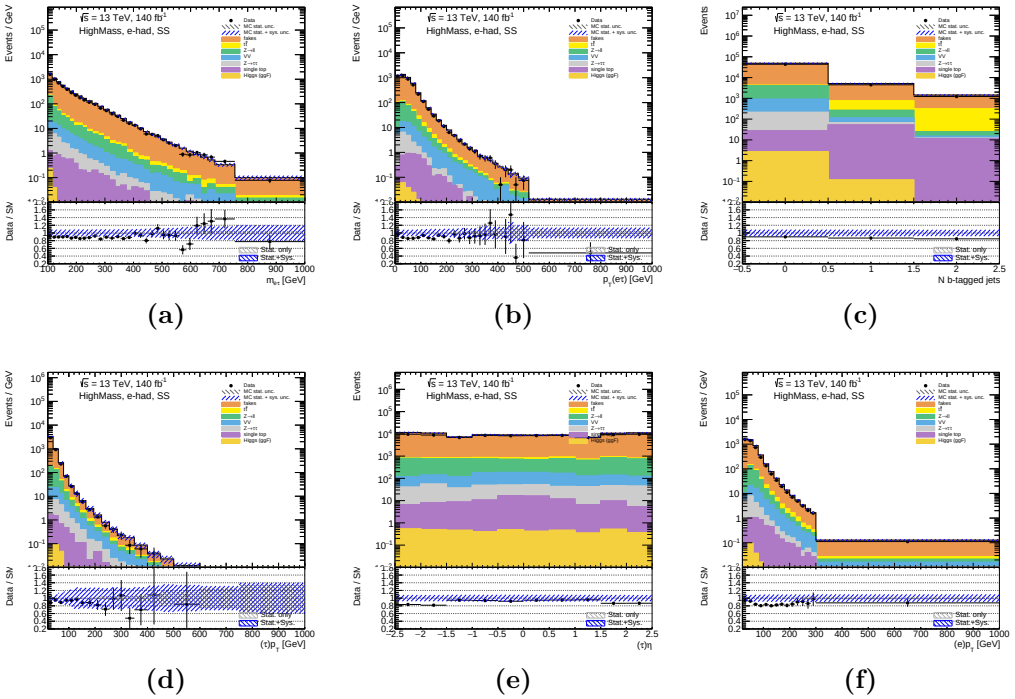

Figure A.2. Validation kinematic plots in the same-sign $e\tau_{\text{had}}$ region for the $m_{e\tau}$ (a), $p_T^{e\tau}$ (b), b-jet multiplicity (c), tau p_T (d) and electron p_T (e).

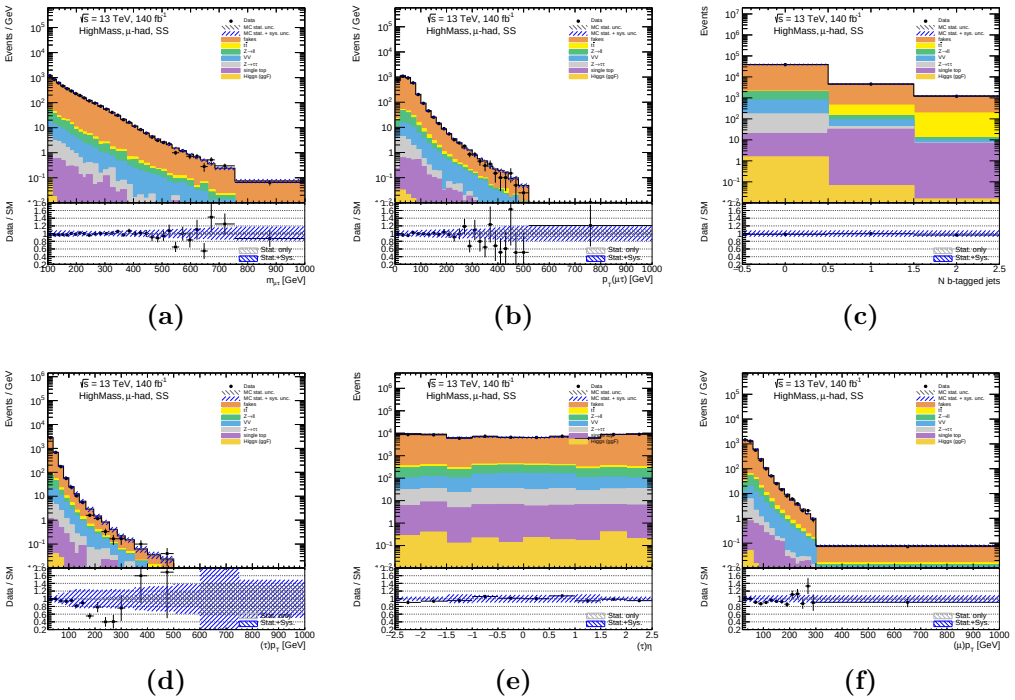

Figure A.3. Validation kinematic plots in the same-sign $\mu\tau_{\text{had}}$ region for the $m_{\mu\tau}$ (a), $p_T^{\mu\tau}$ (b), b-jet multiplicity (c), tau p_T (d) and muon p_T (e).

Appendix B

Kinematic distributions in the light-lepton regions

The following plots show the distributions for some kinematic variables of interest obtained from data and MC simulation in the ee (Figure B.1), $\mu\mu$ (Figure B.2) and $e\mu$ (Figure B.3) regions. All the distributions presented here are inclusive with respect to the b-jet multiplicity.

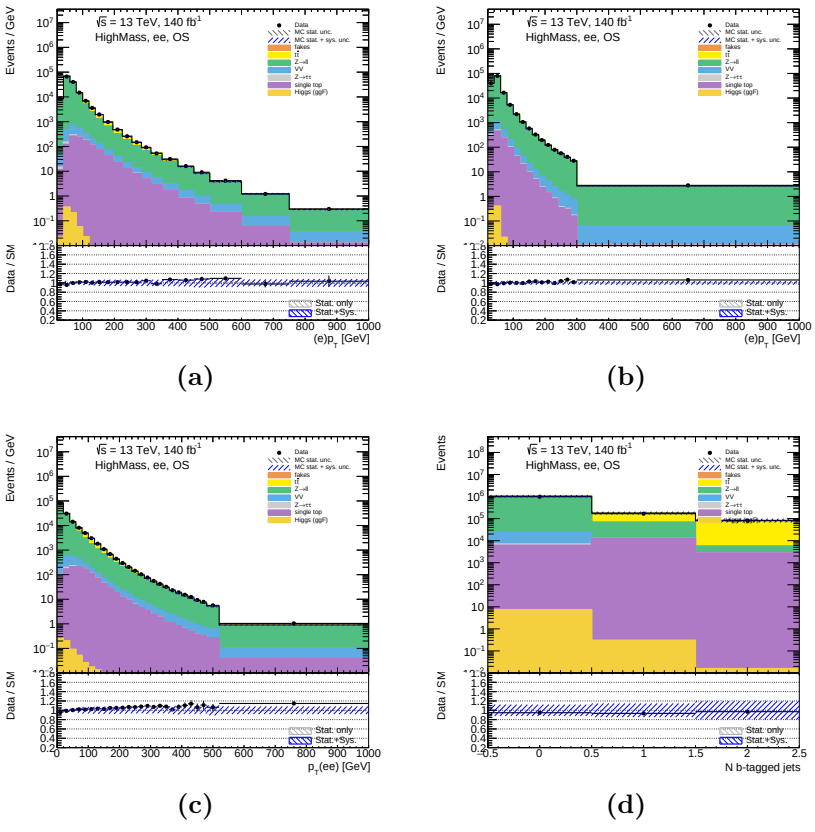

(a) **(b)**

(c) **(d)**

Figure B.1. Distributions of the leading electron p_{T} (a), subleading electron p_{T} (b), ee p_{T} (c) and b-jet multiplicity (d) obtained in data and MC simulation for the ee region.

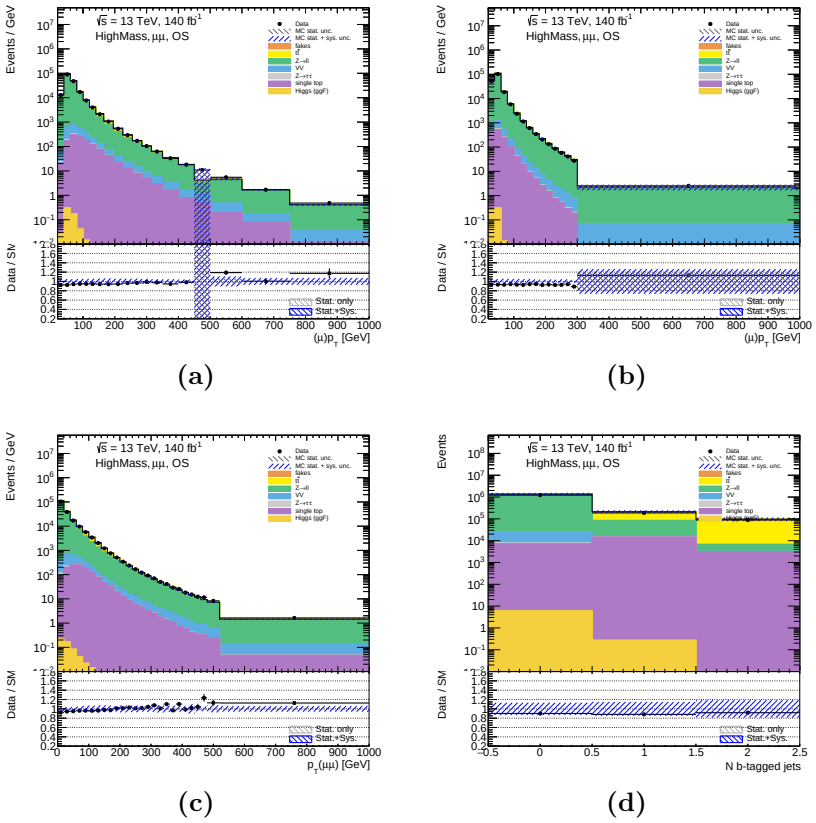

Figure B.2. Distributions of the leading muon p_{T} (a), subleading muon p_{T} (b), $\mu\mu$ p_{T} (c) and b-jet multiplicity (d) obtained in data and MC simulation for the $\mu\mu$ region.

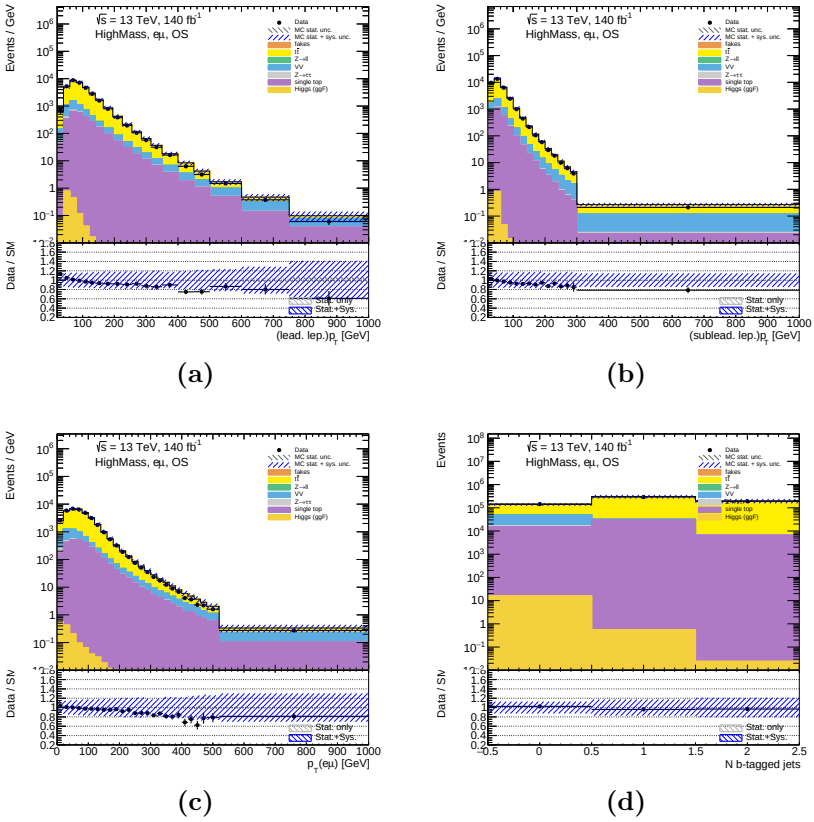

Figure B.3. Distributions of the leading lepton p_{T} (a), subleading lepton p_{T} (b), $e\mu$ p_{T} (c) and b-jet multiplicity (d) obtained in data and MC simulation for the $e\mu$ region.

Appendix C

Uncertainties

C.1 Uncertainty on the fakes' background

Figure C.1 shows the absolute (upper pad) and relative (lower pad) uncertainty bands on the extrapolated fakes' estimate for the same-sign regions.

C.2 Experimental uncertainties

Among the considered experimental systematic uncertainties, the ones having the largest impact on the $m_{\ell\ell}$ distribution in the $\tau_{\text{had}}\tau_{\text{had}}$ region are related to the hadronic tau objects. The dominant uncertainty is on the Tau Energy Scale (TES), followed by the uncertainty on the tau identification, the tau triggers and the tau reconstruction. The jet-related uncertainties have a non-negligible impact in the $\tau_{\text{had}}\tau_{\text{had}}$ region, too. The impact of these uncertainties on the $m_{\ell\ell}$ distribution in the $\tau_{\text{had}}\tau_{\text{had}}$ region is reported in Figure C.2.

In the $e\tau_{\text{had}}$ region, the uncertainty on the Tau Energy Scale is still the dominant one. The other relevant uncertainties are related to tau-leptons, electrons and jets. Their impact on the $m_{\ell\ell}$ distribution in the $e\tau_{\text{had}}$ region is reported in Figure C.3.

In the $\mu\tau_{\text{had}}$ region the most relevant experimental uncertainties are related to tau-leptons (the TES uncertainty dominates in this case too) and muons. The impact of some of the most relevant uncertainties on the $m_{\ell\ell}$ distribution in the $\mu\tau_{\text{had}}$ region is reported in Figure C.4.

The list of the experimental systematic uncertainties passing the pruning procedure and therefore used for the maximum likelihood fit described in Section 4.8 is given below. The uncertainties are divided according to the objects they are related to.

Muon uncertainties

- Resolution:
  - MUON_ID

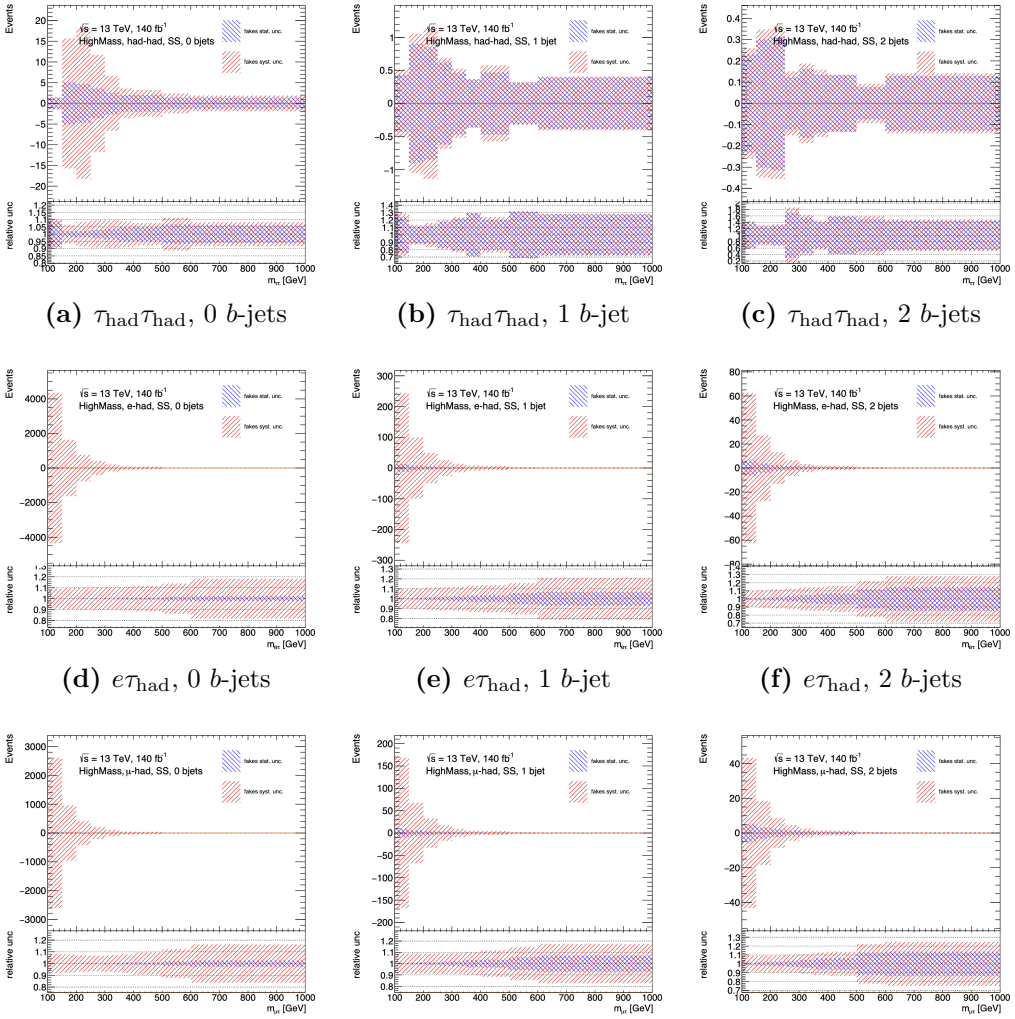

(a) $\tau_{\text{had}}\tau_{\text{had}}$, 0 b-jets **(b)** $\tau_{\text{had}}\tau_{\text{had}}$, 1 b-jet **(c)** $\tau_{\text{had}}\tau_{\text{had}}$, 2 b-jets

(d) $e\tau_{\text{had}}$, 0 b-jets **(e)** $e\tau_{\text{had}}$, 1 b-jet **(f)** $e\tau_{\text{had}}$, 2 b-jets

(g) $\mu\tau_{\text{had}}$, 0 b-jets **(h)** $\mu\tau_{\text{had}}$, 1 b-jet **(i)** $\mu\tau_{\text{had}}$, 2 b-jets

Figure C.1. Absolute (upper pad) and relative (lower pad) uncertainties on the final fakes estimate in the same-sign regions. (a)-(c) show the $\tau_{\text{had}}\tau_{\text{had}}$ region, (d)-(f) show the $e\tau_{\text{had}}$ region, (g)-(i) show the $\mu\tau_{\text{had}}$ region, all of them divided per b-jet multiplicity.

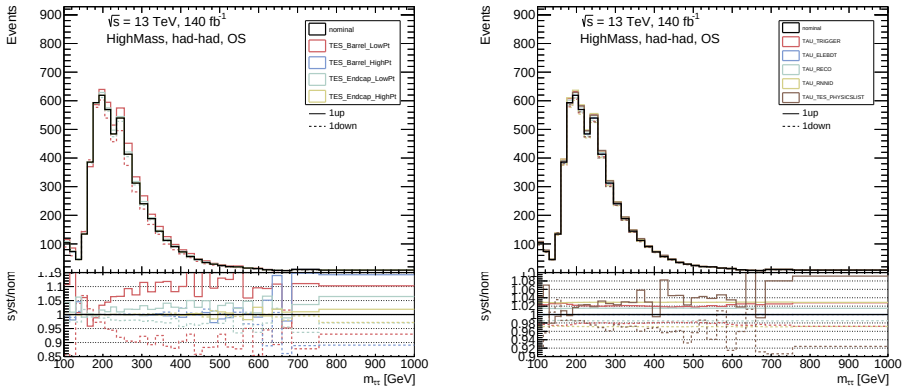

(a)

(b)

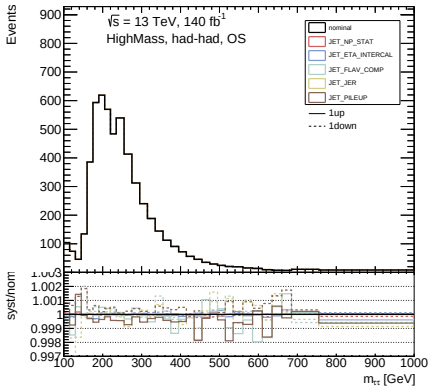

(c)

Figure C.2. Impact of the most relevant experimental systematic uncertainties on the $m_{\ell\ell}$ distribution in the $\tau_{\text{had}}\tau_{\text{had}}$ region: (a) reports the TES detector systematics, (b) other tau-related systematics and (c) some jet-related systematics.

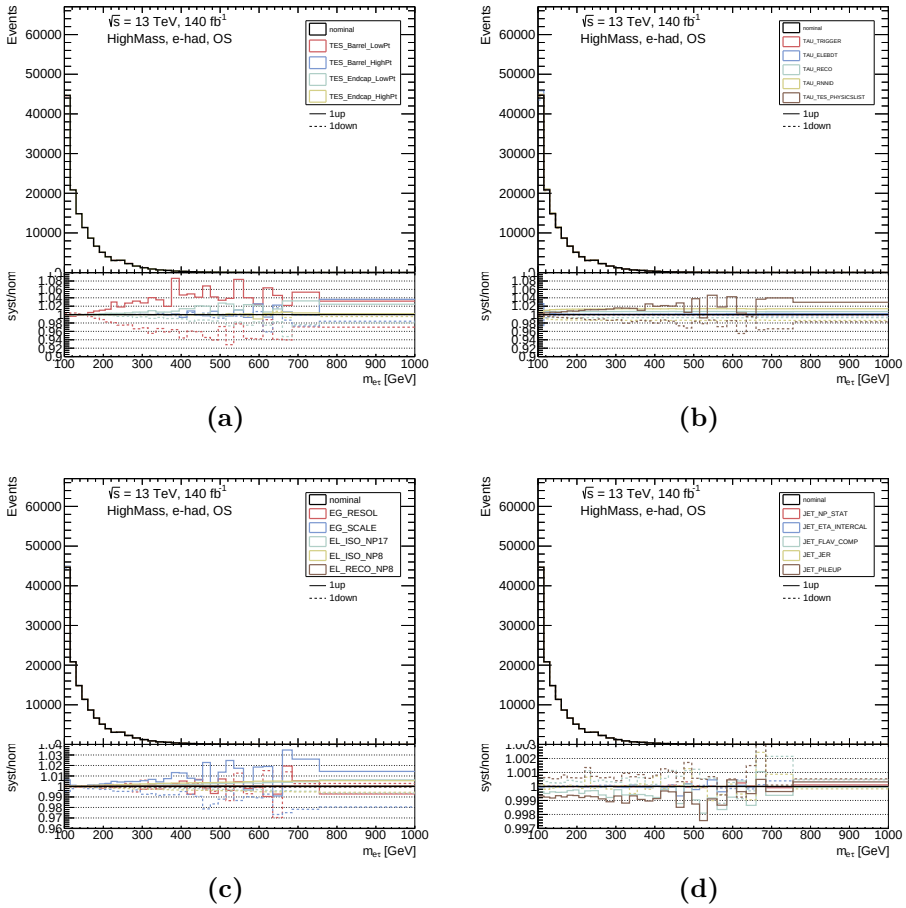

Figure C.3. Impact of the most relevant experimental systematic uncertainties on the $m_{\ell\ell}$ distribution in the $e\tau_{\text{had}}$ region: (a) reports the TES detector systematics, (b) other tau-related systematics, (c) some electron-related systematics and (d) some jet-related systematics.

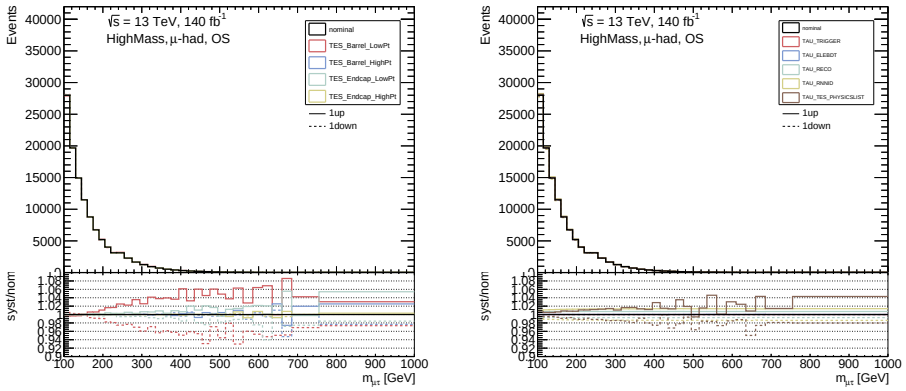

(a)

(b)

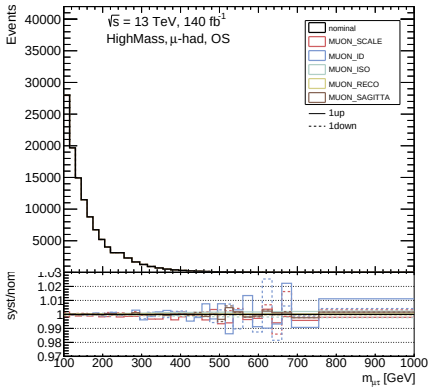

(c)

Figure C.4. Impact of the most relevant experimental systematic uncertainties on the $m_{\ell\ell}$ distribution in the $\mu\tau_{\text{had}}$ region: (a) reports the TES detector systematics, (b) other tau-related systematics and (c) some muon-related systematics.

  - MUON_MS
  - MUON_SAGITTA_RESBIAS
- Energy scale:
  - MUON_SCALE
- Reconstruction:
  - MUON_EFF_RECO_STAT
  - MUON_EFF_RECO_SYS
- Isolation:
  - MUON_EFF_ISO_SYS
- Track to vertex association:
  - MUON_EFF_TTVA_STAT
  - MUON_EFF_TTVA_SYS

Electron uncertainties

- Energy scale:
  - EG_SCALE_ALL
- Reconstruction:
  - EL_EFF_Reco_SIMPLIFIED_UncorrUncertaintyNP8
- Isolation:
  - EL_EFF_Iso_SIMPLIFIED_UncorrUncertaintyNP[8|17]

Tau uncertainties

- Energy scale:
  - TAUS_TRUEHADTAU_SME_TES_DETECTOR
  - TAUS_TRUEHADTAU_SME_TES_INSITUEXP
  - TAUS_TRUEHADTAU_SME_TES_INSITUFIT
  - TAUS_TRUEHADTAU_SME_TES_MODEL_CLOSURE
  - TAUS_TRUEHADTAU_SME_TES_PHYSICSLIST
- Reconstruction:
  - TAUS_TRUEHADTAU_EFF_RECO_TOTAL
- Identification:
  - TAUS_TRUEHADTAU_EFF_RNNID_1PRONGSTATSYSTPTGE40

  - TAUS_TRUEHADTAU_EFF_RNNID_3PRONGSTATSYSTPTGE40
  - TAUS_TRUEHADTAU_EFF_RNNID_HIGHPT
  - TAUS_TRUEHADTAU_EFF_RNNID_SYST
- Trigger:
  - TAUS_TRUEHADTAU_EFF_TRIGGER_STATDATA[2016|161718]
  - TAUS_TRUEHADTAU_EFF_TRIGGER_STATMC[2016|161718]
  - TAUS_TRUEHADTAU_EFF_TRIGGER_SYST[2016|161718]
- Electron veto and overlap removal:
  - TAUS_TRUEELECTRON_EFF_ELEBDT_STAT
  - TAUS_TRUEHADTAU_EFF_ELEOLR_TOTAL

Jet uncertainties

- Energy scale:
  - JET_EffectiveNP_Mixed2
  - JET_EffectiveNP_Modelling[1|2|3]
  - JET_EffectiveNP_Statistical2
  - JET_EtaIntercalibration_Modelling
  - JET_EtaIntercalibration_NonClosure_2018data
  - JET_EtaIntercalibration_TotalStat
  - JET_Pileup_Offset[Mu|NPV]
  - JET_Pileup_RhoTopology
- Energy resolution:
  - JET_JER_DataVsMC_MC16
  - JET_JER_EffectiveNP_[1-11|12restTerm]
- Flavor:
  - JET_Flavor_Composition
  - JET_Flavor_Response
- Flavor tagging:
  - FT_EFF_Eigen_B_[1|2|3]
  - FT_EFF_Eigen_C_0
  - FT_EFF_Eigen_Light_[0|1|2]
  - FT_EFF_extrapolation
  - FT_EFF_extrapolation_from_charm

Appendix D

Kinematic distributions in the signal regions

The following plots show the distributions for some kinematic variables of interest obtained from data and MC simulation in the $\tau_{\text{had}}\tau_{\text{had}}$ (Figure D.1), $e\tau_{\text{had}}$ (Figure D.2) and $\mu\tau_{\text{had}}$ (Figure D.3) signal regions. All the distributions presented here are inclusive with respect to the b-jet multiplicity.

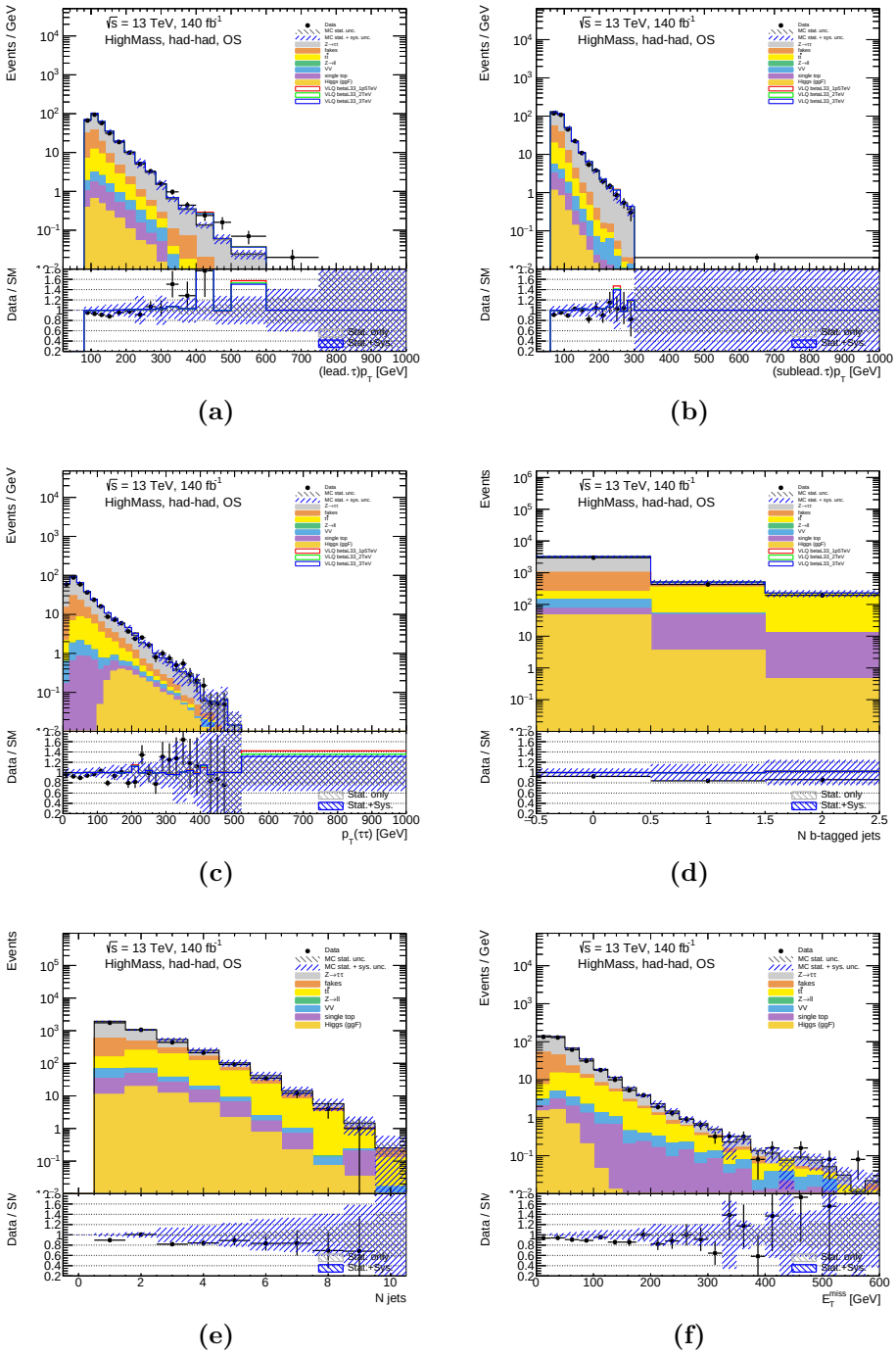

Figure D.1. Distributions of the leading tau p_{T} (a), subleading tau p_{T} (b), $\tau\tau$ p_{T} (c), b-jet multiplicity (d), number of jets (e) and missing transverse momentum (f) obtained in data and MC simulation for the $\tau_{\mathrm{had}}\tau_{\mathrm{had}}$ signal region.

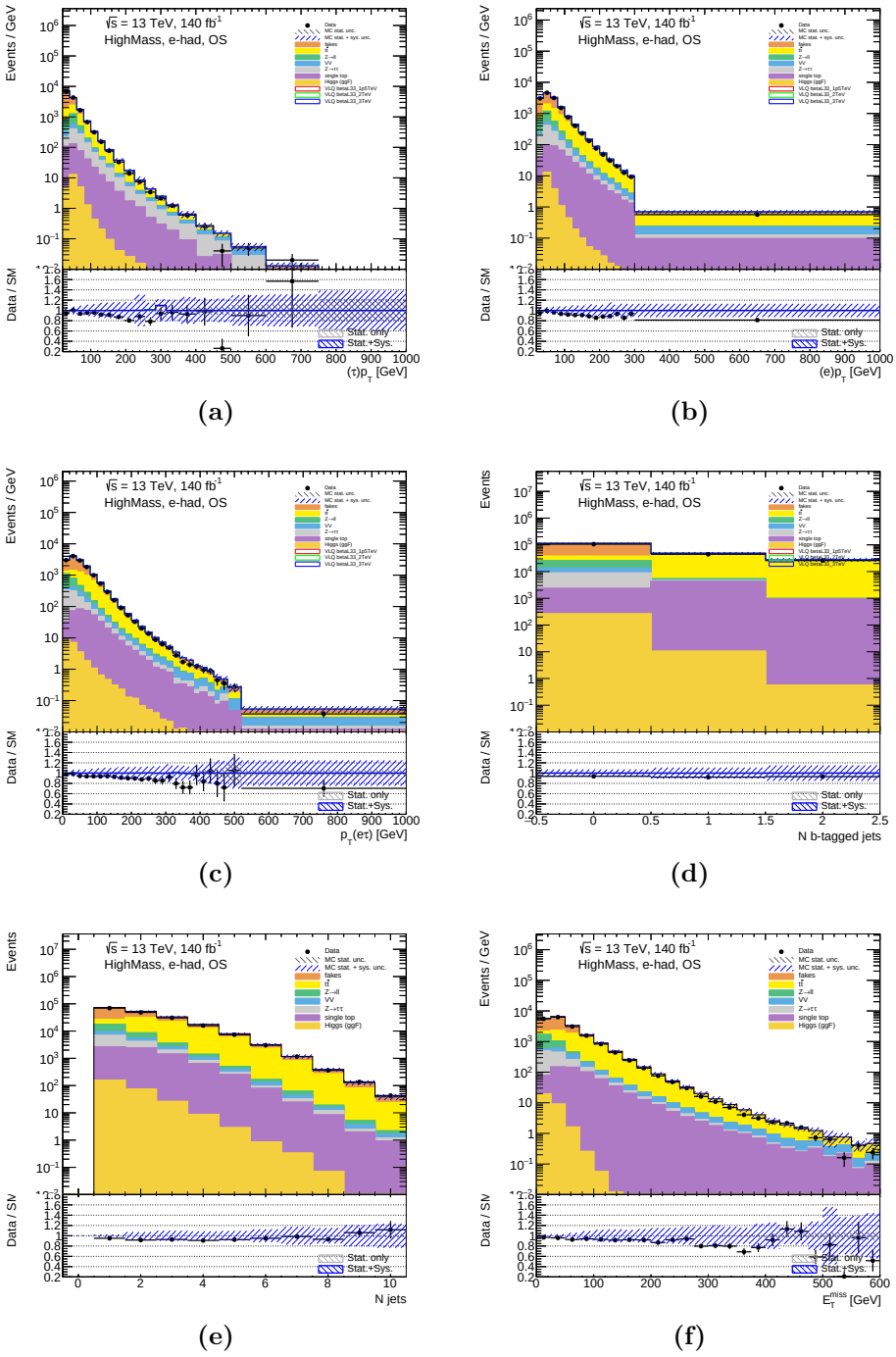

Figure D.2. Distributions of the tau p_{T} (a), electron p_{T} (b), $e\tau$ p_{T} (c), b-jet multiplicity (d), number of jets (e) and missing transverse momentum (f) obtained in data and MC simulation for the $e\tau_{\mathrm{had}}$ signal region.

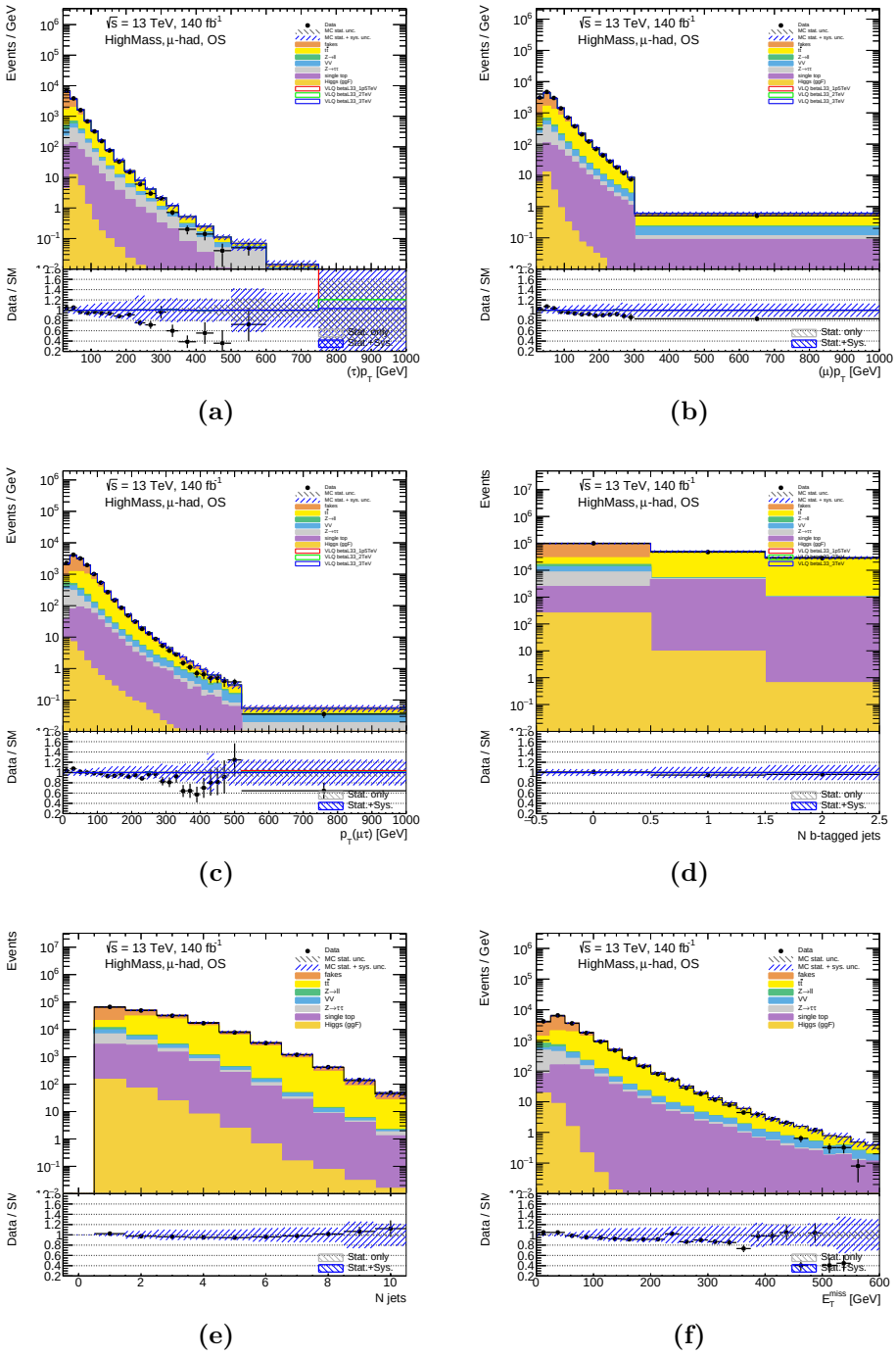

Figure D.3. Distributions of the tau p_{T} (a), muon p_{T} (b), $\mu\tau$ p_{T} (c), b-jet multiplicity (d), number of jets (e) and missing transverse momentum (f) obtained in data and MC simulation for the $\mu\tau_{\mathrm{had}}$ signal region.

Bibliography

[1] ATLAS Collaboration. Observation of a new particle in the search for the Standard Model Higgs boson with the ATLAS detector at the LHC. *Physics Letters B*, **716** (2012), 1. URL: http://arxiv.org/abs/1207.7214, arXiv:1207.7214, DOI: 10.1016/j.physletb.2012.08.020.

[2] CMS Collaboration. Observation of a new boson at a mass of 125 GeV with the CMS experiment at the LHC. *Physics Letters B*, **716** (2012), 30. URL: http://arxiv.org/abs/1207.7235, arXiv:1207.7235, DOI: 10.1016/j.physletb.2012.08.021.

[3] Luciano Maiani. *Electroweak Interactions*. CRC Press (2016). ISBN 978-1-4987-2226-1.

[4] Higgs, P. W. Broken Symmetries and the Masses of Gauge Bosons. *Physical Review Letters*, **13** (1964), 508. URL: https://link.aps.org/doi/10.1103/PhysRevLett.13.508, DOI: 10.1103/PhysRevLett.13.508.

[5] Englert, F. and Brout, R. Broken Symmetry and the Mass of Gauge Vector Mesons. *Physical Review Letters*, **13** (1964), 321. URL: https://link.aps.org/doi/10.1103/PhysRevLett.13.321, DOI: 10.1103/PhysRevLett.13.321.

[6] Workman, R. L. et al. Review of Particle Physics. *PTEP*, **2022** (2022), 083C01. DOI: 10.1093/ptep/ptac097.

[7] Altarelli, G. and Parisi, G. Asymptotic Freedom in Parton Language. *Nucl. Phys. B*, **126** (1977), 298. DOI: 10.1016/0550-3213(77)90384-4.

[8] Gribov, V. N. and Lipatov, L. N. Deep inelastic electron scattering in perturbation theory. *Physics Letters B*, **37** (1971), 78. URL: https://www.sciencedirect.com/science/article/pii/0370269371905764, DOI: 10.1016/0370-2693(71)90576-4.

[9] Dokshitzer, Y. L. Calculation of the Structure Functions for Deep Inelastic Scattering and e+ e- Annihilation by Perturbation Theory in Quantum Chromodynamics. *Sov. Phys. JETP*, **46** (1977), 641.

[10] ATLAS Collaboration. Standard Model Summary Plots October 2023 (2023). URL: https://cds.cern.ch/record/2882448.

[11] BaBar Collaboration. Evidence for an excess of $\overline{B} \to D^{(*)}\tau^-\overline{\nu}_\tau$ decays. *Physical Review Letters*, **109** (2012), 101802. URL: https://link.aps.org/doi/10.1103/PhysRevLett.109.101802, DOI: 10.1103/PhysRevLett.109.101802.

[12] BaBar Collaboration. Measurement of an excess of $\overline{B} \to D^{(*)}\tau^-\overline{\nu}_\tau$ decays and implications for charged Higgs bosons. *Physical Review D*, **88** (2013), 072012. URL: http://arxiv.org/abs/1303.0571, arXiv:1303.0571, DOI: 10.1103/PhysRevD.88.072012.

[13] Belle Collaboration. Measurement of the branching ratio of $\bar{B} \to D^{(*)}\tau^-\bar{\nu}_\tau$ relative to $\bar{B} \to D^{(*)}\ell^-\bar{\nu}_\ell$ decays with hadronic tagging at Belle. *Physical Review D*, **92** (2015), 072014. URL: http://arxiv.org/abs/1507.03233, arXiv:1507.03233, DOI: 10.1103/PhysRevD.92.072014.

[14] Belle Collaboration. Measurement of the τ lepton polarization and $R(D^*)$ in the decay $\bar{B} \to D^*\tau^-\bar{\nu}_\tau$. *Physical Review Letters*, **118** (2017), 211801. URL: http://arxiv.org/abs/1612.00529, arXiv:1612.00529, DOI: 10.1103/PhysRevLett.118.211801.

[15] LHCb Collaboration. Measurement of the Ratio of Branching Fractions $\mathscr{B}(\bar{B}^0 \to D^{*+}\tau^-\bar{\nu}_\tau)/\mathscr{B}(\bar{B}^0 \to D^{*+}\mu^-\bar{\nu}_\mu)$. *Physical Review Letters*, **115** (2015), 111803. URL: https://link.aps.org/doi/10.1103/PhysRevLett.115.111803, DOI: 10.1103/PhysRevLett.115.111803.

[16] LHCb Collaboration. Measurement of the ratios of branching fractions $\mathscr{R}(D^*)$ and $\mathscr{R}(D^0)$. *Physical Review Letters*, **131** (2023), 111802. URL: http://arxiv.org/abs/2302.02886, arXiv:2302.02886, DOI: 10.1103/PhysRevLett.131.111802.

[17] Heavy Flavor Averaging Group. Semileptonic B Decays. URL: https://hflav.web.cern.ch/content/semileptonic-b-decays.

[18] Pati, J. C. and Salam, A. Lepton number as the fourth "color". *Physical Review D*, **10** (1974), 275. URL: https://link.aps.org/doi/10.1103/PhysRevD.10.275, DOI: 10.1103/PhysRevD.10.275.

[19] Buttazzo, D., Greljo, A., Isidori, G., and Marzocca, D. B-physics anomalies: A guide to combined explanations. *Journal of High Energy Physics*, **2017** (2017), 44. URL: http://arxiv.org/abs/1706.07808, arXiv:1706.07808, DOI: 10.1007/JHEP11(2017)044.

[20] Cornella, C., Faroughy, D. A., Fuentes-Martín, J., Isidori, G., and Neubert, M. Reading the footprints of the B-meson flavor anomalies. *Journal of High Energy Physics*, **2021** (2021), 50. URL: https://doi.org/10.1007/JHEP08(2021)050, DOI: 10.1007/JHEP08(2021)050.

[21] Schmaltz, M. and Zhong, Y.-M. The Leptoquark Hunter's Guide: Large Coupling. *Journal of High Energy Physics*, **2019** (2019), 132. URL: http://arxiv.org/abs/1810.10017, arXiv:1810.10017, DOI: 10.1007/JHEP01(2019)132.

[22] ATLAS Collaboration. Searches for third-generation scalar leptoquarks in $\sqrt{s} = 13$ TeV pp collisions with the ATLAS detector. *Journal of High Energy Physics*, **2019** (2019), 144. URL: http://arxiv.org/abs/1902.08103, arXiv:1902.08103, DOI: 10.1007/JHEP06(2019)144.

[23] ATLAS Collaboration. Search for new phenomena in pp collisions in final states with tau leptons, b-jets, and missing transverse momentum with the ATLAS detector. *Physical Review D*, **104** (2021), 112005. URL: https://link.aps.org/doi/10.1103/PhysRevD.104.112005, DOI: 10.1103/PhysRevD.104.112005.

[24] ATLAS Collaboration. Search for pair production of third-generation scalar leptoquarks decaying into a top quark and a τ-lepton in pp collisions at $\sqrt{s}$= 13 TeV with the ATLAS detector. *Journal of High Energy Physics*, **2021** (2021), 179. URL: https://doi.org/10.1007/JHEP06(2021)179, DOI: 10.1007/JHEP06(2021)179.

[25] ATLAS Collaboration. Search for excited τ-leptons and leptoquarks in the final state with τ-leptons and jets in pp collisions at $\sqrt{s} = 13$ TeV with the ATLAS detector. *Journal of High Energy Physics*, **2023** (2023), 199. URL: http://arxiv.org/abs/2303.09444, arXiv:2303.09444, DOI: 10.1007/JHEP06(2023)199.

[26] CMS Collaboration. Search for heavy neutrinos and third-generation leptoquarks in hadronic states of two τ leptons and two jets in proton-proton collisions at $\sqrt{s} = 13$ TeV. *Journal of High Energy Physics*, **2019** (2019), 170. URL: https://doi.org/10.1007/JHEP03(2019)170, DOI: 10.1007/JHEP03(2019)170.

[27] CMS Collaboration. Search for singly and pair-produced leptoquarks coupling to third-generation fermions in proton-proton collisions at $\sqrt{s}$=13 TeV. *Physics Letters B*, **819** (2021), 136446. URL: https://www.sciencedirect.com/science/article/pii/S0370269321003865, DOI: 10.1016/j.physletb.2021.136446.

[28] CMS Collaboration. Searches for additional Higgs bosons and for vector leptoquarks in $\tau\tau$ final states in proton-proton collisions at $\sqrt{s}$= 13 TeV. *Journal of High Energy Physics*, **2023** (2023), 73. URL: https://doi.org/10.1007/JHEP07(2023)073, DOI: 10.1007/JHEP07(2023)073.

[29] ATLAS Collaboration. Search for Heavy Higgs Bosons Decaying into Two Tau Leptons with the ATLAS Detector Using pp Collisions at $\sqrt{s} = 13\,\text{TeV}$. *Physical Review Letters*, **125** (2020), 051801. URL: https://link.aps.org/doi/10.1103/PhysRevLett.125.051801, DOI: 10.1103/PhysRevLett.125.051801.

[30] Aebischer, J., Isidori, G., Pesut, M., Stefanek, B. A., and Wilsch, F. Confronting the vector leptoquark hypothesis with new low- and high-energy data. *The European Physical Journal C*, **83** (2023), 153. URL: http://

arxiv.org/abs/2210.13422, arXiv:2210.13422, DOI: 10.1140/epjc/s10052-023-11304-5.

[31] CMS Collaboration. Search for a third-generation leptoquark coupled to a τ lepton and a b quark through single, pair, and nonresonant production in proton-proton collisions at $\sqrt{s} = 13$ tev (2023). URL: http://arxiv.org/abs/2308.07826, arXiv:2308.07826, DOI: 10.48550/arXiv.2308.07826.

[32] Evans, L. and Bryant, P. LHC Machine. *Journal of Instrumentation*, **3** (2008), S08001. URL: https://dx.doi.org/10.1088/1748-0221/3/08/S08001, DOI: 10.1088/1748-0221/3/08/S08001.

[33] The High Luminosity LHC Project. URL: https://hilumilhc.web.cern.ch/content/hl-lhc-project.

[34] Lopienska, E. The CERN accelerator complex, layout in 2022 (2022). URL: https://cds.cern.ch/record/2800984.

[35] ATLAS Collaboration. The ATLAS Experiment at the CERN Large Hadron Collider. *Journal of Instrumentation*, **3** (2008), S08003. URL: https://dx.doi.org/10.1088/1748-0221/3/08/S08003, DOI: 10.1088/1748-0221/3/08/S08003.

[36] CMS Collaboration. The CMS experiment at the CERN LHC. *Journal of Instrumentation*, **3** (2008), S08004. URL: https://dx.doi.org/10.1088/1748-0221/3/08/S08004, DOI: 10.1088/1748-0221/3/08/S08004.

[37] ALICE Collaboration. The ALICE experiment at the CERN LHC. *Journal of Instrumentation*, **3** (2008), S08002. URL: https://dx.doi.org/10.1088/1748-0221/3/08/S08002, DOI: 10.1088/1748-0221/3/08/S08002.

[38] LHCb Collaboration. The LHCb Detector at the LHC. *Journal of Instrumentation*, **3** (2008), S08005. URL: https://dx.doi.org/10.1088/1748-0221/3/08/S08005, DOI: 10.1088/1748-0221/3/08/S08005.

[39] TOTEM Collaboration. The TOTEM Experiment at the CERN Large Hadron Collider. *Journal of Instrumentation*, **3** (2008), S08007. URL: https://dx.doi.org/10.1088/1748-0221/3/08/S08007, DOI: 10.1088/1748-0221/3/08/S08007.

[40] FASER Collaboration. FASER: ForwArd Search ExpeRiment at the LHC (2019). URL: http://arxiv.org/abs/1901.04468, arXiv:1901.04468, DOI: 10.48550/arXiv.1901.04468.

[41] Pinfold, J., et al. Technical Design Report of the MoEDAL Experiment. CERN-LHCC-2009-006 (2009). URL: https://cds.cern.ch/record/1181486.

[42] LHCf Collaboration. The LHCf detector at the CERN Large Hadron Collider. *Journal of Instrumentation*, **3** (2008), S08006. URL: https://dx.doi.org/10.1088/1748-0221/3/08/S08006, DOI: 10.1088/1748-0221/3/08/S08006.

[43] SND@LHC Collaboration. SND@LHC: The Scattering and Neutrino Detector at the LHC (2023). URL: http://arxiv.org/abs/2210.02784, arXiv:2210.02784, DOI: 10.48550/arXiv.2210.02784.

[44] ATLAS Collaboration. Operation of the ATLAS trigger system in Run 2. *Journal of Instrumentation*, **15** (2020), P10004. URL: http://arxiv.org/abs/2007.12539, arXiv:2007.12539, DOI: 10.1088/1748-0221/15/10/P10004.

[45] ATLAS Collaboration. Public ATLAS Luminosity Results for Run-1 of the LHC. URL: https://twiki.cern.ch/twiki/bin/view/AtlasPublic/LuminosityPublicResultsRun1.

[46] ATLAS Collaboration. Public ATLAS Luminosity Results for Run-2 of the LHC. URL: https://twiki.cern.ch/twiki/bin/view/AtlasPublic/LuminosityPublicResultsRun2.

[47] ATLAS Collaboration. Measurement of the Inelastic Proton-Proton Cross Section at $\sqrt{s} = 13\,\text{TeV}$ with the ATLAS Detector at the LHC. *Physical Review Letters*, **117** (2016), 182002. URL: http://arxiv.org/abs/1606.02625, arXiv:1606.02625, DOI: 10.1103/PhysRevLett.117.182002.

[48] ATLAS Collaboration. Public ATLAS Luminosity Results for Run-3 of the LHC. URL: https://twiki.cern.ch/twiki/bin/view/AtlasPublic/LuminosityPublicResultsRun3.

[49] ATLAS Collaboration. ATLAS magnet system: Technical Design Report (1997). URL: https://cds.cern.ch/record/338080, DOI: 10.17181/CERN.9O5C.VDTM.

[50] Yamamoto, A., et al. The ATLAS central solenoid. *Nuclear Instruments and Methods in Physics Research Section A: Accelerators, Spectrometers, Detectors and Associated Equipment*, **584** (2008), 53. URL: https://www.sciencedirect.com/science/article/pii/S0168900207020414, DOI: 10.1016/j.nima.2007.09.047.

[51] ATLAS Collaboration. ATLAS inner detector: Technical Design Report. CERN-LHCC-97-016, CERN, Geneva (1997). URL: https://cds.cern.ch/record/331063.

[52] Capeans, M., et al. ATLAS Insertable B-Layer Technical Design Report. CERN-LHCC-2010-013 (2010). URL: https://cds.cern.ch/record/1291633.

[53] ATLAS Collaboration. ATLAS liquid-argon calorimeter: Technical Design Report. CERN-LHCC-96-041, CERN, Geneva (1996). URL: https://cds.cern.ch/record/331061, DOI: 10.17181/CERN.FWRW.FOOQ.

[54] ATLAS Collaboration. ATLAS tile calorimeter: Technical Design Report. CERN-LHCC-96-042, CERN, Geneva (1996). URL: https://cds.cern.ch/record/331062, DOI: 10.17181/CERN.JRBJ.7O28.

[55] ATLAS Collaboration. ATLAS muon spectrometer: Technical Design Report. CERN-LHCC-97-022, CERN, Geneva (1997). URL: https://cds.cern.ch/record/331068.

[56] ATLAS Collaboration. ATLAS level-1 trigger: Technical Design Report. CERN-LHCC-98-014, CERN, Geneva (1998). URL: https://cds.cern.ch/record/381429.

[57] ATLAS Collaboration. Athena. Zenodo (2021). URL: https://zenodo.org/record/4772550, DOI: 10.5281/zenodo.4772550.

[58] ATLAS Collaboration. The ATLAS Simulation Infrastructure. *Eur. Phys. J. C*, **70** (2010), 823. DOI: 10.1140/epjc/s10052-010-1429-9.

[59] Sjöstrand, T., Mrenna, S., and Skands, P. A brief introduction to PYTHIA 8.1. *Computer Physics Communications*, **178** (2008), 852. URL: https://www.sciencedirect.com/science/article/pii/S0010465508000441, DOI: 10.1016/j.cpc.2008.01.036.

[60] Bothmann, E., et al. Event generation with Sherpa 2.2. *SciPost Physics*, **7** (2019), 034. URL: https://scipost.org/10.21468/SciPostPhys.7.3.034, DOI: 10.21468/SciPostPhys.7.3.034.

[61] Alioli, S., Nason, P., Oleari, C., and Re, E. A general framework for implementing NLO calculations in shower Monte Carlo programs: The POWHEG BOX. *Journal of High Energy Physics*, **2010** (2010), 43. URL: https://doi.org/10.1007/JHEP06(2010)043, DOI: 10.1007/JHEP06(2010)043.

[62] Agostinelli, S., et al. Geant4—a simulation toolkit. *Nuclear Instruments and Methods in Physics Research Section A: Accelerators, Spectrometers, Detectors and Associated Equipment*, **506** (2003), 250. URL: https://www.sciencedirect.com/science/article/pii/S0168900203013688, DOI: 10.1016/S0168-9002(03)01368-8.

[63] Barrand, G., et al. GAUDI — A software architecture and framework for building HEP data processing applications. *Computer Physics Communications*, **140** (2001), 45. URL: https://www.sciencedirect.com/science/article/pii/S0010465501002545, DOI: 10.1016/S0010-4655(01)00254-5.

[64] ATLAS Collaboration. Event Displays from Run 2 physics analyses not included in publications. URL: https://twiki.cern.ch/twiki/bin/view/AtlasPublic/EventDisplayRun2Physics.

[65] ATLAS Collaboration. Performance of the ATLAS track reconstruction algorithms in dense environments in LHC Run 2. *The European Physical Journal C*, **77** (2017), 673. URL: https://doi.org/10.1140/epjc/s10052-017-5225-7, DOI: 10.1140/epjc/s10052-017-5225-7.

[66] Frühwirth, R. Application of Kalman filtering to track and vertex fitting. *Nuclear Instruments and Methods in Physics Research Section*

A: Accelerators, Spectrometers, Detectors and Associated Equipment, **262** (1987), 444. URL: https://www.sciencedirect.com/science/article/pii/0168900287908874, DOI: 10.1016/0168-9002(87)90887-4.

[67] ATLAS Collaboration. Reconstruction of primary vertices at the ATLAS experiment in Run 1 proton–proton collisions at the LHC. *The European Physical Journal C*, **77** (2017), 332. URL: https://doi.org/10.1140/epjc/s10052-017-4887-5, DOI: 10.1140/epjc/s10052-017-4887-5.

[68] ATLAS Collaboration. Vertex Reconstruction Performance of the ATLAS Detector at $\sqrt{s} = 13\,\text{TeV}$. ATL-PHYS-PUB-2015-026, Geneva (2015). URL: https://cds.cern.ch/record/2037717.

[69] ATLAS Collaboration. Electron and photon performance measurements with the ATLAS detector using the 2015–2017 LHC proton-proton collision data. *Journal of Instrumentation*, **14** (2019), P12006. URL: https://dx.doi.org/10.1088/1748-0221/14/12/P12006, DOI: 10.1088/1748-0221/14/12/P12006.

[70] ATLAS Collaboration. Topological cell clustering in the ATLAS calorimeters and its performance in LHC Run 1. *The European Physical Journal C*, **77** (2017), 490. URL: https://doi.org/10.1140/epjc/s10052-017-5004-5, DOI: 10.1140/epjc/s10052-017-5004-5.

[71] ATLAS Collaboration. Muon reconstruction and identification efficiency in ATLAS using the full Run 2 pp collision data set at $\sqrt{s} = 13\,\text{TeV}$. *The European Physical Journal C*, **81** (2021), 578. URL: https://doi.org/10.1140/epjc/s10052-021-09233-2, DOI: 10.1140/epjc/s10052-021-09233-2.

[72] Illingworth, J. and Kittler, J. A survey of the hough transform. *Computer Vision, Graphics, and Image Processing*, **44** (1988), 87. URL: https://www.sciencedirect.com/science/article/pii/S0734189X88800331, DOI: 10.1016/S0734-189X(88)80033-1.

[73] ATLAS Collaboration. Reconstruction, Energy Calibration, and Identification of Hadronically Decaying Tau Leptons in the ATLAS Experiment for Run-2 of the LHC. ATL-PHYS-PUB-2015-045, Geneva (2015). URL: https://cds.cern.ch/record/2064383.

[74] ATLAS Collaboration. Measurement of the tau lepton reconstruction and identification performance in the ATLAS experiment using pp collisions at $\sqrt{s} = 13\,\text{TeV}$. ATLAS-CONF-2017-029, Geneva (2017). URL: https://cds.cern.ch/record/2261772.

[75] Cacciari, M., Salam, G. P., and Soyez, G. The anti-k_t jet clustering algorithm. *Journal of High Energy Physics*, **2008** (2008), 063. URL: http://arxiv.org/abs/0802.1189, arXiv:0802.1189, DOI: 10.1088/1126-6708/2008/04/063.

[76] Barillari, T., et al. Local Hadronic Calibration. ATL-LARG-PUB-2009-001-2, Geneva (2008). URL: https://cds.cern.ch/record/1112035.

[77] ATLAS Collaboration. Reconstruction of hadronic decay products of tau leptons with the ATLAS experiment. *The European Physical Journal C*, **76** (2016), 295. URL: https://doi.org/10.1140/epjc/s10052-016-4110-0, DOI: 10.1140/epjc/s10052-016-4110-0.

[78] ATLAS Collaboration. Identification and energy calibration of hadronically decaying tau leptons with the ATLAS experiment in pp collisions at $\sqrt{s} = 8\,\text{TeV}$. *The European Physical Journal C*, **75** (2015), 303. URL: https://doi.org/10.1140/epjc/s10052-015-3500-z, DOI: 10.1140/epjc/s10052-015-3500-z.

[79] ATLAS Collaboration. Identification of hadronic tau lepton decays using neural networks in the ATLAS experiment. ATL-PHYS-PUB-2019-033, Geneva (2019). URL: https://cds.cern.ch/record/2688062.

[80] Hochreiter, S. and Schmidhuber, J. Long Short-Term Memory. *Neural Computation*, **9** (1997), 1735. URL: https://doi.org/10.1162/neco.1997.9.8.1735, DOI: 10.1162/neco.1997.9.8.1735.

[81] ATLAS Collaboration. Jet reconstruction and performance using particle flow with the ATLAS Detector. *The European Physical Journal C*, **77** (2017), 466. URL: https://doi.org/10.1140/epjc/s10052-017-5031-2, DOI: 10.1140/epjc/s10052-017-5031-2.

[82] Cacciari, M. and Salam, G. P. Pileup subtraction using jet areas. *Physics Letters B*, **659** (2008), 119. URL: https://www.sciencedirect.com/science/article/pii/S0370269307011094, DOI: 10.1016/j.physletb.2007.09.077.

[83] ATLAS Collaboration. Jet energy scale and resolution measured in proton-proton collisions at $\sqrt{s} = 13\,\text{TeV}$ with the ATLAS detector (2021). URL: http://arxiv.org/abs/2007.02645, arXiv:2007.02645, DOI: 10.1140/epjc/s10052-021-09402-3.

[84] ATLAS Collaboration. Jet global sequential corrections with the ATLAS detector in proton-proton collisions at $\sqrt{(s)} = 8\,\text{TeV}$. ATLAS-CONF-2015-002, Geneva (2015). URL: https://cds.cern.ch/record/2001682.

[85] ATLAS Collaboration. Tagging and suppression of pileup jets with the ATLAS detector. ATLAS-CONF-2014-018, Geneva (2014). URL: https://cds.cern.ch/record/1700870.

[86] ATLAS Collaboration. Performance of b-Jet Identification in the ATLAS Experiment. *Journal of Instrumentation*, **11** (2016), P04008. URL: http://arxiv.org/abs/1512.01094, arXiv:1512.01094, DOI: 10.1088/1748-0221/11/04/P04008.

[87] ATLAS Collaboration. ATLAS *b*-jet identification performance and efficiency measurement with $t\bar{t}$ events in pp collisions at $\sqrt{s} = 13\,\text{TeV}$. *The European Physical Journal C*, **79** (2019), 970. URL: https://doi.org/10.1140/epjc/s10052-019-7450-8, DOI: 10.1140/epjc/s10052-019-7450-8.

[88] ATLAS Collaboration. Optimisation and performance studies of the ATLAS b-tagging algorithms for the 2017-18 LHC run. ATL-PHYS-PUB-2017-013, Geneva (2017). URL: https://cds.cern.ch/record/2273281.

[89] ATLAS Collaboration. Secondary vertex finding for jet flavour identification with the ATLAS detector. ATL-PHYS-PUB-2017-011, Geneva (2017). URL: https://cds.cern.ch/record/2270366.

[90] ATLAS Collaboration. Topological b-hadron decay reconstruction and identification of b-jets with the JetFitter package in the ATLAS experiment at the LHC. ATL-PHYS-PUB-2018-025, Geneva (2018). URL: https://cds.cern.ch/record/2645405.

[91] ATLAS Collaboration. Identification of Jets Containing b-Hadrons with Recurrent Neural Networks at the ATLAS Experiment. ATL-PHYS-PUB-2017-003, Geneva (2017). URL: https://cds.cern.ch/record/2255226.

[92] ATLAS Collaboration. ATLAS flavour-tagging algorithms for the LHC Run 2 pp collision dataset. *The European Physical Journal C*, **83** (2023), 681. URL: https://doi.org/10.1140/epjc/s10052-023-11699-1, DOI: 10.1140/epjc/s10052-023-11699-1.

[93] ATLAS Collaboration. E_T^{miss} performance in the ATLAS detector using 2015-2016 LHC p-p collisions. ATLAS-CONF-2018-023, Geneva (2018). URL: https://cds.cern.ch/record/2625233.

[94] ATLAS Collaboration. Performance of missing transverse momentum reconstruction with the ATLAS detector using proton–proton collisions at $\sqrt{s} = 13\,\text{TeV}$. *The European Physical Journal C*, **78** (2018), 903. URL: https://doi.org/10.1140/epjc/s10052-018-6288-9, DOI: 10.1140/epjc/s10052-018-6288-9.

[95] ATLAS Collaboration. Measurement of the Z to tau tau cross section with the ATLAS detector. *Physical Review D*, **84** (2011), 112006. URL: http://arxiv.org/abs/1108.2016, arXiv:1108.2016, DOI: 10.1103/PhysRevD.84.112006.

[96] ATLAS Collaboration. Test of CP invariance in vector-boson fusion production of the Higgs boson in the $h \to \tau\tau$ channel in proton−proton collisions at $\sqrt{s} = 13$ TeV with the ATLAS detector. *Physics Letters B*, **805** (2020), 135426. URL: http://arxiv.org/abs/2002.05315, arXiv:2002.05315, DOI: 10.1016/j.physletb.2020.135426.

[97] ATLAS Collaboration. Measurements of Higgs boson production cross-sections in the $h \to \tau^+\tau^-$ decay channel in pp collisions at $\sqrt{s}$= 13 TeV with the ATLAS detector. *Journal of High Energy Physics*, **2022** (2022), 175. URL: https://doi.org/10.1007/JHEP08(2022)175, DOI: 10.1007/JHEP08(2022)175.

[98] Swain, A. K. and Konar, P. Constrained $\sqrt{\hat{s}_{min}}$ and reconstructing with semi-invisible production at hadron colliders. *Journal of High Energy Physics*, **2015** (2015), 142. URL: http://arxiv.org/abs/1412.6624, arXiv:1412.6624, DOI: 10.1007/JHEP03(2015)142.

[99] Gleisberg, T. and Höche, S. Comix, a new matrix element generator. *Journal of High Energy Physics*, **2008** (2008), 039. URL: https://dx.doi.org/10.1088/1126-6708/2008/12/039, DOI: 10.1088/1126-6708/2008/12/039.

[100] Buccioni, F., Lang, J.-N., Lindert, J. M., Maierhöfer, P., Pozzorini, S., Zhang, H., and Zoller, M. F. OpenLoops 2. *The European Physical Journal C*, **79** (2019), 866. URL: https://doi.org/10.1140/epjc/s10052-019-7306-2, DOI: 10.1140/epjc/s10052-019-7306-2.

[101] Schumann, S. and Krauss, F. A parton shower algorithm based on Catani-Seymour dipole factorisation. *Journal of High Energy Physics*, **2008** (2008), 038. URL: https://dx.doi.org/10.1088/1126-6708/2008/03/038, DOI: 10.1088/1126-6708/2008/03/038.

[102] Höche, S., Krauss, F., Schönherr, M., and Siegert, F. QCD matrix elements + parton showers. The NLO case. *Journal of High Energy Physics*, **2013** (2013), 27. URL: https://doi.org/10.1007/JHEP04(2013)027, DOI: 10.1007/JHEP04(2013)027.

[103] Ball, R. D., et al. Parton distributions for the LHC run II. *Journal of High Energy Physics*, **2015** (2015), 40. URL: https://doi.org/10.1007/JHEP04(2015)040, DOI: 10.1007/JHEP04(2015)040.

[104] ATLAS Collaboration. Measurement of the Z/Γ* boson transverse momentum distribution in pp collisions at $\sqrt{s} = 7$ TeV with the ATLAS detector. *Journal of High Energy Physics*, **2014** (2014), 145. URL: https://doi.org/10.1007/JHEP09(2014)145, DOI: 10.1007/JHEP09(2014)145.

[105] Lai, H.-L., Guzzi, M., Huston, J., Li, Z., Nadolsky, P. M., Pumplin, J., and Yuan, C.-P. New parton distributions for collider physics. *Physical Review D*, **82** (2010), 074024. URL: https://link.aps.org/doi/10.1103/PhysRevD.82.074024, DOI: 10.1103/PhysRevD.82.074024.

[106] Pumplin, J., Stump, D. R., Huston, J., Lai, H. L., Nadolsky, P., and Tung, W. K. New Generation of Parton Distributions with Uncertainties from Global QCD Analysis. *Journal of High Energy Physics*, **2002** (2002), 012. URL: http://arxiv.org/abs/hep-ph/0201195, arXiv:hep-ph/0201195, DOI: 10.1088/1126-6708/2002/07/012.

[107] Golonka, P. and Was, Z. PHOTOS Monte Carlo: A precision tool for QED corrections in Z and W decays. *The European Physical Journal C*, **45** (2006), 97. URL: http://arxiv.org/abs/hep-ph/0506026, arXiv:hep-ph/0506026, DOI: 10.1140/epjc/s2005-02396-4.

[108] Lange, D. J. The EvtGen particle decay simulation package. *Nuclear Instruments and Methods in Physics Research Section A: Accelerators, Spectrometers, Detectors and Associated Equipment*, **462** (2001), 152. URL: https://www.sciencedirect.com/science/article/pii/S0168900201000894, DOI: 10.1016/S0168-9002(01)00089-4.

[109] Sjöstrand, T., et al. An introduction to PYTHIA 8.2. *Computer Physics Communications*, **191** (2015), 159. URL: https://www.sciencedirect.com/science/article/pii/S0010465515000442, DOI: 10.1016/j.cpc.2015.01.024.

[110] ATLAS Collaboration. ATLAS Pythia 8 tunes to 7 TeV data. ATL-PHYS-PUB-2014-021, CERN, Geneva (2014). URL: https://cds.cern.ch/record/1966419.

[111] Ball, R. D., et al. Parton distributions with LHC data. *Nuclear Physics B*, **867** (2013), 244. URL: https://www.sciencedirect.com/science/article/pii/S0550321312005500, DOI: 10.1016/j.nuclphysb.2012.10.003.

[112] Bähr, M., et al. Herwig++ physics and manual. *The European Physical Journal C*, **58** (2008), 639. URL: https://doi.org/10.1140/epjc/s10052-008-0798-9, DOI: 10.1140/epjc/s10052-008-0798-9.

[113] Bellm, J., et al. Herwig 7.0/Herwig++ 3.0 release note. *The European Physical Journal C*, **76** (2016), 196. URL: https://doi.org/10.1140/epjc/s10052-016-4018-8, DOI: 10.1140/epjc/s10052-016-4018-8.

[114] Harland-Lang, L. A., Martin, A. D., Motylinski, P., and Thorne, R. S. Parton distributions in the LHC era: MMHT 2014 PDFs. *The European Physical Journal C*, **75** (2015), 204. URL: https://doi.org/10.1140/epjc/s10052-015-3397-6, DOI: 10.1140/epjc/s10052-015-3397-6.

[115] Frixione, S., Laenen, E., Motylinski, P., White, C., and Webber, B. R. Single-top hadroproduction in association with a W boson. *Journal of High Energy Physics*, **2008** (2008), 029. URL: https://dx.doi.org/10.1088/1126-6708/2008/07/029, DOI: 10.1088/1126-6708/2008/07/029.

[116] Studies on top-quark Monte Carlo modelling for Top2016. ATL-PHYS-PUB-2016-020, CERN, Geneva (2016). URL: https://cds.cern.ch/record/2216168.

[117] Alwall, J., et al. The automated computation of tree-level and next-to-leading order differential cross sections, and their matching to parton shower simulations. *Journal of High Energy Physics*, **2014** (2014), 79. URL: https://doi.org/10.1007/JHEP07(2014)079, DOI: 10.1007/JHEP07(2014)079.

[118] Lönnblad, L. and Prestel, S. Matching tree-level matrix elements with interleaved showers. *Journal of High Energy Physics*, **2012** (2012), 19. URL: https://doi.org/10.1007/JHEP03(2012)019, DOI: 10.1007/JHEP03(2012)019.

[119] Doršner, I. and Greljo, A. Leptoquark toolbox for precision collider studies. *Journal of High Energy Physics*, **2018** (2018), 126. URL: https://doi.org/10.1007/JHEP05(2018)126, DOI: 10.1007/JHEP05(2018)126.

[120] Cacciari, M., Salam, G. P., and Soyez, G. FastJet user manual. *The European Physical Journal C*, **72** (2012), 1896. URL: https://doi.org/10.1140/epjc/s10052-012-1896-2, DOI: 10.1140/epjc/s10052-012-1896-2.

[121] ATLAS Collaboration. Performance of the ATLAS muon triggers in Run 2. *Journal of Instrumentation*, **15** (2020), P09015. URL: https://dx.doi.org/10.1088/1748-0221/15/09/P09015, DOI: 10.1088/1748-0221/15/09/P09015.

[122] ATLAS Collaboration. Performance of electron and photon triggers in ATLAS during LHC Run 2. *The European Physical Journal C*, **80** (2020), 47. URL: https://doi.org/10.1140/epjc/s10052-019-7500-2, DOI: 10.1140/epjc/s10052-019-7500-2.

[123] ATLAS Collaboration. The ATLAS Tau Trigger in Run 2. ATLAS-CONF-2017-061, CERN, Geneva (2017). URL: https://cds.cern.ch/record/2274201.

[124] Pleskot, V., Martinovicova, G., Scheirich, D., Padovano, G., Hamity, G. N., and Fomin, N. Universal Fake Factor Method. ATL-COM-PHYS-2023-610, CERN, Geneva (2023). URL: https://cds.cern.ch/record/2864863.

[125] ATLAS Collaboration. Luminosity determination in pp collisions at $\sqrt{s} =$ 13 TeV using the ATLAS detector at the LHC. ATLAS-CONF-2019-021, CERN, Geneva (2019). URL: https://cds.cern.ch/record/2677054.

[126] Read, A. L. Presentation of search results: The CLs technique. *Journal of Physics G: Nuclear and Particle Physics*, **28** (2002), 2693. URL: https://dx.doi.org/10.1088/0954-3899/28/10/313, DOI: 10.1088/0954-3899/28/10/313.

[127] Cowan, G., Cranmer, K., Gross, E., and Vitells, O. Asymptotic formulae for likelihood-based tests of new physics. *The European Physical Journal C*, **71** (2011), 1554. URL: https://doi.org/10.1140/epjc/s10052-011-1554-0, DOI: 10.1140/epjc/s10052-011-1554-0.

[128] Heinrich, L., Feickert, M., Stark, G., and Cranmer, K. Pyhf: Pure-Python implementation of HistFactory statistical models. *Journal of Open Source Software*, **6** (2021), 2823. URL: https://joss.theoj.org/papers/10.21105/joss.02823, DOI: 10.21105/joss.02823.

[129] Cranmer, K. and Held, A. Building and steering template fits with cabinetry (2021). URL: https://zenodo.org/records/4627038, DOI: 10.5281/zenodo.4627038.

[130] Béjar Alonso, I., et al. High-Luminosity Large Hadron Collider (HL-LHC): Technical design report. *CERN Yellow Reports: Monographs*, **10** (2020). URL: https://e-publishing.cern.ch/index.php/CYRM/article/view/1153, DOI: 10.23731/CYRM-2020-0010.1.

[131] ATLAS Collaboration. ATLAS Phase-II Upgrade Scoping Document. CERN-LHCC-2015-020, Geneva (2015). URL: https://cds.cern.ch/record/2055248, DOI: 10.17181/CERN.7CRX.AJHP.

[132] ATLAS Collaboration. Expected tracking and related performance with the updated ATLAS Inner Tracker layout at the High-Luminosity LHC. ATL-PHYS-PUB-2021-024, CERN, Geneva (2021). URL: https://cds.cern.ch/record/2776651.

[133] ATLAS Collaboration. Technical Design Report for the ATLAS Inner Tracker Pixel Detector. CERN-LHCC-2017-021, CERN, Geneva (2017). URL: https://cds.cern.ch/record/2285585, DOI: 10.17181/CERN.FOZZ.ZP3Q.

[134] ATLAS Collaboration. Technical Design Report for the ATLAS Inner Tracker Strip Detector. CERN-LHCC-2017-005, CERN, Geneva (2017). URL: https://cds.cern.ch/record/2257755.

[135] ATLAS Collaboration. Technical Design Report: A High-Granularity Timing Detector for the ATLAS Phase-II Upgrade. CERN-LHCC-2020-007, CERN, Geneva (2020). URL: https://cds.cern.ch/record/2719855.

[136] ATLAS Collaboration. ATLAS Liquid Argon Calorimeter Phase-II Upgrade: Technical Design Report. CERN-LHCC-2017-018, CERN, Geneva (2017). URL: https://cds.cern.ch/record/2285582, DOI: 10.17181/CERN.6QIO.YGHO.

[137] ATLAS Collaboration. Technical Design Report for the Phase-II Upgrade of the ATLAS Tile Calorimeter. CERN-LHCC-2017-019, CERN, Geneva (2017). URL: https://cds.cern.ch/record/2285583.

[138] ATLAS Collaboration. New Small Wheel Technical Design Report. CERN-LHCC-2013-006 (2013). URL: https://cds.cern.ch/record/1552862.

[139] ATLAS Collaboration. The ATLAS BIS78 Project. ATL-MUON-INT-2016-002, CERN, Geneva (2016). URL: https://cds.cern.ch/record/2161109.

[140] ATLAS Collaboration. Technical Design Report for the Phase-II Upgrade of the ATLAS Muon Spectrometer. CERN-LHCC-2017-017, CERN, Geneva (2017). URL: https://cds.cern.ch/record/2285580.

[141] ATLAS Collaboration. Technical Design Report for the Phase-II Upgrade of the ATLAS TDAQ System. CERN-LHCC-2017-020, CERN, Geneva (2017). URL: https://cds.cern.ch/record/2285584, DOI: 10.17181/CERN.2LBB.4IAL.

[142] Moreira, P., et al. lpGBT documentation: Release (2022). URL: https://cds.cern.ch/record/2809058.

[143] Reed, I. S. and Solomon, G. Polynomial Codes Over Certain Finite Fields. *Journal of the Society for Industrial and Applied Mathematics*, **8** (1960), 300. URL: https://epubs.siam.org/doi/10.1137/0108018, DOI: 10.1137/0108018.

[144] LpGBT-FPGA: Main Page. URL: https://lpgbt-fpga.web.cern.ch/doc/html/.

[145] AMD Kintex7 FPGA KC705 Evaluation Kit. URL: https://www.xilinx.com/products/boards-and-kits/ek-k7-kc705-g.html.

[146] Corradi, M., Gkountoumis, P., Kyriakis-Bitzaros, E., Longarini, I., Mesolongitis, I., Morodei, F., Vari, R., and Zachariadou, K. Upgraded Data Readout and Transmission Electronics for the Resistive Plate Chambers of the ATLAS Muon Trigger System for the High Luminosity LHC. In *2021 IEEE Nuclear Science Symposium and Medical Imaging Conference (NSS/MIC)*, pp. 1–4 (2021). DOI: 10.1109/NSS/MIC44867.2021.9875551.

[147] lpGBT emulator (2023). URL: https://gitlab.cern.ch/gbt-fpga/lpgbt-emul.

[148] Vivado Overview. URL: https://www.xilinx.com/products/design-tools/vivado.html.

[149] Corradi, M., et al. Specifications of the RPC Data Collector and Transmitter (DCT) board. URL: https://edms.cern.ch/ui/#!master/navigator/document?D:100544643:100544643:subDocs.

[150] Artix 7 FPGA Family. URL: https://www.xilinx.com/products/silicon-devices/fpga/artix-7.html.

[151] Kintex 7 FPGA Family. URL: https://www.xilinx.com/products/silicon-devices/fpga/kintex-7.html.

[152] Interactive web pages for radiation environment exploration of ATLAS. ATL-SOFT-PUB-2020-003, CERN, Geneva (2020). URL: https://cds.cern.ch/record/2742378.

[153] Versatile Link PLUS. URL: https://espace.cern.ch/project-Versatile-Link-Plus/SitePages/Home.aspx.

[154] Update on Latency Figures and Mitigation Strategies. URL: https://edms.cern.ch/ui/#!master/navigator/document?D:100827848:100827848:subDocs.

[155] Bauce, M., et al. Specification document of the Barrel Sector Logic board. URL: https://edms.cern.ch/ui/#!master/navigator/document?D:101013128:101013128:subDocs.

[156] Virtex UltraScale+ FPGA family. URL: https://www.xilinx.com/products/silicon-devices/fpga/virtex-ultrascale-plus.html.

[157] Mercury XU5 Zynq UltraScale+ MPSoC. URL: https://www.xilinx.com/products/boards-and-kits/1-1hm4mgj.html.

[158] Morodei, F., et al. Status of the Level-0 ATLAS barrel muon trigger for High-Luminosity LHC. *Journal of Instrumentation*, **18** (2023), C02047. URL: https://dx.doi.org/10.1088/1748-0221/18/02/C02047, DOI: 10.1088/1748-0221/18/02/C02047.